



DESIGN AND EVALUATION OF DUAL-EXPANDER AEROSPIKE NOZZLE

UPPER STAGE ENGINE

DISSERTATION

Joseph R. Simmons, III,

AFIT-ENY-DS-14-S-06

**DEPARTMENT OF THE AIR FORCE
AIR UNIVERSITY**

AIR FORCE INSTITUTE OF TECHNOLOGY

Wright-Patterson Air Force Base, Ohio

**DISTRIBUTION STATEMENT A:
APPROVED FOR PUBLIC RELEASE; DISTRIBUTION UNLIMITED**

The views expressed in this dissertation are those of the author and do not reflect the official policy or position of the United States Air Force, the Department of Defense, or the United States Government.

This material is declared a work of the U.S. Government and is not subject to copyright protection in the United States.

AFIT-ENY-DS-14-S-06

DESIGN AND EVALUATION OF DUAL-EXPANDER AEROSPIKE NOZZLE UPPER
STAGE ENGINE

DISSERTATION

Presented to the Faculty
Dean, Graduate School of Engineering and Management
Air Force Institute of Technology
Air University
Air Education and Training Command
in Partial Fulfillment of the Requirements for the
Degree of Doctor of Philosophy

Joseph R. Simmons, III, BFA, MS

September 2014

DISTRIBUTION STATEMENT A:
APPROVED FOR PUBLIC RELEASE; DISTRIBUTION UNLIMITED

DESIGN AND EVALUATION OF DUAL-EXPANDER AEROSPIKE NOZZLE UPPER
STAGE ENGINE

DISSERTATION

Joseph R. Simmons, III, BFA, MS

Approved:

<u>//signed//</u> Jonathan Black, PhD (Chairman)	<u>15 Jul 2014</u> Date
<u>//signed//</u> LtCol Ronald Simmons, PhD (Member)	<u>15 Jul 2014</u> Date
<u>//signed//</u> LtCol Richard Branam, PhD (Member)	<u>15 Jul 2014</u> Date
<u>//signed//</u> Carl Hartsfield, PhD (Member)	<u>15 Jul 2014</u> Date
<u>//signed//</u> David Jacques, PhD (Member)	<u>15 Jul 2014</u> Date

Accepted:

<u>//signed//</u> Adedeji B. Badiru Dean, Graduate School of Engineering and Management	<u>30 Jul 2014</u> Date
---	----------------------------

Abstract

The goal of the Dual-Expander Aerospike Nozzle, a modification to traditional engine architectures, is to find those missions and designs for which it has a competitive advantage over traditional upper stage engines such as the RL10. Previous work focused on developing an initial design to demonstrate the feasibility of the Dual-Expander Aerospike Nozzle. This research expanded the original cycle model in preparation for optimizing the engine's specific impulse and thrust-to-weight ratio. The changes to the model allowed automated parametric and optimization studies. Preliminary parametric studies varying oxidizer-to-fuel ratio, total mass flow, and chamber length showed significant improvements. Drawing on modeling lessons from previous research, this research developed a new engine simulation capable of achieving a specific impulse comparable to the RL10. Parametric studies using the new model verified the Dual-Expander Aerospike Nozzle architecture conforms to rocket engine theory while exceeding the RL10's performance. Finally, this research concluded by optimizing the Dual-Expander Aerospike Nozzle engine for three US government missions: the Next Generation Engine program, the X-37 mission, and the Space Launch System. The optimized Next Generation Engine design delivers 35,000 lbf of vacuum thrust at 469.4 seconds of vacuum specific impulse with a thrust-to-weight ratio of 127.2 in an engine that is one quarter the size of a comparable RL10. For the X-37 mission, the optimized design operates at 6,600 lbf of vacuum thrust and has a vacuum specific impulse of 457.2 seconds with a thrust-to-weight ratio of 107.5. The Space Launch System design produces a vacuum thrust of 100,000 lbf with a vacuum specific impulse of 465.9 seconds and a thrust-to-weight ratio of 110.2. When configured in a cluster of three engines, the Dual-Expander Aerospike Nozzle matches the J2-X vacuum thrust with a 4% increase in specific impulse while more than doubling the J2-X's thrust-to-weight ratio.

*Dedicated to the men and women of Mach 30: past, present, and future.
ad astra per civitatem — to the stars through community*

Acknowledgments

I would like to begin by thanking my committee for their support and mentorship. I am especially thankful to my advisor, Dr. Black, who encouraged me to continue my academic career beyond my masters work. I had not really considered pursuing a PhD until he first asked me about it.

I would also like to thank all of the other students who have contributed to the DEAN research efforts. Each and every paper, thesis, and model contributed to this research.

The following companies and organizations provided software used in this research: National Aeronautics and Space Administration provided the Numerical Propulsion System Simulation package, Phoenix Integration provided ModelCenter, and SpaceWorks Software provided REDTOP-Lite.

Extra thanks goes out to Phoenix Integration and its staff for being so flexible and supportive. I cannot imagine a better place to work or better people to work with.

Special thanks go out to my friends and family who have been so supportive of my academic career. You have all at one time or another been flexible, generous, or understanding as I have worked my way from technical theatre to space systems engineering. Thank you. Oh, and Capt. Bellows, don't forget "you did good work today..." – Well, you know the rest.

Finally, I would like to conclude my acknowledgments by recognizing the organizations which helped fund my research.

This research was supported in part by a PhD fellowship from the Dayton Area Graduate Studies Institute.

This research was supported in part by an appointment to the Postgraduate Research Participation Program at U.S. Air Force Research Laboratory, Air Force Institute of

Technology, administered by the Oak Ridge Institute for Science and Education through an interagency agreement between the U.S. Department of Energy and USAFRL.

This research was supported in part by the US Air Force Research Lab, Edwards AFB.

Joseph R. Simmons, III

Table of Contents

	Page
Abstract	iv
Dedication	v
Acknowledgments	vi
Table of Contents	viii
List of Figures	xii
List of Tables	xviii
List of Symbols	xxii
List of Source Code	xxxii
 I. Introduction	 1
1.1 Research Motivation	1
1.2 Problem Statement	5
1.3 Research Objective	6
1.4 Method Overview	6
1.5 Research Contributions	7
1.6 Dissertation Overview	8
 II. Background	 11
2.1 Rocket Propulsion	11
2.1.1 Rocket Fundamentals	11
2.1.2 Liquid Rocket Engines	16
2.1.3 Liquid Rocket Engine Design	21
2.1.4 Modeling Liquid Rocket Engines	26
2.1.4.1 REDTOP	27
2.1.4.2 Rocket Propulsion Analysis	28
2.1.4.3 Numerical Propulsion System Simulation	29
2.1.4.4 Rocket Engine Transient Simulator	30
2.2 Government Demand for Improved Rocket Engines	30
2.2.1 Current Launch Vehicles	31

	Page
2.2.2 US Air Force Next Generation Launch Programs	32
2.2.3 NASA's Space Launch System	34
2.2.4 US Air Force Space Plane Program	37
2.3 The Dual-Expander Aerospike Nozzle Upper Stage Engine	40
2.3.1 DEAN Architecture	40
2.3.2 Research History of Core Technologies	42
2.3.2.1 Dual-Expander Cycles	42
2.3.2.2 Aerospike Nozzles	43
2.3.3 DEAN Research History	46
2.3.3.1 First Generation DEAN	47
2.3.3.2 Second Generation DEAN	49
2.3.3.3 Third Generation DEAN	50
2.3.3.4 Methane DEAN	52
2.4 Engineering Optimization	53
2.4.1 Optimization Terminology	53
2.4.2 Defining Optimization Problems	54
2.4.2.1 Unconstrained Single Objective Problem	55
2.4.2.2 Unconstrained Multi-Objective Problem	56
2.4.2.3 Constrained Single Objective Problem	57
2.4.2.4 Constrained Multi-Objective Problem	58
2.4.3 Optimization Algorithms	59
2.5 Concluding Remarks	60
III. Parametric Study of Dual-Expander Aerospike Nozzle Upper Stage Rocket Engine	61
3.1 Introduction	61
3.2 Existing NPSS DEAN Model	62
3.2.1 Existing DEAN Architecture	63
3.2.2 NPSS Model Details	65
3.3 Parameteric NPSS DEAN Model	69
3.3.1 Updated DEAN Architecture	70
3.3.2 NPSS Model Details	71
3.4 System-Level DEAN Model	77
3.5 Results and Analysis	85
3.5.1 Parametric Studies	85
3.5.2 Scaling the DEAN Engine	94
3.6 Conclusion	97
IV. Fourth Generation DEAN Model	99
4.1 Introduction	99
4.2 Motivation	99

	Page
4.3 Model Improvements	101
4.3.1 Updated Parametrization	101
4.3.2 Model Simplification	102
4.3.3 Calculating Initial Estimates for NPSS Solver	103
4.4 System Model Structure	104
4.5 Results	108
4.6 Conclusion	108
V. Verification of Dual-Expander Aerospike Nozzle Upper Stage Rocket Engine . .	110
5.1 Introduction	110
5.2 Background	111
5.2.1 DEAN Architecture	111
5.2.2 Previous Research	113
5.3 Current Research	116
5.4 Results and Analysis	120
5.4.1 DEAN Performance Trade Studies	120
5.4.1.1 Chamber and Thrust Trade Studies	122
5.4.1.2 Specific Impulse Trade Studies	126
5.4.1.3 Weight Trade Studies	130
5.4.2 Scalability of the DEAN	137
5.4.3 DEAN Thrust-to-Weight Ratio and Turbopump Power	139
5.5 Conclusion	140
VI. Fourth Generation DEAN Materials	141
6.1 Introduction	141
6.2 Background	141
6.2.1 Cooling Channel Design Constraints	141
6.2.2 Third Generation DEAN Materials Selection	142
6.2.3 Cooling Channel Design	143
6.3 Designing the DEAN Cooling Channels for Fourth Generation DEAN Model	146
6.3.1 Phase I - Identify Key Design Variables	148
6.3.2 Phase II - Determine Values for Design Variables	152
6.3.3 Phase III - Verification	158
6.4 Materials Selection Study	160
6.5 Conclusion	173
VII. Optimization Studies of Dual-Expander Aerospike Nozzle Upper Stage Rocket Engine	174
7.1 Introduction	174

	Page
7.2 Background	175
7.2.1 DEAN Architecture	175
7.2.2 Previous Research	177
7.2.3 Government Demand for Improved Upper Stage Rocket Engines . .	179
7.3 Current Research	183
7.4 Results and Analysis	186
7.4.1 Physical Constraints	189
7.4.2 Optimizing for the IHPRPT/NGE Programs	190
7.4.3 Optimizing for the X-37 Mission	209
7.4.4 Optimizing for the Space Launch System	216
7.5 Conclusion	223
VIII Conclusions and Recommendations	225
8.1 Research Objectives Answered	225
8.2 Research Summary	226
8.3 Research Contributions	230
8.4 Recommendations for Future Research	232
8.4.1 Extending Current Results	232
8.4.1.1 Update Turbopump Design Studies	232
8.4.1.2 Update the Methane DEAN Study	232
8.4.2 Fifth Generation DEAN Research	233
8.4.2.1 Recommended Model Updates	233
8.4.2.2 Additional Design Studies	234
8.4.2.3 Detailed Comparison of DEAN to RL10 and J-2X Using an Upper Stage Model	234
Appendix A: Verification and Validation of the Fourth Generation DEAN Model . . .	235
Appendix B: Revisiting Previous Results with the Fourth Generation DEAN Model .	324
Bibliography	337

List of Figures

Figure	Page
1.1 Pratt & Whitney RL10, credit NASA[1]	3
1.2 The Dual-Expander Aerospike Nozzle Upper Stage Engine	4
2.1 Liquid Rocket Engine Elements	17
2.2 Cross-Section of a Truncated Aerospike Nozzle, taken from Martin [2]	19
2.3 Typical Liquid Rocket Engine Cycles from Huzel and Huang[3], credit J. Hall[4]	21
2.4 Liquid Rocket Engine Design Process	22
2.5 Example Pressure Plot of a Gas Generator Cycle; redrawn from Humble [5]	24
2.6 Delta IV Upper Stage, credit NASA KSC [6]	31
2.7 Centaur Upper Stage, credit NASA KSC [7]	32
2.8 SLS Upper Stage with Four RL10 Engines, credit The Boeing Corporation [8]	35
2.9 SLS Upper Stage with Single J-2X Engine, credit The Boeing Corporation [8]	37
2.10 X-37 Orbital Test Vehicle, credit US Air Force [9]	39
2.11 Rear View of X-37 including the AR2-3 Engine, credit US Air Force [10]	40
2.12 DEAN Architecture, credit J. Hall (unpublished)	41
2.13 Example Aerospike Engines	46
2.14 Second Generation DEAN Model	49
2.15 Comparison of First, Second, and Third Generation DEAN Geometry	52
3.1 Original DEAN Geometry	61
3.2 DEAN Architecture	64
3.3 DEAN Geometry (dim in inches), credit D. Martin	67
3.4 Updated DEAN Architecture	71
3.5 Comparison of Simplified Geometry to Martin's Original Geometry	72
3.6 I_{sp} vs O/F, Original NPSS Model	75

Figure	Page
3.7 Thrust vs O/F , Original NPSS Model	76
3.8 Thrust vs O/F and Total Mass Flow, Original NPSS Model	77
3.9 System-level Model of DEAN	78
3.10 Comparison of Fluid Mach Number Calculations	84
3.11 I_{sp} vs O/F Ratio, System-level Model	85
3.12 Fluid Mach Numbers vs O/F Ratio, System-level Model	87
3.13 Detailed I_{sp} vs O/F Ratio, System-level Model	88
3.14 Detailed Chamber Pressure vs O/F Ratio, System-level Model	89
3.15 Detailed Chamber Temperature vs O/F Ratio, System-level Model	89
3.16 I_{sp} vs O/F Ratio, Chamber Pressure, and Chamber Temperature, System-level Model	90
3.17 Vacuum Thrust vs Total Mass Flow, System-level Model	92
3.18 Vacuum Thrust vs Chamber Length, System-level Model	94
3.19 Comparison of Geometry for the scaled DEAN to the Original Geometry	96
4.1 Key Radii in the DEAN Engine	101
4.2 Primary Elements of Revised DEAN Model	104
5.1 DEAN Architecture, credit J. Hall (unpublished)	112
5.2 Comparison of First, Second, and Third Generation DEAN Geometry	116
5.3 Fourth Generation DEAN Model	117
5.4 Key Radii in the DEAN Engine	117
5.5 Trade Study Baseline Design Geometry	120
5.6 Total Mass Flow Variation with Vacuum Thrust for Five Expansion Ratios	123
5.7 Chamber Pressure Variation with Thrust for Five Expansion Ratios	125
5.8 Chamber Pressure Variation with Throat Area for Five Thrust Levels	126

Figure	Page
5.9 Vacuum Specific Impulse Variation with Expansion Ratio for a Generic LOX/LH2 Engine ($P_c = 500$ psia)	127
5.10 Vacuum Specific Impulse Variation with Expansion Ratio for Five Thrust Levels	128
5.11 Specific Impulse Variation with Molecular Weight for Five Thrust Levels . . .	129
5.12 Specific Impulse Variation with Oxidizer-to-Fuel Ratio for Five Expansion Ratios	130
5.13 Total Engine Weight Variation with Throat Area for Five Thrust Levels	131
5.14 Total Engine Weight Variation with Throat Area for Five Thrust Levels without the Pressure Profile Converger	132
5.15 Total Engine Weight Variation with Expansion Ratio for Five Thrust Levels . .	133
5.16 Total Engine Weight Variation with Chamber Length for Five Expansion Ratios	133
5.17 Impact of Characteristic Length on DEAN Geometry	135
5.18 Total Engine Weight Variation with Characteristic Length for Five Expansion Ratios	136
5.19 Aerospike Thickness Variation with Characteristic Length for Five Expansion Ratios	137
6.1 DEAN Cooling Channels Variable Influence Chart	149
6.2 DEAN Chamber Cooling Channels Variable Influence Chart	151
6.3 DEAN Aerospike Cooling Channels Variable Influence Chart	152
6.4 Chamber Wall Temperature Variation with Chamber Stations Adjustment . . .	153
6.5 Chamber Maximum Mach Number Variation with Chamber Stations Adjustment	154
6.6 Channel Design Optimization Model	156
6.7 Chamber Percent Melting Point Variation with Material for Various Throat Areas and Thrust Levels	164
6.8 Aerospike Percent Melting Point Variation with Material for Various Throat Areas and Thrust Levels	165

Figure	Page
6.9 Chamber Structural Jacket Thickness Variation with Material Selection for Various Expansion Ratios and Thrust Levels	167
6.10 Chamber Structural Jacket Weight Variation with Material Selection for Various Expansion Ratios and Thrust Levels	167
6.11 Aerospike Structural Jacket Thickness Variation with Material Selection for Various Expansion Ratios and Thrust Levels	169
6.12 Aerospike Weight Variation with Material Selection for Various Expansion Ratios and Thrust Levels	169
6.13 Aerospike Tip Weight Variation with Material Selection for Various Expansion Ratios and Thrust Levels	170
6.14 LOX Plumbing Weight Variation with Material Selection for Various Expansion Ratios and Thrust Levels	171
6.15 LH2 Plumbing Weight Variation with Material Selection for Various Expansion Ratios and Thrust Levels	172
7.1 The Dual-Expander Aerospike Nozzle Upper Stage Engine	175
7.2 DEAN Architecture, credit J. Hall (unpublished)	176
7.3 Comparison of First, Second, and Third Generation DEAN Geometry	179
7.4 X-37 Space Maneuvering Vehicle, credit US Air Force	181
7.5 SLS Upper Stage Designs, credit The Boeing Corporation	182
7.6 Fourth Generation DEAN Model	184
7.7 Optimization Variable Influence Chart	193
7.8 Chamber Wall Temperature Variation with Throat Area	193
7.9 Thrust-to-Weight Ratio Variation with Characteristic Length	194
7.10 Vacuum Specific Impulse Variation with Oxidizer-to-Fuel Ratio	195
7.11 LH2 Injector Face Pressure Drop Variation with Oxidizer-to-Fuel Ratio	196

Figure	Page
7.12 Wall Temperatures Variation with Throat Area for 30,000 lbf DEAN	198
7.13 Specific Impulse Variation with Expansion Ratio and Chamber Length for 30,000 lbf DEAN	200
7.14 Darwin Configuration for the 30,000 lbf IHPRPT/NGE Case	202
7.15 Specific Impulse Variation with Thrust-to-Weight Ratio Pareto Front for the 30,000 lbf IHPRPT/NGE Case	203
7.16 30,000 lbf IHPRPT/NGE DEAN Optimal Design Geometry	204
7.17 Specific Impulse Variation with Thrust-to-Weight Ratio Pareto Fronts for IHPRPT/NGE Cases	205
7.18 Specific Impulse Variation with Thrust-to-Weight Ratio Pareto Front for the X-37 DEAN Engine	213
7.19 X-37 DEAN Optimal Design Geometry	213
7.20 Specific Impulse Variation with Thrust-to-Weight Ratio Pareto Front for the SLS DEAN Engine	220
7.21 SLS DEAN Optimal Design Geometry	220
A.1 Fourth Generation DEAN Model	235
A.2 ModelCenter Process Components	238
A.3 ModelCenter Converger	239
A.4 ModelCenter Surface of Revolution Component	239
A.5 DEAN Preprocessing Components	240
A.6 Pressure Profile Converger Components	248
A.7 Cooling Channel Pressure Study Results (without converger)	255
A.8 Cooling Channel Pressure Study Results (with converger)	256
A.9 Engine Cycle Analysis Components	258
A.10 DEAN Geometry	260

Figure	Page
A.11 DEAN Chamber Volume Elements	265
A.12 Calculating Conical Nozzle Length	269
A.13 Comparison of Angelino Approximation to TDK (Martin Design Point)	275
A.14 Comparison of Angelino Approximation to TDK (Hall Design Point)	276
A.15 Comparison of Angelino Approximation to TDK (Hall Design Point with Expansion Ratio of 10)	276
A.16 Angelino Approximation Correction (Hall Design Point)	277
A.17 Angelino Approximation Correction (Hall Design Point with expansion ratio of 10)	278
A.18 Coordinating Angelino Approximation with Chamber Geometry	279
A.19 Cooling Channel Design - Cross-Section View [4]	281
A.20 Performance Sequence	292
A.21 Cross-Section of the DEAN Engine	294
A.22 Pressure Level Plots Spreadsheet	308
A.23 Example LOX Cycle Pressure Level Plot	309
A.24 Geometry Sequence	310
A.25 Example Renderings from the Geometry Sequence	311
A.26 Constraints Parallel Branch	312
A.27 LOX and LH2 Mach Number Sequences	313
A.28 LOX RSM Actual vs Predicted Plots	316
A.29 LOX RSM Actual vs Predicted Plots	316
B.1 Geometry Comparison for First Generation DEAN Design	329
B.2 Geometry for Second Generation DEAN Design	331
B.3 Geometry Comparison for Third Generation DEAN Design	336

List of Tables

Table	Page
2.1 Thrust-to-Weight Range Based on Propellants	33
2.2 Key Performance Parameters for the SLS RL10 Rocket Engine Cluster [8, 11] .	36
2.3 Key Performance Parameters for the J-2X Rocket Engine [12, 13]	36
2.4 Key Performance Parameters for the AR2-3 Rocket Engine [14]	39
3.1 Existing DEAN Design Results versus Requirements	62
3.2 Existing DEAN Design Point[2]	68
3.3 Parametric Study over LH2 Pump 1 PR	75
3.4 System-level DEAN Model Components	79
3.5 Design of Experiments over O/F , Total Mass Flow, and Chamber Length . . .	82
3.6 Data Ranges for Speed of Sound Tables	83
3.7 Parametric Study over O/F	86
3.8 Parametric Study over Total Mass Flow	91
3.9 Parametric Study over Chamber Length	93
3.10 Scaled DEAN Design Parameters	95
4.1 Assumed Performance Compared to Actual Performance for Previous DEAN Generations	100
4.2 Updated DEAN Parametrization	102
4.3 Fourth Generation DEAN Model Components	105
5.1 Fourth Generation DEAN Model Components	118
5.2 Trade Study Baseline Design	121
5.3 Responses to Vacuum Thrust Trade Study Design	122
5.4 Responses to Throat Trade Study Design	125
5.5 Responses to Expansion Ratio Trade Study Design	126

Table	Page
5.6 Comparison of DEAN and RL10B-2 Sizes	128
5.7 Responses to Oxidizer-to-Fuel Ratio Trade Study Design	129
5.8 Responses to Chamber Length Trade Study Design	133
5.9 Responses to Characteristic Length Trade Study Design	134
5.10 Design Variable Ranges	138
5.11 DEAN Simulation Reliability	138
5.12 Comparison of RL10 Engine Family to DEAN Designs	139
6.1 Generation 3 DEAN Materials Selection [4]	143
6.2 Cooling Channel Design Variables	145
6.3 Cooling Channel Design Study Base Design	147
6.4 Design Variables for Cooling Channel Design Study DOE 1 - Influence of System Level Design Variables	149
6.5 Design Variables for Cooling Channel Design Study DOE 2 - Chamber Channel Design Study	150
6.6 Design Variables for Cooling Channel Design Study DOE 3 - Aerospike Channel Design Study	152
6.7 Cooling Channel Optimization Model Components	157
6.8 Final Cooling Channel Design Variable Values	157
6.9 Cooling Channel Design Verification Results	159
6.10 Cooling Channel Design Comparison	160
6.11 Materials Studies Base Design	162
6.12 Materials Options for DEAN Components	163
6.13 Design Variables for Chamber Cooling Jacket Material Study	164
6.14 Design Variables for Aerospike Cooling Jacket Material Study	165
6.15 Design Variables for Chamber Structural Jacket Material Study	166

Table	Page
6.16 Design Variables for Aerospike Structural Jacket Material Study	168
6.17 Design Variables for LOX Plumbing Material Study	170
6.18 Design Variables for LH2 Plumbing Material Study	171
6.19 Generation 4 DEAN Design Materials Selection	173
7.1 IHRPT/NGE Requirements Compared to RL10 Performance	180
7.2 SLS Designs Compared to RL10 Performance	183
7.3 Fourth Generation DEAN Model Components	185
7.4 DEAN Preassigned Parameters	188
7.5 DEAN Design Variables	189
7.6 Base Design for IHRPT/NGE Optimization Study	191
7.7 Design Variables for IHRPT/NGE Optimization Study DOE 1 - Trade Space Exploration	192
7.8 Key Constraints for the DEAN Engine	194
7.9 DEAN Optimization Process	197
7.10 Design Variables for IHRPT/NGE 30,000 lbf Step 3 DOE	199
7.11 Preassigned Parameters for IHRPT/NGE 30,000 lbf Optimization Study . . .	200
7.12 IHRPT/NGE Optimal Designs	206
7.13 IHRPT/NGE Optimal Designs Compared to RL10B-2	207
7.14 Base Design for X-37 Optimization Study	210
7.15 Preassigned Parameters for X-37 Optimization Study	211
7.16 X-37 Optimal Design	214
7.17 X-37 Optimal Design Compared to RL10A-4	215
7.18 Base Design for SLS Optimization Study	217
7.19 Preassigned Parameters for SLS Optimization Study	218
7.20 SLS Optimal Design compared to Baseline Designs	221

Table	Page
7.21 SLS Optimal Design	222
A.1 Fourth Generation DEAN Model Components	236
A.2 DEAN Engine Design Variables	241
A.3 DEAN Modeling Assumption Design Variables	241
A.4 DEAN Cooling Channel Design Variables	242
A.5 Design Variables for Cooling Channel Pressure Study	254
A.6 DEAN Independent Variables Listing	261
A.7 Angelino Approximation Error Analysis	277
A.8 Corrected Angelino Approximation Error Analysis	278
A.9 Component Material Compatibility Analysis	288
A.10 Parametric Study Results for Beryllium Copper	290
A.11 Expected Results for Beryllium Copper [4]	291
B.1 Shared Design Variable Values for Model Comparisons	324
B.2 Design Variable Values for Generation 1 DEAN Model	325
B.3 Results of Generation 1 DEAN Design Comparison	328
B.4 Design Variable Values for Generation 2 DEAN Model	330
B.5 Results of Generation 2 DEAN Design Comparison	332
B.6 Design Variable Values for Generation 3 DEAN Model	334
B.7 Results of Generation 3 DEAN Design Comparison	335

List of Symbols

α = conical nozzle half-angle (°)

β = empirical exponent (range 0.6 - 0.667)

Δl = coolant channel wall thickness (in)

Δr_{throat} = difference between chamber and aerospike radii at the throat

ΔT = change in temperature (R)

Δv = change in vehicle velocity (ft/s)

\dot{m} = total mass flow (lbm/s)

\dot{m}_{LH2} = LH2 mass flow (lbm/s)

\dot{m}_{LOX} = LOX mass flow (lbm/s)

\dot{Q} = total heat transfer (BTU)

\dot{q} = heat transfer per unit area (BTU/in²)

\dot{w} = total propellant weight flow (lbf/s)

ϵ = expansion ratio

$\epsilon_{\text{aerospike}}$ = aerospike expansion ratio

η_p = pump efficiency

η_{c^*} = combustion efficiency (frozen flow range: 1.0-1.15; equilibrium flow range: 0.9-0.98)

- γ = isentropic parameter
- γ = ratio of specific heats
- λ = nozzle efficiency (0.9-0.98)
- σ_i = bending stress on the inner surface (psi)
- σ_o = bending stress on the outer surface (psi)
- σ_r = radial stress in thick walled cylinder pressure vessel (psi)
- σ_t = tangential stress in thick walled cylinder pressure vessel (psi)
- τ = pump shaft torque (N m)
- τ_{max} = maximum shear stress (psi)
- Θ = angle of flow to centerline of spike (deg)
- A = cross-sectional area (in²)
- A = empirical coefficient (range 1.3 - 2.6)
- A = exit area (in²)
- a = half spacing of channel (in)
- a = lower bound of integration
- $A(x)$ = cross-sectional area of the volume of revolution at point x (in²)
- A_C = area of the heat exchange on the cold (inner) wall (in²)
- A_c = average cross-sectional area of the chamber (in²)

A_e = nozzle exit area (in²)

A_H = area of the heat exchange on the hot (outer) wall (in²)

A_t = throat area (in²)

A_{c_throat} = area of the chamber at the throat (in²)

$A_{cv,i}$ = cross-sectional area of cooling volume at i^{th} station (in²)

$A_{flow,i}$ = combusted flow's cross-sectional area at i^{th} station (in²)

$A_{hx_{cv,i}}$ = area for heat exchange to cooling volume at i^{th} station (in²)

$A_{hx_{nozz,i}}$ = area of heat exchange to aerospike nozzle at i^{th} station (in²)

A_{hx} = area of heat exchange for chamber (in²)

$a_{LH2,i}$ = LH2 Mach number at i^{th} station

$a_{LOX,i}$ = LOX Mach number at i^{th} station

alt = altitude of orbit (ft)

AR = channel aspect ratio

B = empirical coefficient (range 0.6 - 0.667)

b = upper bound of integration

c^* = characteristic exit velocity (ft/s)

c_F = thrust coefficient (none)

c_i = distance from neutral axis to inner fiber (in)

c_o = distance from neutral axis to outer fiber (in)

D_e = nozzle exit diameter (in)

D_t = nozzle throat diameter (in)

e = distance from the centroid axis to the neutral axis (in)

F = total thrust (lbf)

F_m = momentum thrust (lbf)

F_p = pressure thrust (lbf)

F_{vac} = vacuum thrust (lbf)

F_{cowl} = thrust acting on the chamber lip (lbf)

f_{inert} = inert mass fraction

$F_{nondesign}$ = thrust from the difference between exit and ambient pressure (lbf)

$F_{pressure}$ = thrust from pressure acting on the surface area of the aerospike (lbf)

g_0 = acceleration due to gravity on Earth (32.18 ft/s²)

h = heat transfer coefficient (BTU/in² R)

h_i = height of channel at i^{th} station (in)

H_p = pump head pressure rise (m)

H_{T_C} = heat transfer coefficient from the cold (inner) side of the wall (BTU/in² R)

H_{T_H} = heat transfer coefficient from the hot (outer) side of the wall (BTU/in² R)

Hx = heat flow (R)

I_{sp_vac} = vacuum specific impulse (s)

I_{sp} = specific impulse (s)

k = thermal conductivity of wall (BTU/in R)

L = length of frustum (in)

l = width (in)

L^* = characteristic length (in)

L_c = chamber length (in)

l_c = chamber length (in)

l_i = length of station = $0.2 \cdot l_c$ (in)

L_n = conical nozzle length (in)

M = chamber Mach number

m_f = final vehicle mass (lbm)

m_i = initial vehicle mass (lbm)

M_x = bending moment (in lbf)

m_{inert} = mass of vehicle excluding propellant and payload (lbm)

m_{pay} = mass of vehicle payload (lbm)

m_{plug} = slope of the aerospike plug

m_{prop} = mass of consumed propellant (lbm)
 m_{tp} = mass of turbopump (kg)
 μ = gravitational parameter = $1.40765 \times 10^{16} \text{ ft}^3/\text{s}^2$ for Earth
 MW = molecular weight of combustion products (lb/lb-mole)
 N = number of points in the numerical integration
 n = number of channels in cooling volume
 N_r = pump rotational speed (rad/s)
 O/F = oxidizer-to-fuel ratio
 p^* = throat pressure (psia)
 p_a = ambient pressure (psia)
 p_c = chamber pressure (psia)
 p_e = exit pressure (psia)
 p_i = fluid pressure at i^{th} station (psia)
 p_i = internal pressure (psia)
 p_o = external pressure (psis)
 p_{amb} = ambient pressure (psia)
 P_{req} = required pump power (W)
 $Percent_Weight_Hardware$ = percent of engine mass accounted for by miscellaneous hardware

PR_e = exit pressure ratio

Q_{in} = total heat transfer into a system

Q_{out} = total heat transfer out of a system

r_1 = radius of base of frustum (in)

r_2 = radius of top of frustum (in)

r_e = radius of exit area (in)

r_i = inner radius of annulus (in)

r_i = inside radius (in)

r_i = radius of inner fiber (in)

r_o = outer radius of annulus (in)

r_o = outside radius (in)

r_o = radius of the outer fiber (in)

$r_{c,i}$ = inner radius of the chamber at i^{th} station (in)

r_{c_i} = inner radius of the chamber (in)

$r_{c_o,i}$ = outer radius of the chamber at i^{th} station (in)

$r_{n,i-1}$ = radius of aerospike nozzle at $(i-1)^{th}$ station (in)

$r_{n,i}$ = radius of aerospike nozzle at i^{th} station (in)

r_{planet} = radius of the planet (ft)

r_{t_i} = inner radius at throat (in)

S = shear force (lbf)

T_0 = chamber temperature (R)

T_i = fluid temperature at i^{th} station (R)

T_{cool} = temperature of coolant fluid (R)

T_{CW} = temperature of the cold (inner) wall of the cooling channel (R)

T_{HW} = temperature of the hot (outer) wall of the cooling channel (R)

V = volume of of revolution (in^3)

v^* = throat velocity (ft/s)

V_1 = volume 1 of chamber volume calculations (in^3)

V_2 = volume 2 of chamber volume calculations (in^3)

V_3 = volume 3 of chamber volume calculations (in^3)

V_c = chamber volume (in^3)

V_c = volume of cylinder (in^3)

v_e = exhaust velocity (ft/s)

V_f = volume of frustum (in^3)

V_{fh} = volume of hollow frustum (in^3)

v_{cir} = circular orbital velocity (ft/s)

$V_{cv,i}$ = volume of cooling volume at i^{th} station (in³)

w = load per unit length (lbf/in)

w_i = half width of channel at i^{th} station (in)

$W_{chamber}$ = weight of chamber (lb)

$W_{hardware}$ = mass of miscellaneous hardware (lb)

w_{init} = initial half width of channel (in)

$W_{plumbing}$ = weight of plumbing (lb)

W_{spike} = weight of aerospike (lb)

W_{total} = total engine weight (lb)

$W_{turbopumps}$ = weight of turbopumps (lb)

x = position along the width of the beam (in)

x_i = i^{th} value of x

x_i = percent of chamber length station is located at

x_{i-1} = $(i-1)^{th}$ value of x

r_{ti} = inner throat radius (in)

r_{to} = outer throat radius (in)

IHPRPT = Integrated High Payoff Rocket Propulsion Technology

LH2 = liquid hydrogen

LOX = liquid oxygen

NGE = Next Generation Engine

SLS = Space Launch System

List of Source Code

A.1 Spike Materials Source Code	243
A.2 Cooling Channels Design Source Code	246
A.3 Pressure Profile Converger Source Code	250
A.4 Find Taget Isp Function Source Code	252
A.5 Set Guess Lower Values Function Source Code	253
A.6 Pressure RMSE Source Code	257
A.7 DEAN Geometry Calculations	262
A.8 DEAN Estimated Pressure Level Calculations	269
A.9 Aerospike Thrust Calculation	274
A.10 Cooling Jacket Bending Moment Function	282
A.11 Cooling Jacket Bending Stress Calculations	282
A.12 Cooling Jacket Shear Stress Calculations	283
A.13 Cooling Jacket Wall Temperature Calculations	286
A.14 Channels Component Average Function	293
A.15 Tangential Stress in a Thick Walled Cylinder Function	296
A.16 Radial Stress in a Thick Walled Cylinder Function	296
A.17 Calculate Wall Thickness Function	297
A.18 Frustum Volume Function	300
A.19 Volume of Revolution Volume Calculation	301
A.20 Aerospike Mass Calculations	302
A.21 Turbopump Mass Calculations	304
A.22 Plumbing Mass Calculations	304
A.23 Incorrect Miscellaneous Hardware Weight Calculation	306

A.24 Corrected Miscellaneous Hardware Weight Calculation	306
A.25 Final Engine Thrust-to-Weight Calculation	306
A.26 GenericSOR Input Format	310
A.27 LOX Max Mach Source Code	317
A.28 Chamber Mach Number Source Code	319
A.29 Sanity Checks Source Code	321

DESIGN AND EVALUATION OF DUAL-EXPANDER AEROSPIKE NOZZLE UPPER STAGE ENGINE

I. Introduction

1.1 Research Motivation

Prices for space launches are literally astronomical. The cost to deliver payload to orbit is estimated to be as much as \$10,000 per pound [15]. A first class stamp to space (that is delivery of up to 3.5 ounces by weight) would cost \$2,200. Current launch costs to place satellites in orbit costs hundreds of millions of dollars. In this time of budgetary constraints, reliance placed on satellites for surveillance, navigation, communication, and meteorology in the US also means there is demand for more efficient and cheaper improvements [16, 17].

At the heart of launch costs is the fundamental science and engineering of rocket powered flight. Payloads represent only a small fraction of the gross lift-off weight (GLOW) of current rockets. Improvements in propulsion performance, measured in specific impulse (I_{sp}) and the propulsion system's thrust-to-weight ratio (T/W), can dramatically increase payload fractions. Increased payload fractions reduce the size of launch vehicles for a given payload leading to lower cost launch vehicles. Increased payload fractions can also increase the size of payloads launched per mission, reducing the per pound cost for fixed mission expenses, such as range and insurance costs. Taken together, the savings can be significant.

Since 1996, the Department of Defense, NASA, and the aerospace propulsion industry have been working to significantly improve rocket propulsion performance to realize these benefits through two US Air Force programs. The first program is the Integrated High Payoff Rocket Propulsion Technology (IHPRPT) program. One of the main goals of

the IHPRT program was to double the thrust-to-weight ratio achieved by traditional LOX/LH2 engines. DEAN research quantified this thrust-to-weight ratio requirement by specifying a minimum value of 106.5 [2]. The second US Air Force program is the Next Generation Engine (NGE) program. The NGE mission requirements include a vacuum thrust between 25,000 lbf and 35,000 lbf and a minimum vacuum specific impulse of 465 s. The NGE physical constraints include a maximum engine length of 90 in and a maximum exit diameter of 73 in [18]. Taken together, the IHPRT/NGE requirements represent a significant improvement in weight and packaging over traditional expander cycle engines such as the RL10, while requiring equal or better performance in terms of thrust and specific impulse. Government estimates predict these performance increases will increase payload mass by 22% and decrease launch costs by 33% for expendable launch vehicles.[19]

Two additional US government programs could benefit from advances in rocket engine design. The US Air Force X-37 is a reusable space plane designed to test various spaceflight hardware and technologies. Its small size and reusability call for compact rocket engines able to operate many times before replacement. The X-37 is currently outfitted with an AR2-3 engine producing 6,600 lbf of thrust and measuring just 32 in long with an outer radius of 10 in [14, 20, 21]. NASA's Space Launch System (SLS) is a shuttle-derived super-heavy lift human-rated launch system which is still in the design phase. Four upper stage configurations are being considered for the SLS including a design powered by four RL10 engines and one powered by a single J-2X, an improved version of the gas generator powered J-2 engine from the Apollo program. The RL10 design provides a vacuum thrust of 99,000 lbf and a vacuum specific impulse of 462.5 s, with a thrust-to-weight ratio of 37.3 and the J-2X design provides a vacuum thrust of 294,000 lbf and a vacuum specific impulse of 448 s, with a thrust-to-weight ratio of 55 [8, 12, 22].

Achieving the significant gains in performance required by these programs will take more than incremental improvements in rocket engine technology. For decades the thrust-

to-weight ratio of high powered liquid rocket engines, including Pratt & Whitney's upper stage RL10 shown in Figure 1.1, has been relatively constant with respect to propellant selection. Engines powered by liquid hydrogen/liquid oxygen have historically had thrust-to-weight ratios between 41 and 61. Engines powered by RP-1/liquid oxygen have historically had thrust-to-weight ratios between 71 and 102. This trend is present across a variety of thrust levels and designs.[23]

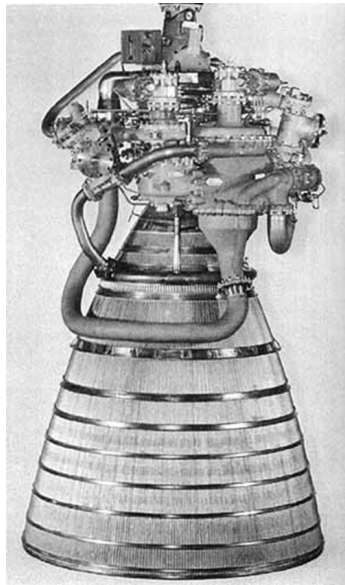


Figure 1.1: Pratt & Whitney RL10, credit NASA[1]

The Air Force Institute of Technology (AFIT) is researching a modification to a traditional upper stage engine architecture as a means of breaking through this performance barrier. The result of this research is the Dual-Expander Aerospike Nozzle (DEAN) upper stage engine. The DEAN, shown in Figure 1.2, uses two novel design choices. The first is the use of separate expander cycles for the fuel and the oxidizer. In a traditional expander cycle, the fuel is pumped through a cooling jacket for the chamber and nozzle. The energy transferred to the fuel from cooling the chamber and nozzle is then used to drive the turbine

turning both the fuel and oxidizer pumps before the fuel is introduced into the chamber [5]. In the DEAN, the fuel and oxidizer each drive their own turbines to power their own pumps.

The second novel design choice of the DEAN is the use of an aerospike, or plug, nozzle. Aerospike nozzles run through the middle of the rocket's propellant flow and up into the chamber, leaving the ambient atmosphere to form the outer boundary for the flow. The interaction with the ambient atmosphere gives aerospike nozzles automatic altitude compensation, making them more efficient over a range of altitudes. Similar bell nozzles operate most efficiently at their specific design altitude [24]. The use of an aerospike nozzle provides a second, physically separate cooling loop from the chamber for use in the fuel expander cycle. This second cooling loop simplifies the propellant feed system and increases the surface area inside the chamber used to drive the turbomachinery, providing for correspondingly increased power to the pumps. The increased pump power leads to increased chamber pressure, and in turn increased engine performance.

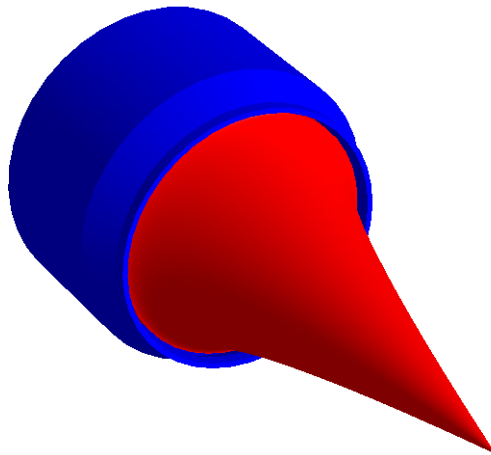


Figure 1.2: The Dual-Expander Aerospike Nozzle Upper Stage Engine

The DEAN's unique architecture offers a number of advantages. The increased chamber pressure yields smaller engines, in terms of both weight and physical dimensions, for similar levels of thrust and specific impulse. The separate expander cycles also ensure the fuel and oxidizer remain physically separated until entering the combustion chamber, eliminating one of the more catastrophic failure modes in traditional expander cycles, namely failure of an inter-propellant seal. The DEAN architecture is also a forerunner to a similar boost stage architecture, where the aerospike nozzle's global performance could result in even greater performance gains [2, 25–27].

The DEAN architecture is not without its challenges, though. The LOX cycle requires a turbine material to operate in an oxygen environment. Materials surveys at AFIT have shown Inconel 718 provides both satisfactory oxygen resistance and suitable mechanical performance for use in both the pump and the turbine in the LOX cycle [26, 27]. Also, the expansion ratio of aerospike nozzles is limited by the ratio of the chamber area at the throat to the throat area [24]. Due to this limit, aerospike nozzles generally need larger chamber diameters to reach useful expansion ratios, potentially limiting the range of engines which offer improved thrust-to-weight while also delivering the required specific impulse.

A number of simulation models of the DEAN have been developed at AFIT for a single design targeting the IHPRT program requirements demonstrating the feasibility of the DEAN architecture. The primary model is a complete cycle model written in NASA's Numerical Propulsion System Simulation (NPSS).[2, 25, 26]

1.2 Problem Statement

The DEAN has been proposed as an improved upper stage rocket engine architecture offering increased performance in a physically compact package. Addressing this proposal requires answering the following questions.

- What are the operational limits of the DEAN architecture in terms of thrust and specific impulse?

- What are the limiting constraints of the DEAN architecture?
- How does the DEAN compare to single expander cycle engines like the RL10 in terms of specific impulse, thrust-to-weight ratio, and size?
- For what missions does the DEAN offer significant advantages over traditional upper stage engines?

1.3 Research Objective

The objective of this research is to determine the viability of the DEAN architecture by finding those missions and designs for which the DEAN has a competitive advantage over traditional upper stage engines. This objective can be broken down into three sub-objectives. The first sub-objective is to address the parametrization of the DEAN model. On the practical level, the simulation must implement parametrization of the cycle model in NPSS. On the architecture level the simulation must select a set of parameters which fully defines the design and provides for robust execution of the model. The second sub-objective is verifying the models used in the research and DEAN architecture. The third sub-objective is comparing the performance of the DEAN to traditional upper stage engines for a selection of missions, both current and proposed, in order to collect the data necessary to satisfy the overall research objective.

1.4 Method Overview

This research built upon the initial work at AFIT on the DEAN. It extended the existing cycle model of the DEAN to enable running parametric and optimization studies. The research occurred in five phases. The first phase covered the development of a proof of concept parametric system model of the DEAN. This first model was used to demonstrate the utility of parametric modeling in rocket engine design by providing an improved design from the results of parametric studies. These initial results led to extending the prototype model to calculate improved performance and engine weight estimates.

The second phase involved the development of a new system level DEAN model integrating the lessons learned from the previous efforts. The resulting model had the necessary fidelity, flexibility, and reliability to address the research questions in the previous section. The improved model was used throughout the remainder of this research starting with phase three. The third phase was a detailed verification of the DEAN models and architecture. The verification process included review and comparison of model source code to engineering principles and parametric studies comparing the DEAN's responses to rocket engineering theory and the RL10 family of expander cycle engines.

With the model and architecture verified, the remaining phases focused on optimizing the DEAN and comparing it to existing engines for the IHPRPT/NGE, X-37, and SLS missions. The fourth phase looked at the materials selection for the DEAN to find a materials selection yielding consistently low weight engines across a wide range of designs. Finally, the fifth phase covered a series of optimization studies of the DEAN for the three selected missions and compared the DEAN's performance and size to traditional upper stage engines.

1.5 Research Contributions

1. A method for parametrically modeling rocket engines in NASA's Numerical Propulsion System Simulation (NPSS) was demonstrated including calculation of initial estimates for key parameters in the NPSS model and calculation of fluid Mach numbers in the cooling channels. The ability to develop a parametric model with the required fidelity, flexibility, and reliability is essential for conceptual design studies of new rocket engine architectures such as the DEAN.
2. The DEAN architecture was verified through a series of parametric studies. These studies confirmed the validity of the DEAN architecture and demonstrated the increased performance generated by the dual-expander cycles.

3. The materials selection proposed in previous research was refined to support a wide variety of missions and engine designs.
4. An optimization process for DEAN engines using the DEAN simulation was developed and demonstrated. This optimization process takes mission specific requirements and constraints and yields a Pareto set of designs, trading off specific impulse and thrust-to-weight ratio.
5. Optimal DEAN engine designs were found for three IHPTRPT/NGE cases, the X-37 space plane, and two upper stage configurations of the SLS. These optimal designs were compared to existing and proposed engines to demonstrate the benefits of the DEAN architecture.

1.6 Dissertation Overview

The dissertation developed from this research follows the scholarly article format. The document is divided into eight chapters and two appendices. Chapter 2 contains the engineering and technical material relevant to the research. The material in Chapter 2 is broken into four sections. The first section covers rocket powered propulsion with emphasis on liquid rocket engines, including design and modeling. The second section documents three US government programs involving advanced rocket propulsion: the US Air Force IHPTRPT and NGE programs, the US Air Force X-37 space plane, and NASA's SLS. The third section presents a detailed review of previous research related to the DEAN. The fourth and final section covers engineering optimization including terminology, problem definition, and optimization algorithms.

Chapter 3 covers the initial parametrization of the DEAN and early conclusions from the resulting parametric model. The parametric studies varied oxidizer-to-fuel ratio, total mass flow, and chamber length. The DEAN can achieve 50,000 lbf vacuum thrust and 489 s vacuum specific impulse with an oxidizer-to-fuel ratio of 6.0, a total propellant weight flow

of 104 lb/s (a reduction of 14%), and an engine length of 27.9 in (a reduction of over 25% from the original design), a significant weight savings. These results validated both the parametric modeling approach of the research and the DEAN architecture. Chapter 3 was submitted to and published in the *AIAA Journal of Spacecraft and Rockets* (see reference [27]).

Chapter 4 documents the final DEAN system model. The chapter opens with a detailed review of the need for an improved system model emphasizing the narrow trade space size and insufficient reliability of the initial parametric model and the models following it. Chapter 4 continues by describing the improvements in the new system model. It concludes with an overview of the system model's structure and execution.

Chapter 5 presents the verification of the final system model and DEAN architecture. Parametric studies using the system model verified the DEAN architecture conforms to rocket engine theory while exceeding the RL10's performance. Improvements in the new model led to designs which can match the RL10's vacuum specific impulse of 465 seconds while retaining thrust-to-weight ratios in excess of 135 and chamber pressures of greater than 1500 pounds psia. These designs are compact, ranging in length from 27 to 38 inches. The parametric studies also demonstrated the new model is flexible and robust, with 98.7% of the specified designs converging successfully on a design point. Chapter 5 was submitted to the *AIAA Journal of Propulsion and Power*.

Chapter 6 covers the optimization of the cooling channel geometry for the DEAN and the selection of materials for the DEAN designed to yield consistently low weight engines across a wide range of designs. The cooling channel optimization process was used in support of the materials study in Chapter 6 and later optimization studies. The materials study confirmed the following findings from previous research: the aerospike tip material selection has little influence on the engine's thrust-to-weight ratio, the chamber cooling jacket should be manufactured from silicon carbide, the LOX plumbing should

be manufactured from INCONEL 718, and the LH2 plumbing should be manufactured from INCOLOY 909. The material study found updated material selections for the aerospike cooling jacket (silicon carbide), chamber structural jacket (INCONEL 718), and the aerospike structural jacket (INCOLOY 909).

Chapter 7 presents the optimized DEAN engine for three US government missions. For the IHPRPT/NGE programs, the optimized design delivered 35,000 lbf of vacuum thrust and 469.4 seconds of vacuum specific impulse with a thrust-to-weight ratio of 127.2 in an engine that is one quarter the size of a comparable RL10. For the X-37 mission, the optimized design operated at 6,600 lbf of vacuum thrust and has a vacuum specific impulse of 457.2 seconds with a thrust-to-weight ratio of 107.5. For the SLS, the optimized design produced a vacuum thrust of 100,000 lbf and a vacuum specific impulse of 465.9 seconds with a thrust-to-weight ratio of 110.2. When configured in a cluster of three engines, the DEAN matched the J2-X vacuum thrust with a 4% increase in specific impulse while more than doubling the J2-X's thrust-to-weight ratio. Chapter 7 was submitted to the *AIAA Journal of Spacecraft and Rockets*.

Chapter 8 concludes the dissertation by covering the research results, contributions, and recommendations for future work. Following Chapter 8 are two appendices. The first appendix covers the verification and validation of the individual analysis modules making up the final system model. The second appendix reevaluates the three designs from previous DEAN research using the final system model to confirm the results of earlier research.

II. Background

This chapter covers the engineering and technical material relevant to the research presented in this work. The first section covers rocket powered propulsion with an emphasis on liquid rocket engines, rocket design, and rocket modeling. The second section documents three US government programs involving advanced rocket propulsion: the US Air Force Integrated High Payoff Rocket Propulsion Technology (IHPRPT) and Next Generation Engine (NGE) programs, the US Air Force X-37 space plane, and NASA's Space Launch System (SLS). The third section presents a detailed review of previous research related to the DEAN. The fourth and final section covers engineering optimization including terminology, problem definition, and optimization algorithms.

2.1 Rocket Propulsion

2.1.1 Rocket Fundamentals.

Rockets belong to the “jet” class of propulsion systems. “Jet” systems impart a force, the thrust, on bodies by ejecting matter. In rockets, the ejected matter is carried with the rocket and is called the propellant(s). For chemical rockets, such as those used in space launch vehicles, the propellants are also the source of the energy for the rocket [24]. Spacecraft use the thrust provided by rockets to perform a number of functions related to their motion (launch, orbit insertion, orbit maintenance/maneuvering) and rotation (attitude control). The spacecraft launch process carries the spacecraft from a planetary surface to orbit and orbit insertion transfers a spacecraft from its initial orbit to its operational orbit. Orbit maintenance is the process of keeping a spacecraft in the required orbit and orbit maneuvering is the process of transitioning to a new orbit. Attitude control is the process of maintaining the required spacecraft pointing [5].

Chemical rockets are classified into three broad categories based on the type of propellants used: liquid, solid, and hybrid. Liquid rockets use liquid propellants stored in tanks and are either bi-propellant or mono-propellant. Bi-propellant systems use the combustion of a fuel and oxidizer as their energy source. Mono-propellant systems use the energy from a chemical decomposition of a single propellant. Feed systems transport the propellants to a combustion chamber where they chemically react to release the necessary energy to eject the products. Liquid rocket engines can have very high performance and control, in some cases including restart capability, but have a high degree of complexity. Solid rockets combine the propellants ahead of time and store them in solid form inside of the combustion chamber. Solid rockets offer simplicity and small size, but have lower performance than liquid rockets and cannot be shut down once they have been started. Finally, hybrid rockets combine traits from both liquid and solid rockets. Generally, hybrid rockets utilize a solid fuel stored in the chamber and a liquid or gaseous oxidizer stored in a tank. Like liquid rockets, a feed system is used to transport the oxidizer from the tank to the chamber. Hybrid rockets' complexity, performance, and size fall between those of liquid and solid rockets, while their safety is generally seen as far better than either that of liquid or solid rockets [5, 24].

Three key performance values are used to describe a rocket propulsion system. The first performance value is its thrust (F). As discussed above, the thrust is the force imparted by the rocket on the body it is propelling. The second performance value is its specific impulse (I_{sp}). Specific impulse is the ratio of a rocket's thrust to its propellant weight flow rate, a measure of fuel economy. The third performance value is the rocket's thrust-to-weight ratio (T/W). The thrust-to-weight ratio is the ratio of a rocket propulsion system's thrust to the propulsion system's weight. In liquid and hybrid rockets, the propulsion system's weight includes the feed system weight [5, 24].

A rocket's thrust comes primarily from two sources: momentum thrust (Equation (2.1)) and pressure thrust (Equation (2.2)). The total thrust, shown in Equation (2.3), is the sum of these two sources times a nozzle efficiency rating (λ) used to account for various losses in the nozzle. The rocket's exhaust velocity (v_e) and exit pressure (p_e) are tightly coupled to the expansion of the rocket's nozzle. These terms also have an inverse relationship where increasing the rocket's expansion leads to increased exhaust velocity with decreased exit pressure and vice versa. Due to their inverse relationship, maximizing a rocket's thrust is not just a matter of maximizing the exhaust velocity and exit pressure. Instead, the maximum thrust corresponds to designs with exit pressures equal to the ambient pressure (p_a) [5, 24].

$$F_m = \dot{m}v_e \quad (2.1)$$

$$F_p = (p_e - p_a)A_e \quad (2.2)$$

$$F = \lambda[\dot{m}v_e + (p_e - p_a)A_e] \quad (2.3)$$

A rocket exhaust flow is said to be ideally expanded when the exit pressure equals the ambient pressure giving the maximum thrust. For steady, supersonic flow (no separation from the nozzle) the exit pressure is constant for a given engine plus nozzle combination and the flow is only ideally expanded at a single altitude. At all other altitudes, the flow is either over or under expanded at other altitudes. Over expansion occurs when the engine is operating below its optimal altitude and the ambient pressure is greater than the exit pressure. This condition makes the effective exit area smaller than the actual exit area and can cause the flow to separate from the nozzle. Under expansion occurs when the engine operates above its optimal altitude and the ambient pressure is less than the exit pressure. Under expanded flows fan out past the nozzle exit area. In both conditions, the thrust is

below maximum. For launch vehicles, where the ambient pressure is constantly changing with altitude, designers ideally want an adjustable nozzle to match the exit pressure to the ambient pressure throughout ascent. For upper stage and other space operating rocket engines, size and weight constraints preclude nozzles large enough to reach exit pressures at or near the ambient pressures found in the near vacuum of space, so they are generally truncated [5, 24].

A rocket's specific impulse relates its thrust to its propellant weight flow rate as defined in Equation (2.4). Higher values of specific impulse are preferred as they require less of a rocket powered vehicle's mass be dedicated to propellant storage. Specific impulse values for liquid rocket engines typically range from 320 s to 460 s depending on propellants selection and engine design [5, 24].

$$I_{sp} = \frac{F}{\dot{m}} \quad (2.4)$$

An additional performance value, characteristic exit velocity (c^*), is used to analyze the propellant and chamber performance independent of a rocket's nozzle. Assuming one-dimensional, steady, and isentropic flow of a perfect gas gives the definition for characteristic exit velocity shown in Equation (2.5). The characteristic exit velocity is independent of a rocket's nozzle because it is only a function of temperature and gas properties defined by the thermochemical process in the chamber. Approximate values for the characteristic exit velocity can be looked up based on the propellants selection and used in the design process to size an engine starting with the throat area as discussed in Section 2.1.2[5, 24].

$$c^* = A_t \frac{P_c}{\dot{m}} \quad (2.5)$$

A rocket powered vehicle's mass at launch is comprised of three components. The mass of the payload it is carrying (m_{pay}), the mass of the rocket's structure or inert

mass (m_{inert}), and the mass of the propellant made up of both the fuel and the oxidizer (m_{prop}). The relationship among these masses is governed by the rocket equation, shown in Equation (2.6). In the rocket equation, Δv is the change in the vehicle's velocity (discussed in more detail below) and v_e is the propellant exhaust velocity which affects the rocket's performance. The masses are related by initial mass (m_i) and final mass (m_f). Equation (2.7) and Equation (2.8) show the relationship between the mass terms of the rocket equation and the payload, inert and propellant masses [5].

$$\Delta v = -v_e \ln \left(\frac{m_f}{m_i} \right) \quad (2.6)$$

$$m_i = m_f + m_{prop} \quad (2.7)$$

$$m_f = m_{pay} + m_{inert} \quad (2.8)$$

In addition to the actual mass values, the inert mass fraction can reveal important insights into a rocket's performance, shown in Equation (2.9). The inert mass fraction represents the structural efficiency of a rocket powered vehicle with smaller values representing more efficient structures. Traditional expendable launch vehicles have inert mass fractions in the range of 0.08 to 0.12. The inert mass fraction can be combined with a rocket's specific impulse to predict the required propellant needed to achieve a specified Δv [5].

$$f_{inert} = \frac{m_{inert}}{m_{prop} + m_{inert}} \quad (2.9)$$

As mentioned above, the rocket equation relates the initial and final masses and the propellant exhaust velocity to the change in the vehicle's velocity. This change in velocity is the primary effect of the rocket and is what enables launch vehicles to propel their payloads into orbit. In order to achieve orbit, the payload must be accelerated to the required orbital

velocity. Many payloads are placed into circular orbits. Equation (2.10) gives the orbital velocity for circular orbits, where μ is a gravitational parameter for the planet, r_{planet} is the radius of the planet, and alt is the altitude of the orbit. As an example, the orbital velocity for circular orbit at approximately 124 mi (656,170 ft) is 25,540 ft/s [28].

$$v_{cir} = \sqrt{\frac{\mu}{r_{planet} + alt}} \quad (2.10)$$

While providing sufficient Δv to reach orbital velocity is a requirement to reach orbit, in reality it is not sufficient. Launch vehicles experience a number of velocity losses during launch. These losses include gravity, atmospheric drag, and the expenses related to steering the vehicle during launch. These losses average between 3280 and 6560 ft/s for launches to Low Earth Orbits. Thus the required Δv for a rocket powered launch vehicle is the sum of the orbital velocity and the losses experienced during launch. For launch vehicles with multiple stages, each stage will have its own required Δv determined by target velocities for the staging points in the launch profile and the losses the stage will encounter [5].

2.1.2 Liquid Rocket Engines.

Liquid rocket engines are a class of chemical rockets which use liquid propellants to create chemical reactions converting thermochemical potential to kinetic energy to drive the propellants out of the rocket and create the thrust. Figure 2.1 shows the primary elements of liquid rocket engines. Bi-propellant liquid rockets use two propellants, an oxidizer and a fuel, to create the required chemical reaction. Mono-propellants use a single propellant, sometimes with a catalyst. In either case, the propellants are transferred from the storage system, usually referred to as the tanks, to the injector face by the propellant feed system. The feed system varies by engine cycle, and includes any required pumps, turbines, feed lines, or pressurization fluids used to transfer the propellants to the combustion chamber. The injector introduces the propellants into the chamber and separates the propellants from the combustion process ensuring the required mixing takes place to support the combustion

process. The chemical reaction occurs in the combustion chamber itself driving the process. This reaction forces the propellants, in the form of the reaction products, out of the engine through the throat. The chamber cross-section contracts as the propellants approach the throat, speeding up the flow from sub-sonic velocities to Mach 1 at the throat. The flow then enters the nozzle turning the flow to direct the momentum. The flow continues to accelerate through the diverging nozzle until reaching the exit plane and leaving the engine [5].

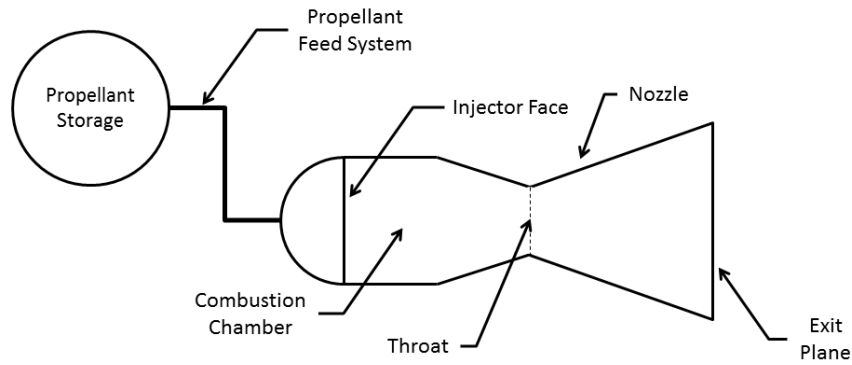


Figure 2.1: Liquid Rocket Engine Elements

The length of a rocket's nozzle depends on two key factors: the type of nozzle (discussed below) and its expansion ratio, shown in Equation (2.11). The expansion ratio, or area ratio, is the ratio of nozzle's exit area to its throat area and is a measure of a nozzle's expansion. All other things being equal, larger expansion ratios lead to longer, and more massive, nozzles. But, this extra mass usually comes with significant improvements in specific impulse [5].

$$\epsilon = \frac{A_e}{A_t} \quad (2.11)$$

Traditional nozzle types are generally named after their shape. The simplest nozzle type is the conical nozzle, described by the half angle (α) of their cone. While still used on relatively small rockets such as missiles, the conical nozzle is not widely used on launch vehicle rocket engines. The most common nozzle used on launch vehicle engines is the bell nozzle, named after its rounded, bell like shape. Bell nozzles offer higher efficiency than conical nozzles, especially at their design altitude, and are still relatively easy to design and manufacture. Full length bell nozzles are usually too long to be practical, so they are often shortened. The actual length is usually described in terms of the percent of a full length conical nozzle with a 15° half angle at the same expansion ratio. For example, an 80% bell nozzle would be 20% shorter than the comparable conical nozzle [24].

An alternative to conical and bell nozzles is the aerospike or plug nozzle. A cross-section of a truncated aerospike nozzle is shown in Figure 2.2. Aerospike nozzles are a center body in the combusted propellant flow often forming the inner wall of the chamber. The ambient atmosphere forms the outer boundary for the flow for these nozzles. The combusted propellant flow expands against the aerospike nozzle radially outward to match ambient pressure at each location in the nozzle flow field. The interaction with the ambient atmosphere gives aerospike nozzles altitude compensation ability, making them more efficient as altitude changes for the rocket than similar bell nozzles [24].

Aerospike nozzles can be quite long, often equaling the length of conical nozzles with half angles between 10° and 12° . The expansion ratio of aerospike nozzles is limited by the chamber geometry as shown in Equation (2.12) [4, 24]. Due to this limit, aerospike nozzles generally need larger chamber diameters to reach useful expansion ratios, potentially limiting the range of engines offering acceptable thrust-to-weight while also delivering the required specific impulse.

$$\epsilon_{aerospike} = \frac{A_{c,throat}}{A_t} \quad (2.12)$$

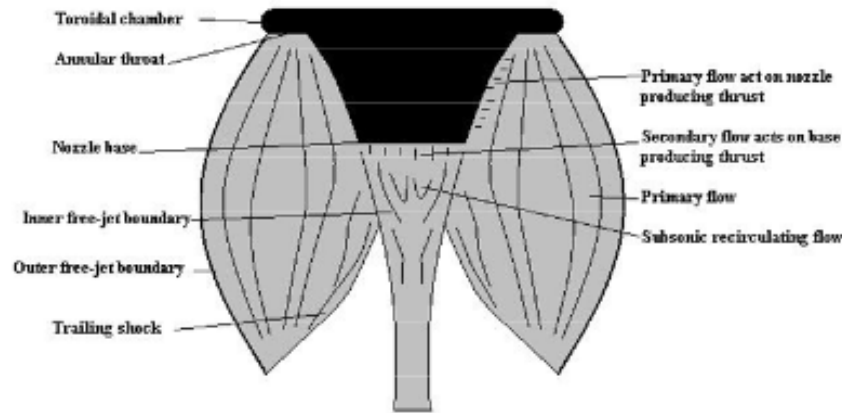


Figure 2.2: Cross-Section of a Truncated Aerospike Nozzle, taken from Martin [2]

The chemical reaction driving liquid rocket engines generates a substantial amount of heat which must be managed to avoid damaging the engine. Four cooling approaches are commonly used to manage this heat. Humble discusses the four approaches to rocket engine cooling in *Space Propulsion Analysis and Design* [5]. The first is simple radiation cooling. In radiation cooling, there is no active cooling system. Instead the structure of the engine is allowed to heat up until it begins to radiate its heat into space. This approach is generally used for small engines with low operating temperatures and short burn durations in vacuum environments. The second approach is ablative cooling. In ablative cooling, the chamber is lined with an expendable material ablating as the engine operates. This approach is relatively simple, but adds weight to the engine and slightly reduces the specific impulse as additional mass is injected into the exhaust without any additional energy. Ablative cooling also limits the lifetime of the engine to the time it takes to fully ablate the expendable liner. The third approach is regenerative cooling. In regenerative cooling, the propellant feed system is integrated into the chamber structure circulating cold propellant through a heat exchanger. The propellant then absorbs some of the heat from the engine before injection into the chamber, keeping the engine within

operating temperatures. This approach is more complex than the other approaches, making its performance more difficult to predict. The final cooling approach is film, or boundary-layer, cooling. In film cooling, a film is injected into the chamber close to its wall. This film can be the engine's fuel, oxidizer, or a dedicated coolant. The resulting oxidizer-to-fuel ratio in the film is very different from the ratio in the main part of the chamber, leading to a lower flame temperature. This approach is more complex than ablative cooling, but is lighter weight. It should be noted film cooling also results in reduced values for specific impulse from the injection of additional mass flow without any additional energy [5].

The propellant feed system for liquid rocket engines can be either tank pressure fed or pump fed. In tank pressure fed rockets, the driving force in the feed system is the pressure difference between the propellant tanks and the chamber pressure. This pressure difference is maintained with the addition of an inert pressurizing fluid stored in additional tanks. Pressure fed engines are relatively simple, but at the cost of performance and increased tank weight driven by the added structure required to maintain the initial tank pressure. In pump fed rockets, pumps drive the propellants from their tanks to chamber. These pumps are powered by turbines. The source of the working fluid for the turbines differentiates a number of different engine cycles for liquid rocket engines. Figure 2.3 shows schematics of the three typical cycles. Starting on the left of the figure is the gas generator cycle. In the gas generator cycle, a small amount of the fuel and oxidizer (2% - 5%) are fed into a small dedicated combustion chamber. The resulting fluid is then used to drive a turbine which drives the fuel and oxidizer pumps before being dumped overboard. Dumping the fluid after driving the turbine leads to a loss in specific impulse (on the order of 2% - 5%). In the center is the expander cycle. The expander cycle dictates the use of regenerative cooling as a cooling approach because the heat picked up from cooling the engine is what drives the turbine. In the expander cycle, a propellant, typically the fuel, is pumped from its tank through the regenerative cooling channels to the turbine and then to the injector.

The other propellant, typically the oxidizer, is pumped directly to the injector. The same turbine drives the pumps for both the fuel and the oxidizer. Expander cycles typically run at lower chamber pressures and thus have lower performance than the other two cycles, but they are relatively simple to design and manufacture. The third cycle, shown on the right in Figure 2.3, is the staged combustion cycle. The staged combustion cycle combines elements of the gas generator and the expander cycles. Just as in the gas generator cycle, there is a small dedicated combustion chamber powering the turbine. However, instead of dumping the products of this combustion overboard, they are fed into the main combustion chamber to complete the combustion process, similar to the expander cycle. The staged combustion cycle avoids the specific impulse penalty of the gas generator cycle while maintaining its high performance, but this comes at the price of increased complexity and cost [5].

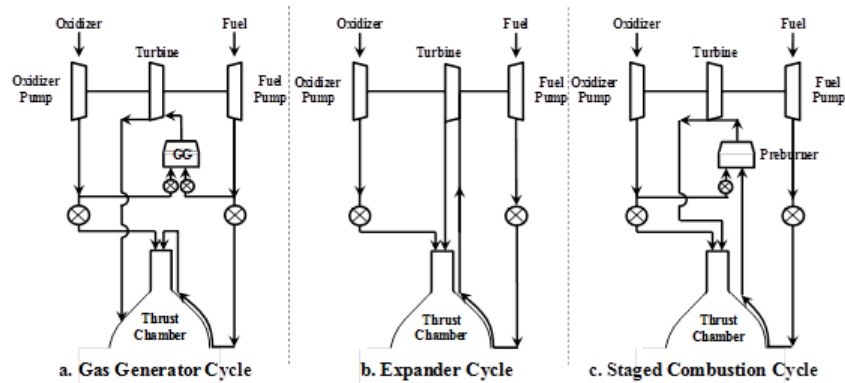


Figure 2.3: Typical Liquid Rocket Engine Cycles from Huzel and Huang[3], credit J. Hall[4]

2.1.3 Liquid Rocket Engine Design.

Liquid rocket engine design starts with requirements analysis followed by a conceptual design study. The goals of the conceptual design study for a liquid rocket engine are

to determine the rocket's layout and dimensions, estimate its weight, and calculate its expected performance generally in terms of thrust and specific impulse. As is common in engineering design, the design process for liquid rocket engines is an iterative one, as can be seen in Figure 2.4. The inputs to the design process are typically generated during a vehicle's mission analysis. Rocket engine design inputs cover both requirements and constraints. The requirements generally include the thrust, specific impulse, Δv per mission segment, the engine's lifetime, and the "-ilities" such as maintainability, reliability, and manufacturability. The constraints generally include cost, risk, geometric envelope, and development schedule [5].

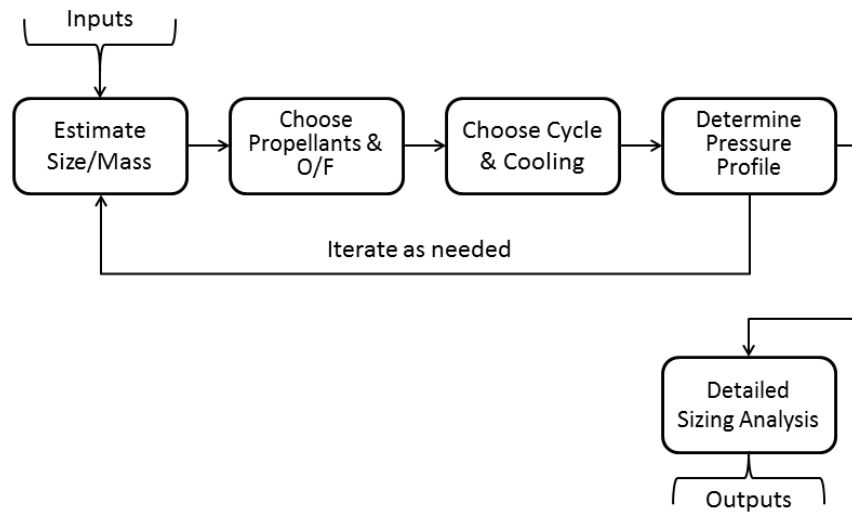


Figure 2.4: Liquid Rocket Engine Design Process

Once the requirements have been specified, the design process begins with an initial estimate of the size and mass of the engine based on historical data. The weight of a liquid rocket engine correlates strongly to thrust, propellant combination, and application (for example in space applications versus launch vehicle boosters). *Space Propulsion Analysis*

and Design provides a number of curve fits to develop initial estimates for the engine's mass and size based on the thrust and application [5].

After estimating the size and mass of the engine, the designer must choose the propellants and the oxidizer-to-fuel ratio (O/F) for bi-propellants. For a given propellant combination, expansion ratio, and engine cycle a specific oxidizer-to-fuel ratio produces a maximum specific impulse. This ratio produces the optimal energy release and exhaust molecular weight from the combustion reaction. For liquid hydrogen/liquid oxygen engines, the optimal oxidizer-to-fuel ratio is between 3.5 and 6.0 [24] [5].

The next steps in the design process are to choose the engine cycle and cooling approach. The determining factors in the choice of engine cycle are a trade off between performance, complexity, and cost. The engine cycle has a significant impact on the pressure levels in the chamber and feed system. For the cooling approach, the choice again comes down to one of performance and complexity. Generally speaking, higher performance engines will require more complex cooling approaches. It should be noted, choosing the expander cycle dictates the use of regenerative cooling in order to drive the cycle's turbine [5].

The final step in the iterative phase of the design process is to determine pressures in the chamber and the feed system. As the propellants flow from the tanks to the combustion chamber and eventually out to the ambient environment through the nozzle, the pressure changes. Causes of pressure changes include losses in the plumbing and the injector face, increases from the pumps, decreases across turbines, and the change in fluid velocity from zero in the tanks to the required velocity to deliver the necessary mass flow. During this step, the propellant mass flow is determined from the required thrust, and the chamber pressure and expansion ratio are varied to obtain a design which meets the required specific impulse. The pressure losses are then accounted for working back from the chamber to the tanks to determine the pressure in the propellant feed lines. For pump-fed cycles, the

required power and pressures are balanced for the turbine(s) and pump(s) from the pressure calculations. In expander cycle engines, lower turbine pressure ratios lead to improved T/W by decreasing the pump mass (lower pump-pressure rise leads to small pumps) or decreasing the chamber mass (higher chamber pressures lead to smaller chambers). The results of the analysis from this step can be plotted in pressure level plots, such as the one in Figure 2.5 to summarize the performance of the propellant feed system [5].

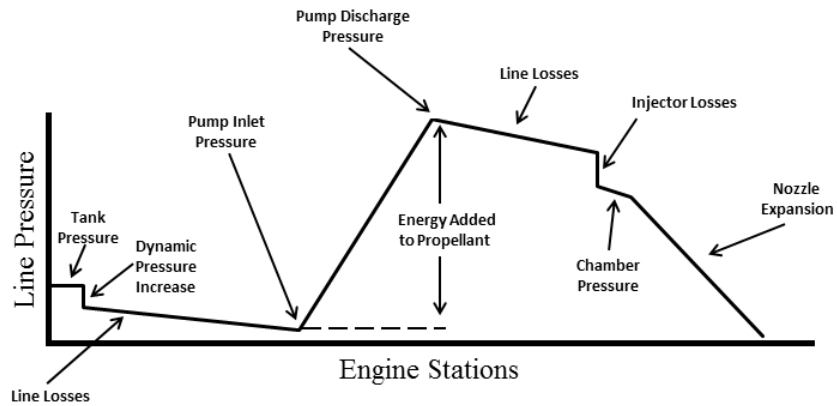


Figure 2.5: Example Pressure Plot of a Gas Generator Cycle; redrawn from Humble [5]

The above steps are iterated to converge on an initial design point. Once the initial design point has been selected, a more detailed sizing analysis can be conducted. This sizing analysis starts with the combustion chamber. The combustion chamber should be as small as possible while still being large enough for the combustion process to occur. Fully accounting for the combustion process is complex, so designers rely on empirical data when initially sizing the combustion chamber. The throat area is the first chamber sizing parameter to be calculated from the total mass flow, characteristic exhaust velocity, and chamber pressure using Equation (2.13) which is based on the definition of the characteristic exit velocity (Equation (2.5)) [5].

$$A_t = \frac{\dot{m}c^*}{p_c} \quad (2.13)$$

The throat area is then combined with the characteristic length (L^*), a design parameter measured in units of length and defined in Equation (2.14), to determine the chamber volume. The characteristic length relates the chamber volume to the throat area using historical data as a guide for sizing the chamber volume. The values computed from Equation (2.14) represent a minimum chamber volume. Shorter values for characteristic length lead to smaller engines, however poor combustion results from engines with values which are too short, so designers must seek a balance between engine size and combustion quality. Historical values for characteristic length range from 31.5 in to 39.4 in depending on the propellant(s). Liquid oxygen and liquid hydrogen engines have values between 29.9 in and 40.2 in. Assuming the chamber is a cylinder, the volume and Mach number can then be used to determine its cross-sectional area (and in turn its diameter) from Equation (2.15) and its length from Equation (2.16). Note, the Mach number (M) in the chamber must be subsonic, with typical values ranging from 0.1 (conservative designs) to 0.6 (aggressive designs) [5].

$$L^* = \frac{V_c}{A_t} \quad (2.14)$$

$$A_c = \frac{A_t}{M} \left[\left(\frac{2}{\gamma + 1} \right) \left(1 + \frac{\gamma - 1}{2} M^2 \right) \right]^{\frac{\gamma + 1}{2(\gamma - 1)}} \quad (2.15)$$

$$L_c = L^* \frac{A_t}{A_c} \quad (2.16)$$

The nozzle is the next component of the engine to be sized. For traditional bell nozzles, three parameters – the throat area, the exit area, and the length – define the size of the nozzle. The nozzle's throat area is already determined from the chamber sizing, since it must match the dimensions of the chamber throat. The exit area can then be calculated

by solving Equation (2.11) for A_e . Finally, the length can be estimated by assuming a percentage of the length of a 15° conical nozzle such as the common 80% bell nozzle. Equation (2.17) gives the length of a conical nozzle based on its throat and exit diameters and its half angle [5].

$$L_n = \frac{D_e - D_t}{2\tan(\alpha)} \quad (2.17)$$

After sizing the chamber and the nozzle, the engine mass can be estimated beginning with the chamber and nozzle, and continuing with the mass of the turbopumps, and feed lines and structural elements. The mass of the chamber and nozzle depend on the material used to fabricate them and the cooling approach used. However, in general, the process used to estimate the mass of the chamber and nozzle is to calculate the required wall thickness based on the material strength and the chamber pressure in order to calculate the volume of material needed for the chamber and nozzle. The total volume of material is then multiplied by the density of the material(s) to complete the mass estimation. The turbopumps, when present, represent design processes of their own. For initial mass estimation, designers can turn to empirical mass estimation relationships such as Equation (2.18). Similar mass estimation relationships exist for the feed lines and the structural elements [5].

$$m_{tp} = A\tau^B \quad (2.18)$$

$$\tau = \frac{P_{req}}{N_r} \quad (2.19)$$

2.1.4 Modeling Liquid Rocket Engines.

Computational modeling tools for rocket propulsion systems fall into two broad categories. The first is high level tools to provide overall performance of traditional rocket engine architectures. These tools generally assume the use of a bell nozzle, and one of the classic rocket engine cycles such as the expander cycle, the gas generator

cycle, or the staged-combustion cycle. Tools in this category include SpaceWorks Engineering's REDTOP and Alexander Ponomarenko's Rocket Propulsion Analysis. The second category is engine cycle analysis tools such as Pratt and Whitney's Rocket Engine Transient Simulator (ROCETS) and NASA's Numerical Propulsion System Simulation (NPSS). These tools allow designers to model entire engine cycles, making them useful in design scenarios involving new propulsion technologies and cycles.

2.1.4.1 REDTOP.

REDTOP is a liquid rocket engine analysis tool developed for use during conceptual design studies. REDTOP runs on MS Windows and Mac OS X, and can be used from the command line, the included graphical user interface, MS Excel, and Phoenix Integration's ModelCenter (through an included Analysis Server fileWrapper). REDTOP comes in standard and lite versions, with the standard version offering more detailed analyses. Both versions use a Gibb's free energy combustion analysis for both included and custom user propellants. Analyses in REDTOP include both ideal performance and real world performance based on estimated efficiencies. REDTOP automatically provides suggested efficiencies for the selected engine cycle and propellants, the chamber and the injector, and the nozzle [29].

Users can model both existing engines and new engines in REDTOP. To model existing engines, users generally specify the required mass flow of the engine being modeled. REDTOP will return the predicted thrust, and the nozzle and exit areas. To model new engines, users specify either required thrust and ambient conditions, the required throat area, or the required exit area. When the required thrust is specified, REDTOP returns the mass flow rate, and the throat and exit areas necessary to achieve the specified thrust. This is the usual method when using REDTOP as part of a vehicle design study. REDTOP can also return the thrust for throttle settings below 100%. After specifying one of the analysis objectives above, users then specify the propellants, the mixture ratio, the desired chamber

pressure, nozzle parameters, and the cycle type. Results for REDTOP analyses include the engine performance, the over all engine areas, and weight prediction based on both the summation of estimated component weights and a power-to-weight ratio. In addition to the performance and sizing analyses, REDTOP can also perform a flow separation analysis on the nozzle, and a gimbal range check for engine clusters [29].

2.1.4.2 Rocket Propulsion Analysis.

Rocket Propulsion Analysis (RPA) is a rocket engine analysis program which runs on MS Windows, Mac OS X, and Linux. The developer provides a free lite version, and a standard paid version. RPA's strengths are its flexibility in propellant options, including a wide range of built in propellants, plus support for both custom user defined propellants and importing CEA2 and PROPEP propellant definitions. Unlike REDTOP, RPA does not allow the user to specify a particular engine cycle. RPA uses a simpler approach of having the user define the chamber pressure, nozzle parameters, and propellant selections. The user must use the RPA results in another analysis to account for the effects of the engine cycle and the chamber design. RPA's calculations are indicative of actual performance for pressure fed and staged-combustion rocket engines [30].

Setting up an analysis in RPA involves three basic steps. The user begins by defining the overall problem. In the lite version the problem definition is simply the chamber pressure. In the standard version, the user also selects a design objective, for example solving for a nominal thrust level at a specified ambient pressure. The second step is to specify the propellant(s) and the mixture ratio. Note, RPA supports mono-propellant, bi-propellant, and tri-propellant engine designs. The final step is to define the nozzle parameters such as the exit pressure or the expansion ratio. RPA returns internal combustion analysis at the injector, throat, and the exit plane. RPA also returns engine performance values, both ideal and with losses, over a range of altitudes. The key engine performance values RPA reports are the vacuum and sea level specific impulse, the

characteristic velocity and the thrust coefficient (c_F) [30]. The engine’s actual thrust can be calculated from the thrust coefficient from Equation (2.20) if a throat area has been determined [24]. The standard version offers two other features over the lite version: a JavaScript Application Programming Interface to facilitate automated analyses and trade studies, and a chamber and nozzle geometry design and export tool [30].

$$F = c_F A_t p_c \quad (2.20)$$

2.1.4.3 Numerical Propulsion System Simulation.

NPSS is a computer simulation tool for modeling aircraft and rocket engines. Engine simulations built in NPSS provide higher fidelity results than engine cycle studies. NPSS has been developed by the NASA Glenn Research Center, with assistance from the aerospace propulsion industry. Models built in NPSS consist of a series of interconnected software objects representing the components of the engine under consideration. The object connections are made using NPSS Application Programming Interfaces, called “ports”, modeling fluid flows, mechanical connections, and thermal flows. A built-in solver in NPSS can then be used to drive the model design variables to balance the fluid flows, mechanical power, and thermal flows in the model and converge on a design point [31].

NPSS models have four classes of variables: the dependent variables the NPSS solver will ensure equal specified values, the independent variables the NPSS solver is free to adjust as necessary to converge the design, component inputs read by the NPSS solver but not altered by it, and component outputs calculated by the NPSS solver, but not driven toward a particular value. Taken together, the NPSS dependent variables and component inputs form the set of user specified design choices or design variables. The NPSS independent variables and component outputs form the set of user specified responses or response variables [31].

As part of the development of NPSS, NASA worked with members of the propulsion industry to verify and validate NPSS. This effort covered both air breathing and rocket engine modeling. Members of the NPSS development team modeled a number of engines and compared the NPSS outputs to the actual performance of the engines in question. Tests of the rocket capabilities in NPSS included modeling the RL10, an expander cycle liquid hydrogen/liquid oxygen upper stage engine. NPSS performed well in these tests, demonstrating its utility in modeling engine cycles [31, 32].

2.1.4.4 Rocket Engine Transient Simulator.

ROCETS is a modular rocket propulsion analysis tool developed by Pratt and Whitney for NASA. ROCETS can perform both steady-state analyses to model full power operation and transient analyses to model engine start up or shut down. Its modular design is built around connecting rocket engine components and reusable engine models. ROCETS supports both built-in components, such as pumps, turbines, and dynamic volumes, and custom user components. Engine models in ROCETS are defined in a formatted text file which is used to generate a FORTRAN program. The reusable engine models allow designers to run multiple analysis scenarios including parametric design, steady-state analysis, transient simulations, and generation of linear models, without recreating the underlying engine model. ROCETS has been used to model the Space Shuttle Main Engine, the RL10 upper stage engine, and the Space Transportation Main Engine design study [33].

2.2 Government Demand for Improved Rocket Engines

This section provides an overview of US government demand for improved rocket engines starting with the current US government launch vehicles and then covering three programs focused on the use of improved rocket engines. These demands are driven by US reliance on satellites and the continued need to effectively and affordably launch them.

2.2.1 Current Launch Vehicles.

The US government relies on satellites for surveillance, navigation, communication, and meteorology. Currently, the US uses the two launch vehicles from the Evolved Expendable Launch Vehicle (EELV) program, the Delta IV and Atlas V, to deliver many of its satellites to orbit. Both use variants of the RL10 to power their upper stages [17, 34].

The Delta IV is a family of medium-weight and heavy-weight launch vehicles. The Delta IV Medium first stage uses a single Common Booster Core. The Delta IV Heavy first stage uses three Common Booster Cores. The Delta IV family of launch vehicles has two upper stage variants: the 4 m upper stage (Figure 2.6) and the 5.2 m upper stage. Both upper stages are powered by a single RL10B-2. The RL10B-2 delivers 24,750 lbf vacuum thrust and uses an extension nozzle to achieve a vacuum specific impulse of 465.5 s. The RL10B-2 has a thrust-to-weight ratio of 37.3 [11, 34].



Figure 2.6: Delta IV Upper Stage, credit NASA KSC [6]

The Atlas V is the latest launch vehicle in the Atlas family going back to 1959. Current Atlas launch vehicles come in two variants offering different sized payload fairings. The

Atlas V 400 series has a 4 m diameter fairing and the Atlas V 500 series has a 5.4 m fairing. Both variants use the same Centaur upper stage (Figure 2.7), powered by one or two RL10A-4-2 rocket engines. The RL10A-4-2 generates 22,300 lbf vacuum thrust with vacuum specific impulse of 451.0 s and thrust-to-weight ratio of 60.3 [34, 35].



Figure 2.7: Centaur Upper Stage, credit NASA KSC [7]

2.2.2 US Air Force Next Generation Launch Programs.

The thrust-to-weight ratio of high thrust liquid rocket engines follows a decades long trend documented by B. McHugh in 1995 [23]. McHugh's research covers bi-propellant liquid rocket engines producing thrust between 60,000 N (13,500 lbf) and 8,000,000 N

(1,800,000 lbf). He based his results on data from fourteen rocket engines developed over 40 years, which included one expander cycle engine, and a mix of gas generator and staged combustion cycle engines. One of McHugh's findings was the clustering of thrust-to-weight ratios for rocket engines, as opposed to the thrust-to-weight ratios of the launch vehicles, based on their propellants. He found liquid hydrogen/liquid oxygen engines have vacuum thrust-to-mass ratios (T/M) between 0.4 and 0.6 kN/kg, and RP-1/liquid oxygen engines have vacuum thrust-to-mass ratio between 0.7 and 1.0 kN/kg. Multiplying these values by 1000 N/kN and dividing by 9.81 m/s^2 converts McHugh's values to traditional vacuum thrust-to-weight ratios, shown in Table 2.1 [23].

Table 2.1: Thrust-to-Weight Range Based on Propellants

	LH2/LOX	RP-1/LOX
T/M (kN/kg)	0.4 - 0.6	0.7 - 1.0
T/W	41 - 61	71 - 102

Since 1996, the Department of Defense, NASA, and the aerospace propulsion industry have been working to double U.S. rocket propulsion capability when compared with 1993 rocket propulsion capability including thrust-to-weight ratios. Two major programs have been started to meet this goal. The first is the Integrated High-Payoff Rocket Propulsion Technology program (IHPRPT). Scheduled to end in 2010 with an extension to 2012, IHPRPT was divided into propulsion categories (boost, orbit transfer, and spacecraft propulsion) and phases. Research into upper stage rocket engines continues in the Phase III orbit transfer efforts. The goals for the Phase III orbit transfer research are to improve vacuum specific impulse and thrust-to-weight ratio, and to reduce the costs and failure rates of launch vehicle upper stages. The anticipated benefits of meeting these goals are to

increase expendable launch vehicle payload mass by 22% and reduce their launch costs by 33% [19].

The second program is the U.S. Air Force's Next Generation Engine (NGE) which seeks to replace the RL10 on both the Delta IV and the Atlas V by 2017. Since the NGE is intended to replace the RL10, the Air Force is requiring the NGE to be compatible with the Delta IV and the Atlas V. The NGE must use the same propellant combination as the RL10, liquid hydrogen/liquid oxygen, and it must be able to integrate on both launch vehicles. Performance requirements include vacuum thrust in the range of 25,000 lbf to 35,000 lbf, a vacuum specific impulse of at least 465 s, and a life expectancy of at least 3000 s. Size constraints for the NGE are a maximum length (gimbal to nozzle exit) of 90 in, and a maximum exit diameter of 73 in [18].

The RL10B-2 falls just outside of these requirements. Its 24,750 lbf vacuum thrust is just under the NGE minimum thrust and its high-expansion ratio nozzle has a diameter of 84.5 in exceeding the NGE constraint by nearly 16%. It is worth noting, the RL10B-2's use of an extendable nozzle gives an engine length of 86.5 in when stowed, meeting the NGE constraint despite its high expansion ratio [11].

2.2.3 NASA's *Space Launch System*.

NASA has its own upper stage engine requirements centered on the Space Launch System (SLS). The SLS is a shuttle derived super-heavy lift human-rated launch system which is still in the design phase. As a human-rated launch vehicle, work on the SLS is closely coordinated with the Orion crew capsule program. Its super-heavy lift capacity, between 70 metric tons and 130 metric tons to low-Earth orbit, is crucial to its role as a launcher for missions beyond Earth orbit [22].

Four upper stage configurations are being considered for the SLS, with two configurations being relevant to this research. The first design is an upper stage powered by four RL10 engines, using the RL10B-2 version or a similar design. This configuration

is shown in Figure 2.8. The quoted performance for the RL10s used in this design is a vacuum thrust of 24,750 lbf and a vacuum specific impulse of 462.5 s. The four RL10 engines together give a total vacuum thrust of 99,000 lbf and have a total weight of 2656 lbf for a thrust-to-weight ratio of 37.3 [8, 36]. Table 2.2 summarizes the four RL-10 cluster performance and dimensions.



Figure 2.8: SLS Upper Stage with Four RL10 Engines, credit The Boeing Corporation [8]

Table 2.2: Key Performance Parameters for the SLS RL10 Rocket Engine Cluster [8, 11]

Parameter	Value
Vacuum Specific Impulse (s)	462.5
Vacuum Thrust (lbf)	99,000
Thrust-to-Weight Ratio	37.3
Outer Radius (in)	108.0
Stowed Length (in)	86.5

The second of these designs is an upper stage powered by a single J-2X engine, shown in Figure 2.9. The J-2X is the successor to the LOX/LH2 engine which powered the Saturn V's upper stage. Like the J-2, the J-2X is powered by a gas generator cycle. The J-2X is being designed to have a vacuum thrust of 294,000 lbf, a vacuum specific impulse of 448 s, and a weight of 5,450 lbf giving it a thrust-to-weight ratio of 55 [8, 12, 37]. Table 2.3 summarizes the J-2X performance and dimensions.

Table 2.3: Key Performance Parameters for the J-2X Rocket Engine [12, 13]

Parameter	Value
Vacuum Specific Impulse (s)	448.0
Vacuum Thrust (lbf)	294,000
Thrust-to-Weight Ratio	55.0
Outer Radius (in)	60.0
Length (in)	180.0



Figure 2.9: SLS Upper Stage with Single J-2X Engine, credit The Boeing Corporation [8]

2.2.4 US Air Force Space Plane Program.

In addition to its research into next generation expendable launch technologies, the US Air Force has also renewed its interest in reusable space planes. The result is the X-37 Space Maneuvering Vehicle, a test platform for advanced spaceflight hardware and

technologies including automated approach and landing, light weight and high performance thermal protection systems, and hot structure control surfaces. Development of the X-37 is a joint project including contributions from the US Air Force, various NASA centers, and private industry. The X-37 has been developed in two phases, each targeting a separate technology demonstration vehicle. The first phase, using the Approach and Landing Vehicle (ALTV), focused on aerodynamic testing and proving the function of the automated approach and landing system.

The second phase, which is ongoing, uses the Orbital Test Vehicle (OTV) to test the on orbit and reentry technologies including the thermal protection systems and the hot structure control surfaces [20]. Two X-37 OTVs have been built and flown to date. The first vehicle, OTV-1, completed its mission of 225 days on December 3, 2010. The second vehicle, OTV-2, was first launched on March 5, 2011.[38] Figure 2.10 shows the OTV in its launch configuration aboard an Atlas V [9].

The X-37 OTV uses an AR2-3 hydrogen-peroxide/kerosene engine for on orbit maneuvers [21]. Figure 2.11 shows a view of the AR2-3 engine on the OTV after one of its missions. The AR2-3 has a long history with the US Air Force. It was developed by the Rocketdyne corporation between 1955 and 1969. The original mission of the AR2-3 engine was to augment jet fighter propulsion systems to give the aircraft increased speed and allow them to reach increased altitudes. The AR2-3 programs were quite successful, accumulating over a dozen hours of operation and allowing aircraft to reach altitudes of 121,000 ft [39].

The AR2-3 generates 6600 lbf of vacuum thrust which can be throttled down to 3300 lbf. Its vacuum specific impulse of 246 s is much lower than the other engines mentioned in this chapter. The AR2-3 is powered by a gas generator cycle using the mono-propellant reaction of the hydrogen-peroxide oxidizer with a catalyst to drive the turbine. Table 2.4 summarizes the AR2-3 performance and dimensions [14].



Figure 2.10: X-37 Orbital Test Vehicle, credit US Air Force [9]

Table 2.4: Key Performance Parameters for the AR2-3 Rocket Engine [14]

Parameter	Value
Vacuum Specific Impulse (s)	246.0
Vacuum Thrust (lbf)	6600
Thrust-to-Weight Ratio	29.3
Outer Radius (in)	10.0
Length (in)	32.0



Figure 2.11: Rear View of X-37 including the AR2-3 Engine, credit US Air Force [10]

2.3 The Dual-Expander Aerospike Nozzle Upper Stage Engine

The focus of this research is the design and evaluation of a new liquid hydrogen/liquid oxygen upper stage rocket engine being studied at the Air Force Institute of Technology. This new engine is the Dual-Expander Aerospike Nozzle (DEAN). The DEAN is named after its two key design choices, the use of two separate expander cycles and an aerospike nozzle. This section covers the DEAN's architecture, research history pertaining to its key design choices, and AFIT's research and design work on the DEAN.

2.3.1 DEAN Architecture.

The DEAN architecture, shown in Figure 2.12, uses two novel design choices. The first is the use of separate expander cycles for the fuel and the oxidizer. In a traditional expander cycle, the fuel is pumped through a cooling jacket for the chamber and nozzle. The heat picked up by the fuel from cooling the chamber and nozzle is then used to drive the turbine that runs both the fuel and oxidizer pumps before the fuel is introduced into the chamber [5]. In the DEAN, the fuel and oxidizer each drive their own turbines to power their own pumps.

The second novel design choice of the DEAN is the use of an aerospike, or plug, nozzle. Aerospike nozzles run through the middle of the rocket's propellant flow and up

into the chamber, leaving the ambient atmosphere to form the outer boundary for the flow. The interaction with the ambient atmosphere gives aerospike nozzles automatic altitude compensation, making them more efficient over a range of altitudes. Similar bell nozzles operate most efficiently at their specific design altitude [24]. In the DEAN, the use of an aerospike nozzle provides a second, physically separate cooling loop from the chamber for use in the fuel expander cycle.

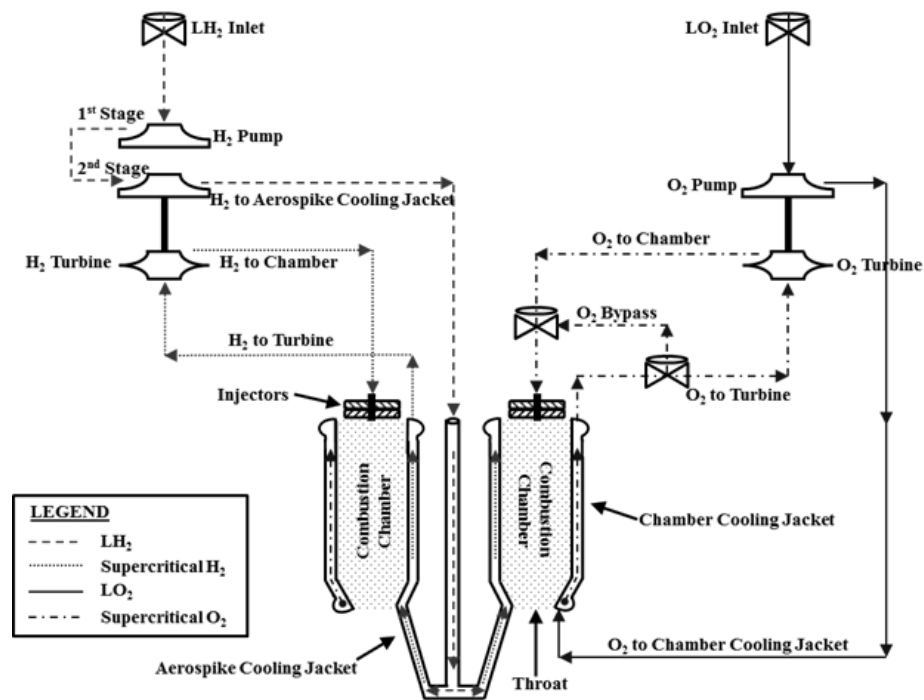


Figure 2.12: DEAN Architecture, credit J. Hall (unpublished)

The DEAN's unique architecture offers a number of advantages. The second cooling loop increases the surface area inside the chamber, transferring greater energy to the propellants and in turn providing more power to the turbines, providing for correspondingly increased power to the pumps and in turn increased chamber pressure. The increased chamber pressure leads to engine performance improvements when compared to traditional

expander cycle engines such as the RL10. This improved performance leads to smaller engines for similar levels of thrust and specific impulse in terms of both weight and physical dimensions. The separate expander cycles also ensure the fuel and oxidizer remain physically separated until entering the combustion chamber, eliminating one of the more catastrophic failure modes in traditional expander cycles, namely failure of an inter-propellant-seal. The DEAN architecture is also a forerunner to a similar boost stage architecture, where the aerospike nozzle's global performance could result in even greater performance gains [2, 25–27].

The DEAN architecture is not without its challenges, though. The LOX cycle requires a turbine material able to withstand an oxygen environment. Material studies at AFIT have shown Inconel 718 provides both satisfactory oxygen resistance and suitable mechanical performance for use in both the pump and the turbine in the LOX cycle [26, 27]. Also, the expansion ratio of aerospike nozzles is limited to the ratio of the area of the chamber at the throat to the throat area [24]. Due to this limit, aerospike nozzles generally need larger chamber diameters to reach useful expansion ratios, potentially limiting the range of engines which offer improved thrust-to-weight ratios while also delivering the required specific impulse.

2.3.2 Research History of Core Technologies.

This section covers the research history of the two key features of the DEAN architecture. First it covers dual-expander research, both dual fuel based cycles and the cycles using separate expander cycles for the two propellants like the DEAN. Second, it reviews the history and testing of aerospike nozzles from the 1950s to the present.

2.3.2.1 Dual-Expander Cycles.

Two separate meanings of dual-expander cycle show up in the literature. The first, and more prevalent meaning is also called the Dual-Fuel/Dual-Expander cycle (DF/DX). Research into the DF/DX engine cycle was conducted in the late 1980s and early 1990s

to develop an engine for use in Single-Stage-to-Orbit launch vehicles. The DF/DX cycle utilizes a dense hydrocarbon fuel, such as RP-1, and liquid hydrogen with liquid oxygen in a dual chamber/dual nozzle configuration. The pervasive dual nature of the engine cycle allows the engine to run with a mix of fuels for low altitude operations during launch, making use of the higher density fuel early in the the flight, and transitioning to pure liquid hydrogen at higher altitudes and in orbit for its high specific impulse. Research showed engines utilizing this cycle to be significantly smaller and lighter than comparable engines utilizing traditional cycles. It should be noted, the DF/DX cycle utilizes preburners to drive its turbines, and is not related to the traditional expander cycle [40–43].

The second, and less prevalent meaning of dual-expander in the literature is that of the DEAN, namely the operation of separate expander cycles for the fuel and oxidizer. Research into this cycle shows chamber pressures as high as 2000 - 3000 psia are possible with the dual-expander cycle, which are significantly higher than traditional expander cycles. Aerojet TechSystems used cooling channels in both the chamber and the nozzle to drive the fuel cycle and cooling channels in chamber to drive the oxidizer cycle in their proposed dual-expander cycle engine. Aerojet's proposed engine had a vacuum thrust of 3750 lbf, and would be grouped into a cluster of four engines to meet the 15,000 lbf vacuum thrust requirement of the Orbital Transfer Vehicle. As part of the research into this engine, Aerojet built and tested a complete oxygen turbine/pump assembly built out of Monel, a nickel/copper alloy used in high performance aerospace applications. The successful testing of this turbine/pump assembly conducted at Aerojet demonstrated the feasibility of building and operating a liquid oxygen expander cycle [44].

2.3.2.2 *Aerospike Nozzles.*

Rocketdyne is credited with developing the aerospike nozzle concept in the 1950s [45, 46], and while the aerospike nozzle has not been used in an operational propulsion system, there are numerous publications in the literature covering the performance, design,

and testing of aerospike nozzles. Research into the performance of aerospike nozzles dates back to the 1950s and continues to this day. NASA research has included investigations into the effect of design parameters including base bleed, nozzle area ratio, and plug length on performance. Results from this research indicate a small base bleed (no more than 1% of total mass flow) can offer significant performance gains [47]. Research at the California State University at Long Beach (CSULB) is investigating the affect of nozzle truncation on aerospike performance. The CSULB researchers developed Computational Fluid Dynamics (CFD) models of full length and 20% truncated aerospike nozzles. Their findings indicate there is a negligible difference (0.2%) in thrust between the full length and 20% truncated aerospike nozzles, which would favor the lighter truncated design. Note, the CSULB research did not address the specific impulse of the two nozzles [46].

Much of the research into the design of aerospike nozzles has focused on means of determining the nozzle contour. As early as 1964, Gianfranco Angelino proposed an approximation method to calculate the contour of two-dimensional and axisymmetric aerospike nozzles. His approximation is based on an assumption of linear characteristic lines with constant properties and a choked (or sonic) throat [48]. Modern computer codes, such as Software Engineering Associates' Two-Dimensional Kinetics (TDK) implement the Method of Characteristics (MoC) to calculate the contour of aerospike nozzles. TDK can also calculate the nozzle's performance in the same analysis run, making it a powerful tool in aerospike modeling [49]. Research in 2001 at the Beijing University of Aeronautics and Astronautics looked at designing aerospike nozzle contours by optimizing the total impulse over the entire proposed trajectory. Their findings indicate this approach not only delivers improved average performance, but also improved performance over bell nozzles at low and high altitudes [50] In recent years, California Polytechnic State University has developed its own software to determine the contour of a minimum length aerospike nozzle. Their software requires three parameters: the pressure ratio between the chamber and

ambient conditions (or Nozzle Pressure Ratio), the ratio of specific heats, and the ambient pressure. Unlike some other techniques, this software does not require the specification of the upstream geometry to calculate the aerospike nozzle's contour [51].

Research tests of aerospike nozzles have led to the development and testing of four aerospike engines, two of which have been flown on experimental sounding rockets. The earliest aerospike engine, the liquid hydrogen/liquid oxygen J-2T (Figure 2.13(a)), was developed by Pratt and Whitney Rocketdyne in the 1960s. As the name implies, the J-2T was a modified Saturn V J-2 upper stage engine. The goal of this program was to compare the performance of the aerospike nozzle with the existing bell nozzle on the production J-2 engine. The J-2T was not flown on any missions, but it was fired on a Pratt and Whitney Rocketdyne test stand [52]. The next aerospike engine to be built was developed in the 1990s in support of NASA's X-33 single-stage-to-orbit launch vehicle. As with the J-2T, the X-33's XRS-2200 linear aerospike engine (Figure 2.13(b)) ran on liquid hydrogen/liquid oxygen, and was only operated on a test stand [53].

Two experimental sounding rockets have been used for flight testing of aerospike nozzles. One, the Optimal 168, was a solid fueled rocket developed as part of a joint research program between NASA, the U.S. Air Force, Blacksky Corporation, and Cesaroni Technology/Cesaroni Aerospace. This research effort included developing two sister sounding rockets, one with a conical nozzle and one with an aerospike nozzle to compare the performance of the two nozzles. Flight tests of the Optimal 168 provided the first set of transonic flight data for aerospike rockets, but did not provide the anticipated comparison between the two nozzles as the chamber pressures and thrusts for the aerospike nozzle were lower than predicted. The authors concluded this discrepancy was caused by a larger than designed throat area in the aerospike nozzle [54]. The second sounding rocket to test aerospike nozzles, Garvey Spacecraft Corporation's (GSC) Prospector-2B (Figure 2.13(c)), included the first liquid propellant aerospike engine to be flown. The Prospector-2B was

powered by a pressure fed ethanol/liquid oxygen ablative cooled engine, and produced 1000 lbf of thrust at sea level. GSC flew the Prospector-2B twice to demonstrate the feasibility of their design. GSC continued their development program by working on a high-expansion ratio aerospike engine for use in a Nanosat Launch Vehicle (NLV) [55, 56].

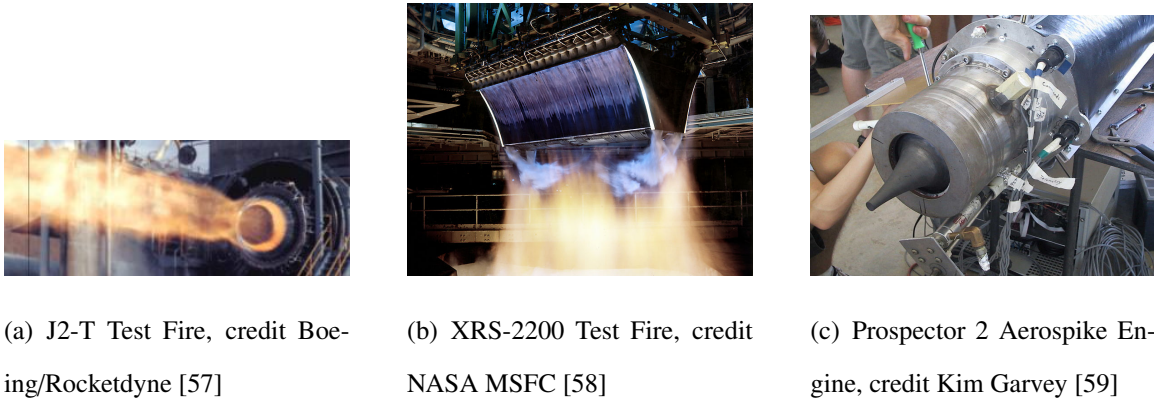


Figure 2.13: Example Aerospike Engines

2.3.3 DEAN Research History.

The research presented here builds on four generations of previous DEAN models. All four generations use NPSS to implement their cycle model. Three of the four previous DEAN models extend the cycle model by embedding it in a system level engine model built in Phoenix Integration's ModelCenter. ModelCenter is a multidisciplinary modeling environment used to study the trade space of a design and optimize that design. ModelCenter can combine analyses developed in a variety of tools including MATLAB, Mathcad, Excel, and command line executables into a single system level model [60]. The system level DEAN simulation automates a parameterized version of the cycle model and connects it to additional analyses to estimate the DEAN's weight and geometry in order to compute the DEAN's physical dimensions and thrust-to-weight ratio.

The first generation research focused on developing the initial cycle model of the DEAN for a single design point. The second generation research implemented parametric modeling of the DEAN by refactoring the cycle model and integrating it into the first system level model. The third generation research extended the system model to include additional calculations such as structural sizing, nozzle contour, and engine weight. Finally, a parallel research effort was conducted to determine the feasibility of developing a DEAN fueled with methane in place of liquid hydrogen. The following subsections summarize the methodology and results of these research efforts.

2.3.3.1 First Generation DEAN.

From 2007 to 2008, AFIT researched the DEAN architecture in a series of three projects. The initial performance goals for the DEAN were a vacuum thrust of 50,000 lbf, a vacuum specific impulse of 464 s, and a thrust-to-weight ratio of 106.5. The first project, conducted by D. Martin, demonstrated the feasibility of the DEAN's over all engine cycle by developing the initial cycle model. This first cycle model was hard coded for a single design. The remaining two projects, conducted by A. Arguello and W. Strain, verified the performance of the individual expander cycles for Martin's design using Pumpal and RITAL, industry standard pump and turbine design software respectively [2, 25, 26].

Martin focused his work on the design and modeling of the chamber, cooling jackets, and nozzle. His design process began by making initial estimates for three key properties of the DEAN: the oxidizer-to-fuel ratio (7.0), the expansion ratio (125), and the chamber pressure (1740 psia). Martin selected these initial values to maximize the vacuum specific impulse, using the RL10 as a guide. Based on these values, Martin then calculated an estimated mass flow and sized the chamber, nozzle, and cooling channels. The inputs Martin chose for the chamber were its radius, length, and the contour of the chamber's outer and inner walls. The outputs for the chamber design were the chamber pressure and temperature. The inputs Martin chose for the nozzle were the throat area, the expansion

ratio, and its length. The outputs for the nozzle were the vacuum thrust and vacuum specific impulse [2].

For the cooling channels, Martin elected to use milled channels over tubular channels. His research indicated the milled channels offered both superior performance and manufacturability. The aspect ratio of the cooling channels was not constant along the length of the engine. Instead, the aspect ratio was varied according to cooling priority. Near the throat, the aspect ratio is relatively low to provide maximum heat transfer, while the aspect ratio is higher toward the end of the cooling channels to keep the flow subsonic. The outputs for the cooling channels were the heat flow and the fluid Mach number [2].

Arguello and Strain studied the DEAN's two expander cycles by modeling the turbopumps in Pumpal/RITAL. These turbopump modules agreed well with Martin's cycle model. For example, the liquid hydrogen pump module showed the required power of the first pump is 2523 HP (less than 1% difference from the value calculated in the cycle model) and the required power of the second pump is 1079 HP (approximately 3% difference from the cycle model). Further, the liquid hydrogen pump's pressure exiting the second pump stage is 4050 psia versus 4000 psia in the cycle model (approximately 1% difference) [25]. The liquid oxygen pump module showed similar agreement. For example, the results for the liquid oxygen pump showed the required power is 2215 HP (approximately 12% difference from the cycle model) and the pressure generated by the liquid oxygen pump is 4600 psia versus 4500 psia in the cycle model (approximately 2% difference) [26].

Martin's final design, shown in Figure 2.15(a), exceeded the design goals. The DEAN model produced a vacuum thrust of over 57,000 lbf (+14%) and a vacuum specific impulse of more than 472 s (+1.8%). The predicted thrust-to-weight ratio was 119, beating the design goal by almost 12%, and engine length was 38 in, 61% shorter than the RL10B-2 [2]. Further, the results of the combined efforts of Martin, Arguello, and Strain confirmed

the feasibility of the DEAN and verified the expander cycles in Martin's NPSS model of the DEAN.

2.3.3.2 *Second Generation DEAN.*

The second generation research focused on the development of the first system level DEAN model, shown in Figure 2.14. The DEAN model employed parametric modeling techniques, modified design variables, and a simplified nozzle geometry. The pressure ratios of the pumps were replaced as inputs with the total mass flow and the oxidizer-to-fuel ratio. The DEAN geometry was determined from the chamber's inner and outer radii and the chamber length parametrization. The assumption of an expansion ratio of 125 was maintained in this model [27].

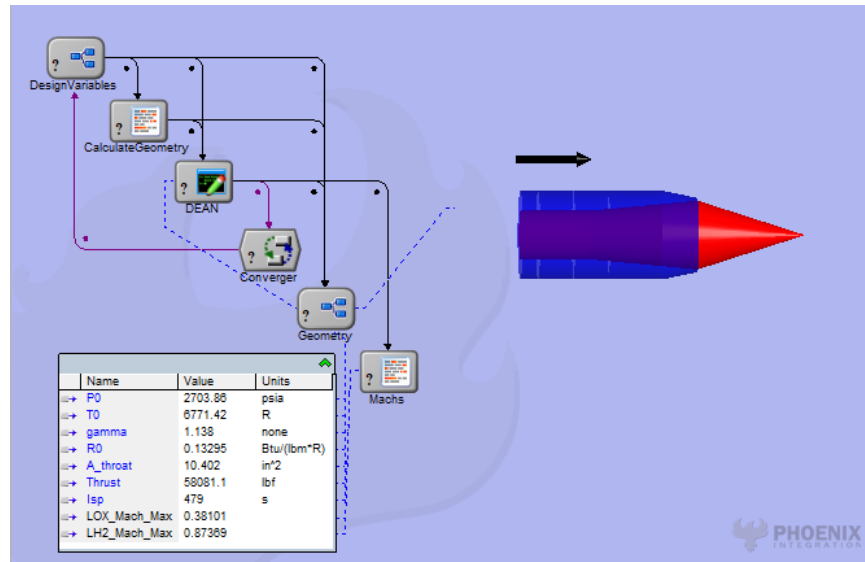


Figure 2.14: Second Generation DEAN Model

The new DEAN model was then used to run parametric studies over the chamber geometry and propellant flow using the chamber length and radii, total mass flow, and oxidizer-to-fuel ratio as design variables. While parametric studies over total mass flow and

the oxidizer-to-fuel ratio yielded a large number of valid designs, parametric studies over chamber geometry were less successful. Only studies over the chamber length produced significant numbers of valid designs. Attempting to vary the chamber's radii resulted in computational errors in the cycle model. In total, the completed parametric studies yielded more than one hundred new designs in the DEAN trade space, further demonstrating the feasibility of the DEAN architecture [27].

The results of the parametric studies were then used to scale down the DEAN design to more closely match the original design goals. The resulting design had a vacuum thrust of 50,900 lbf and a vacuum specific impulse of 489 s, while being 25% shorter in total length and reducing the size of the turbomachinery by reducing the total mass flow. Figure 2.15 compares the original DEAN geometry with the scaled DEAN [27].

This research both expanded the DEAN trade space and demonstrated the power of combining engine cycle models with parametric modeling in the development of new liquid rocket engines. The expanded trade space resulted in a significantly improved design for the DEAN. Further, finding such an improved design using basic parametric modeling capabilities showcased the power of parametric modeling in rocket engine design [27]. Chapter 3 covers the research in more detail, and also appears as an article in the March/April 2011 volume of the *AIAA Journal of Spacecraft and Rockets* [27].

2.3.3.3 Third Generation DEAN.

Hall built upon the initial system level model in the second generation DEAN to perform a detailed estimation of the DEAN's performance, weight, and geometry. Hall continued to work towards the original design goals of 50,000 lbf vacuum thrust, 464 s vacuum specific impulse, and a thrust-to-weight ratio of 106.5. The third generation DEAN includes a number of new analysis codes including a custom implementation of the aerospike's geometry, NASA's Chemical Equilibrium with Applications (CEA) to estimate

chamber properties for analyses, executed before the cycle model, and Two Dimensional Kinetics (TDK) to improve the model's performance estimates [4].

Hall's research noted the assumed expansion ratio did not match the DEAN geometry. As discussed in Section 2.1.2, the expansion ratio of an aerospike nozzle is limited by the area of the chamber at the throat. Additionally, the length of an aerospike nozzle is directly related to its expansion ratio [24]. Previous DEAN research efforts simply assumed an expansion ratio of 125 and a similarly assumed nozzle length. Hall updated the nozzle module to calculate the expansion ratio from the outer throat radius and throat area, significantly reducing the vacuum specific impulse. Hall ran a number of trade studies in search of designs to improve the vacuum specific impulse result. However, the third generation DEAN model was unstable during studies varying the chamber radii, making it difficult to improve the expansion ratio and in turn the vacuum specific impulse [4].

Hall used the updated DEAN system level model for verification studies showing the underlying cycle model provides reliable results. An initial survey into the component materials to be used to construct the DEAN was necessary to estimate the thrust-to-weight ratio of the engine for the third generation's final design. The survey results conclude the chamber should use silicon carbide for its cooling jacket and aluminum 7075 T6 for its structural jacket. The aerospike nozzle would best benefit from being fabricated from a single material, oxygen-free copper (C10100) [4].

The third generation research produced a final design with a vacuum thrust of 50,000 lbf, 430 s vacuum specific impulse, and a thrust-to-weight ratio of 142 (27 inch envelope). This design exceeds the required thrust-to-weight ratio and delivers the required vacuum thrust; however, it falls far short of the desired vacuum specific impulse. These results highlight the need for a parametrization of the DEAN geometry enabling the model to run over a wider range of expansion ratios. Additionally, exposing more turbomachinery

variables to the ModelCenter environment will allow for the execution of trade studies over turbine efficiencies and shaft speeds [4].

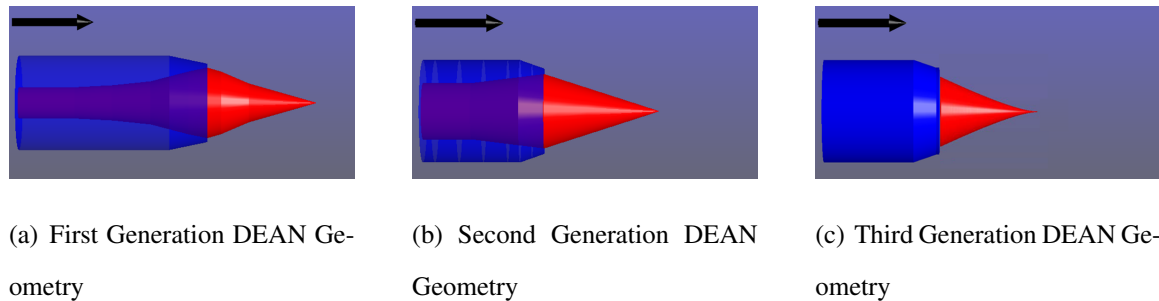


Figure 2.15: Comparison of First, Second, and Third Generation DEAN Geometry

2.3.3.4 Methane DEAN.

From 2011 to 2012, AFIT conducted a parallel line of research to explore the feasibility of a methane powered DEAN engine. This research was carried out by M. Moen. The focus of Moen's work was to adapt the cycle model to utilize methane as the fuel in place of liquid hydrogen. Adjusting for the different performance characteristics of methane versus liquid hydrogen and changes in research goals at the US Air Force led Moen to target a different design goal with the Methane DEAN. This new design goal was to develop an engine with 25,000 lbf vacuum thrust, 383.0 s vacuum specific impulse, and a thrust-to-weight ratio of 108.0. In addition to implementing the required changes to the cycle model to support methane as a fuel, Moen also utilized a number of improvements to the system level model developed by the author based on Hall's recommendations from the third generation DEAN, research demonstrating their utility and function [61].

Moen's research resulted in a design delivering 25,000 lbf vacuum thrust with a vacuum specific impulse of 349.3 s and a thrust-to-weight ratio of 120.7 in a 23 inch long engine. As with previous DEAN research, the initial Methane DEAN design exceeds the thrust-to-weight ratio requirement while falling short of the specific impulse requirement.

Similarly, the Methane DEAN's physical dimensions are also much smaller than traditional upper stage engines. Moen completed his study of the Methane DEAN by conducting a first order comparison of stage sizes and payload capacities between the Methane DEAN and traditional upper stages engines. As expected, he found the shortfall in specific impulse was not completely accounted for by the excess in thrust-to-weight or the compact size of the Methane DEAN [61].

2.4 Engineering Optimization

This section covers a number of topics concerning engineering optimization. It opens with essential terminology used to define and discuss engineering optimization problems. The section continues with a discussion of how optimization problems are formally defined. Finally, the section closes with a review of optimization algorithms used in this research.

2.4.1 Optimization Terminology.

Engineering optimization is the process of finding designs with the minimum “costs” or the maximum “benefits” subject to technical and business limitations. The formal application of optimization to engineering problems seeks to minimize or maximize a function describing one or more aspects of the system being designed. This function is called the objective of the optimization problem and represents the criterion for selecting the best design among the available designs. Optimization problems may have one objective function or many. If the problem has only one objective function, it is said to be a single objective problem. If the problem has more than objective, it is said to be a multi-objective problem [62].

The parameters defining the design of a system fall into two categories. Those parameters that can be set to fixed values during earlier stages of the design process are called preassigned parameters. The remaining parameters are the design variables, so called because they represent unknown values to be determined by the design process. The objectives defined above are functions of the design variables. The design variables can

be recorded as a vector with each element in the vector representing an individual design variable. The n -dimensional space defined by treating the design vector as a coordinate vector is the design space [62].

Optimization problems can be unconstrained or constrained. Unconstrained optimization problems do not have any constraints placed on the results of the optimization. Constraints are additional functions of the design variables that must satisfy various equality or inequality conditions for the design to be feasible. Constrained optimization problems are problems with one or more constraints [62].

For multi-objective optimization problems with convex and competing objective functions no single design will optimize all objectives simultaneously. Instead, these problems yield a set of “optimal” designs called the Pareto optimum solution or Pareto front. Each Pareto design is one such that to improve one of the objectives one or more other objectives must be lessened [62].

2.4.2 Defining Optimization Problems.

Optimization problems are defined formally using mathematical expressions of the objective(s), design variable(s), and constraint(s) (if present). Four examples will be discussed below: an unconstrained single objective problem, an unconstrained multi-objective problem, a constrained single objective problem, and a constrained multi-objective problem.

2.4.2.1 Unconstrained Single Objective Problem.

Equation (2.21) gives the prototype for an unconstrained single objective optimization problem. The problem definition starts by stating to find the value for design vector \mathbf{X} which solves the optimization problem. The definition then defines whether to maximize or minimize the objective function $f(\mathbf{X})$ and proceeds to define the objective function mathematically. Finally, the definition lists any bounds on the design vector if present [62].

$$\text{Find } \mathbf{X} = \begin{Bmatrix} x_1 \\ x_2 \\ \vdots \\ x_n \end{Bmatrix} \text{ which minimizes}$$

$$f(\mathbf{X}) = \text{objective definition}$$

where

$$\mathbf{X} = \text{design vector bounds}$$

(2.21)

2.4.2.2 Unconstrained Multi-Objective Problem.

Equation (2.22) gives the prototype for an unconstrained multi-objective optimization problem. The definition is similar to the one for a single objective problem shown in Equation (2.21). The key difference is the inclusion of multiple objective function definitions $f_1(\mathbf{X})$ through $f_n(\mathbf{X})$. An alternative form of multi-objective problem definitions replaces the list of objective functions with a new, single objective function constructed as the weighted average of the individual objective functions as shown in Equation (2.23) [62].

$$\text{Find } \mathbf{X} = \begin{Bmatrix} x_1 \\ x_2 \\ \vdots \\ x_n \end{Bmatrix} \text{ which minimizes}$$

$$f_1(\mathbf{X}) = \text{objective 1 definition}$$

$$f_2(\mathbf{X}) = \text{objective 2 definition}$$

$$\vdots$$

$$f_n(\mathbf{X}) = \text{objective n definition}$$

where

$$\mathbf{X} = \text{design vector bounds}$$

(2.22)

$$f(\mathbf{X}) = \alpha_1 f_1(\mathbf{X}) + \alpha_2 f_2(\mathbf{X}) + \dots + \alpha_n f_n(\mathbf{X}) \quad (2.23)$$

2.4.2.3 Constrained Single Objective Problem.

Equation (2.24) gives the prototype for a constrained single objective optimization problem. The definition begins with the same structure as the definition of an unconstrained problem (Equation (2.21)). The inclusion of the constraints begins with the *subject to* clause followed by the list of constraint functions ($C_1(\mathbf{X})$ through $C_n(\mathbf{X})$) and their definitions. The constraint functions may be bound by inequalities ($<$, \leq , $>$, \geq , \neq) or equalities ($=$). Notice the constraints, like the objective, are functions of the design vector (\mathbf{X}) [62].

$$\text{Find } \mathbf{X} = \begin{Bmatrix} x_1 \\ x_2 \\ \vdots \\ x_n \end{Bmatrix} \text{ which minimizes}$$

$$f(\mathbf{X}) = \text{objective definition}$$

where

$$\mathbf{X} = \text{design vector bounds}$$

subject to

$$C_1(\mathbf{X}) \leq \text{Constraint 1 Value}$$

$$C_2(\mathbf{X}) \leq \text{Constraint 2 Value}$$

$$\vdots$$

$$C_n(\mathbf{X}) \leq \text{Constraint n Value}$$

(2.24)

2.4.2.4 Constrained Multi-Objective Problem.

Equation (2.25) gives the prototype for a constrained multi-objective optimization problem. It follows the same convention discussed above to add constraints to the multi-objective problem definition shown in Equation (2.22) [62].

$$\text{Find } \mathbf{X} = \begin{Bmatrix} x_1 \\ x_2 \\ \vdots \\ x_n \end{Bmatrix} \text{ which minimizes}$$

$$f_1(\mathbf{X}) = \text{objective 1 definition}$$

$$f_2(\mathbf{X}) = \text{objective 2 definition}$$

$$\vdots$$

$$f_n(\mathbf{X}) = \text{objective n definition}$$

where

$$\mathbf{X} = \text{design vector bounds}$$

subject to

$$C_1(\mathbf{X}) \leq \text{Constraint 1 Value}$$

$$C_2(\mathbf{X}) \leq \text{Constraint 2 Value}$$

$$\vdots$$

$$C_n(\mathbf{X}) \leq \text{Constraint n Value}$$

(2.25)

2.4.3 Optimization Algorithms.

Two major classes of optimization algorithms are used in this research: gradient algorithms and genetic algorithms. Gradient optimization algorithms use the gradient of the objective function and the constraints to guide the search for the optimal design. They are suitable for use with single objective optimization problems using continuous design variables. Gradient algorithms can be applied to multi-objective problems if they have been defined using a single overall objective function like Equation (2.23). The gradient of a function indicates the direction of steepest ascent. This property gives gradient methods the ability to seek solutions to the optimization problem in the direction of greatest rate of change toward the objective from the current design. However, the steepest ascent is a local property of a function, so gradient optimization algorithms are subject to finding local optimums. For smooth functions with no local optimums, gradient algorithms can be efficient optimization tools as they can find optimal designs with a small number of function evaluations. However, objective functions with local optimums which are not smooth are generally not good candidates for use with gradient algorithms [60, 62].

Genetic optimization algorithms (GAs) apply the principles of natural selection to engineering optimization. They are suitable for single or multi-objective optimization problems using continuous, discrete, or a combination of continuous and discrete design variables. The biological principles of reproduction, crossover, and mutation all play a role in GAs. GAs operate on sets of designs called populations. Using multiple candidate designs makes GAs less likely to become trapped in local optimums. In GAs, design variables are represented as strings of binary variables. This representation correlates to chromosomes in biology and facilitates the generation of subsequent generations using “genetic” crossover between parents. The objective values are used to determine fitness in the natural selection process implemented in GAs during the selection of the next

generation to intelligently and efficiently explore the trade space to find new generations with improved values of the objective function(s) [60, 62].

2.5 Concluding Remarks

This chapter covered the engineering and technical material relevant to the research presented in this work. The first section's coverage of rocket powered propulsion included essential rocket performance and design parameters used throughout the remainder of the dissertation and reviewed traditional rocket engine cycles for comparison to the DEAN's architecture. The second section's review of US space launch vehicles and demand for improved rocket engines demonstrated the need for new rocket engine architectures like the DEAN. The third section's review of DEAN research history set the stage for the research presented in the remainder of the dissertation. Lastly, the fourth section's coverage of engineering optimization reviewed terminology used in the final stages of this research comparing optimized DEAN designs to traditional upper stage engines.

III. Parametric Study of Dual-Expander Aerospike Nozzle Upper Stage Rocket Engine

The text of this chapter was published in the AIAA Journal of Spacecraft and Rockets, Vol. 48, No. 2, 2011. It is unaltered from the published version except in its formatting as required by the AFIT dissertation style guide.

3.1 Introduction

The Air Force Institute of Technology (AFIT) is studying the dual-expander aerospike nozzle (DEAN) rocket engine architecture to significantly improve upper stage rocket performance. The specific performance goals of this research are to provide 50,000 lbf vacuum thrust with a vacuum I_{sp} of 464 s. The DEAN, shown in Figure 3.1, is a liquid hydrogen (LH₂)/liquid oxygen (LOX) engine using separate expander cycles to pump the fuel and oxidizer and an aerospike nozzle to improve efficiency.[2].

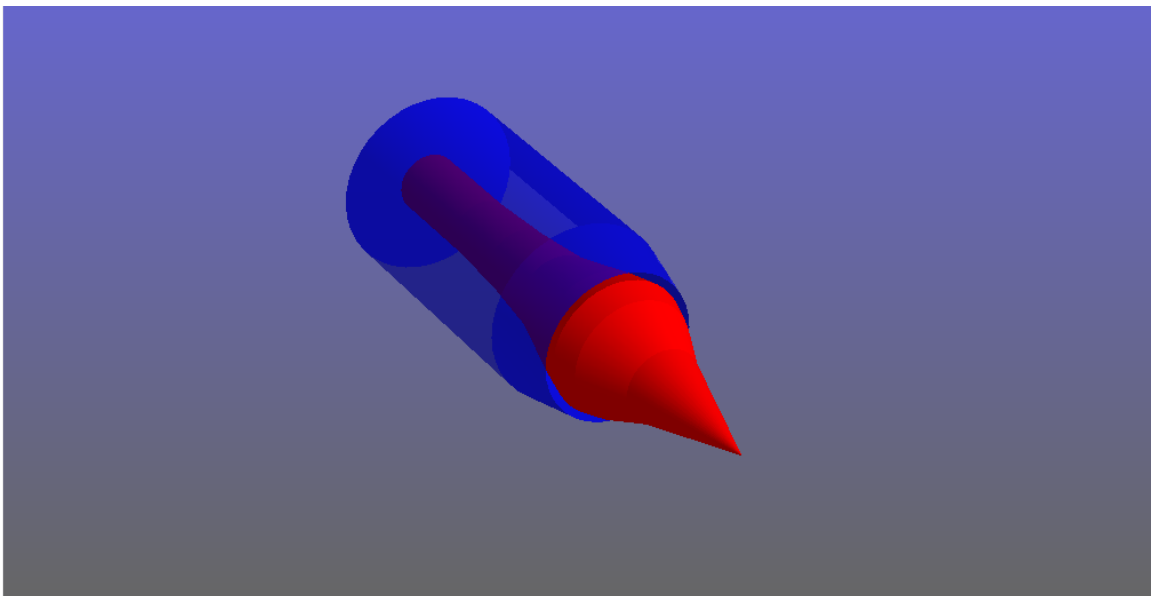


Figure 3.1: Original DEAN Geometry

Previous work at AFIT by Masters student David Martin focused on developing an initial design to demonstrate the feasibility of the DEAN architecture by building a computational model using the Numerical Propulsion System Simulation (NPSS™) software package. That work culminated in a design exceeding the requirements.[2] This paper outlines the current work at AFIT to optimize the DEAN's thrust-to-weight ratio (T/W) by expanding Martin's model through simplifying the calculations of the DEAN geometry and adding parametric variables to the model to support automated trade studies in ModelCenter™. The results of those trade studies indicate the DEAN can run at the specified performance using a lower total mass flow and a significantly shorter engine than the previous design.

3.2 Existing NPSS DEAN Model

The original NPSS DEAN model was prepared by David Martin as part of his masters thesis at AFIT. This model uses NPSS elements to represent the pumps, turbines, pipes, valves, chamber, nozzle, and cooling channels to accurately model the DEAN architecture. The results of Martin's analysis converge to a working design, validating the DEAN concept. The DEAN thrust, I_{sp} , and T/W exceed both its requirements and the performance of the upper stage single-expander cycle based RL10A-3 as can be seen in Table 3.1.

Table 3.1: Existing DEAN Design Results versus Requirements

	DEAN[2]	Requirement[2]	Delta	RL10A-3[63]	Delta
Vac Thrust (lbf)	57,231	50,000	+14.5%	16,500	+247%
Vac I_{sp} (s)	472	464	+1.7%	443	+6.5%
T/W	119	106	+12%	53	+124%

This excess in thrust performance suggests the the dual-expander cycle offers an advantage in thrust over the single-expander cycle, and it indicates room to optimize

the DEAN design further. Before discussing the changes made to Martin's model[2], necessary to facilitate this optimization, it is useful to review the key elements of the DEAN architecture and Martin's model.

3.2.1 Existing DEAN Architecture.

The DEAN uses two novel design choices. The first is the use of separate expander cycles for the fuel and the oxidizer. In a traditional expander cycle, the fuel is pumped through a cooling jacket for the chamber and nozzle. The heat picked up by the fuel from cooling the chamber and nozzle is then used to drive the turbine that runs both the fuel and oxidizer pumps, before the fuel is introduced into the chamber.[5]

Figure 3.2 shows the DEAN's two separate expander cycles. The fuel loop is on the left. Here, the LH2 flows from the fuel tank into the first fuel pump. Half of the liquid hydrogen then flows through a bypass, while the remainder is fed into a second fuel pump. This flow then continues into the aerospike nozzle, where it absorbs heat while cooling the nozzle. The heated flow then drives the fuel turbine before joining with the bypass flow and entering the combustion chamber through the injector. On the right is the oxidizer loop. In this loop, the LOX flows from the oxidizer tank into the single oxidizer pump. This flow then enters the cooling jacket for the combustion chamber, where it absorbs heat while cooling the chamber. The heated oxygen then flows toward the oxidizer turbine, with a small amount (roughly 10%) sent around the turbine using a bypass and the remainder used to drive the turbine. Finally, the oxygen flows are joined before entering the combustion chamber through an injector.[2]

The two separate expander cycles present benefits and challenges. Increased chamber pressures and in turn engine performance can be obtained by separating the power demands between two separate turbines driven by separate working fluids. The separate expander cycles also ensure the fuel and oxidizer remain physically separated until entering the combustion chamber, eliminating one of the more catastrophic failure modes in traditional

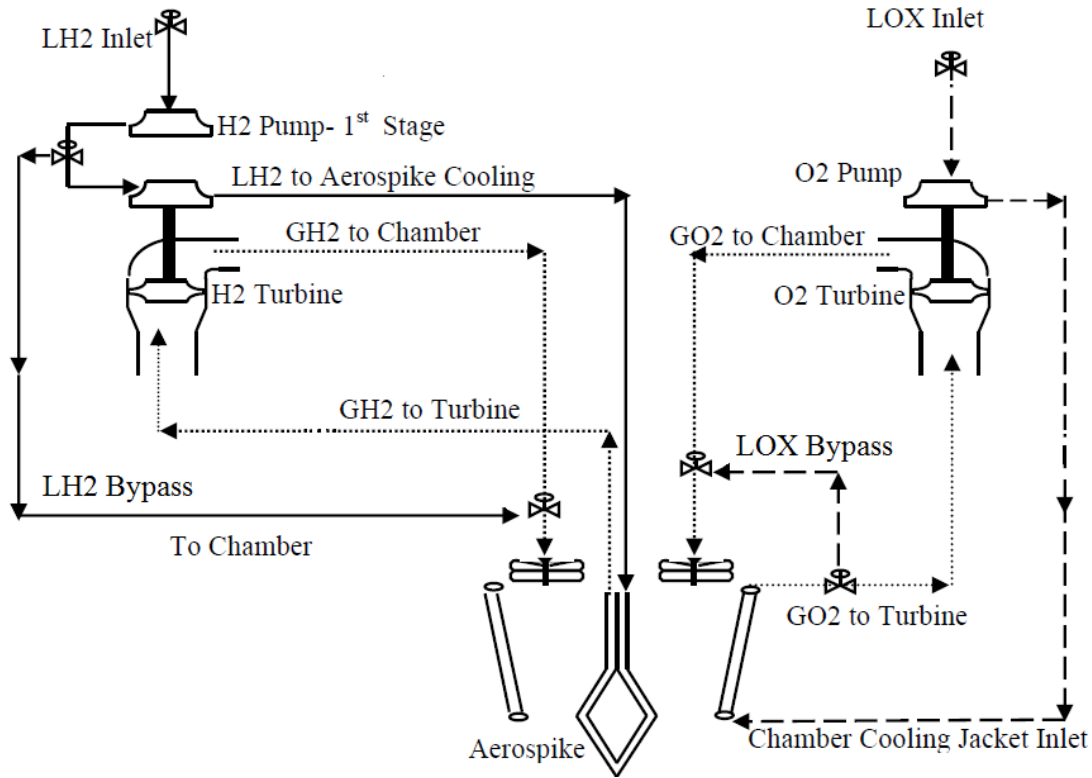


Figure 3.2: DEAN Architecture

expander cycles, namely failure of an inter-propellant-seal.[2] However, the LOX cycle requires a turbine material which will work well in an oxygen environment. Additional research at AFIT showed that Inconel 718 provides both satisfactory oxygen resistance and suitable mechanical performance for use in both the pump and the turbine in the LOX cycle.[26]

The second novel design choice is the use of an aerospike, or plug, nozzle. Traditional bell nozzles are optimized to perform at a single pressure or altitude. This optimization makes them very efficient at their design point, but much less so for the remainder of the flight. Aerospike nozzles on the other hand, due to their geometry, adapt their performance to the current altitude. Even though aerospike nozzles perform less efficiently than bell nozzles at the design altitude of a given bell nozzle, when considering the altitudes seen

by a launch vehicle, the global performance of an aerospike nozzle exceeds the global performance of a bell nozzle, making the aerospike nozzle an attractive design for launch vehicles. More importantly for the DEAN the use of an aerospike nozzle provides a second, physically separate cooling loop from the chamber for use in the second expander cycle. This second cooling loop increases the surface area inside the chamber used to drive the turbomachinery, providing for correspondingly increased power to the pumps and increased chamber pressure, and in turn increased engine performance.[2] The aerospike nozzle is also shorter and lighter than a traditional bell nozzle, leading to improved packaging and T/W . Finally, the DEAN architecture is a forerunner to similar boost stage architecture, where the aerospike nozzle's global performance will result in even greater gains than in an upper stage engine.

3.2.2 NPSS Model Details.

NPSS is a computer simulation tool for modeling aircraft and rocket engines. Engine simulations built in NPSS provide higher fidelity results than engine cycle studies. NPSS has been developed by the NASA Glenn Research Center, with assistance from the aerospace propulsion industry. Models built in NPSS consist of a series of interconnected software objects representing the components of the engine under consideration. The object connections are made using NPSS Application Programming Interfaces modeling fluid flows, mechanical connections, and thermal flows called "ports". A built-in solver in NPSS can then be used to drive the model design variables to balance the fluid flows, mechanical connections, and thermal flows in the model and converge on a design point.[31]

Martin's model[2] of the DEAN engine includes elements to simulate the various components of the engine. The combustion chamber is modeled using a RocketComb1 element which requires the chamber radius and volume. The RocketComb element also includes ThermalOutputPorts to model heat exchange to the fuel and oxidizer. The ThermalOutputPorts require the radius at the port's location, the cross-sectional area

of the combusting flow in the chamber, and the surface area of the portion of the chamber in contact with the combusting flow. The model calculates the heat exchange between the chamber walls for the oxidizer expander cycle and the internal portion of the aerospike for the fuel expander cycle. The aerospike nozzle is modeled using a RocketNozzle element which requires the throat area and the expansion ratio and includes more ThermalOutputPorts for use in the heat exchange between the aerospike and the fuel expander cycle.

The fuel and oxidizer tanks are modeled using Starter elements. The plumbing connecting the engine components to the tanks and each other is modeled using Valve04 elements which require the cross-sectional area to model the pressure drop in the plumbing and customized CoolingVolume elements which require the cross-sectional area and fluid volume to model the heat loss in the lines. The cooling jackets around the combustion chamber and the aerospike nozzle are modeled using the ThermalOutputPorts in the chamber and nozzle and the plumbing elements connected by Wall2 elements. The pumps are modeled using customized Pump elements which require the efficiency, pressure ratio, and mass flow of each pump. Finally, the turbines are modeled using customized Turbine elements which require the efficiency, pressure ratio, mass flow and the cross-sectional area of the flow.

While the cooling jackets in the DEAN are continuous volumes, the NPSS model represents them as a series of eight discrete stations. Figure 3.3 shows the locations of these stations in the model. The chamber (24 inches long in Martin's design) consists of five equally spaced sections, with stations (represented by stars) at the mid point of each section plus a station at the throat of the rocket. Note that the oxidizer loop (the outer wall of the chamber) and the fuel loop (the aerospike) are represented by separate sets of stations. The external portion of the aerospike (14 inches long in Martin's design) has two additional stations in the first half of the nozzle that are only in the fuel loop.

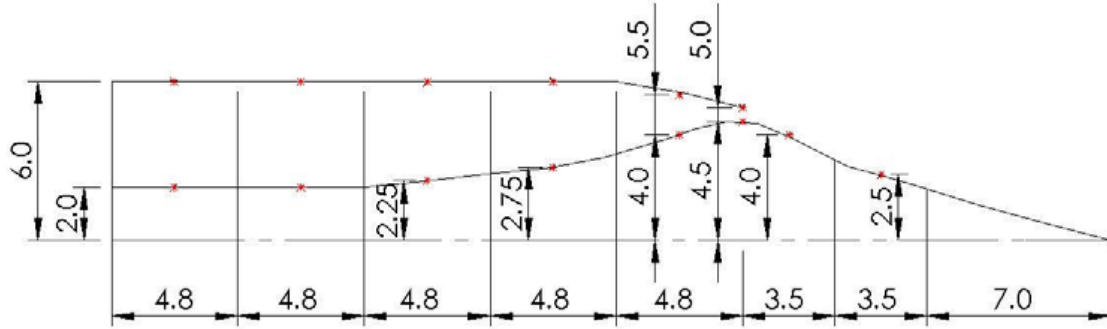


Figure 3.3: DEAN Geometry (dim in inches), credit D. Martin

NPSS models have four classes of variables: the dependent variables the NPSS solver will ensure equal specified values, the independent variables the NPSS solver is free to adjust as necessary to converge the design, component inputs read by the NPSS solver but not altered by it, and component outputs calculated by the NPSS solver, but not driven toward a particular value. Taken together, the NPSS dependent variables and component inputs form the set of user specified design choices or design variables. The NPSS independent variables and component outputs form the set of user specified responses or response variables. In the previous model, the design variables include the user specified dependent variables (the pressure ratios for the three pumps) and the component inputs (for example the volume of the combustion chamber and the nozzle expansion ratio). The response variables include the user specified independent variables (the efficiencies of the first liquid hydrogen pump and of the liquid oxygen pump) and the component outputs (for example the vacuum thrust and I_{sp}). Table 3.2 summarizes the design and response variables of the previous model.

Table 3.2: Existing DEAN Design Point[2]

Design Variables		Response Variables	
LOX Pump PR ($PR_{p,LOX}$)	103	Vac Thrust (F_{vac})	57,000 lbf
LH2 Pump 1 PR ($PR_{p,LH2,1}$)	45	Vac I_{sp}	472 s
LH2 Pump 2 PR ($PR_{p,LH2,2}$)	2	Mass Flow (\dot{m})	121 lbm/s
LH2 Pump 2 Eff ($\eta_{p,LH2,2}$)	0.83	O/F	7.03
Chamber Length (l_c)	24 in	Chamber Pres (P_0)	1739 psia
Outer Chamber Radius (r_{c_o})	6 in	Chamber Temp (T_0)	6586 R
Inner Chamber Radius (r_{c_i})	2 in	LOX Pump Eff ($\eta_{p,LOX}$)	0.66
Chamber Vol (V_c)	2075 in ³	LOX Pump Power	2587 HP
Throat Area (A_t)	15.9 in ²	LH2 Pump 1 Eff ($\eta_{p,LH2,1}$)	0.67
Nozzle Length (l_n)	14 in	LH2 Pump 1 Power	2527 HP
Expansion Ratio (ϵ)	125	LH2 Pump 2 Power	1046 HP
		LOX Turbine PR ($PR_{t,LOX}$)	1.82
		LOX Turbine Eff ($\eta_{t,LOX}$)	0.949
		LOX Turbine Power	2587 HP
		LH2 Turbine PR ($PR_{t,LH2}$)	1.84
		LH2 Turbine Eff ($\eta_{t,LH2}$)	0.9
		LH2 Turbine Power	3573 HP
		LOX Temp ($T_{LOX,i}$)	179-617 R
		LOX Pres ($P_{LOX,i}$)	3810-4500 psia
		LOX Max Mach ($M_{max,LOX}$)	0.56
		LH2 Temp ($T_{LH2,i}$)	145-610 R
		LH2 Pres ($P_{LH2,i}$)	3670-4000 psia
		LH2 Max Mach ($M_{max,LH2}$)	0.67

Follow on research at AFIT focusing on designs for the LH2 and LOX pumps provides verification for the NPSS model of the DEAN. In each design study, the respective expander cycle is modeled using spreadsheet calculations, and Pumpal®/RITAL®. These additional models agree well with the NPSS model. For example, the Pumpal model of the LH2 pumps shows the required power of the first pump is 2523 HP (less than 1% difference from the NPSS value) and the required power of the second pump is 1079 HP (approximately 3% difference from the NPSS model). Further, the pressure coming out of the second pump is 4050 psia versus 4000 psia in the NPSS model (approximately 1% difference).[25] The LOX pump values show similar agreement. For example, the Pumpal model of the LOX pump shows the required power is 2215 HP (approximately 12% difference from the NPSS model) and the pressure coming out of the LOX pump is 4600 psia versus 4500 psia in the NPSS model (approximately 2% difference).[26]

Given the importance of balancing the heat and mechanical flows in an expander cycle, it is worth noting the performance of the turbomachinery in the existing DEAN design. Naturally, the converged design point balances the power required by the pumps with that provided by the turbines for each of the two expander cycles. And while the performance of the turbomachinery may appear high when compared to RL10A which provides only 789 HP from its turbine, Pratt and Whitney built an LH2 expander cycle that produces 5900 HP as part of the an upper stage demonstrator engine.[25] This puts the LH2 cycle well within demonstrated capability. As for the LOX cycle, research at AFIT has proposed designs for the LOX pump and turbine which provide the required performance as a part of this architecture.[26]

3.3 Parameteric NPSS DEAN Model

The goal of the current research at AFIT is to optimize the DEAN engine to provide the maximum T/W while maintaining the required thrust and I_{sp} and not violating operational limits for the materials and working fluids. The T/W can be maximized by either increasing

the thrust or decreasing the weight. Since the DEAN has a fixed thrust requirement, the optimization problem can be restated as optimizing the DEAN engine to provide the minimum weight, subject to the previously mentioned constraints. Identifying the design variables driving the weight of the engine and updating the model to use those variables as the design variables enables automated searching over the design trade space for optimal designs.

The rocket engine chamber, nozzle, and turbomachinery are the elements used to estimate the total mass (weight) of the rocket engine during conceptual design. The chamber and nozzle masses are driven by their geometry and material, while the turbomachinery masses are driven by their local mass flows[5]. The model previously captured the geometry of the DEAN as hard-coded values, tying the model to a single design point. Additionally, the model treated the mass flows as responses. In order to use the model to optimize the design, the NPSS model must be altered to use the chamber and nozzle geometries and the local mass flows to the turbomachinery as design variables. This section details the modifications made to the previous model to convert it into a parametric model based on the design variable needs and two changes made while the NPSS model was being modified to reflect the most recent DEAN architecture being considered.

3.3.1 Updated DEAN Architecture.

Before modifying the DEAN model to support parametric trade studies, two architecture changes were made to the fuel expander cycle to reflect refinements in the design. Figure 3.4 shows this updated DEAN architecture. The first change was to remove the liquid hydrogen bypass, feeding the cooling jacket for the aerospike with the full mass flow of the liquid hydrogen instead of only half. The second change was to require the two fuel pumps run at the same pressure ratio, to minimize the maximum pressure ratio required for the fuel pumps.

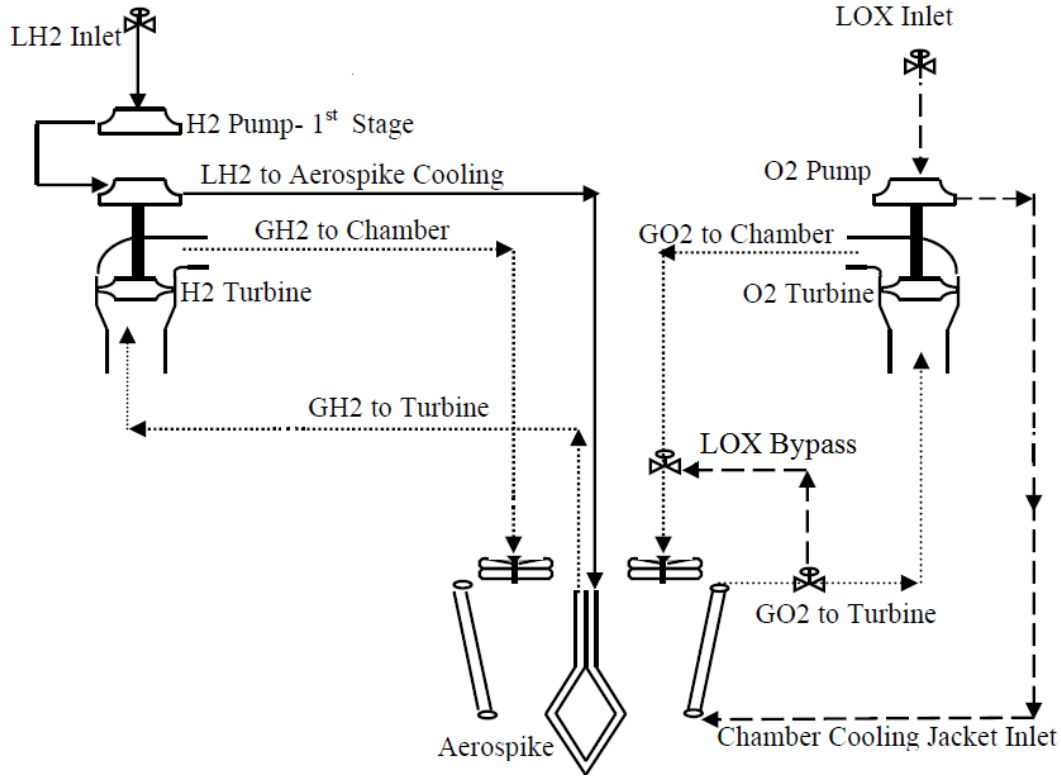
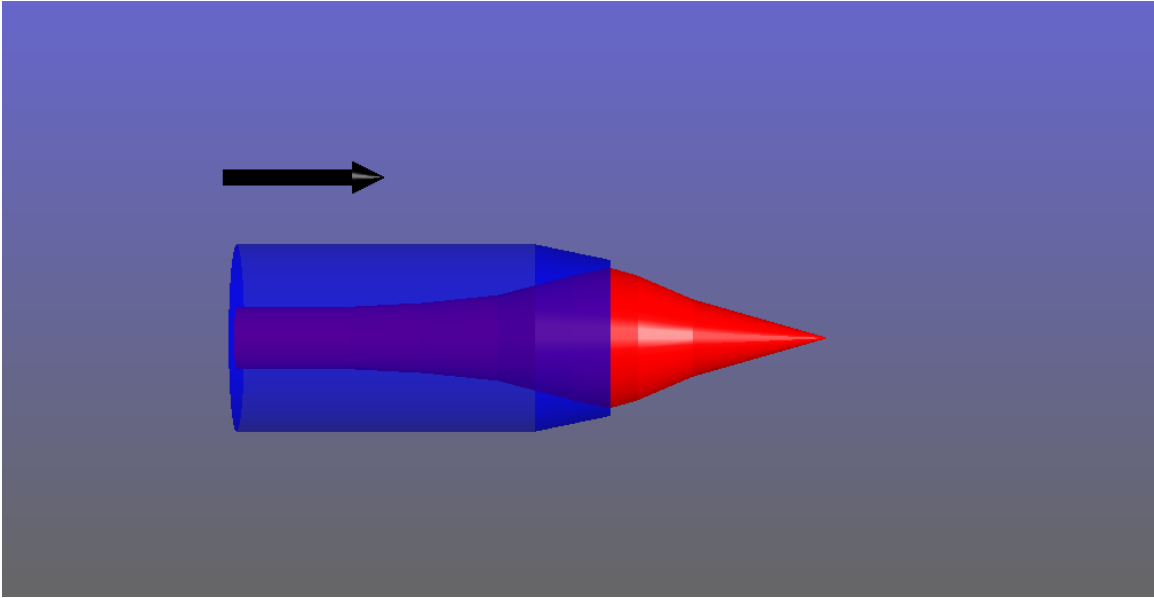


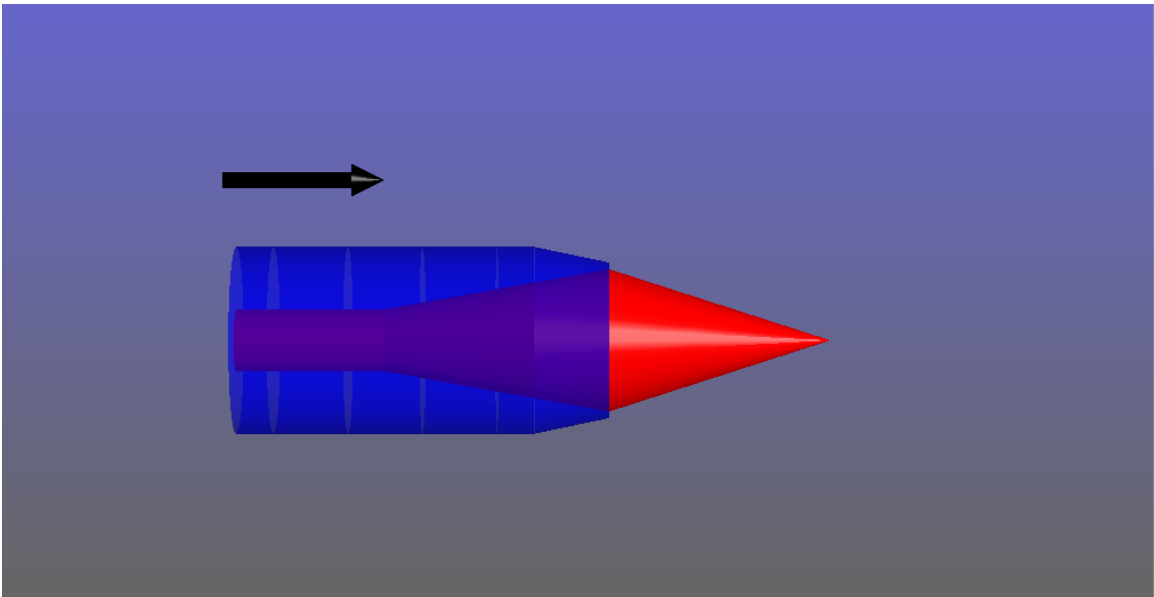
Figure 3.4: Updated DEAN Architecture

3.3.2 NPSS Model Details.

The modifications to convert the NPSS DEAN model into a parametric model involved the chamber and nozzle geometry and the mass flows through the turbomachinery. The system-level parameters chosen to drive the chamber and nozzle geometry are the chamber length, the inner and outer chamber radii, and the shape of the nozzle. A number of intermediate geometric values are determined by the shape of the nozzle. To facilitate calculating these values, the geometry of the aerospike and cooling volumes were simplified to linear approximations from their higher order calculations (the aerospike radii are calculated using the method of characteristics[2]). Figure 3.5 compares the results of these simplifications to the original geometry.



(a) Martin's Geometry for the DEAN



(b) Parametric Geometry with Simplified Aerospike

Figure 3.5: Comparison of Simplified Geometry to Martin's Original Geometry

The calculations based on these simplifications include the radius of the aerospike at each station, Equation (3.2); the combusted flow cross-sectional area, Equation (3.3);

the surface area of the heat exchanges for the chamber, Equation (3.4), the aerospike nozzle, Equation (3.5), and the cooling volumes, Equation (3.9); the cross-sectional area, Equation (3.10) and volume of the fluid in the cooling volumes, Equation (3.11). These values are calculated from the inner and outer radii of the chamber and the throat, the chamber and aerospike lengths, the cooling channel half widths and half spacings, and aspect ratios (ARs):

$$m_{plug} = (r_{t_i} - r_{c_i}) / (0.6 * l_c) \quad (3.1)$$

$$r_{c_i,i} = r_{c_i} + m_{plug} * x_i * l_c \quad (3.2)$$

$$A_{flow,i} = \pi * (r_{c_o,i}^2 - r_{c_i,i}^2) \quad (3.3)$$

$$A_{hx} = 2 * \pi * r_{c_o,i} * l_i \quad (3.4)$$

$$A_{hx_{nozz},i} = \pi * (r_{n,i} + r_{n,i-1}) * \sqrt{(r_{n,i} + r_{n,i-1})^2 + l_i^2} \quad (3.5)$$

$$n = round(\pi * r / (w_{init} + a)) \quad (3.6)$$

$$w_i = \pi * r / n_{channels} + a \quad (3.7)$$

$$h_i = 2 * w_i * AR \quad (3.8)$$

$$A_{hx_{cv},i} = 2 * w_i * n * l_i \quad (3.9)$$

$$A_{cv,i} = 2 * w_i * h_i * n \quad (3.10)$$

$$V_{cv,i} = A_{cv,i} * l_i \quad (3.11)$$

The system-level parameters chosen to drive the mass flows to the turbomachinery are the oxidizer-to-fuel ratio (O/F) and total mass flow. These parameters also drive the performance constraints of thrust and I_{sp} . Equation (3.12)[5] determines the LOX mass flow from these system-level parameters and Equation (3.13)[5] determines the LH2 mass flow. In the original model, the O/F can only be controlled indirectly by changing the pressure ratios of the pumps, leading to coupling effects appearing in the O/F plots. For example, a parametric study, described in Table 3.3, varied the pressure ratio of the first LH2 pump.

$$\dot{m}_{LOX} = \frac{O/F}{1 + O/F} * \dot{m} \quad (3.12)$$

$$\dot{m}_{LH2} = \frac{1}{1 + O/F} * \dot{m} \quad (3.13)$$

Figure 3.6 shows the relationship between I_{sp} and O/F for the DEAN based on this parametric study. The peak I_{sp} is at an O/F ratio of approximately 6. Ordinarily, this result would be produced by a parametric study as a function of the independent variable, O/F , implying the total mass flow was constant. Equation (3.14)[5], supports the conclusion thrust versus O/F would follow the trend in Figure 3.6. However, Figure 3.7 shows a peak at an O/F of 6, and then a rise toward another peak for $O/F < 5$.

$$I_{sp} = \frac{F}{\dot{m}g_0} \quad (3.14)$$

Table 3.3: Parametric Study over LH2 Pump 1 PR

Design Variables		Response Variables	
LOX Pump PR ($PR_{p,LOX}$)	103	Vac Thrust (F_{vac})	49,500-60,000 lbf
LH2 Pump 1 PR ($PR_{p,LH2,1}$)	30-60	Vac I_{sp}	416-491 s
LH2 Pump 2 PR ($PR_{p,LH2,2}$)	2	Mass Flow (\dot{m})	119-132 lbm/s
LH2 Pump 2 Eff ($\eta_{p,LH2,2}$)	0.83	O/F	4.2-11.3
Expansion Ratio (ϵ)	125	Chamber Pres (P_0)	1500-1940 psia
		Chamber Temp (T_0)	5000-6660 R

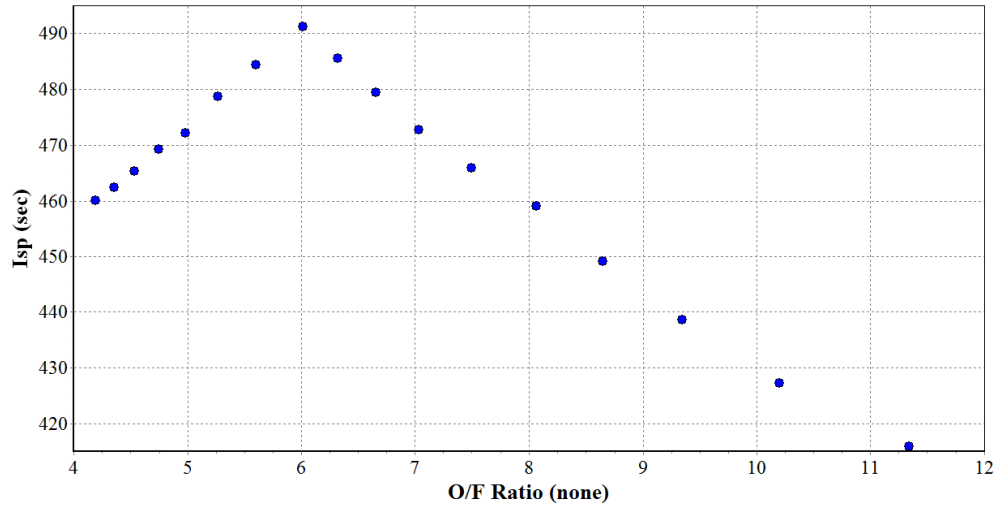


Figure 3.6: I_{sp} vs O/F , Original NPSS Model

The deviation from the describing equations rests with the assumption of constant total mass flow. Figure 3.8 is a three dimensional plot showing thrust vs both O/F and total mass flow. The vertical axis is the thrust, the left axis is O/F , and the back axis is the total mass flow. The starred point is O/F equals 6. The total mass flow has a sharp turn

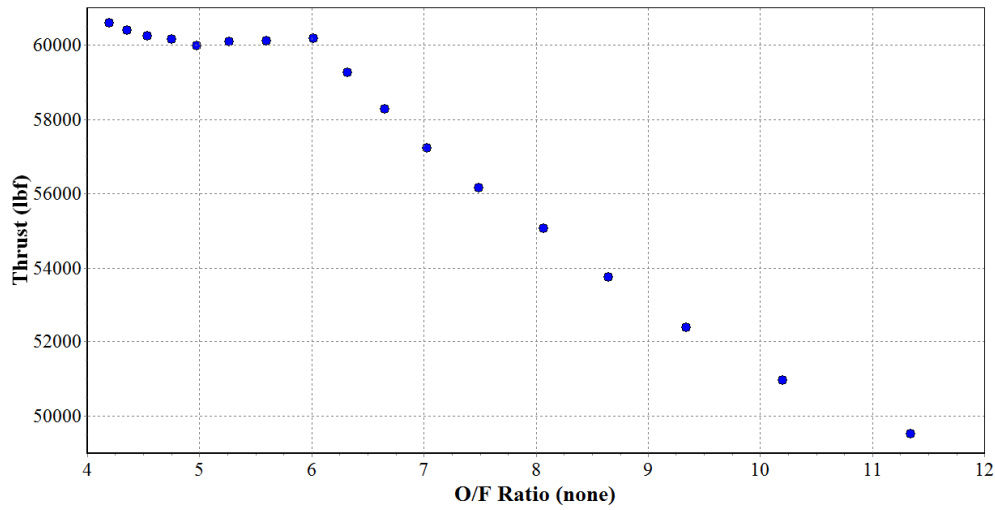


Figure 3.7: Thrust vs O/F, Original NPSS Model

as O/F decreases beyond that point, leading to the second increase in thrust as total mass flow reaches its peak during the parametric study. To eliminate coupling effects like this example, and an instability in the LH2 efficiencies, the user defined dependent variables were changed to the total mass flow and an equation setting the two fuel pumps to the same pressure ratio. The user defined independent variables were changed to the throat area, and to the pressure ratios for all three pumps.

One final change was made to the NPSS model. In the model, the mass flow through the oxidizer bypass was hard coded to a specific value, resulting in instabilities in the model when the system mass flow or the O/F ratio changed. The oxidizer mass flow through the bypass was set to be 10% of the oxidizer mass flow, and the mass flow to the oxidizer turbine was set to 90%. These percentages were also made user configurable.

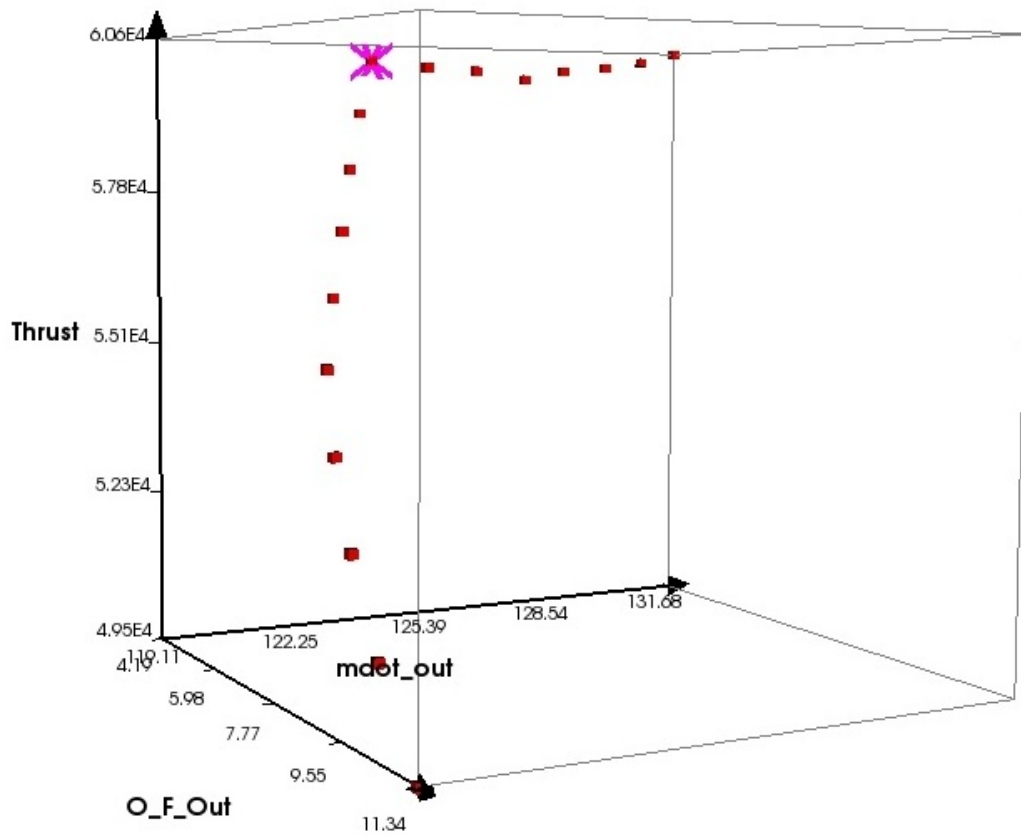


Figure 3.8: Thrust vs O/F and Total Mass Flow, Original NPSS Model

3.4 System-Level DEAN Model

A system-level model of the DEAN engine was built around the parametric NPSS model in order to run automated trade studies. This system-level DEAN model was built in ModelCenter™. ModelCenter is a multidisciplinary modeling environment used to study the trade space of a design and optimize that design. ModelCenter can combine analyses developed in a variety of tools including MATLAB, Mathcad, Excel, command line executables (for example) into a single system-level model. Users can then use the built-in trade study and visualization tools to conduct sensitivity studies to gain insight into

what aspects of the design are the key drivers influencing the desired results. ModelCenter also provides a rich set of built-in optimization tools used to find values for the key drivers optimizing the design for a given goal (such as minimizing the mass of the DEAN engine) while ensuring constraints are not violated (such as maintaining the required thrust and I_{sp}). These optimization tools include a gradient optimizer, a genetic optimizer called Darwin™, and an optimizer that utilizes surrogate models of the design space during optimization called DesignExplorer™.[64]

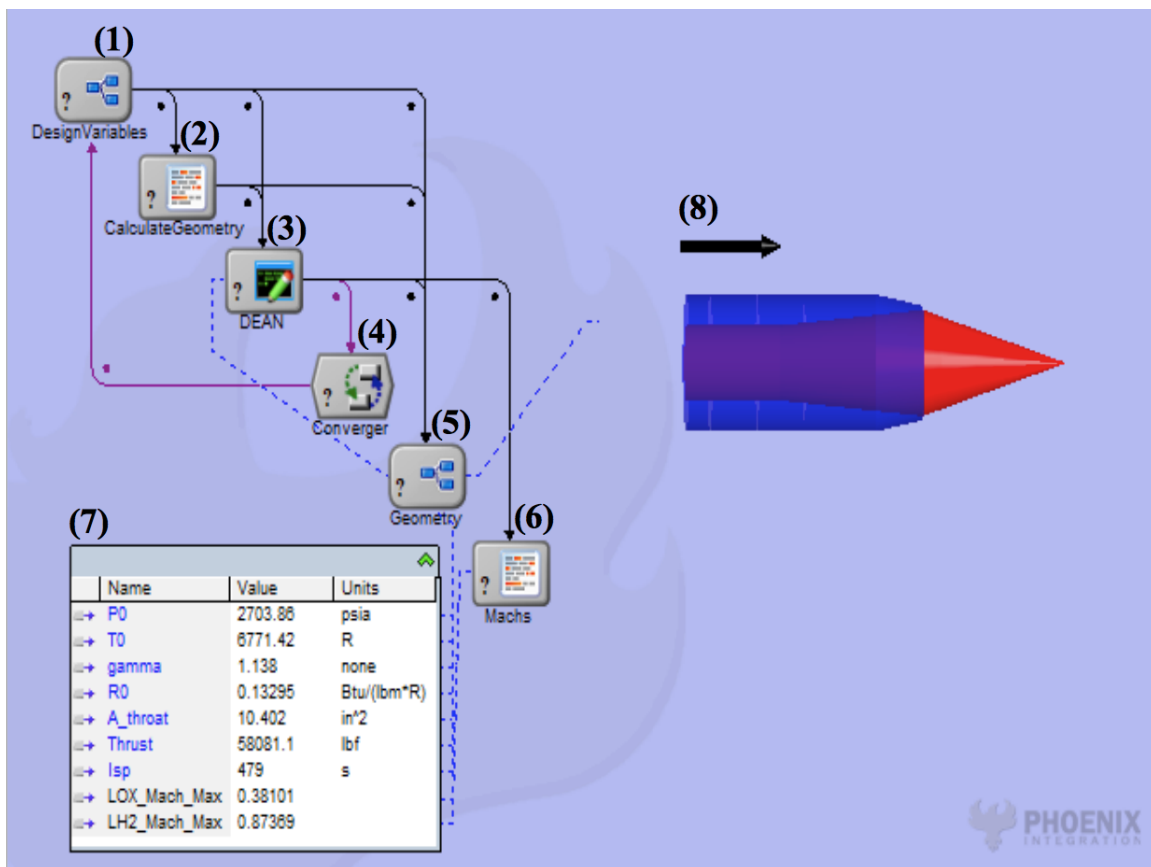


Figure 3.9: System-level Model of DEAN

Figure 3.9 shows the system-level DEAN model in the ModelCenter interface. The model consists of six components and two data display elements. Table 3.4 summarizes these components.

Table 3.4: System-level DEAN Model Components

Label	Name	Description
1	DesignVariables	a component storing the system-level design variables
2	CalculateGeometry	a script component calculating the geometry parameters for the DEAN model from the design variables
3	DEAN	the parametric NPSS DEAN model imported into the ModelCenter framework using the embedded Quick-Wrap tool
4	Converger	a direct substitution convergence loop used to converge the guessed throat area to the calculated throat area
5	Geometry	a collection of geometry primitives (surfaces of revolution and an arrow) and a script component to render the live view of the DEAN geometry seen in (8)
6	Machs	a script component that uses polynomial interpolation to calculate the Mach numbers for the LOX and LH2 fluid flows in the cooling volumes
7	Data Monitor	a built-in ModelCenter component set to display the key performance values from the DEAN model
8	Geometry Rendering	a live preview of the DEAN geometry based on the geometry components in (5)

The first four components in the DEAN system-level model are used to run the DEAN NPSS model. The first component stores the system-level design variables. They are the total mass flow, the O/F ratio, the inner chamber radius, the outer chamber radius, the chamber length, and a guessed value for the throat area. The second component calculates the nozzle radius using Equation (3.3), nozzle length based on the slope of the aerospike nozzle, and the chamber volume using volume equations for cylinders and cones from the design variables. The third component runs the NPSS DEAN model using the values of the design variables and the values calculated in the CalculateGeometry component. Since the throat area is an independent variable in the NPSS model, the NPSS solver may select a value that does not match the guessed value. If the model chooses such a value, the geometry values calculated from the guessed throat area (specifically the nozzle radius and cooling volume sizes) are incorrect. The fourth component addresses this problem using a direct substitution iteration solver. The solver directs the system-level model to be run in a loop, substituting the NPSS calculated throat area for the guessed throat area, until the two are the same value, closing the design.

The remaining two components in the DEAN system-level model are used for post processing the DEAN NPSS model. The fifth component is actually four components that are part of a ModelCenter assembly component. ModelCenter assembly components allow model developers to group related components together to simplify the display and management of the model. Three of the four sub-components in the geometry component are built-in ModelCenter geometry primitives: two surfaces of revolution to render the chamber in blue and the aerospike in red, and a twelve inch long arrow to provide a scale for the DEAN geometry. The final sub-component is a ModelCenter script component transforming the output from the DEAN NPSS model into geometry strings that define the curves for the surface of revolution components.

The last analysis component calculates the Mach numbers for the LOX and LH2 fluid flows in the cooling volumes. These values are critical constraints on the engine design, as the flows cannot be allowed to reach sonic conditions. Previous constraints for these values were a maximum Mach in the LOX flows of 0.6, and a maximum Mach in the LH2 flows of 0.9[2]. Martin calculated the Mach numbers at each station by looking up the speed of sound for the fluids in the Thermophysical Properties of Fluid Systems online handbook (<http://webbook.nist.gov/chemistry/fluid/>)[65] from the National Institute of Standards and Technology, based on the fluid temperatures and pressures. The Machs component automates this process by using third order polynomials to interpolate the speed of sound for LOX and LH2 over the temperature and pressure ranges seen in the DEAN model. Table 3.5 summarizes the Design of Experiments (DOE) trade study used to establish these ranges.

To create the interpolation polynomials, a set of isothermal speed-of-sound versus pressure tables for both oxygen and hydrogen were downloaded from the Thermophysical Properties of Fluid Systems online handbook. Table 3.6 shows the temperatures and pressures selected for these tables. Note, the LH2 pressure range was truncated after determining pressures above 7200 psia represented designs no longer being considered.

Table 3.5: Design of Experiments over O/F , Total Mass Flow, and Chamber Length

Design Variables		Response Variables	
O/F	5.5-7.5	Vac Thrust (F_{vac})	39,700-69,500 lbf
Mass Flow (\dot{m})	85-140 lbm/s	Vac I_{sp}	466-499 s
Chamber Length (l_c)	22-30 in	Chamber Pres (P_0)	1798-3243 psia
Outer Chamber Radius (r_{c_o})	6 in	Chamber Temp (T_0)	6130-6850 R
Inner Chamber Radius (r_{c_i})	2 in	Throat Area (A_t)	7.2-17.5 in ²
Expansion Ratio (ϵ)	125	Nozzle Length (l_n)	13.7-14.8 in
LOX Bypass (%)	90	Chamber Vol (V_c)	1810-2480 in ³
LOX Pump Eff ($\eta_{p,LOX}$)	0.773	LOX Temps (T_{LOX})	162-886R
LOX Turbine Eff ($\eta_{t,LOX}$)	0.949	LOX Pres (p_{LOX})	2865-5864 psia
LH2 Pump 1 Eff ($\eta_{p,LH2,1}$)	0.8	LH2 Temps (T_{LH2})	73-634R
LH2 Pump 2 Eff ($\eta_{p,LH2,2}$)	0.83	LH2 Pres (p_{LH2})	3220-10,750 psia
LH2 Pump Eff ($\eta_{p,LH2}$)	0.9		

Table 3.6: Data Ranges for Speed of Sound Tables

Fluid	Temperatures (R)	Pressure Range (psia), step size = 100 psia
LOX	150, 275, 400, 525, 650, 775, 900	2800-6000
LH2	70, 165, 260, 355, 450, 545, 640	3200-7200

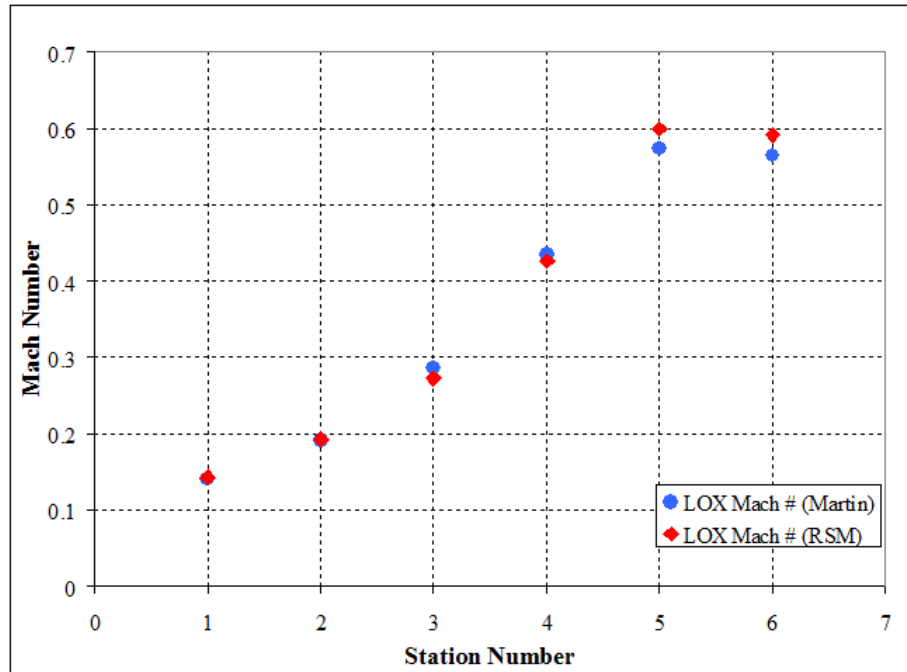
The speed-of-sound tables were then imported into ModelCenter for surface fitting using the Data Import Plug-In. The interpolation polynomials were then created by running a cubic fit to the data in ModelCenter's Response Surface Modeling Toolkit (RSM Toolkit). Equation (3.15) shows the polynomial generated for the speed of sound in LOX and Equation (3.16) shows the polynomial generated for the speed of sound in LH2. Both equations are good fits to the data as can be seen from their adjusted R^2 values and a graphical comparison to the results from the earlier design. Equation (3.15) has an adjusted R^2 value of 0.995 and Equation (3.16) has an adjusted R^2 value of 0.988. Figure 3.10 shows that Mach numbers calculated from both equations also compare favorably to results from the earlier design of the DEAN.

$$a_{LOX,i} = 6009.519 - 25.08448T_i + 0.05203138p_i + 0.03725712T_i^2 \quad (3.15)$$

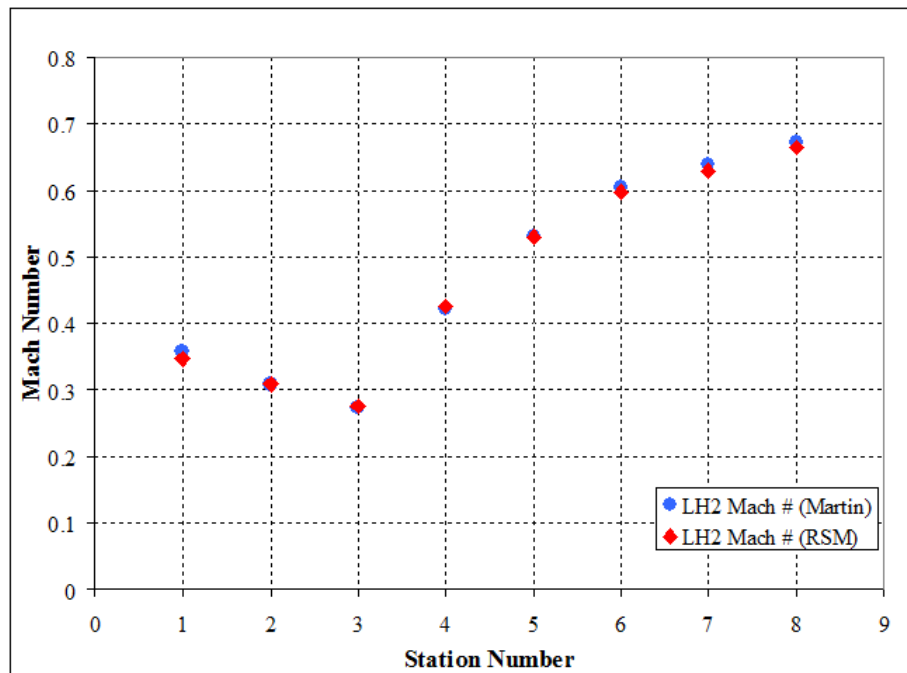
$$+0.0004540472T_i p_i - 1.669077 * 10^{-05}T_i^3 - 5.292126 * 10^{-07}p_i T_i^2$$

$$a_{LH2,i} = 4014.306 - 15.03106T_i + 0.7100687p_i + 0.04704292T_i^2 \quad (3.16)$$

$$\begin{aligned} & -2.660187 * 10^{-05}p_i^2 - 0.0009330969T_i p_i \\ & -3.34523 * 10^{-05}T_i^3 + 4.862856 * 10^{-08}T_i p_i^2 \end{aligned}$$



(a) LOX Mach Numbers



(b) LH2 Mach Numbers

Figure 3.10: Comparison of Fluid Mach Number Calculations

3.5 Results and Analysis

The analysis of the system-level DEAN model took place in two phases. First, parametric studies were run over the chamber length, the O/F ratio, and the total mass flow to establish the boundaries of the design trade space. The results of the parametric studies were then used to scale the original DEAN design to more closely match the performance goals.

3.5.1 Parametric Studies.

Table 3.7 summarizes the first parametric study of the DEAN system-level model, which varied the O/F ratio from 5.5 to 7.5. Initial results from this trade study are promising. The plot of I_{sp} versus O/F in Figure 3.11 shows the peak I_{sp} occurs at an O/F ratio of approximately 6, just as in the previous study shown in Figure 3.6.

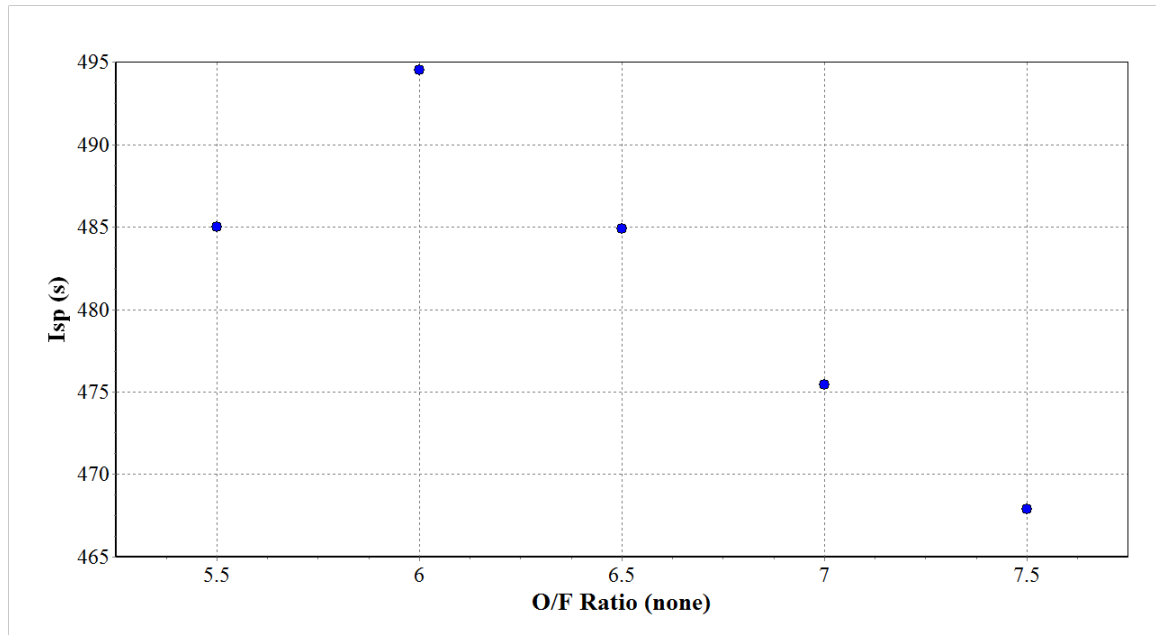


Figure 3.11: I_{sp} vs O/F Ratio, System-level Model

Table 3.7: Parametric Study over O/F

Design Variables		Response Variables	
O/F	5.5-7.5	Vac Thrust (F_{vac})	56,700-60,000 lbf
Mass Flow (\dot{m})	121.25 lbm/s	Vac I_{sp}	468-495 s
Chamber Length (l_c)	24 in	Chamber Pres (P_0)	2135-2415 psia
Outer Chamber Radius (r_{co})	6 in	Chamber Temp (T_0)	6180-6705 R
Inner Chamber Radius (r_{ci})	2 in	Throat Area (A_t)	12.1-12.8 in ²
Expansion Ratio (ϵ)	125	Nozzle Length (l_n)	14.2-14.3 in
LOX Bypass (%)	90	Chamber Vol (V_c)	1576-1579 in ³
LOX Pump Eff ($\eta_{p,LOX}$)	0.773	LOX Temp (T_{LOX})	166-657R
LOX Turbine Eff ($\eta_{t,LOX}$)	0.949	LOX Pres (p_{LOX})	3860-4380 psia
LH2 Pump 1 Eff ($\eta_{p,LH2,1}$)	0.8	Max LOX Mach	0.40-0.41
LH2 Pump 2 Eff ($\eta_{p,LH2,2}$)	0.83	LH2 Temp (T_{LH2})	85-436R
LH2 Pump Eff ($\eta_{p,LH2}$)	0.9	LH2 Pres (p_{LH2})	4590-8340 psia
		Max LH2 Mach	0.99-1.20

However, the max LH2 Mach numbers exceed the constraint value established by Martin across the entire parametric study, as can be seen Figure 3.12. A review of the LH2 Mach numbers at all of the stations reveals the Mach numbers are within acceptable limits for nozzle radii greater than 3.3 in. To test this conclusion, the inner chamber radius was increased from 2.0 in to 3.3 in. However, the NPSS model could not converge because some of the LH2 cooling volumes had become too large. Addressing this result, several cooling volume aspect ratio calculations were adjusted until the model converged. As expected, the maximum LH2 Mach number for this new design fell within the constraint value of 0.9. Running the parametric study with the adjusted aspect ratios resulted in maximum LH2

Mach numbers between 0.81 and 0.88, enabling continued exploration of the DEAN trade space.

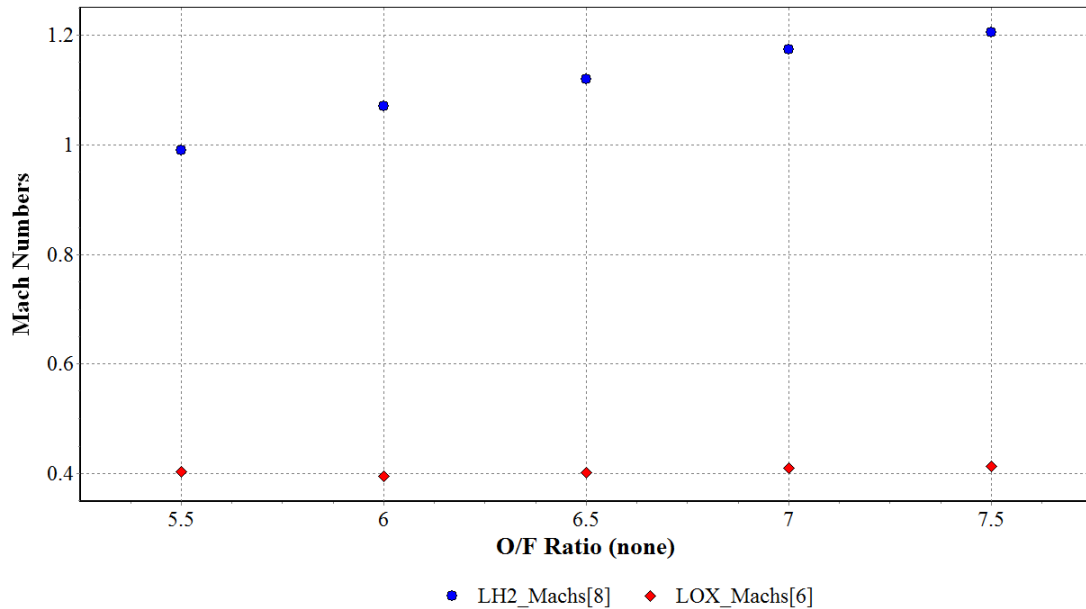


Figure 3.12: Fluid Mach Numbers vs O/F Ratio, System-level Model

Figure 3.13 is the plot of I_{sp} versus O/F ratio for the updated inner chamber radius. The added detail in this plot shows the O/F ratio for max I_{sp} is between 5.9 and 6.1, higher than might be expected just based on the O/F ratio, given the RL10 upper stage engine runs at an O/F ratio of 5.0[5]. However, while the total mass flow and most of the geometric parameters are constant in Figure 3.13, the chamber pressure and temperature are not. Figure 3.14 shows how chamber pressure varies with O/F and Figure 3.15 shows how the chamber temperature varies with O/F . The chamber pressures seen in Figure 3.14 range from 2625 psia to 2875 psia. These values are considerably higher than the 640 psia of the RL10B-2[5], or even the practical limits of a single expander cycle LOX/LH2 engine,

which Krach and Sutton determined to be between 1375 psia and 2300 psia[66]. This dramatic difference in chamber pressures suggests higher chamber pressures are possible with the dual-expander cycle of the DEAN architecture than with single expander cycles.

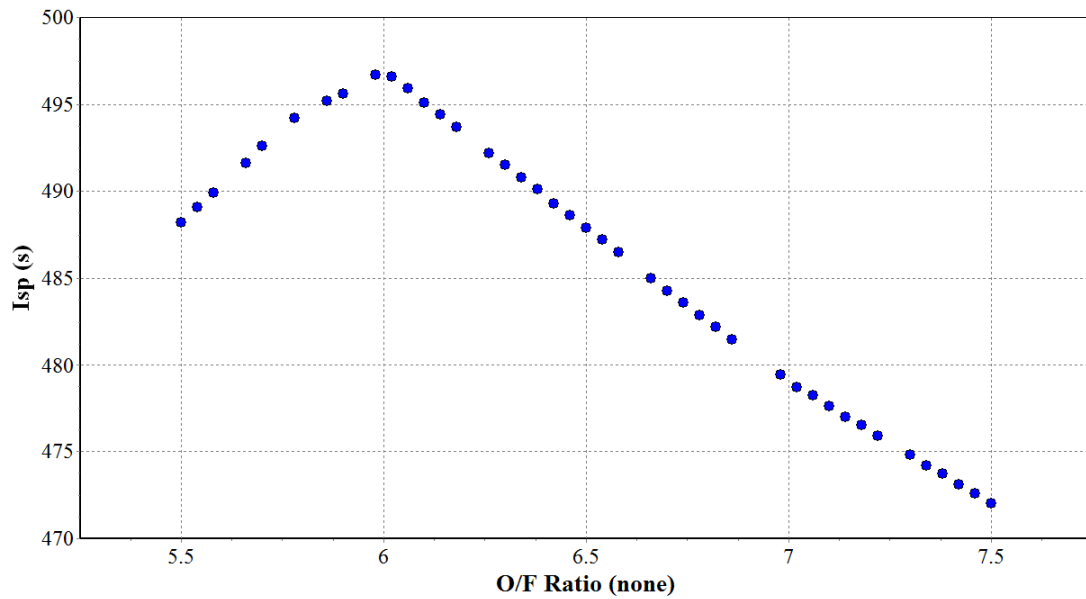


Figure 3.13: Detailed I_{sp} vs O/F Ratio, System-level Model

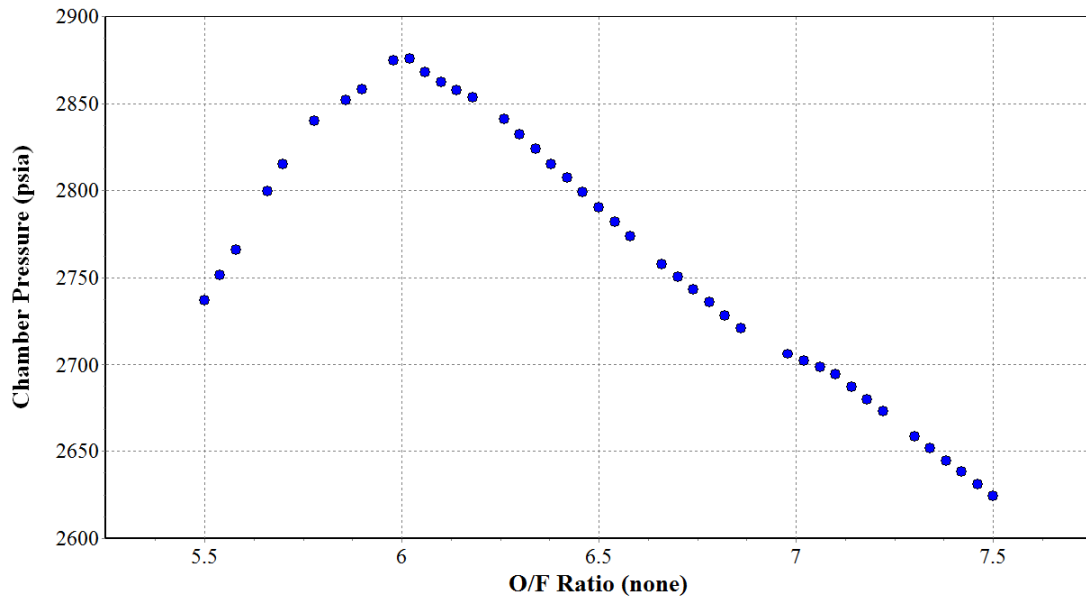


Figure 3.14: Detailed Chamber Pressure vs O/F Ratio, System-level Model

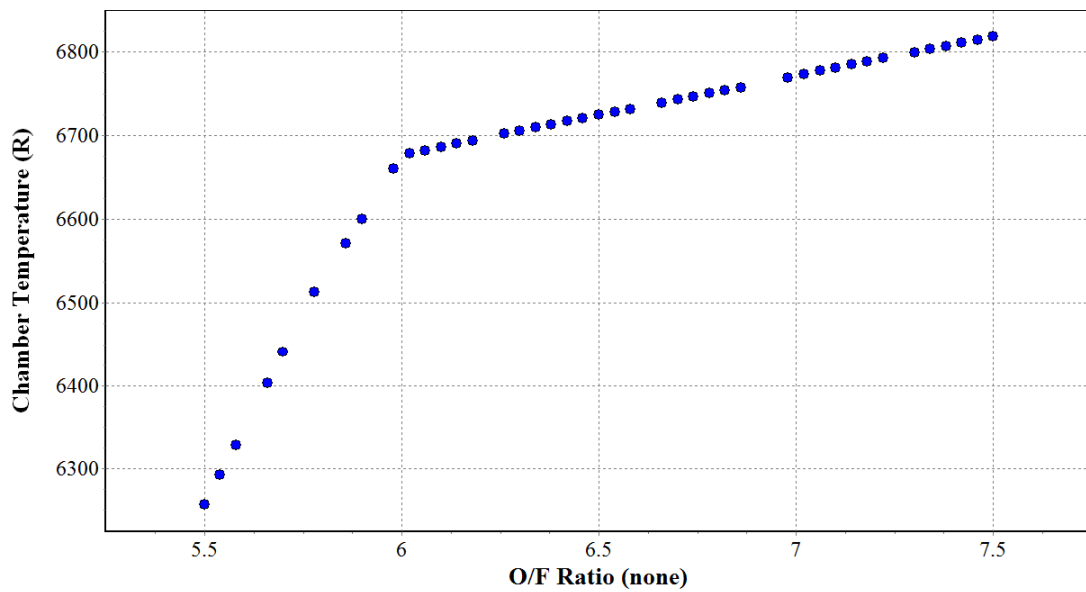


Figure 3.15: Detailed Chamber Temperature vs O/F Ratio, System-level Model

Figure 3.16 uses a three dimensional plot with varying colors on the data points to present all four of these variables, I_{sp} , O/F , chamber pressure, and chamber temperature, in a combined plot to present a unified view of their interactions. The O/F ratio is on the left axis, the chamber pressure is on the rear axis, and I_{sp} is on the vertical axis. Finally, the chamber temperature is shown as the colors of the data points. This figure shows the maximum I_{sp} not only happens at an O/F of 6, but also at the maximum chamber pressure, and somewhere in the middle of the chamber temperature range seen in this study. Returning to Figure 3.15 reveals the chamber temperature for the O/F where the maximum I_{sp} occurs is located at a knee in the temperature curve. The trends evident in Figure 3.16 suggest the solution is simply one possible curve on a solution surface space.

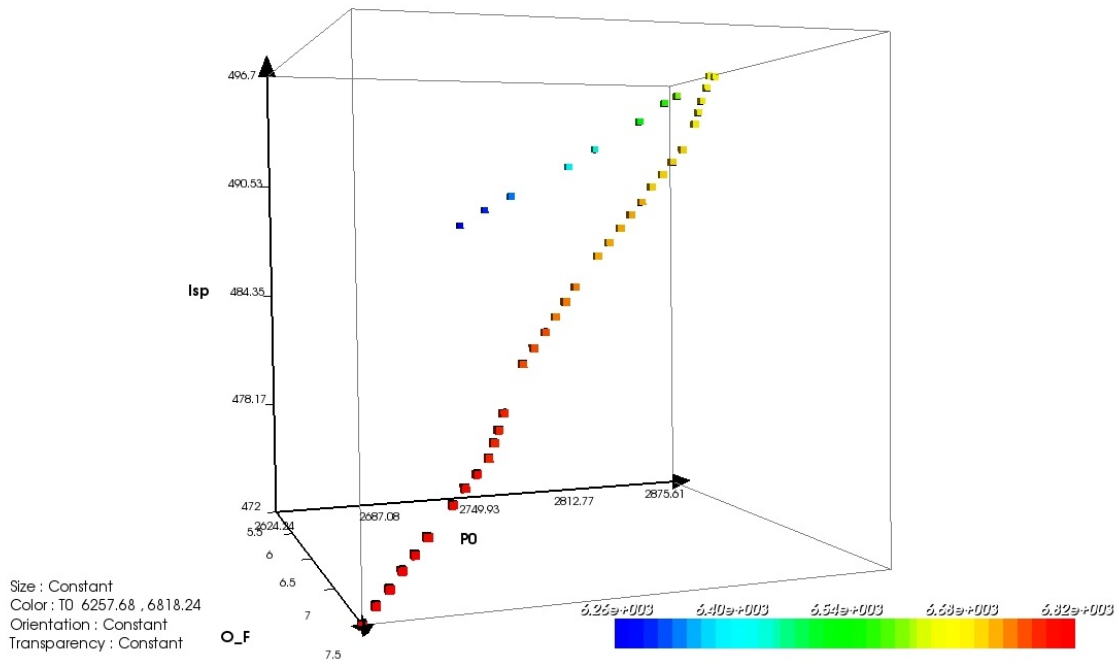


Figure 3.16: I_{sp} vs O/F Ratio, Chamber Pressure, and Chamber Temperature, System-level Model

Table 3.8 summarizes the second parametric study run of DEAN system-level model, which varied the total mass flow from 85 lbm/s to 122 lbm/s. As one would expect, thrust is linearly related to total mass flow (Figure 3.17). A total mass flow of only 104 lbm/s is sufficient to achieve 50,000 lbf thrust. Optimizing DEAN design near 104 lbm/s will result in another weight savings over the original design.

Table 3.8: Parametric Study over Total Mass Flow

Design Variables		Response Variables	
O/F	7	Vac Thrust (F_{vac})	40,800-58,400 lbf
Mass Flow (\dot{m})	85-122 lbm/s	Vac I_{sp}	479-481 s
Chamber Length (l_c)	24 in	Chamber Pres (P_0)	2525-2710 psia
Outer Chamber Radius (r_{co})	6 in	Chamber Temp (T_0)	6770-6790 R
Inner Chamber Radius (r_{ci})	2 in	Throat Area (A_t)	7.8-10.4 in ²
Expansion Ratio (ϵ)	125	Nozzle Length (l_n)	14.5-14.8 in
LOX Bypass (%)	90	Chamber Vol (V_c)	1560-1578 in ³
LOX Pump Eff ($\eta_{p,LOX}$)	0.773	LOX Temp (T_{LOX})	165-766R
LOX Turbine Eff ($\eta_{t,LOX}$)	0.949	LOX Pres (p_{LOX})	3650-4850 psia
LH2 Pump 1 Eff ($\eta_{p,LH2,1}$)	0.8	Max LOX Mach	0.35-0.39
LH2 Pump 2 Eff ($\eta_{p,LH2,2}$)	0.83	LH2 Temp (T_{LH2})	75-645R
LH2 Pump Eff ($\eta_{p,LH2}$)	0.9	LH2 Pres (p_{LH2})	3850-5900 psia
		Max LH2 Mach	0.87-0.91

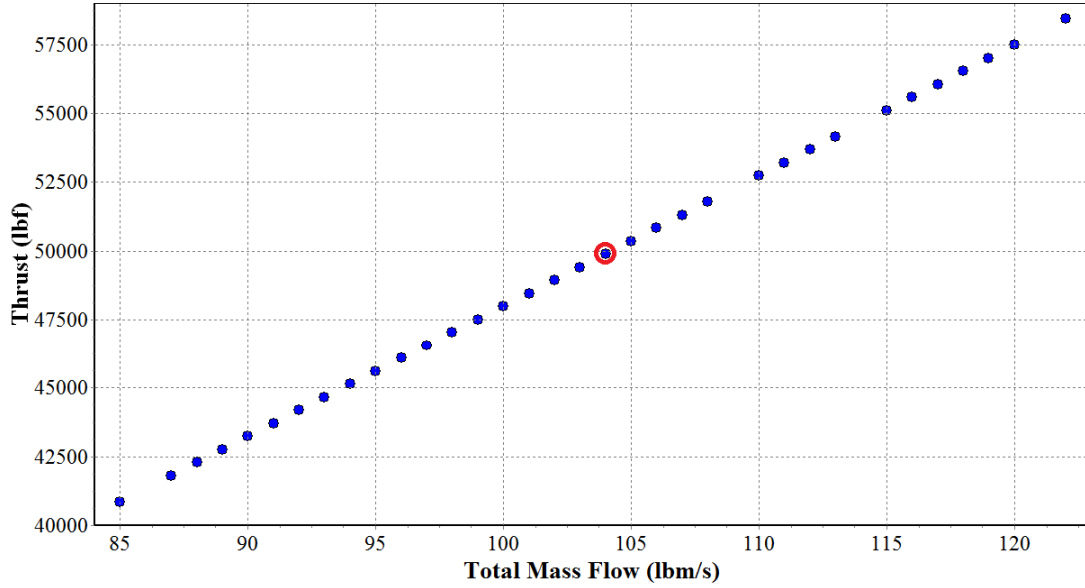


Figure 3.17: Vacuum Thrust vs Total Mass Flow, System-level Model

Table 3.9 summarizes the final parametric study run on the DEAN system-level model, considering the chamber length from 14 in to 26 in. The curve in Figure 3.18 showing thrust versus chamber length has two transitions, one at 14.25 in and one at 22.75 in. Noting shorter chamber lengths result in lighter engines since they require less material drives the engine design toward the shortest chamber able to achieve the goal. This result supports selecting a chamber not longer than 14.25 in, but further optimization is warranted. Selecting a chamber length of 14.25 in results in a total engine length of 27.85 in. The new length is nearly 25% shorter than the original design, and 69% shorter than the RL10B-2[24]. This result suggests that the DEAN architecture can be packaged in a considerably smaller volume than existing upper stage engines.

Table 3.9: Parametric Study over Chamber Length

Design Variables		Response Variables	
O/F	7	Vac Thrust (F_{vac})	57,100-58,200 lbf
Mass Flow (\dot{m})	121.25 lbm/s	Vac I_{sp}	471-480 s
Chamber Length (l_c)	14-26 in	Chamber Pres (P_0)	950-2975 psia
Outer Chamber Radius (r_{c_o})	6 in	Chamber Temp (T_0)	6435-6805 R
Inner Chamber Radius (r_{c_i})	2 in	Throat Area (A_t)	9.8-28.9 in ²
Expansion Ratio (ϵ)	125	Nozzle Length (l_n)	12.4-14.6 in
LOX Bypass (%)	90	Chamber Vol (V_c)	1000-1700 in ³
LOX Pump Eff ($\eta_{p,LOX}$)	0.773	LOX Temp (T_{LOX})	160-780R
LOX Turbine Eff ($\eta_{t,LOX}$)	0.949	LOX Pres (p_{LOX})	2300-5200 psia
LH2 Pump 1 Eff ($\eta_{p,LH2,1}$)	0.8	Max LOX Mach	0.32-0.42
LH2 Pump 2 Eff ($\eta_{p,LH2,2}$)	0.83	LH2 Temp (T_{LH2})	70-610R
LH2 Pump Eff ($\eta_{p,LH2}$)	0.9	LH2 Pres (p_{LH2})	2450-6250 psia
		Max LH2 Mach	0.86-0.97

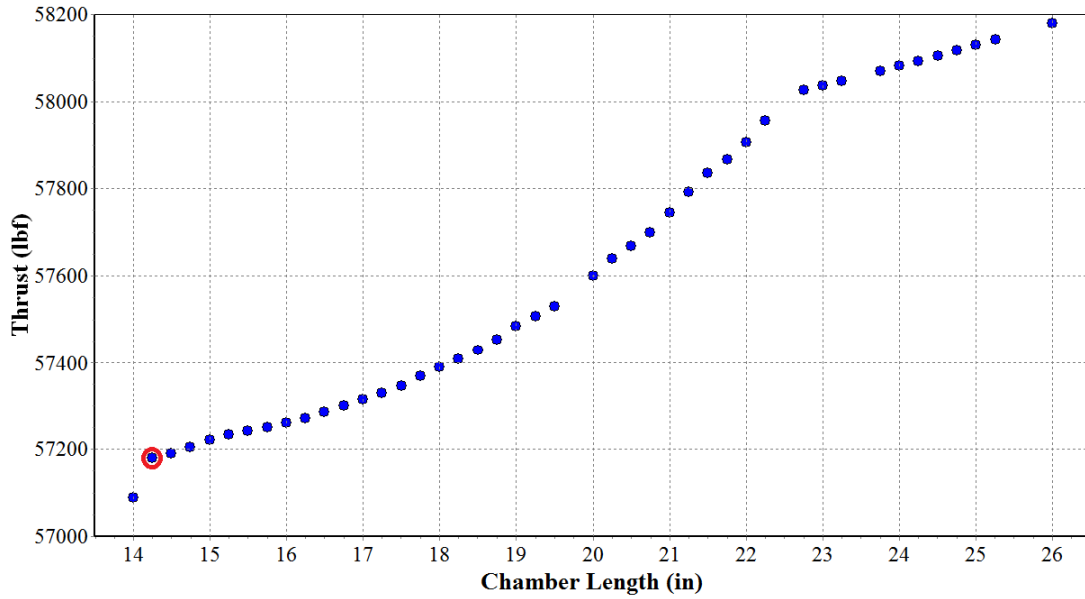


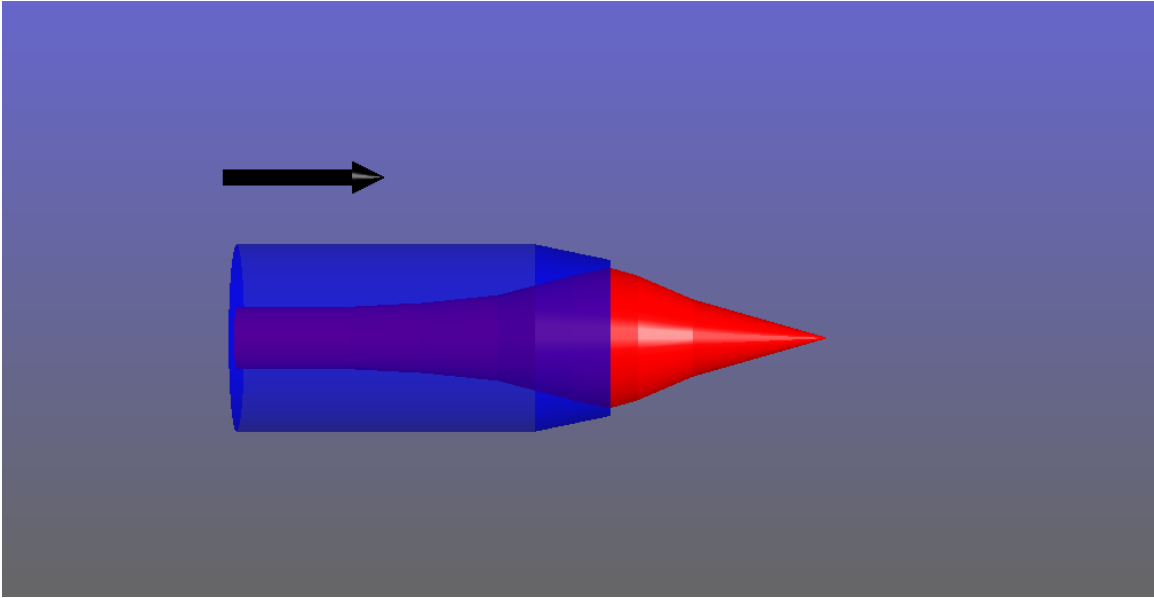
Figure 3.18: Vacuum Thrust vs Chamber Length, System-level Model

3.5.2 Scaling the DEAN Engine.

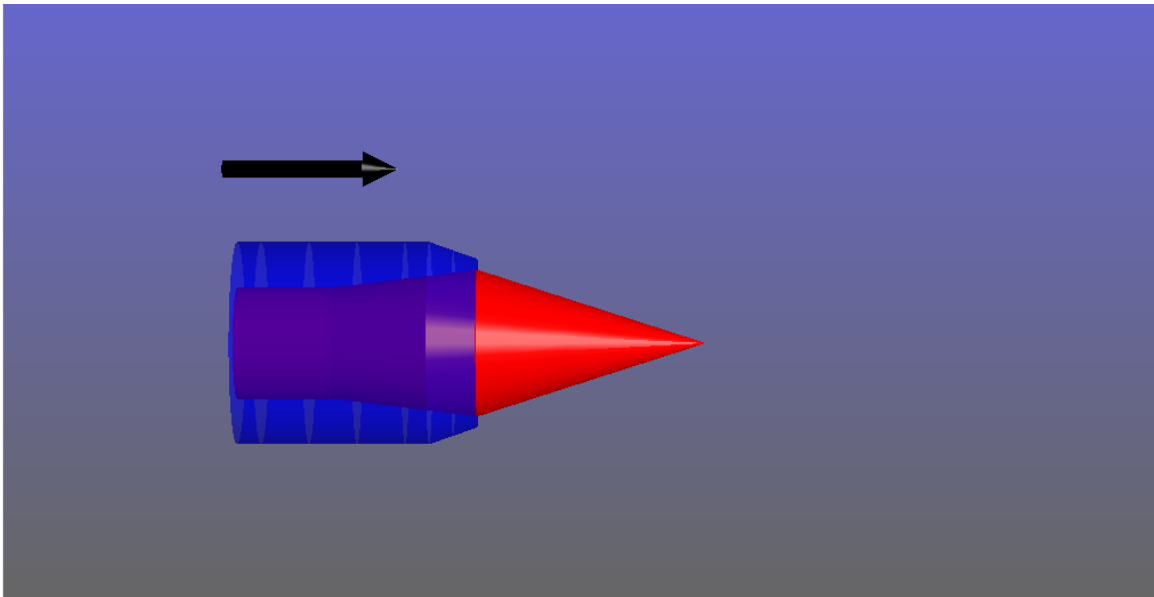
The previous parametric studies examined how three parameters, the O/F ratio, the total mass flow, and the chamber length, affect the weight and performance of the DEAN. Those three parameters will be the design variables to be modified in scaling the DEAN to the 50,000 lbf thrust target. The parametric studies suggest values for each of these parameters. As noted earlier, the engine provides the greatest I_{sp} at $O/F = 6$ for these parametric choices. Similarly, the study indicates a mass flow of approximately 104 lbm/s achieves the design vacuum thrust of 50,000 lbf. This result is for an engine operating at $O/F = 7$. With an O/F of six, the thrust will likely be higher. Finally, the results from the chamber length parametric study suggest a chamber length of 14.25 in is an acceptable value. Entering these values into the system-level model results in a significantly smaller engine performing at 50,900 lbf thrust and 489 s I_{sp} . Table 3.10 summarizes this new design and Figure 3.19 shows this new, much smaller design next to the original design.

Table 3.10: Scaled DEAN Design Parameters

Design Variables		Response Variables	
O/F	6	Vac Thrust (F_{vac})	50,900 lbf
Mass Flow (\dot{m})	104 lbm/s	Vac I_{sp}	489 s
Chamber Length (l_c)	14.25 in	Chamber Pres (P_0)	1310 psia
Outer Chamber Radius (r_{c_o})	6 in	Chamber Temp (T_0)	6413 R
Inner Chamber Radius (r_{c_i})	2 in	Throat Area (A_t)	18.9 in ²
Expansion Ratio (ϵ)	125	Nozzle Length (l_n)	13.6 in
LOX Bypass (%)	90	Chamber Volume (V_c)	970 in ³
LOX Pump Eff ($\eta_{p,LOX}$)	0.773	LOX PR Ratio ($PR_{p,LOX}$)	58
LOX Turbine Eff ($\eta_{t,LOX}$)	0.949	LOX Pump Power	1053 HP
LH2 Pump 1 Eff ($\eta_{p,LH2,1}$)	0.8	LOX Turbine PR ($PR_{t,LOX}$)	1.6
LH2 Pump 2 Eff ($\eta_{p,LH2,2}$)	0.83	LOX Turbine Power	1053 HP
LH2 Pump Eff ($\eta_{p,LH2}$)	0.9	LOX Temp (T_{LOX})	160-435R
		LOX Pres (p_{LOX})	2450-2600 psia
		Max LOX Mach	0.37
		LH2 Pumps PR ($PR_{p,LH2}$)	9.3
		LH2 Pump 1 Power	417 HP
		LH2 Pump 2 Power	3430 HP
		LH2 Turbine PR ($PR_{t,LH2}$)	1.8
		LH2 Turbine Power	3847 HP
		LH2 Temp (T_{LH2})	73-324R
		LH2 Pres (p_{LH2})	2960-3770 psia
		Max LH2 Mach	0.96



(a) Original Geometry for the DEAN



(b) Geometry for the scaled DEAN

Figure 3.19: Comparison of Geometry for the scaled DEAN to the Original Geometry

The performance values of this design are favorable. The 50,900 lbf thrust not only more closely matches the design requirements, but it is also falls within the

demonstrated 50,300 lbf of expander cycle engines as seen in the upper stage demonstrator engine.[25] The lengths of the engine chamber and nozzle are significantly smaller than the previous design, indicating the weight is similarly reduced. The converged values for the turbomachinery are equally promising. The power required by the pumps is properly balanced by power generated in the turbines, and in the LOX cycle this power is 40% of original design, while in the LH2 cycle the power is only increased by 8% over the original design. Together with the reduced mass flows and the pressure ratios, the turbomachinery of the scaled DEAN design has both lighter and more robust options over the original design.

The results also indicate opportunities for improvement, both in areas where requirements are still exceeded by the design, including T/W , I_{sp} , and chamber pressure, and in areas where there are concerns including fluid Mach numbers and wall temperatures. The original design of the DEAN had an estimated weight of 479 lbm.[2] This gives an upper limit for the scaled DEAN T/W of 106, meeting or exceeding the required T/W . The vacuum I_{sp} is now over 5% higher than the requirement, suggesting the nozzle can be modified to save weight and meet the I_{sp} requirement. The chamber pressure is 25% lower than the previous design, which leads to a more robust chamber design. Turning to areas of concern, at least one constraint, the max LH2 Mach number, is still higher than desired. Additionally, the wall temperatures, which must stay within their material limits still need to be determined. To determine the wall temperatures, notional materials need to be chosen.

3.6 Conclusion

The results of this study support two key conclusions. First, parametric modeling with automated trade studies is a powerful approach in conceptual design of rocket engines. Significant improvements were made to the design of the DEAN engine by modifying the numerical model to support parametric modeling and exploring the trade

space through automated trade studies. These improvements included reducing the size of the turbomachinery by reducing the total mass flow, improving the oxidizer-to-fuel ratio for optimal thrust performance, and reducing the overall length by 25%. All of these savings were realized while maintaining the required vacuum thrust performance of 50,000 lbf and increasing the vacuum specific impulse from 472 s to 489 s.

Second, the DEAN architecture offers significant performance gains over single-expander cycle based upper stage engines such as the RL10B-2. The DEAN has a chamber pressure that is twice that of the RL10B-2. This increased chamber pressure results in twice the vacuum thrust and a 5% higher vacuum specific impulse. Finally, the DEAN engine is 69% shorter than the RL10B-2, despite its increased thrust and specific impulse.

IV. Fourth Generation DEAN Model

4.1 Introduction

A review of the DEAN research history presented in Section 2.3.3 indicates two key conclusions about the DEAN models. Beginning with the third generation DEAN model, the research has reached the point of providing the required system details with the necessary level of fidelity. The inclusion of weight estimation analyses and improved performance analyses yield high quality estimates for the DEAN's vacuum specific impulse and thrust-to-weight ratio. However, the results of engineering studies using the third generation DEAN model, and the later Methane DEAN model, consistently lead to designs with thrust-to-weight ratios in excess of requirements while delivering specific impulse values far below requirements. The fourth generation DEAN model addresses these results by providing a flexible model capable of exploring a wide range of DEAN designs while still providing the required level of fidelity.

4.2 Motivation

The underlying causes of the results described above are limited trade space size and low model reliability. The results shown in Table 4.1 summarize the challenge associated with the limited trade space size as seen with the range of expansion ratios tested. When the expansion ratio (ϵ) has been assumed, as was the case in the first two generations, the vacuum specific impulse (I_{sp}) exceeds the required value. However, when the physical expansion ratio (occupying the narrow band between 4.0 and 7.0) is used in place of an assumed value, the resulting specific impulse falls far short of the required value. Further, the small chamber radii generated by these expansion ratios lead to thrust-to-weight ratios (T/W) far above the requirements. These results are consistent across all generations of research. The narrow range of available expansion ratios is driven by design

inconsistencies stemming from the original parametrization of the DEAN cycle model. Clearly, the DEAN system model needs to support running trade studies over a wider range of designs, especially those with greater expansion ratios, in order to find designs with the required vacuum specific impulse. The fourth generation DEAN model addresses this challenge through an updated parametrization using traditional rocket engine design parameters designed to ensure model consistency.

Table 4.1: Assumed Performance Compared to Actual Performance for Previous DEAN Generations

	Gen 1	Gen 1	Gen 2	Gen 2	Gen 3	Methane
	Assumed[2]	Actual	Assumed[27]	Actual	Actual[4]	DEAN[61]
F_{vac} (lbf)	57,231	57,231	50,900	50,900	50,161	25,000
ϵ	125.0	4.94	125.0	4.16	4.16	7.0
T/W_{req}	106.5	106.5	106.5	106.5	106.5	108.0
T/W	119.0	138.6	-	194.1	142.2	120.7
$I_{sp_{req}}$ (s)	464.0	464.0	464.0	464.0	464.0	383.0
I_{sp} (s)	472.7	412.9	489.0	422.8	430.6	349.3

The reliability of the parametric DEAN models has been a source of many challenges throughout the DEAN research. The reliability has been as low as 25% in the Methane DEAN [61] and 30% in author's work leading up to the fourth generation model. Most often these challenges are encountered when running trade studies involving the radial geometry of the engine. Given the expansion ratio is directly related to the radial geometry of the engine as noted in Section 2.3.3.3, improving the reliability of the DEAN model improves the search space in both size and quality. The fourth generation DEAN model addressed the model's reliability through the updated parametrization discussed above,

simplification of the system model, and calculating the initial estimates used by the cycle model to bootstrap the NPSS solver.

4.3 Model Improvements

4.3.1 Updated Parametrization.

The initial parametrization presented in Chapter 3 used a direct approach, exposing a number of internal variables in the cycle model as top level design variables. Among this original set of design variables are two key radii in the DEAN engine, the inner and outer chamber radii (r_{ci} and r_{co}). Figure 4.1 shows the positions of these radii and the corresponding inner and outer throat radii (r_{ti} and r_{to}). Treating these radii as top level design variables led to two sources of error. The first source of error was the generation of inconsistent geometry. When the inner and outer chamber radii are treated as separate design variables, they become independent of one another in the system model, allowing users and trade studies to generate designs where the inner chamber radius is larger than the outer chamber radius. Such inconsistent designs lead to model failures.

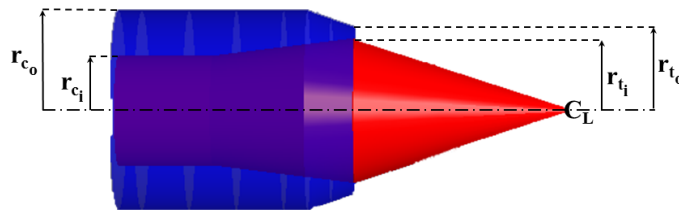


Figure 4.1: Key Radii in the DEAN Engine

The second source of error was a lack of isolation in design variables during parametric studies. Traditional rocket engine design parameters such as the expansion ratio and the chamber volume are coupled to the chamber radii. The lack of design variable isolation led to trade studies which are unable to separate the effects of varying the expansion ratio from

the effects of varying the chamber volume. Coupling traditional rocket engine parameters in this fashion made it difficult to verify the model as predicted relationships from rocket engine theory cannot be isolated for comparison.

The updated parametrization, shown in Table 4.2, derived the engine geometry from traditional rocket engine parameters, ensuring consistent designs and results. The outer chamber radius, the inner throat radius, and the outer throat radius are derived from the expansion ratio and throat area. The chamber volume is derived from the characteristic length and the throat area. Finally, the chamber inner radius is derived from the chamber volume and the outer chamber radius. Section A.3.1 covers the calculations used to compute the geometry from the updated parametrization.

Table 4.2: Updated DEAN Parametrization

Variable	Description
Expansion Ratio	Ratio of the exit area (A_e) to the throat area (A_t)
Throat Area (in ²)	Area of the nozzle at the throat
Chamber Length (in)	Length of the chamber, runs from the back of the engine to the throat
Characteristic Length (in)	Ratio of the chamber volume (V_c) to the throat area (A_t)
Vacuum Thrust (lbf)	Specified thrust to be produced by the engine
Oxidizer-to-Fuel Ratio	Ratio between the propellants

4.3.2 Model Simplification.

The third generation DEAN model introduced a number of new analyses to compute the performance and weight of the DEAN. Most of these new analyses were part of the aerospike performance module used to calculate the aerospike's geometry, thrust,

and specific impulse. The aerospike performance module included NASA's Chemical Equilibrium with Applications (CEA) and SEA's Two Dimensional Kinetic (TDK). The inclusion of these tools gave the DEAN system model improved fidelity in its results. However, CEA and TDK also introduced additional reliability challenges. The connection between the NPSS cycle model and the TDK analysis in the aerospike performance module was particularly difficult to manage and was the source of many failed model runs. Further, when this connection worked, it was computationally expensive, requiring several iterations of the system model to converge on compatible results between NPSS and TDK [4].

To improve the reliability of the system level model, the aerospike performance module from the third generation DEAN simulation was replaced with a modified NPSS rocket nozzle element. This new rocket nozzle element uses aerospike nozzle theory to compute the DEAN's thrust from values available in the DEAN cycle model, eliminating the need to run TDK in sequence with NPSS. Section A.3.1 covers the theory and implementation of this improvement.

4.3.3 Calculating Initial Estimates for NPSS Solver.

The second and third generation DEAN models relied on the assumed values from the first generation DEAN model and user inputs for the initial estimates used by the NPSS solver in the cycle model. These estimates covered the following values: estimated specific impulse, turbopump pressure ratios, propellant pressures inside the plumbing in the two expander cycles, and the cooling jacket wall thicknesses. These values worked well in the parametric DEAN models for designs with similar performance and cooling channel geometries to the first generation DEAN model. However, they led to a large number of failed model runs when trade space exploration moved away from the first generation DEAN design.

The fourth generation DEAN model addressed these model failures by calculating these estimates from other design variables. These calculations occur in three levels of

Table 4.3: Fourth Generation DEAN Model Components

Label	Name	Description
A	Data Monitors	ModelCenter Data Monitors to provide access to key design and response variables
B	Final Geometry	DEAN geometry (chamber and aerospike) after sizing wall thicknesses
C	Pressure Profile Plots	pressure profiles for the LOX and LH2 expander cycles
D	Design Variables	system level design variables and the preprocessing analyses, including cooling channel design and initial estimates for the turbopump pressure ratios
D1	Pressure Profile Converger	a secondary module, solves for the initial estimates for the turbopump pressure ratios
E	Wall Thickness Converger	module to balance the pressure and mechanical systems and to size the cooling channel wall thicknesses
F	Performance	performance values, structural jacket wall thicknesses and T/W
G	Geometry	geometry module
H	Constraints	constraint module; maximum Mach numbers in the cooling channels and the pressure drops across the injector face

Analysis of a design begins with the selection of the design to test. A user enters the design by specifying values for the top level design variables described in Table 4.2 using the model's Data Monitors (labeled A in Figure 4.2) or ModelCenter's Component Tree. The analysis continues with the execution of the model started when the user selects

the Run command in ModelCenter. The first set of analysis modules to execute are the three analyses in the Design Variables *sequence* (labeled D in Figure 4.2) starting with the Spike Materials and the Cooling Channels Design. These two modules combine secondary design variables (see Section A.2) with the top level design variables to derive materials and cooling channel geometry values used by downstream modules. Following the execution of these two components, the Pressure Profile Converger (labeled D1 in Figure 4.2) finds the best initial estimates for the specific impulse and turbopump pressure ratios. These analyses constitute the preprocessing step for the DEAN system level model.

The model execution continues with the execution of the engine cycle analysis. The engine cycle analysis is driven by the Wall Thickness Converger (labeled E in Figure 4.2), a fixed point iteration solver used to find the cooling channel wall thicknesses. This converger sets initial estimates (0.02 in) for the fourteen wall thickness values (one each for the six chamber stations and the eight aerospike stations) and then iteratively calls the DEAN cycle analysis, the Angelino aerospike geometry analyses, and the Cooling Jacket wall sizing loop until the estimated cooling jacket wall thicknesses equal the calculated wall thicknesses. The DEAN cycle analysis takes the top level design variables, the derived values from the Spike Materials and Cooling Channel Design modules, and the estimated cooling jacket wall thicknesses from the converger and uses these values to execute the NPSS analysis for the current design. The results from this analysis are used in all subsequent modules. Next, the Angelino and Angelino Correction modules calculate the aerospike contour for the current design. Then, the Cooling Jacket wall sizing loop iterates over the cooling jacket wall temperatures and wall thicknesses, calling the Materials Property analysis for updated strength values based on material selections and wall temperatures, until it finds the cooling jacket wall thickness for the current design. The results of the Cooling Jacket wall sizing loop are compared to the estimated values in the converger to determine if the Wall Thickness Converger loop continues.

Assuming the Wall Thickness Converger completes without error (often caused by insufficient material strength for the current cooling jacket material selections), the system level model continues with the first post processing step: the Performance *sequence* (labeled F in Figure 4.2). The first analysis in the Performance *sequence* is the Channels script. This module takes the channel dimensions, reported by the DEAN cycle model as vectors, and converts them into scalar values for use by the Structural Jacket Sizing module. Following the Channels script, the Structural Jacket Sizing module determines the thicknesses of the chamber and aerospike structural jackets and the propellant plumbing modeling these structures as thick walled pressure vessels. At the completion of the Structural Jacket Sizing module, the DEAN system model has sufficient data to calculate the total engine weight and the thrust-to-weight ratio. These calculations are implemented in the Thrust-to-Weight Calculation module. The final analysis in the Performance *sequence*, Pressure Profiles, renders the pressure levels in the two expander cycles (labeled C in Figure 4.2).

The model execution continues with the Geometry *sequence* (labeled G in Figure 4.2). This *sequence* contains a series of scripts and ModelCenter geometry components used to generate conceptual geometry (linear aerospike nozzle without wall thicknesses) and final geometry (calculated aerospike nozzle contour with wall thicknesses).

The final section of the system level model to run is the Constraints block (labeled H in Figure 4.2). This section contains analyses used to calculate the constraint values in the DEAN system level model not calculated by earlier modules. The first two analyses, the LOX and LH2 *sequences*, calculate the maximum Mach numbers in the cooling channels by iteratively calling response surface models of the speed of sound in liquid oxygen and liquid hydrogen for each station in the DEAN cycle model. Following the cooling channel Mach number calculations, the Pressure RMSE module computes the root mean square error between the estimated pressure profiles and the calculated pressure profiles in the

two expander cycles. Next the Chamber Mach script uses a secant root solver to compute the chamber Mach number. Then, the system level model completes its execution with the Sanity Checks module computing the pressure drops across the injector face for both expander cycles, ensuring the aerospike structure does not violate the engine's physical dimensions, and calculating the outer chamber radius and the difference between the throat radii.

Manual runs of the model initiated by the user end with the completion of the Sanity Checks module. Automated trade studies execute each of the steps above for each design under consideration.

4.5 Results

The results of the verification studies in Chapter 5 and Appendix A showed the updates in the fourth generation DEAN model address the modeling challenges discussed in Section 4.2 while preserving the fidelity of the third generation DEAN model. The trade studies used to verify the DEAN architecture and the fourth generation model showed the model now supports a wide range of designs, including expansion ratios from 6.0 to 25.0 (see Table 5.10). These trade studies also indicated the model's reliability has improved significantly, with 98.7% of the 1500 runs succeeding (see Table 5.11). Verification tests on the Pressure Profile Converger showed it improves both the reliability and the quality of the model's results (see Section A.2.3). Finally, comparisons to previous results demonstrated the fourth generation DEAN model matches the fidelity of the third generation DEAN model (see Appendix B).

4.6 Conclusion

The fourth generation DEAN model met the modeling needs for the remaining research. The improved reliability and expanded trade space open up previously unavailable design options necessary to reach the DEAN design goals. Further, the

improved reliability was essential for running the optimization studies in the final phase of the current DEAN research. Lastly, the fourth generation DEAN model included these improvements without sacrificing fidelity.

V. Verification of Dual-Expander Aerospike Nozzle Upper Stage Rocket Engine

The text of this chapter was submitted to the AIAA Journal of Propulsion and Power in July 2014. It is unaltered from the submitted version except in its formatting as required by the AFIT dissertation style guide.

5.1 Introduction

Prices for space launches are literally astronomical. The cost to deliver payload to orbit is estimated to be as much as \$10,000 per pound [15]. A first class stamp to space (that is delivery of up to 3.5 ounces by weight) would cost \$2,200. Current launch costs to place satellites in orbit costs hundreds of millions of dollars. In this time of budgetary constraints, reliance on satellites for surveillance, navigation, communication, and meteorology in the US also means there is demand for more efficient and cheaper improvements [16, 17].

At the heart of launch costs is the fundamental science and engineering of rocket powered flight. Payloads represent only a small fraction of the gross lift-off weight (GLOW) of current rockets. Improvements in propulsion performance, measured in specific impulse (I_{sp}) and the propulsion system's thrust-to-weight ratio (T/W), can dramatically increase payload fractions. Increased payload fractions reduce the size of launch vehicles for a given payload leading to lower cost launch vehicles. Increased payload fractions can also increase the size of payloads launched per mission, reducing the per pound cost for fixed mission expenses, such as range and insurance costs. Taken together, the savings can be significant. However, achieving these gains in performance will require more than incremental improvements in rocket engine technology. Consider that for decades the thrust-to-weight ratio of high powered liquid rocket engines has been relatively constant with respect to propellant selection regardless of thrust levels and designs [23].

The Air Force Institute of Technology (AFIT) is researching a modification to the expander cycle as a means of breaking through this performance barrier. The result of this research is the Dual-Expander Aerospike Nozzle (DEAN) rocket engine. The DEAN is a liquid oxygen (LOX)/liquid hydrogen (LH2) reusable upper stage engine which includes two separate expander cycles and uses an aerospike nozzle. The DEAN architecture offers a performance advantage over a standard expander cycle in a compact package leading to dramatically improved thrust-to-weight ratios while maintaining a vacuum specific impulse comparable to current LOX/LH2 upper stage engines.

AFIT's goal with its research into the DEAN is to determine the viability of the DEAN architecture by finding those missions and designs for which the DEAN has a competitive advantage over traditional upper stage engines such as the RL10. Current research is focused on verifying the DEAN architecture by comparing the performance and packaging of the DEAN to engineering principles and the RL10.

5.2 Background

5.2.1 DEAN Architecture.

The DEAN architecture, shown in Figure 5.1, uses two novel design choices. The first is the use of separate expander cycles for the fuel and the oxidizer. In a traditional expander cycle, the fuel is pumped through a cooling jacket for the chamber and nozzle. The energy transferred to the fuel from cooling the chamber and nozzle is then used to drive the turbine turning both the fuel and oxidizer pumps before the fuel is introduced into the chamber [5]. In the DEAN, the fuel and oxidizer each drive their own turbines to power their own pumps.

The second novel design choice of the DEAN is the use of an aerospike, or plug, nozzle. Aerospike nozzles run through the middle of the rocket's propellant flow and up into the chamber, leaving the ambient atmosphere to form the outer boundary for the flow. The interaction with the ambient atmosphere gives aerospike nozzles automatic altitude compensation, making them more efficient over a range of altitudes than similar bell

nozzles which must be designed for a single, specific altitude [24]. In the DEAN, the use of an aerospike nozzle provides a second, physically separate cooling loop from the chamber for use in the fuel expander cycle, greatly simplifying the implementation of a dual-expander cycle.

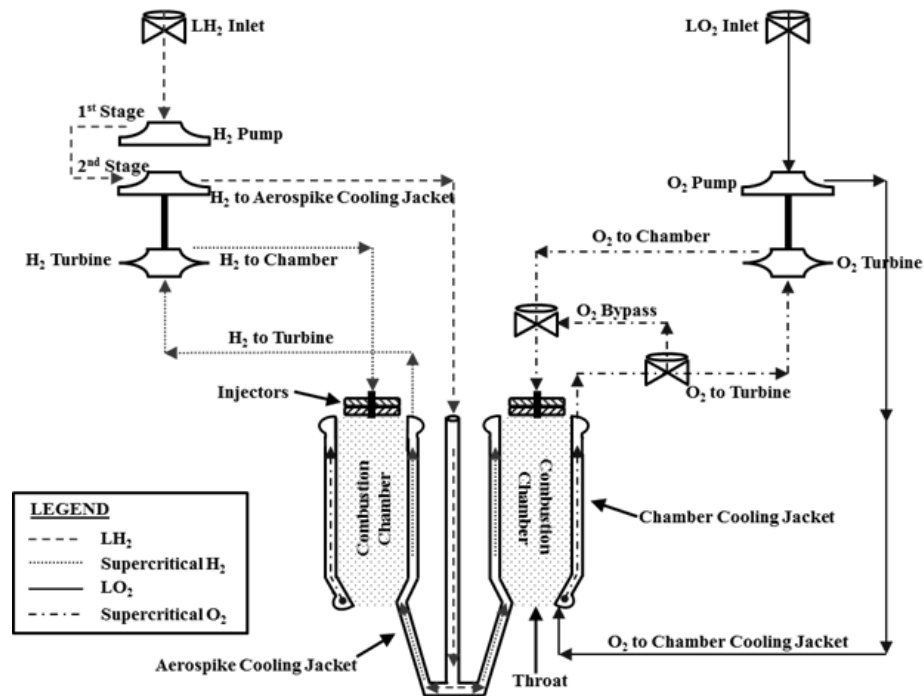


Figure 5.1: DEAN Architecture, credit J. Hall (unpublished)

The DEAN's unique architecture offers a number of advantages. The second cooling loop increases the surface area inside the chamber, transferring greater energy to the propellants and providing more power to the turbines. This increased power is transferred to the pumps and in turn leads to increased chamber pressures. The increased chamber pressure yields engine performance improvements when compared to traditional expander cycle engines such as the RL10. This improved performance leads to smaller engines, in terms of both weight and physical dimensions, for similar levels of thrust and specific

impulse. The separate expander cycles also ensure the fuel and oxidizer remain physically separated until entering the combustion chamber, eliminating one of the more catastrophic failure modes in traditional expander cycles, namely failure of an inter-propellant seal. Finally, the DEAN architecture is a forerunner to a similar boost stage architecture, where the aerospike nozzle's global performance could result in even greater performance gains [2, 25–27].

The DEAN architecture is not without its challenges, though. First, the LOX cycle requires a turbine material to operate in an oxygen environment. Material studies at AFIT have shown Inconel 718 provides both satisfactory oxygen resistance and suitable mechanical performance for use in both the pump and the turbine in the LOX cycle [26, 27]. Second, the expansion ratio of aerospike nozzles is limited to the ratio of the area of the chamber at the throat to the throat area [24]. Due to this limit, aerospike nozzles generally need larger chamber diameters to reach useful expansion ratios, potentially limiting the range of engines which offer improved thrust-to-weight while also delivering the required specific impulse.

5.2.2 Previous Research.

The current research builds on three generations of DEAN simulations. The performance goals for the DEAN have been a vacuum thrust of 50,000 lbf, a vacuum specific impulse of 464 s, and a thrust-to-weight ratio of 106.5. All three generations use NASA's Numerical Propulsion System Simulation (NPSS) to explore the cycle. NPSS is a computer simulation tool for modeling aircraft and rocket engines. Engine simulations built in NPSS provide higher fidelity results than engine cycle studies. NPSS has been developed by the NASA Glenn Research Center with assistance from the aerospace propulsion industry [31]. The DEAN cycle simulation balances the fluid flows, mechanical power, and thermal flows in the two expander cycles to converge on the engine performance parameters for a given design point.

Two of the three previous DEAN simulations extended the cycle model by embedding it into a system level engine simulation built in Phoenix Integration's ModelCenter. ModelCenter is a multidisciplinary modeling environment used to study the trade space of a design and optimize that design. ModelCenter can combine analyses developed in a variety of tools including MATLAB, Mathcad, Excel, and command line executables into a single system level model [60]. The system level DEAN simulation automates a parameterized version of the cycle model and connects it to additional analyses to estimate the DEAN's weight and geometry in order to compute the DEAN's physical dimensions and thrust-to-weight ratio.

The first generation research focused on developing the initial cycle balance of the DEAN for a single design. This design, shown in Figure 5.2(a), included an assumed expansion ratio of 125 and produced a vacuum thrust of over 57,000 lbf and a vacuum specific impulse of more than 472 s, with a thrust-to-weight ratio of 119. The cycle balance was verified using stand alone models of the two expander cycles. These separate cycle simulations, which used Pumpal and RITAL to model the pump and turbine respectively, showed strong agreement with the overall DEAN simulation for the required pump power and the pressure levels in both the LOX and LH2 cycles. The results from the first generation DEAN research confirmed the feasibility of the DEAN and verified the expander cycles in DEAN cycle simulation [2, 25, 26].

The second generation research implemented parametric modeling of the DEAN by refactoring the cycle model and integrating it into the first system level simulation. The new DEAN simulation employed parametric modeling techniques, modified design variables, and a simplified nozzle geometry. The assumption of an expansion ratio of 125 was maintained in this model. The DEAN system level simulation was then used to run a series of parametric studies over the DEAN geometry and cycle parameters. Parametric studies over cycle parameters yielded a large number of valid designs, however, parametric studies

varying the chamber radii resulted in computational errors in the cycle model. The results of the parametric studies were then used to scale down the DEAN design to more closely match the original design goals. The resulting design had a vacuum thrust of 50,900 lbf and a vacuum specific impulse of 489 s, while being 25% shorter in total length and reducing the size of the turbomachinery by reducing the total mass flow. Figure 5.2 compares the original DEAN with the scaled DEAN. The results from the second generation DEAN research both expanded the DEAN trade space and demonstrated the power of combining engine cycle models with parametric modeling in the development of new liquid rocket engines [27].

The third generation research extended the system simulation to include additional calculations such as structural sizing, nozzle contour, and engine weight. The third generation DEAN research also moved from an assumed value for the expansion ratio to a calculated value based on the DEAN's geometry. This change led to significantly smaller expansion ratios which reduced the vacuum specific impulse compared to previous generations of the DEAN. Additionally, the aerospike performance module in the third generation simulation integrated NASA's CEA and SEA's TDK to provide detailed information concerning the aerospike nozzle's geometry and the thrust it produced.

Numerous trade studies were run using the updated DEAN system level simulation, including an initial survey into the materials which should be used to construct the DEAN. The results indicated the chamber should use silicon carbide for its cooling jacket and aluminum 7075 T6 for its structural jacket, and the aerospike nozzle should be fabricated from a single material, oxygen-free copper (C10100). As with the second generation DEAN research, the third generation DEAN simulation was unstable during studies varying the chamber radii, making it difficult to improve the expansion ratio and in turn the vacuum specific impulse. The final design for the third generation research, shown in Figure 5.2(c), provided a vacuum thrust of just over 50,000 lbf and a vacuum specific impulse of just over

430 s, with a thrust-to-weight ratio of 142 in a 27 inch long engine. This design exceeded the required thrust-to-weight ratio and delivered the required vacuum thrust. However, it fell far short of the desired vacuum specific impulse. Further, while third generation DEAN simulation included high fidelity modules for the aerospike performance, these modules added significant complexity to the simulation. This added complexity, especially the integration of the TDK analysis, resulted in higher model failure rates during trade study execution [4].

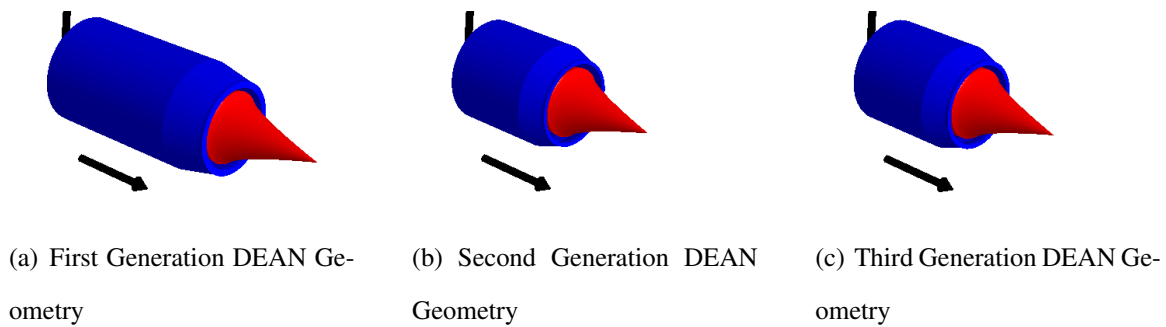


Figure 5.2: Comparison of First, Second, and Third Generation DEAN Geometry

5.3 Current Research

The fourth generation DEAN simulation built on the lessons learned from the previous generation models. The new simulation included an updated geometry parametrization, simplified model structure, and a custom solver to compute initial estimates for the cycle balance. The improvements allowed for the exploration of a wide range of designs while maintaining fidelity. Figure 5.3 and Table 5.1 outline the overall structure of the fourth generation DEAN model.

The fourth generation DEAN simulation included a new parametrization of the DEAN cycle model. In the previous parametrization, design variables included two of the key radii

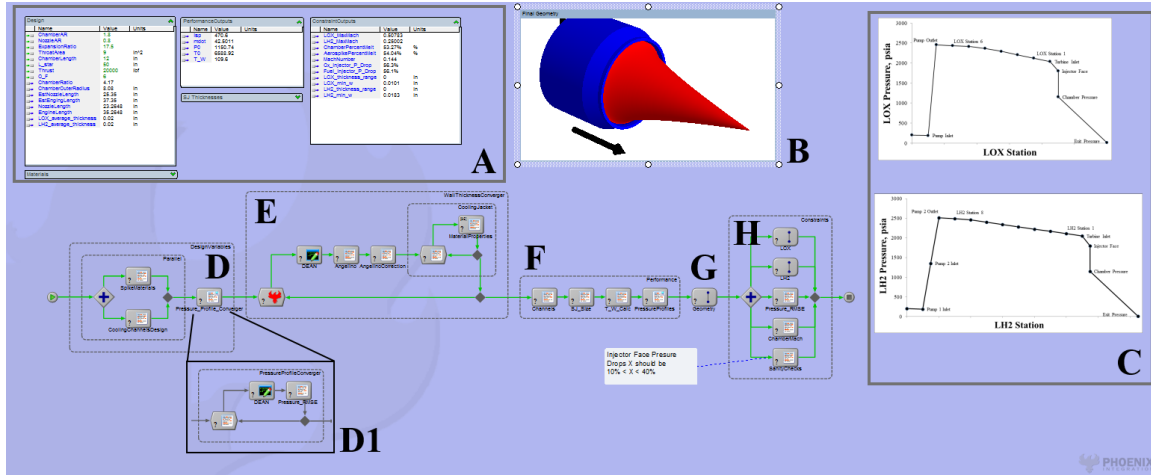


Figure 5.3: Fourth Generation DEAN Model

in the DEAN engine, the inner and outer chamber radii, r_{ci} and r_{co} respectively. Figure 5.4 shows the positions of these radii and the corresponding inner and outer throat radii. This parametrization allowed for the specification of inconsistent designs such as ones where the inner chamber radius is greater than the outer chamber radius. The new parametrization connected all four radii into a common conceptual design relationship ensuring consistency and improving model success. Further, the simulation now describes the design using traditional rocket engine design parameters such as expansion ratio, chamber length, thrust, and characteristic length.

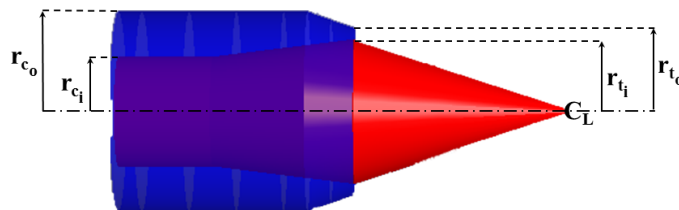


Figure 5.4: Key Radii in the DEAN Engine

Table 5.1: Fourth Generation DEAN Model Components

Label	Name	Description
A	Data Monitors	ModelCenter Data Monitors to provide access to key design and response variables
B	Final Geometry	DEAN geometry (chamber and aerospike) after sizing wall thicknesses
C	Pressure Profile Plots	pressure profiles for the LOX and LH2 expander cycles
D	Design Variables	system level design variables and the preprocessing analyses, including cooling channel design and initial estimates for the turbopump pressure ratios
D1	Pressure Profile Converger	a secondary module, solves for the initial estimates for the turbopump pressure ratios
E	Wall Thickness Converger	module to balance the pressure and mechanical systems and to size the cooling channel wall thicknesses
F	Performance	performance values, structural jacket wall thicknesses and T/W
G	Geometry	geometry module
H	Constraints	constraint module; maximum Mach numbers in the cooling channels and the pressure drops across the injector face

To improve the robustness of the thrust calculation, the aerospike performance module from the third generation DEAN simulation was replaced with a modified NPSS rocket nozzle element. The thrust for an aerospike nozzle can be calculated with Equation (5.1).

The momentum thrust for an aerospike nozzle, Equation (5.2), is produced by the momentum exchange between the propellant and the vehicle. The non-design thrust, Equation (5.3), accounts for the thrust component generated from operating the engine above or below its design altitude [4, 24].

$$F_{aerospike} = F_m + F_{nondesign} + F_{pressure} + F_{cowl} \quad (5.1)$$

$$F_m = \dot{m}v^* \cos\Theta + (p^* - p_{amb})A_t \quad (5.2)$$

$$F_{nondesign} = (p_e - p_{amb})A_e \quad (5.3)$$

The last two terms in Equation (5.1), $F_{pressure}$ and F_{cowl} , are related to the geometry of the aerospike nozzle. The pressure thrust is result of the the pressure acting along the length of the aerospike over its cross-sectional area and the cowl thrust is the force acting on the exit lip of the chamber. The fourth generation DEAN model conservatively assumed these components can be accounted for in the $F_{nondesign}$ term and then included it directly in the modified NPSS nozzle element. The calculation of the non-design thrust assumed the the minimum exit area for the aerospike, the design flow exit area, to give a conservative estimate for the total thrust [4]. Tests between the fourth and third generation simulations showed good agreement between the models, verifying the new nozzle element. This modification allowed for the removal of the aerospike performance module, eliminating one of the key sources of model failure.

A key improvement to the DEAN simulation in this research is the inclusion of a custom solver script to determine initial estimates for the pressure ratios of the DEAN pumps. The initial estimates have a significant impact on the solution found for the pressure levels in the cooling channels. Starting with high quality estimates reduced convergence time to a solution for a specified design and improved robustness of the overall simulation.

The values for these estimates depend on other design variables: thrust, expansion ratio, etc. The estimates were determined using a root mean square technique comparing the estimated pressure profiles and the computed pressure profiles.

Verification of the fourth generation DEAN analysis modules was primarily carried out through source code inspection. The inspection process ensured the source code for each module in the simulation agreed with the underlying physics. The data flow connections between the modules were also inspected to verify the system level model passed the correct values between modules and in turn calculated the correct performance for the DEAN.

5.4 Results and Analysis

5.4.1 *DEAN Performance Trade Studies.*

A series of six trade studies using the fourth generation DEAN simulation were developed to test specific design considerations: chamber and thrust, specific impulse, and engine weight. The six trade studies used the same baseline design, shown in Figure 5.5 and Table 5.2. This design was chosen through manual testing and user guided trade studies to maximize the model reliability over a wide trade space.

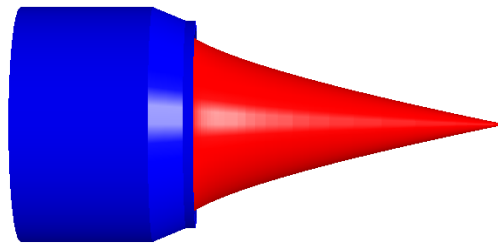


Figure 5.5: Trade Study Baseline Design Geometry

Table 5.2: Trade Study Baseline Design

Variable	Value
Expansion Ratio	17.5
Throat Area (in ²)	9.0
Chamber Length (in)	12
Characteristic Length (in)	50
Vacuum Thrust (lbf)	20,000
Oxidizer-to-Fuel Ratio	6.0
Chamber Throat AR	1.0
Chamber Stations Adjustment	1.2
Chamber Station 5 Adjustment	1.0
Chamber Cooling Channels Ratio	14.4
Nozzle Throat AR	0.86
Nozzle Station 1 Adjustment	1.7
Nozzle Station Spike Adjustment	1.0
Aerospike Cooling Channels Ratio	9.4
Ambient Pressure Decision	Operational
Operational Pressure (psia)	0.001
Cooling Geometry Option	Channel Cover + Structural Jacket
Percent Weight of Hardware	5.0 %
Cowl Length	0.1
Factor of Safety	1.5
Material Strength Option	Yield Strength
Chamber & Aerospike Materials	Silicon Carbide
LOX Pipe Material	INCONEL 718
LH2 Pipe Material	INCOLOY 909

All six trade studies use a similar design of experiments. A pairwise relationship between a design variable and a response (i.e. total mass flow and thrust) was selected as the test objective. A second design variable related to either geometry or performance (i.e. expansion ratio) was then selected to ensure the observed results were not isolated to a single band of designs for the DEAN. A parameter scan design of experiments was then specified with fifty levels for the first design variable and five levels for the second design variable. This experimental design process yielded results across a wide range of DEAN designs while limiting the number of computational runs to a manageable size. The result of running these trade studies is the equivalent of running five separate parametric studies over the pairwise relationship, one for each value of the second design variable.

5.4.1.1 Chamber and Thrust Trade Studies.

For a constant specific impulse the relationship between chamber pressure and thrust is linear, making it a good verification of the fourth generation DEAN simulation. The trade study “Responses to Vacuum Thrust” looked at the relationships between total mass flow and chamber pressure with thrust. The common design variable in both of these pairwise relationships is the vacuum thrust. The second design variable for this trade study was the expansion ratio. The design for this trade study is shown in Table 5.3.

Table 5.3: Responses to Vacuum Thrust Trade Study Design

Variable	Low	High	Levels
Vacuum Thrust (lbf)	10,000	35,000	50
Expansion Ratio	6	25	5

The relationship between total mass flow and thrust can be tested using the definition of specific impulse shown in Equation (5.4). Solving for total mass flow yields

Equation (5.5) [5, 24]. Equation (5.5) shows the direct relationship between total mass flow and thrust.

$$I_{sp} = \frac{F}{\dot{m}g_0} \quad (5.4)$$

$$\dot{m} = \frac{F}{I_{sp}g_0} \quad (5.5)$$

Figure 5.6 shows the results of the DEAN simulation for total mass flow and thrust. As expected, the relationship between the mass flow and thrust is linear, generating one curve for each expansion ratio. The values were verified by computing the total mass flow from the vacuum thrust and vacuum specific impulse using Equation (5.5). As can be seen in Figure 5.6, the model's values agree with the calculated values.

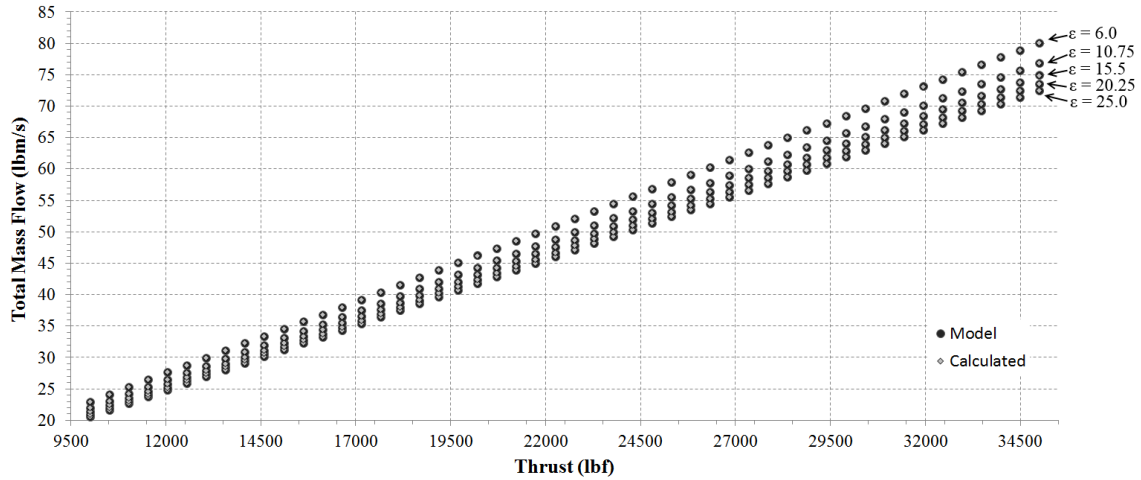


Figure 5.6: Total Mass Flow Variation with Vacuum Thrust for Five Expansion Ratios

The relationship between the chamber pressure and thrust can be tested by combining the definition of the characteristic velocity with Equation (5.5) and solving for chamber pressure. The characteristic velocity, shown in Equation (5.6), is a performance property of

a rocket engine which measures propellant and chamber performance independent of the nozzle [5, 24]. Solving Equation (5.6) for chamber pressure and substituting Equation (5.5) for the mass flow gives the relationship between chamber pressure and thrust shown in Equation (5.7). With the specific impulse, throat area, and characteristic velocity constant the relationship is linear.

$$c^* = \frac{A_t p_c}{\dot{m}} \quad (5.6)$$

$$p_c = \frac{c^* F}{I_{sp} A_t g_0} \quad (5.7)$$

Figure 5.7 shows the results of testing the relationship between chamber pressure and thrust for the DEAN. As expected a series of linear relationships between the chamber pressure and thrust resulted, one for each expansion ratio. The values were verified by computing the chamber pressure from the vacuum thrust, vacuum specific impulse, throat area, and the characteristic velocity using Equation (5.7). The simulation agrees with the calculated values. Figure 5.7 also includes the chamber pressures for the RL10A-4 and RL10B-2, 610 psia and 640 psia respectively, for comparison to the DEAN [24]. The DEAN's chamber pressure nearly doubles the chamber pressure of the RL10's expander cycle for comparable thrust levels.

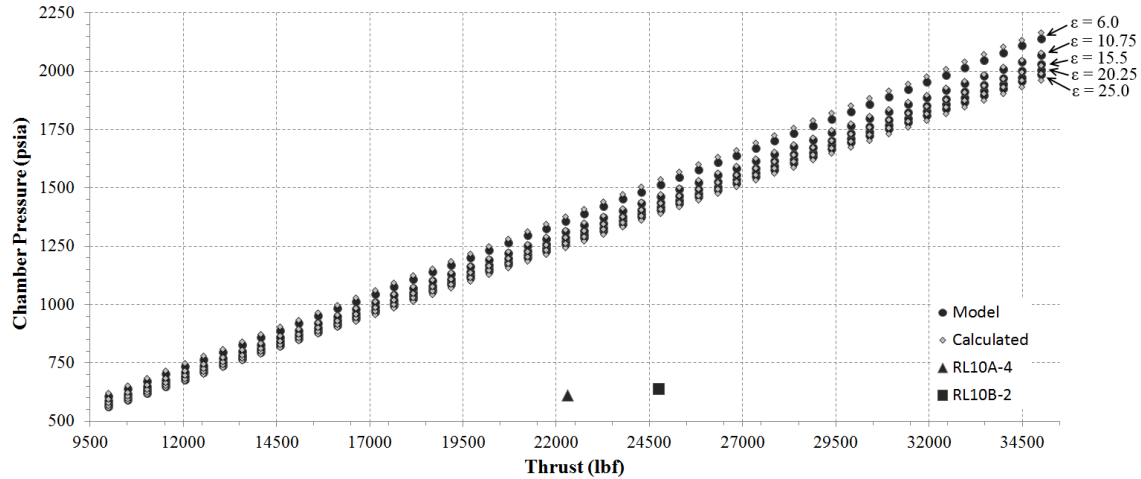


Figure 5.7: Chamber Pressure Variation with Thrust for Five Expansion Ratios

The “Responses to Throat Area” trade study explored the relationship between chamber pressure and the throat area. The design variable in this pairwise relationship was the throat area. The second design variable for this trade study was the vacuum thrust. The design for this trade study is shown in Table 5.4.

Table 5.4: Responses to Throat Trade Study Design

Variable	Low	High	Levels
Throat Area (in ²)	7	12	50
Vacuum Thrust (lbf)	10,000	35,000	5

The chamber pressure and the throat area showed an inverse relationship, which can be tested using Equation (5.7). Figure 5.8 shows the results of testing this relationship for the DEAN. As expected, the inverse trends for the chamber pressure with respect to the throat area confirmed the simulation’s validity using Equation (5.7).

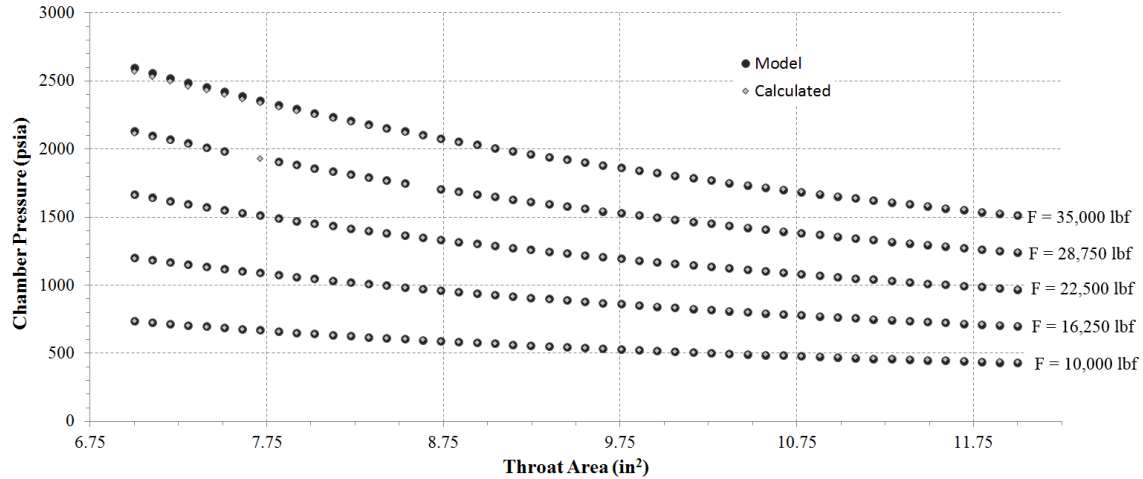


Figure 5.8: Chamber Pressure Variation with Throat Area for Five Thrust Levels

5.4.1.2 Specific Impulse Trade Studies.

The trade study “Responses to Expansion Ratio” explored the relationships specific impulse has with expansion ratio and the molecular weight of the combustion products. The common design variable in both of these pairwise relationships was the expansion ratio (Table 5.5).

Table 5.5: Responses to Expansion Ratio Trade Study Design

Variable	Low	High	Levels
Expansion Ratio	6	25	50
Vacuum Thrust (lbf)	10,000	35,000	5

The relationship between vacuum specific impulse and expansion ratio can be tested using expected theoretical results shown in Equation (5.8) and Figure 5.9 [5, 24].

$$I_{sp} = \lambda \left[\frac{c^* \gamma}{g_0} \sqrt{\left(\frac{2}{\gamma-1}\right) \left(\frac{2}{\gamma+1}\right)^{\frac{\gamma+1}{\gamma-1}} \left[1 - \frac{p_e}{p_c} \frac{\gamma-1}{\gamma}\right]} + \frac{c^* \epsilon}{g_0 p_c} (p_e - p_a) \right] \quad (5.8)$$

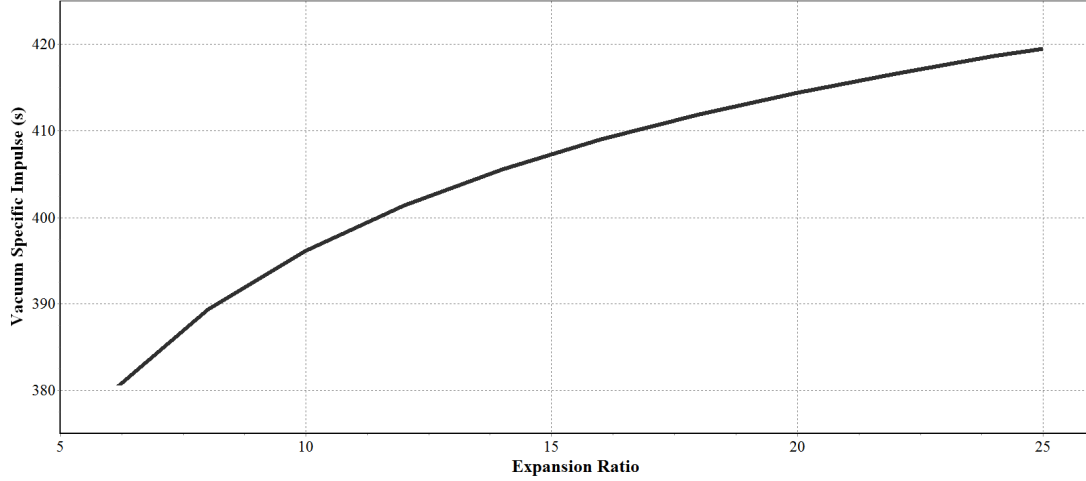


Figure 5.9: Vacuum Specific Impulse Variation with Expansion Ratio for a Generic LOX/LH2 Engine ($P_c = 500$ psia)

Figure 5.10 shows the DEAN simulation is clearly in agreement with the underlying physics. The results also confirm the DEAN provides comparable performance to the RL10 in a far more compact package (i.e. higher thrust-to-weight). Table 5.6 lists the engine length and outer diameter for both the RL10B-2 and a DEAN engine.

Using the alternate definition for the characteristic velocity, shown in Equation (5.9), the characteristic exit velocity is clearly related to $1/\sqrt{MW}$. Combining Equation (5.8) and Equation (5.9) shows the specific impulse is proportional to $1/\sqrt{MW}$ [5].

$$c^* = \frac{\eta_{c^*} \sqrt{\gamma T_0 (8314/MW)}}{\gamma \left(\frac{2}{\gamma+1}\right)^{\frac{\gamma+1}{2\gamma-2}}} \quad (5.9)$$

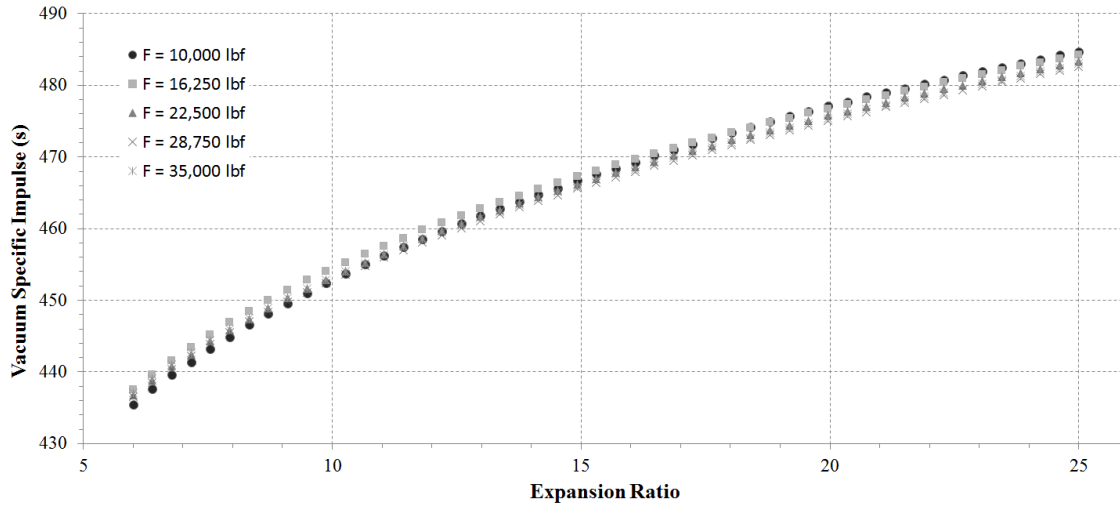


Figure 5.10: Vacuum Specific Impulse Variation with Expansion Ratio for Five Thrust Levels

Table 5.6: Comparison of DEAN and RL10B-2 Sizes

Variable	DEAN	RL10B-2 [11, 24]	Delta
Vacuum Thrust (lbf)	28,750	24,750	+16%
Vacuum Specific Impulse (s)	465.6	465.5	0.0%
Engine Length (in)	32.9	163.5	-80%
Engine Outer Diameter	16.3	84.5	-81%

The relationship between the specific impulse and molecular weight is a negative root relationships as shown in Figure 5.11.

The “Responses to Oxidizer-to-Fuel Ratio” trade study showed how the vacuum specific impulse and the oxidizer-to-fuel ratio (O/F) are related. The design variable in

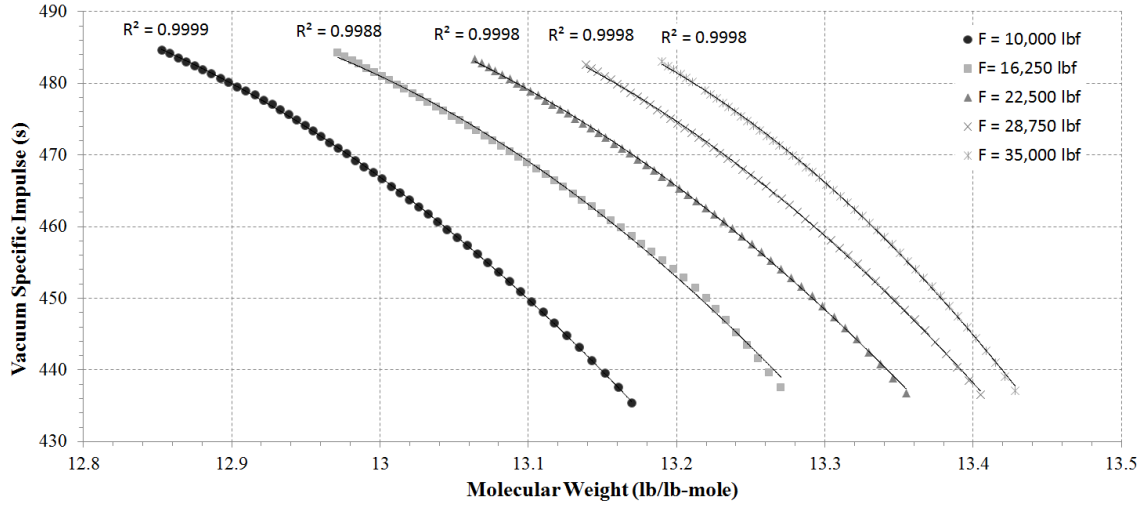


Figure 5.11: Specific Impulse Variation with Molecular Weight for Five Thrust Levels

this pairwise relationship was the oxidizer-to-fuel ratio. The second design variable for this trade study was the expansion ratio (Table 5.7).

Table 5.7: Responses to Oxidizer-to-Fuel Ratio Trade Study Design

Variable	Low	High	Levels
Oxidizer-to-Fuel Ratio	5	8	50
Expansion Ratio	6	25	5

For a given propellant combination, expansion ratio, and engine cycle a specific oxidizer-to-fuel ratio produces a maximum specific impulse. This ratio produces the optimal energy release and exhaust molecular weight from the combustion reaction. For liquid hydrogen/liquid oxygen engines, the optimal oxidizer-to-fuel ratio is between 3.5 and 6.0 [24]. Figure 5.12 shows the DEAN's specific impulse is maximized by an oxidizer-to-fuel ratio of 6.0 across a range of geometries.

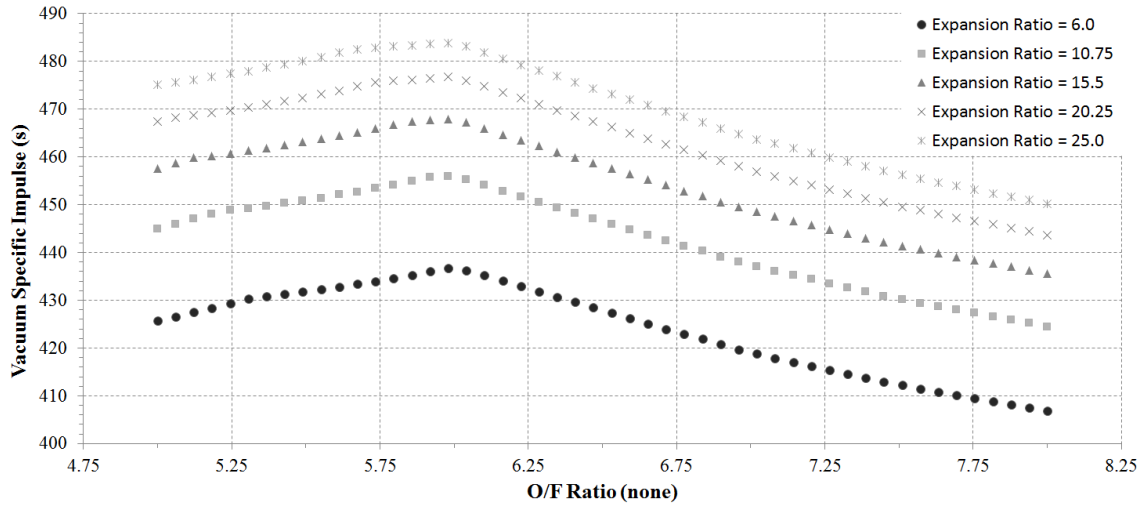


Figure 5.12: Specific Impulse Variation with Oxidizer-to-Fuel Ratio for Five Expansion Ratios

The results above demonstrate the DEAN simulation's performance is consistent with rocket engine theory and the underlying physics. The results also confirm the DEAN architecture produces the predicted compact packaging compared to a single expander cycle engine.

5.4.1.3 Weight Trade Studies.

The "Responses to Throat Area" trade study looked at the relationship between total engine weight and throat area. In general, reducing the throat area leads to lighter engines [5].

Figure 5.13 shows a more complex relationship between throat area and engine weight than expected. Investigation of the underlying data showed the turbopump weight is driving the variability of the total engine weight. The variability in turbopump weight is driven by the Pressure Profile Converger loop, shown in Figure 5.3 and Table 5.1. The Pressure Profile Converger minimized the pump pressure ratios to account for the changes

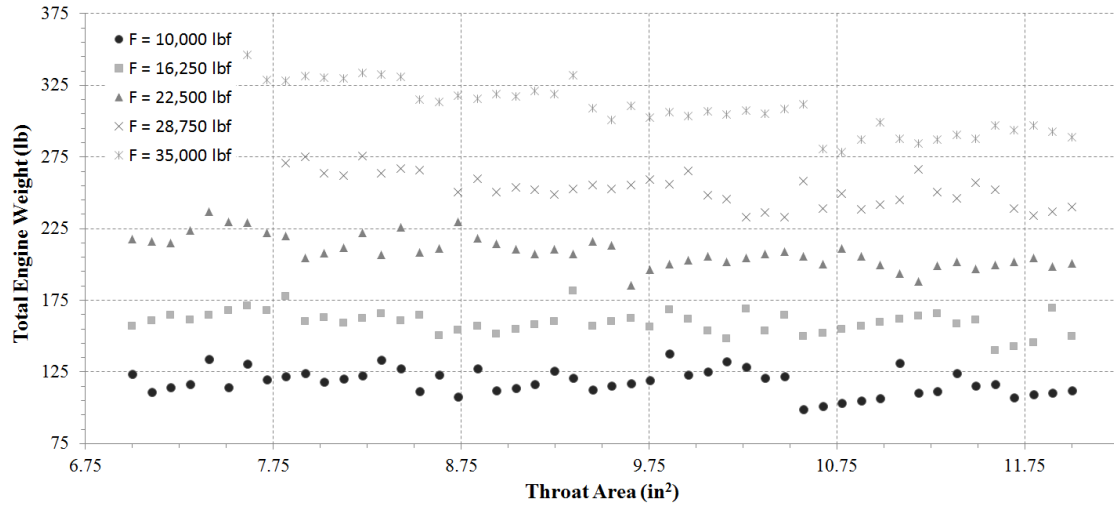


Figure 5.13: Total Engine Weight Variation with Throat Area for Five Thrust Levels

in chamber pressure associated the varying throat area, introducing an additional variation in the trade study beyond the variation driven by the thrust and throat area. Repeating the “Responses to Throat Area” trade study with the Pressure Profile Converger loop disabled, fixing the pump pressure ratios and isolating the model from unintended design variable changes, reveals the expected direct relationship driven by the thrust and throat area as shown in Figure 5.14.

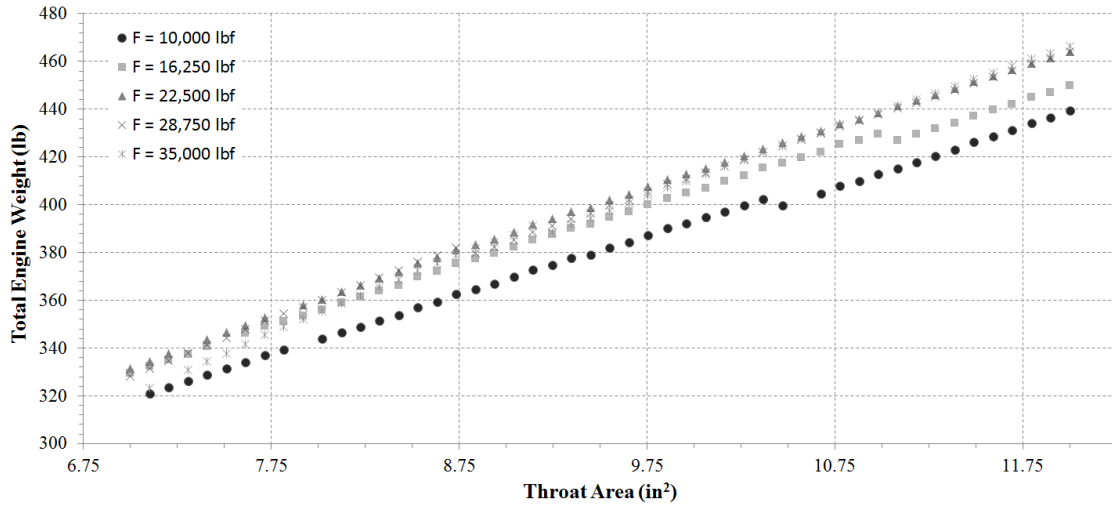


Figure 5.14: Total Engine Weight Variation with Throat Area for Five Thrust Levels without the Pressure Profile Converger

The expansion ratio is directly related to the area of the chamber at the throat. This relationship ties the overall engine diameter, and in turn the engine weight, to the expansion ratio in a direct relationship, Figure 5.15 [24].

The “Responses to Chamber Length” trade study explored the relationship between total engine weight and the chamber length, producing interesting results (design variable chamber length, second design variable expansion ratio, Table 5.8). It is clear there should be a direct relationship between the chamber length and the engine weight given the volume of material comprising the engine walls is directly related to the chamber length. As expected, the results of this trade study, shown in Figure 5.16, indicated shorter engines are lighter than longer engines across the range of expansion ratios considered. Additionally, larger expansion ratios led to a larger impact for increases in chamber length.

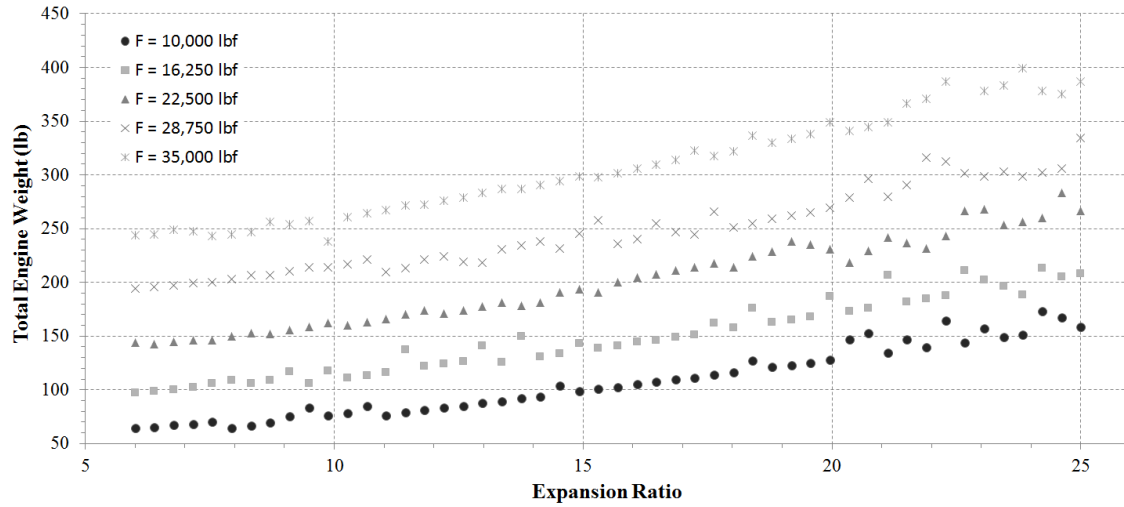


Figure 5.15: Total Engine Weight Variation with Expansion Ratio for Five Thrust Levels

Table 5.8: Responses to Chamber Length Trade Study Design

Variable	Low	High	Levels
Chamber Length (in)	6.5	20	50
Expansion Ratio	6	25	5

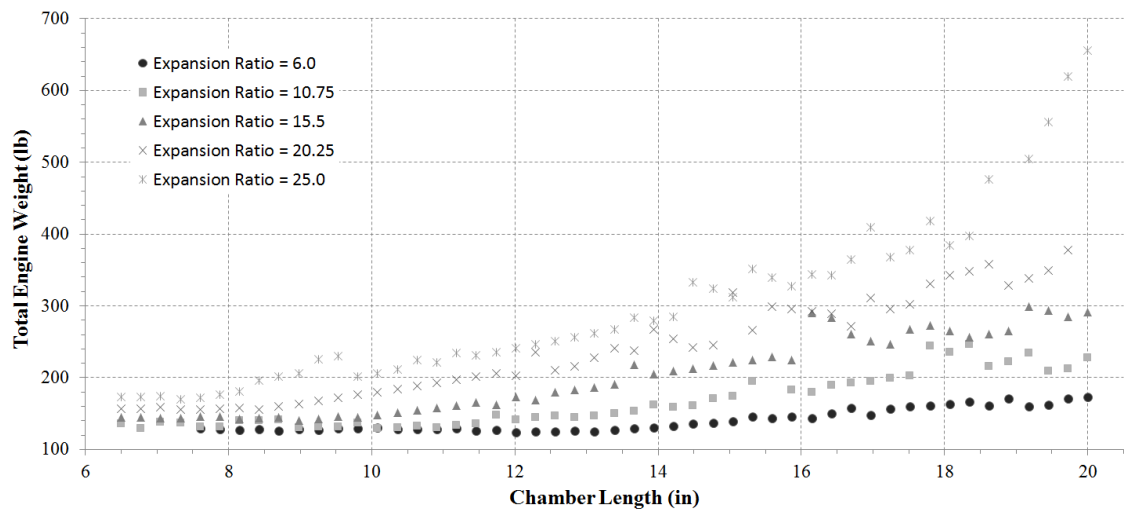


Figure 5.16: Total Engine Weight Variation with Chamber Length for Five Expansion Ratios

The trade study “Responses to Characteristic Length” looked at the relationship between total engine weight and the characteristic length. The design variable in this pairwise relationship was the characteristic length. The second design variable for this trade study was the expansion ratio (Table 5.9).

Table 5.9: Responses to Characteristic Length Trade Study Design

Variable	Low	High	Levels
Characteristic Length (in)	35	100	50
Expansion Ratio	6	25	5

The characteristic length, shown in Equation (5.10), is the ratio of the chamber volume to the throat area. Typical values for characteristic length vary from 30 inches to 100 inches. Generally, smaller values for characteristic length lead to smaller, and lighter weight, engines. However, there is a minimum acceptable value for characteristic length for a given propellant combination based on the combustion residence time, below which the combustion will not be complete. For chambers with a constant cylindrical cross-section, the relationship between the characteristic length and the chamber volume leads to a direct relationship between the characteristic length and the chamber diameter [5].

$$L^* = V_c/A_t \quad (5.10)$$

However, for the DEAN, the chamber diameter is not related to the characteristic length. Instead, the chamber diameter is determined by the expansion ratio and the throat area. The characteristic length determines the diameter of the aerospike within the chamber. This inverse relationship is shown in Figure 5.17. Increases in chamber volume due to increases in the characteristic length (with the chamber diameter fixed) must be accounted for by decreases in the aerospike diameter. These decreases can be dramatic, with a

decrease in characteristic length of 65 inches resulting in an increase in the space between the chamber and aerospike walls of 1.6 inches for the base trade study design.

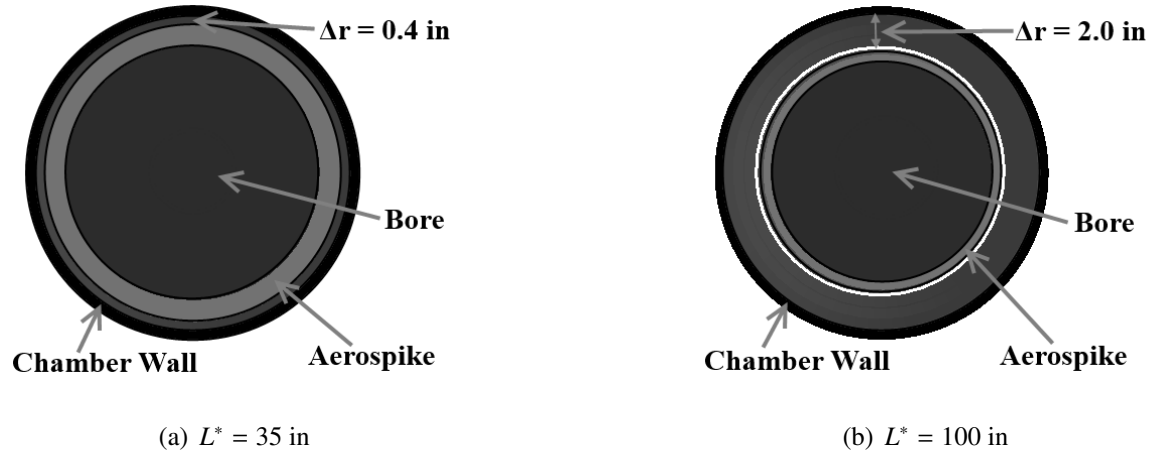


Figure 5.17: Impact of Characteristic Length on DEAN Geometry

The engine weight decreased initially and then followed the expected direct relationship with the characteristic length, Figure 5.18. Inspection of the aerospike geometry data in the trade study results showed the cause of the initial decrease in engine weight. The results in Figure 5.19 show the aerospike wall thickness varied with characteristic length, first decreasing over an initial range of characteristic lengths, then settling to a constant value. This transition to a constant wall thickness was the result of competing design objectives in the structural jacket sizing in the simulation. The first objective is to minimize the wall thickness based on the stresses in the wall as calculated by Equation (5.11) and Equation (5.12). The second objective is to create a uniform bore in the aerospike to simplify manufacturing while reducing the weight of the aerospike by removing unnecessary material. As the characteristic length increases, the driving factor between these two objectives switched from minimizing the wall thickness to simplifying the manufacturing, leading to a constant wall thickness.

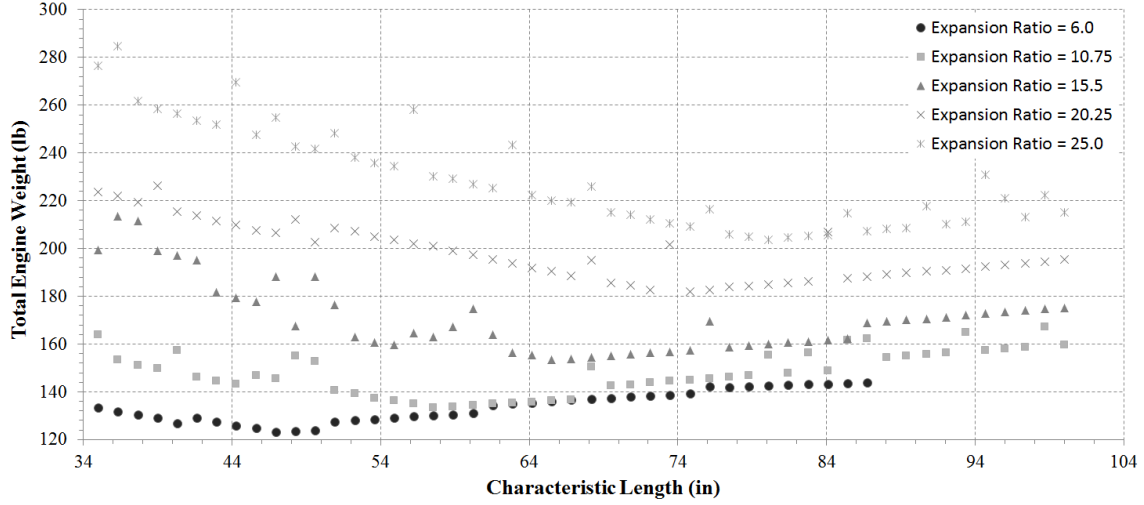


Figure 5.18: Total Engine Weight Variation with Characteristic Length for Five Expansion Ratios

$$\sigma_t = \frac{p_i r_i^2 - p_o r_o^2 - r_i^2 r_o^2 (p_o - p_i) / r^2}{r_o^2 - r_i^2} \quad (5.11)$$

$$\sigma_r = \frac{p_i r_i^2 - p_o r_o^2 + r_i^2 r_o^2 (p_o - p_i) / r^2}{r_o^2 - r_i^2} \quad (5.12)$$

Further inspection of the results indicated larger expansion ratios lead to thicker aerospikes as shown in the figure. This result is driven by stresses in the wall. The larger expansion ratios led to larger aerospoke radii, and larger radii led to higher stresses in the aerospoke wall. The structural jacket sizing analysis compensated for the increased stresses by increasing the wall thickness.

The transitions to constant values for aerospoke thickness corresponded to the transition in the total engine weight from an inverse relationship with the characteristic length to a direct one. These results indicate the weight savings from the reduced

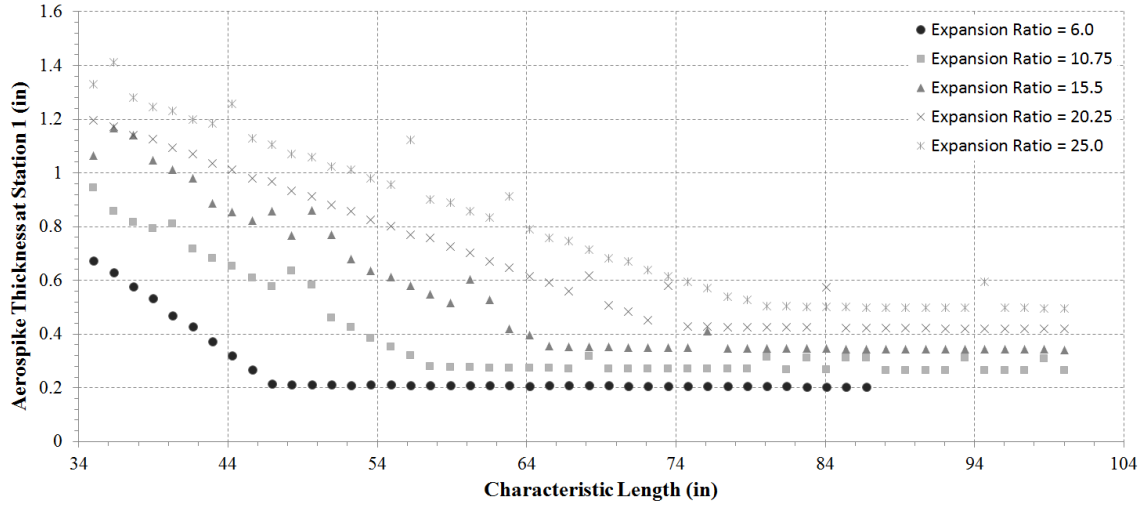


Figure 5.19: Aerospike Thickness Variation with Characteristic Length for Five Expansion Ratios

aerospike wall thickness exceeded the weight growth otherwise associated with increase in characteristic length and explain the observed deviation from expected relationship.

The DEAN simulation predicted weight is consistent with liquid rocket engine theory with respect to throat area, expansion ratio, chamber length, and characteristic length. The study of the throat area relationship demonstrated the impact of scaling the turbopumps for each design. Also, studying the characteristic length demonstrated the differences between the DEAN's chamber design and traditional constant cross-section cylindrical chambers.

5.4.2 Scalability of the DEAN.

The common unanswered question in previous generations of DEAN research was “is the DEAN scalable?”. Previous results were unclear regarding how flexible the DEAN architecture was in terms of varying geometry and performance. Using the improvements in the current DEAN simulation, the trade studies above demonstrated the DEAN is quite scalable. Table 5.10 summarizes the ranges for the DEAN's key design variables. The

results also demonstrate the DEAN exceeds the RL10 in terms of both performance and packaging.

Table 5.10: Design Variable Ranges

Design Variable	Low Value	High Value
Vacuum Thrust (lbf)	10,000	35,000
Expansion Ratio	6.0	25.0
Throat Area (in ²)	7.0	12.0
Oxidizer-to-Fuel Ratio	5.0	8.0
Chamber Length (in)	6.5	20.0
Characteristic Length (in)	35	100

Further, the current generation DEAN model is capable of exploring the full range of DEAN designs. Over the course of six trade studies and 1500 runs, the DEAN simulation had a reliability of 98.7% as shown in Table 5.11.

Table 5.11: DEAN Simulation Reliability

Trade Study Name	Runs	Failed Runs	Reliability
Responses to Vacuum Thrust	250	0	100.0%
Responses to Throat Area	250	2	99.2%
Responses to Expansion Ratio	250	1	99.6%
Responses to Oxidizer-to-Fuel Ratio	250	0	100.0%
Responses to Chamber Length	250	6	97.6%
Responses to Characteristic Length	250	10	96.0%
All Runs	1500	19	98.7%

5.4.3 DEAN Thrust-to-Weight Ratio and Turbopump Power.

Comparing previous results to the RL10 confirmed expectations about the DEAN architecture in terms of thrust-to-weight and the power available to the turbopumps. The three designs from previous DEAN research were reevaluated using the fourth generation DEAN model to generate a consistent set of data to compare to the RL10 family of engines. Table 5.12 lists the thrust-to-weight ratio and the LH2 pump power for three generations of the RL10 and the first three generations of the DEAN. In each comparison, the DEAN exhibited the expected increase in pump power from the second cooling loop. This increase is dramatic, yielding over four times the power of the RL10A-3, while still remaining under the 5900 HP demonstrated by Pratt and Whitney as part of the an upper stage demonstrator engine [25]. Similarly, the DEAN showed the expected improvements in thrust-to-weight ratio over the RL10 family. Further, while previous DEAN results fell short of the vacuum specific impulse of the RL10, results from the performance trade studies above demonstrated the DEAN can match or exceed the RL10 with the appropriate designs.

Table 5.12: Comparison of RL10 Engine Family to DEAN Designs

Engine	F_{Vac} (lbf)	I_{sp-Vac} (s)	T/W	LH2 Pump Power (HP)
RL10A-3 [24, 25]	16,500	444.4	53.2	789
RL10A-4 [24]	20,800	448.9	56.2	-
RL10B-2 [24]	24,750	465.5	37.3	-
Generation 1 DEAN	57,231	412.9	138.6	4562
Generation 2 DEAN	50,900	422.8	194.1	3688
Generation 3 DEAN	50,161	425.7	163.9	3340

5.5 Conclusion

The results of this study support four key conclusions. First, the DEAN architecture, utilizing an aerospike nozzle to implement a dual-expander cycle, is feasible and delivers improved performance over single expander cycle engines in a compact package. The DEAN architecture consistently achieved thrust-to-weight ratios well in excess of the design goal of 106.5 and vacuum thrust levels of 50,000 lbf. These designs were also compact, ranging in length from 27 to 38 inches.

Second, the DEAN's simulation is consistent with the scientific and engineering principles of rocket propulsion. A series of six trade studies over a wide range of designs and performance levels verified its performance.

Third, the DEAN exceeds the performance of the RL10 for comparable thrust levels. Comparison of previous generation designs to the RL10 showed the DEAN's second cooling loop gives it more than four times the pumping power of the RL10A-3 and more than twice the thrust-to-weight ratio of the RL10A-4 and RL10B-2. Trade study results showed the increased pumping power gives the DEAN more than twice the chamber pressure of the RL10A-4 and RL10B-2 while being less than half the length.

Fourth, the DEAN architecture is ready for mission specific comparisons to existing upper stage engines. Trade studies have verified the DEAN's architecture and demonstrated its advantages over single expander cycle engines. Further, the results of these trade studies have also demonstrated the current DEAN simulation has the required flexibility and robustness for use in engineering optimization studies.

VI. Fourth Generation DEAN Materials

6.1 Introduction

One of the key aspects of the third generation DEAN research was an initial study on the impact of material selection on the DEAN's thrust-to-weight ratio. This study was performed by J. Hall for the third generation DEAN design and was implemented by parametrically varying the material selection for each of the seven engine components in the DEAN model which have material options. This study focused on the materials selection for a single DEAN design. The results of the study indicated the chamber should use silicon carbide for its cooling jacket and aluminum 7075 T6 for its structural jacket. The aerospike nozzle should be fabricated from a single material, oxygen-free copper (C10100) [4].

With the fourth generation DEAN simulation's ability to model a wide range of engine designs, it is critical to ensure the DEAN's materials selection performs well across the range of designs under consideration. This chapter covers the process and results used in an updated materials selection study. This study began by optimizing the cooling channel designs for both the chamber and aerospike cooling channels to ensure the cooling channels provide a high degree of cooling while minimizing the fluid Mach numbers in the channels over a wide range of engine designs. The study then examined the material choices for the DEAN using designs of experiments covering a variety of engine designs with significant influence on component weight.

6.2 Background

6.2.1 Cooling Channel Design Constraints.

From the beginning DEAN research has targeted reusability as one of its objectives. During the first generation DEAN research, this objective was met by constraining the

cooling jacket wall temperatures to 50% of the melting point for the selected material [2]. The third generation DEAN research indicated this requirement was overly conservative and so it was modified to 60% of the melting point [4].

Constraints on the maximum Mach number in the cooling channels have been consistently used to ensure shock waves do not form in the cooling channels, increasing the risk of catastrophic failure. The requirements are the maximum Mach number in the LOX cooling channels must be less than or equal to 0.6 and the maximum Mach number in the LH2 cooling channels must be less than or equal to 0.9 [2].

6.2.2 Third Generation DEAN Materials Selection.

The materials selection study for the third generation DEAN design consisted of a number of trade studies over the materials options for the DEAN. The objectives of these trade studies were to identify the components with the greatest contribution to engine weight and to select the best combination of materials for the DEAN in order to maximize the thrust-to-weight ratio while considering reusability and manufacturability.

The results of these initial studies showed the chamber and aerospike structural jackets consistently generated the greatest change in the thrust-to-weight ratio for changes in material selection. The results also indicated the aerospike tip and plumbing have very little influence on the total engine weight, and that they should be set to a reasonable material selection in future optimization studies [4].

Hall concluded his materials studies by considering reuseability and manufacturability. Plotting the variation of the wall temperatures for the chamber and aerospike cooling jackets with the material options showed which materials met the reuseability constraint of maintaining wall temperatures less than 60% of their melting point. From this data, Hall concluded the copper (pure and oxygen-free) was a viable material for the aerospike cooling jacket and silicon carbide was a viable material for both the chamber and aerospike cooling jackets. Hall's consideration of manufacturing concerns led him to conclude the

aerospike should be manufactured from a single material to simplify the machining processes and material interfaces. Further testing indicated the only material option for the aerospike was oxygen-free copper. Table 6.1 summarizes the final material selection for the third generation DEAN [4].

Table 6.1: Generation 3 DEAN Materials Selection [4]

Component	Material
Chamber Structural Jacket	Aluminum 7075-T6
Chamber Cooling Jacket	Silicon Carbide
Aerospike Structural Jacket	Oxygen-Free Copper
Aerospike Cooling Jacket	Oxygen-Free Copper
Aerospike Tip	Oxygen-Free Copper
LOX Plumbing	INCONEL 718
LH2 Plumbing	INCOLOY 909

6.2.3 Cooling Channel Design.

The effectiveness of cooling jackets in liquid rocket engines is driven by the design of the cooling channels. The number of channels and their cross-sectional areas are the two primary factors influencing cooling channel performance. They directly influence the area in contact with the cooling fluid. These two factors are specified by the channel ratio and aspect ratio design variables in the model [2].

In the first generation DEAN research, Martin used varying aspect ratios along the length of the cooling channels to balance the cooling needs with the maximum Mach number constraints. In both cooling jackets, Martin selected low aspect ratios (shorter channels, smaller cross-sectional area) at the throat to increase the cooling rate and higher aspect ratios (taller channels, larger cross-sectional areas) at the end of the cooling jacket

to maintain a velocity below the maximum allowable Mach number. The smaller cross-sectional area in the low aspect ratio regions increases the fluid velocity and in turn the power required to pump the fluid. This increase in required pump power drives the solver in the cycle model toward designs yielding more power from the turbine by increasing the amount of heat extracted from cooling the engine, effectively increasing the cooling rate in those regions. The larger cross-sectional areas in the high aspect ratio regions reduce the velocity of the fluid and account for the decrease in density (increase in volume) caused by heating the fluid. Combined, these two effects ensure the fluid stays below its Mach number limit, preventing catastrophic failure of the engine [2].

The parametrization of the second and third generation DEAN models did not include design variables for the cooling channels. In the second generation model, the author used Martin's aspect ratio schedules and computed the number of channels based on the ratios in Martin's design. In the third generation model, Hall used constant aspect ratios along the length of each cooling channel and again computed the number of channels based on the ratios in Martin's design.

The fourth generation DEAN model includes parametrization for the cooling channels. Eight design variables, four for each cooling jacket, control the number of channels and the aspect ratios for the cooling channels, Table 6.2. The aspect ratio schedule generally follows Martin's design. Note: when the adjustment variables for a given cooling jacket are set to a value of 1.0, the resulting cooling channels will use constant aspect ratios. This mode of operation is included to support analyzing designs developed using the third generation model.

Table 6.2: Cooling Channel Design Variables

Variable	Description
Chamber Throat AR	Aspect ratio of chamber cooling channels at the throat
Chamber Stations Adjustment	Aspect ratio multiplier for chamber cooling channels
Chamber Station 5 Adjustment	Aspect ratio multiplier for chamber cooling channels at station 5
Chamber Cooling Channels Ratio	Ratio of the number of chamber cooling channels to the chamber circumference at the throat
Nozzle Throat AR	Aspect ratio of aerospike cooling channels at the throat
Nozzle Station 1 Adjustment	Aspect ratio multiplier for aerospike cooling channels at stations 1 and 2
Nozzle Station Spike Adjustment	Aspect ratio multiplier for aerospike cooling channels at stations 7 and 8
Aerospike Cooling Channels Ratio	Ratio of the number of aerospike cooling channels to the nozzle circumference at the throat

6.3 Designing the DEAN Cooling Channels for Fourth Generation DEAN Model

The cooling channel design study was conducted using a series of designs of experiment (DOE), parametric studies, and optimization studies. All of these trade studies used a common base design shown in Table 6.3. The cooling channel design study was conducted in three phases. The first phase used three designs of experiments to identify the design variables with significant influence on the cooling channel performance. The second phase used a series of parametric studies and optimization studies to determine values for the key channel design variables, yielding designs for the cooling channels performing well across a range of engine designs. Finally, the third phase verified the results of the second phase by testing them at four engine designs representing a cross section of the DEAN trade space.

Table 6.3: Cooling Channel Design Study Base Design

Variable	Value
Expansion Ratio	17.5
Throat Area (in ²)	9.0
Chamber Length (in)	12
Characteristic Length (in)	50
Vacuum Thrust (lbf)	20,000
Oxidizer-to-Fuel Ratio	6.0
Chamber Throat AR	1.3
Chamber Stations Adjustment	1.0
Chamber Station 5 Adjustment	1.0
Chamber Cooling Channels Ratio	25.1
Nozzle Throat AR	0.54
Nozzle Station 1 Adjustment	1.0
Nozzle Station Spike Adjustment	1.0
Aerospike Cooling Channels Ratio	15.5
Cooling Geometry Option	Channel Cover + Structural Jacket
Chamber Structural Jacket Material	Silicon Carbide
Chamber Cooling Jacket Material	Silicon Carbide
Aerospike Structural Jacket Material	Silicon Carbide
Aerospike Cooling Jacket	Silicon Carbide
Aerospike Tip Material	Silicon Carbide
LOX Pipe Material	INCONEL 718
LH2 Pipe Material	INCOLOY 909

6.3.1 Phase I - Identify Key Design Variables.

In order to identify the key design variables, three distinct designs of experiments (DOE 1, DOE 2, DOE 3) were employed. All three designs of experiments were based on the trade studies used in the system level verification tests. The ranges for the design variables were developed to maximize the range of designs considered and the reliability of the model execution. All trade studies used a randomized space filling design covering 250 points made up of a 125 Design Explorer Orthogonal Array with 125 additional points from a Latin-Hypercube unless otherwise specified. The results of the three DOEs are shown in Figure 6.1, Figure 6.2, and Figure 6.3 below. The rows list the design variables and the columns list the response variables. Cells with an 'X' in them indicate the design variable for that row has a significant influence on the response variable in that column. The relationships were determined using ModelCenter's Variable Influence Profiler. The Variable Influence Profiler uses Analysis of Variance methods over a Kriging model of the data to compute variable importance levels [67].

The objective of DOE 1 (Table 6.4) was to determine which system level design variables have significant influence on the heat transfer (i.e. wall temperature) and maximum Mach numbers in the cooling channels. The influence of the system level design variables on sizing of the structural jackets and plumbing was also investigated for use in the materials selection trade studies. These key system level design variables will be used in later trade studies to create the range of engine configurations for both designing the cooling channels and selecting materials for the primary DEAN components.

The results of DOE 1 are shown in Figure 6.1. The vacuum thrust and throat area showed considerable influence on the wall temperatures for both the chamber and the aerospike. The vacuum thrust and expansion ratio influenced the maximum Mach numbers most significantly. Historically, ensuring the cooling channels meet the maximum Mach number constraints is easier than the wall temperature constraints. So the remaining designs

of experiments emphasized engine designs which drive the wall temperatures by varying vacuum thrust and throat area.

Table 6.4: Design Variables for Cooling Channel Design Study DOE 1 - Influence of System Level Design Variables

Variable	Low	High	Levels
Expansion Ratio	6	25	Space Filling
Throat Area (in ²)	7	10	Space Filling
Chamber Length (in)	10	15	Space Filling
Characteristic Length (in)	35	75	Space Filling
Vacuum Thrust (lbf)	10,000	35,000	Space Filling
Oxidizer-to-Fuel Ratio	5	8	Space Filling

	LH2 Plumbing Weight	LOX Plumbing Weight	Aerospike Structural Jacket Thickness	Chamber Structural Jacket Thickness	Aerospike Wall Temperature	Chamber Wall Temperature	LH2 Maximum Mach Number	LOX Maximum Mach Number
Expansion Ratio	X	X	X	X			X	
Throat Area					X	X		
Chamber Length								X
Characteristic Length							X	
Vacuum Thrust	X	X	X	X	X	X		X
Oxidizer-to-Fuel Ratio							X	

Figure 6.1: DEAN Cooling Channels Variable Influence Chart

DOE 2 targeted the influence of the cooling channel design variables on the LOX cooling circuit. The four cooling channel design variables are the chamber throat AR, the chamber stations adjustment, the chamber station 5 adjustment, and the chamber cooling channels Ratio. Ranges for these variables are shown in Table 6.5.

Table 6.5: Design Variables for Cooling Channel Design Study DOE 2 - Chamber Channel Design Study

Variable	Low	High	Levels
Throat Area (in ²)	7	10	Space Filling
Vacuum Thrust (lbf)	10,000	35,000	Space Filling
Chamber Throat AR	1.2	4.0	Space Filling
Chamber Stations Adjustment	0.75	2.0	Space Filling
Chamber Station 5 Adjustment	0.75	2.9	Space Filling
Chamber Cooling Channels Ratio	10	20	Space Filling

The results of DOE 2 are shown in Figure 6.2. The station 5 adjustment had little impact on the wall temperature or maximum Mach number. Additionally, the throat aspect ratio and the chamber cooling channels ratio had significant influence on both the wall temperature and the maximum Mach number in the LOX cooling channels. The chamber stations adjustment only had significant influence on wall temperature.

	LOX Maximum Mach Number	Chamber Wall Temperature
Chamber Throat AR	X	X
Chamber Stations Adjustment		X
Chamber Station 5 Adjustment		
Chamber Cooling Channels Ratio	X	X

Figure 6.2: DEAN Chamber Cooling Channels Variable Influence Chart

DOE 3 focused on the design variables for the aerospike cooling channels and their influence. These variables are the nozzle throat AR, the nozzle station 1 adjustment, the nozzle station spike adjustment, and the aerospike cooling channels ratio (Table 6.6). DOE 3 (Figure 6.3) indicates the spike adjustment had little impact on the wall temperature or maximum Mach number. Additionally, the throat aspect ratio and the aerospike cooling channels ratio had significant influence on both the wall temperature and the maximum Mach number in the LH2 cooling channels, while the nozzle station 1 adjustment only had significant influence on wall temperature.

Table 6.6: Design Variables for Cooling Channel Design Study DOE 3 - Aerospike Channel Design Study

Variable	Low	High	Levels
Throat Area (in ²)	7	10	Space Filling
Vacuum Thrust (lbf)	10,000	35,000	Space Filling
Aerospike Throat AR	0.5	1.4	Space Filling
Aerospike Station 1 Adjustment	1.0	13	Space Filling
Aerospike Station Spike Adjustment	1.0	5.0	Space Filling
Aerospike Cooling Channels Ratio	5.0	15.0	Space Filling

	LH2 Maximum Mach Number	Aerospike Wall Temperature
Nozzle Throat AR	X	
Nozzle Station 1 Adjustment		X
Nozzle Station Spike Adjustment		
Aerospike Cooling Channels Ratio	X	X

Figure 6.3: DEAN Aerospike Cooling Channels Variable Influence Chart

6.3.2 Phase II - Determine Values for Design Variables.

The results of DOE 2 and DOE 3 were used to structure the process of determining values for the cooling channel design variables by working from the least complex decisions to the most complex decisions. The least complex decisions are for the two

variables which do not influence either the wall temperatures or the maximum Mach numbers, namely the chamber station 5 adjustment and the aerospike station spike adjustment. Both variables were arbitrarily set to 1.0 since they have no impact on the response variables.

The next most complex decisions concern the variables only influencing one response, namely the chamber stations adjustment and the aerospike station 1 adjustment. Both variables only have significant influence on wall temperatures. A series of parametric studies were run over each of these variables across a number of engine designs. The results for all of these parametric variables indicated the same trends, Figure 6.4 and Figure 6.5. These trends show a range of values producing a minimum wall temperature and a minimum value for the maximum Mach number.

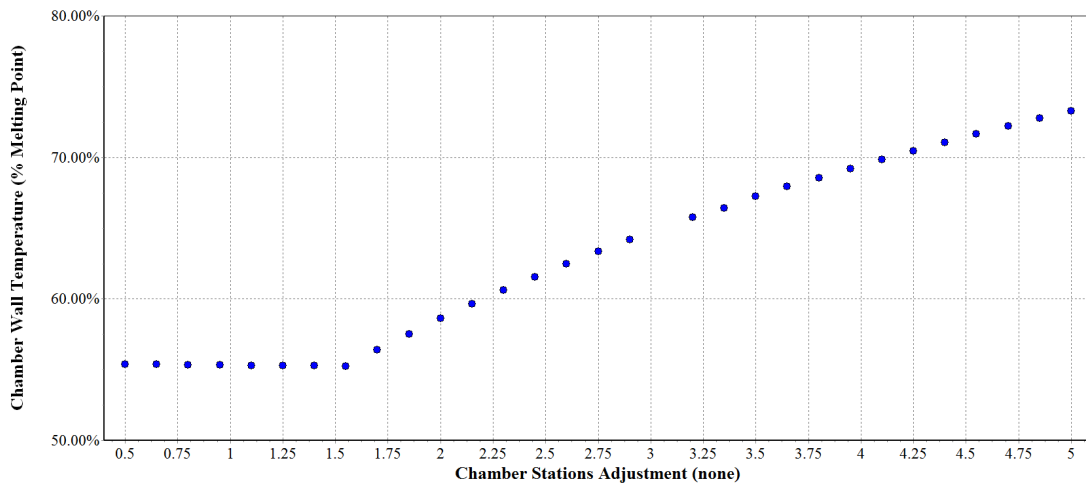


Figure 6.4: Chamber Wall Temperature Variation with Chamber Stations Adjustment

From these trends, values were selected to ensure the channel designs minimized the wall temperature and maximum Mach number for a wide range of engine designs. For the

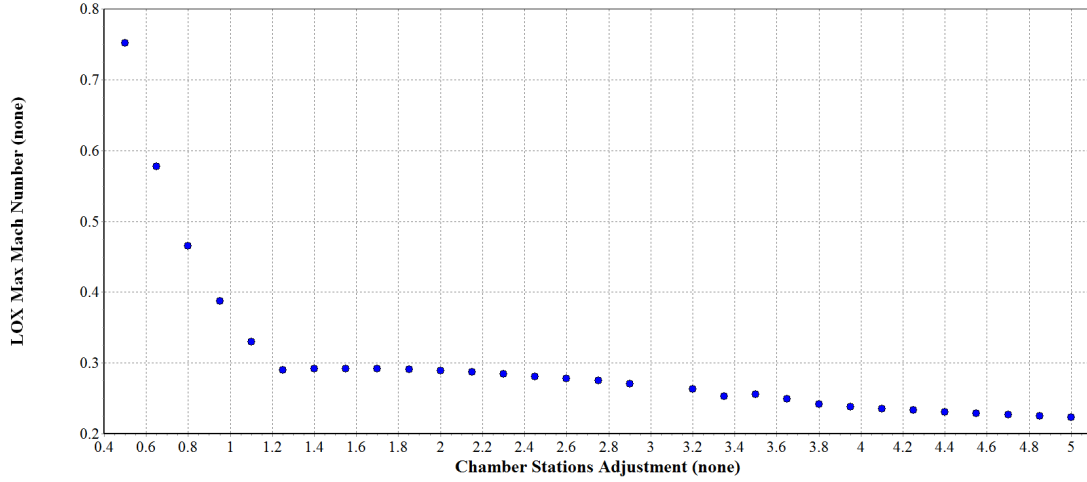


Figure 6.5: Chamber Maximum Mach Number Variation with Chamber Stations Adjustment

chamber, this analysis led to a value of 1.2 for the chamber stations adjustment. For the aerospike, this analysis led to a value of 1.7 for the aerospike station 1 adjustment.

The final four values, two for each set of cooling channels, involve the most complex decisions. These variables influence both wall temperatures and the cooling channel Mach numbers and for some values interact with each other. To address this complexity, the values for these variables were determined through a pair of sequentially run optimization problems. Each problem minimized the wall temperature and the maximum Mach numbers by adjusting the related pair of design variables. No constraints were applied to these optimization problems due to the significant influence of system level design variables on the specific values for both the wall temperature and the maximum Mach numbers. Equation (6.1) gives the mathematical definition of the optimization problem for the chamber cooling channels and Equation (6.2) gives the mathematical definition of the optimization problem for the aerospike cooling channels. The wall temperature was given twice the weight of the maximum Mach number since it is historically the more challenging

constraint to enforce and the maximum values for the channel ratios were chosen to ensure the minimum channel widths meet or exceed the required minimum value of 0.02 in based on manufacturing assumptions of precision machining using a minimum tool size of 1/64 inch making two passes (one for each wall of the channel).

$$\text{Find } \mathbf{X} = \left\{ \begin{array}{l} \text{Chamber Throat AR} \\ \text{Chamber Cooling Channels Ratio} \end{array} \right\} \text{ which minimizes}$$

$$f(\mathbf{X}) = 2T_{\text{chamber_wall}}(\mathbf{X}) + \text{Mach}_{\text{chamber_max}}(\mathbf{X})$$

where

$$\left\{ \begin{array}{l} 0.5 \\ 10.0 \end{array} \right\} \leq \mathbf{X} \leq \left\{ \begin{array}{l} 5.0 \\ 25.0 \end{array} \right\}$$

(6.1)

$$\text{Find } \mathbf{X} = \left\{ \begin{array}{l} \text{Aerospike Throat AR} \\ \text{Aerospike Cooling Channels Ratio} \end{array} \right\} \text{ which minimizes}$$

$$f(\mathbf{X}) = 2T_{\text{aerospike_wall}}(\mathbf{X}) + \text{Mach}_{\text{aerospike_max}}(\mathbf{X})$$

where

$$\left\{ \begin{array}{l} 0.25 \\ 5.0 \end{array} \right\} \leq \mathbf{X} \leq \left\{ \begin{array}{l} 2.0 \\ 15.5 \end{array} \right\}$$

(6.2)

The two optimization problems above were implemented in ModelCenter using Optimization Tool components. The Optimization Tool component is a built-in ModelCenter component which uses industry standard optimization algorithms to create a loop which drives model elements toward specified objectives. Figure 6.6 and Table 6.7 show the cooling channel optimization model. This model runs the optimization problems in series. The loop labeled B implements Equation (6.1) and the loop labeled C implements Equation (6.2).

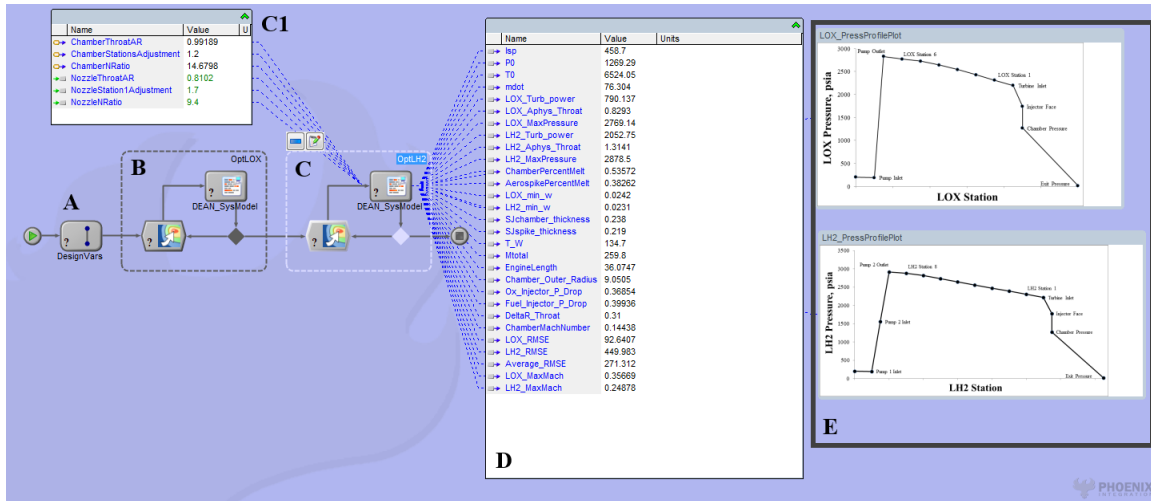


Figure 6.6: Channel Design Optimization Model

Each embedded optimization loop consists of an Optimization Tool component and an embedded copy of the DEAN system model. The cooling channel optimization model uses the values from the Design Variables component (labeled A) to ensure DEAN system models in the two optimization loops are synchronized to the same design. The optimization model then solves for the chamber cooling channels design using the Chamber Optimization Loop (labeled B). The optimized chamber cooling channel design is used in the aerospike nozzle cooling channel optimization study (labeled C). The results of the cooling channel optimization model are displayed in the Data Monitor (labeled D) and the pressure level renderings (labeled E).

The model was run using the base design point in Table 6.2 for several starting values of the cooling channel design variables. The results from the set of model runs clustered around a single set of values, which were used to determine the cooling channel design variable values shown in Table 6.8.

Table 6.7: Cooling Channel Optimization Model Components

Label	Name	Description
A	Design Variables	DEAN system level design variables describing the DEAN design for both optimization loops
B	Chamber Opt Loop	embedded optimization study to size the cooling channels for the chamber
C	Nozzle Opt Loop	embedded optimization study to size the cooling channels for the aerospike nozzle
C1	Chamber Opt Results	ModelCenter Data Monitor displaying the results of the chamber optimization loop
D	Optimization Results	ModelCenter Data Monitor displaying the final results of the two optimization studies
E	Pressure Profile Plots	pressure profiles for the LOX and LH2 expander cycles post cooling channel optimization

Table 6.8: Final Cooling Channel Design Variable Values

Variable	Value
Chamber Throat AR	1.0
Chamber Stations Adjustment	1.2
Chamber Station 5 Adjustment	1.0
Chamber Cooling Channels Ratio	14.4
Nozzle Throat AR	0.86
Nozzle Station 1 Adjustment	1.7
Nozzle Station Spike Adjustment	1.0
Aerospike Cooling Channels Ratio	9.4

6.3.3 Phase III - Verification.

The results of the second phase were verified through testing and comparison to the previous designs. The testing used four engine designs representing a cross section of the DEAN trade space. These engines vary in vacuum thrust from approximately 16,000 lbf to 35,000 lbf and meet the physical constraints of the DEAN model. For each engine, the design was loaded into the optimization model from the second phase and the model was run to find updated cooling channel design variable values. The results of these optimization studies were compared with the results using the second phase design, Table 6.9. In all four cases, the verification run results yield slight to no reduction in the maximum Mach numbers for the cooling channels with corresponding increases in the wall temperatures. Given the higher priority of reducing the wall temperatures, these results were not improvements, confirming the proposed cooling channel designs produce universally high quality cooling channels.

Table 6.10 compares the updated cooling channel designs with Martin's original designs. In the chamber cooling jacket, fewer channels with lower aspect ratios are used in the updated design to improve the thermal performance. In the aerospike cooling jacket, a greater number of channels with a more consistent set of aspect ratios are used to balance out the thermal performance along the entire length of the engine. These results are consistent with the updated designs' emphasis on thermal performance, which further verifies the updated designs.

Table 6.9: Cooling Channel Design Verification Results

F_{Vac} (lbf)	ϵ	A_t (in ²)	$T_{Cham.Wall}$ (%)	$Mach_{LOX.Max}$	$T_{Spike.Wall}$ (%)	$Mach_{LH2.Max}$
16,250	6.0	7.0				
		As Designed Run	56.9	0.24	55.9	0.18
		Verification Run	58.5	0.16	56.8	0.10
22,500	6.0	10.75				
		As Designed Run	52.2	0.29	35.4	0.28
		Verification Run	53.4	0.22	38.7	0.17
28,750	13.0	10.75				
		As Designed Run	57.6	0.31	57.4	0.21
		Verification Run	57.4	0.31	57.6	0.19
35,000	13.0	14.5				
		As Designed Run	53.7	0.35	38.6	0.25
		Verification Run	53.6	0.36	38.3	0.25

Table 6.10: Cooling Channel Design Comparison

Station	Chamber		Aerospike	
	Martin	As Designed	Martin	As Designed
Number of Channels				
-	785	654	314	413
Aspect Ratios				
1	3.57	1.50	5.00	1.46
2	2.86	1.20	5.00	1.46
3	2.86	1.20	3.20	1.26
4	2.86	1.20	1.71	1.06
5	3.33	1.00	0.67	0.86
6	3.00	1.00	0.57	0.86
7	-	-	0.67	0.86
8	-	-	1.33	0.86

6.4 Materials Selection Study

The materials selection study was carried out as a series of trade studies over the material options for each relevant DEAN component. The objective of the materials selection trade studies was to find the “best materials selection” for the overall DEAN architecture. The “best materials selection” was defined as the materials selection yielding consistently low weight engines over a wide range of designs. Using this definition, optimal materials are ones producing tightly clustered data points with low values on weight variation with material selection plots. Conversely, materials are not considered optimal if they produce a wide range of engine weights, even when some of those weights

may be lower than optimal materials. This distinction ensures the selected materials are globally optimal instead of locally optimal depending on the selected DEAN design.

The results of the cooling channel design study drove the materials selection study. First the new cooling channel designs were incorporated into a base design for the trade studies in the materials selection study. This design is summarized in Table 6.11.

Next, the results of the cooling channel design studies, indicating which design variables have significant influence on the cooling jacket wall temperatures, the structural jacket sizes, and the weight of the plumbing, were used to design the individual materials selection trade studies to ensure a wide range of relevant engine designs were considered. The throat area and the vacuum thrust showed the most influence on the wall temperatures. The expansion ratio and the vacuum thrust had the greatest influence on the structural jacket sizes. Additionally, the cooling channel design studies indicated the expansion ratio and vacuum thrust drive the plumbing weight.

Before beginning the materials selection trade studies, the third generation DEAN material list was filtered to eliminate extraneous material options. This filtering included removal of materials for manufacturing and modeling reasons. Silicon carbide was removed as an option for structural jackets and the aerospike tip to limit the amount of ceramic material required to manufacture the DEAN. The material lists for the aerospike structural jacket and aerospike tip were configured to use the same material for both elements to simplify the manufacturing process and reduce the number of materials in any given DEAN design. Oxygen-free copper was removed as an option for cooling jackets because thermal conductivity was not available over the necessary range of temperatures. Beryllium copper was removed completely as no data was found detailing the temperature impacts on ultimate and yield strengths. Table 6.12 lists the DEAN components and the materials available for each one.

Table 6.11: Materials Studies Base Design

Variable	Value
Expansion Ratio	17.5
Throat Area (in ²)	9.0
Chamber Length (in)	12
Characteristic Length (in)	50
Vacuum Thrust (lbf)	20,000
Oxidizer-to-Fuel Ratio	6.0
Chamber Throat AR	1.0
Chamber Stations Adjustment	1.2
Chamber Station 5 Adjustment	1.0
Chamber Cooling Channels Ratio	14.4
Nozzle Throat AR	0.86
Nozzle Station 1 Adjustment	1.7
Nozzle Station Spike Adjustment	1.0
Aerospike Cooling Channels Ratio	9.4
Cooling Geometry Option	Channel Cover + Structural Jacket
Chamber Structural Jacket Material	Silicon Carbide
Chamber Cooling Jacket Material	Silicon Carbide
Aerospike Structural Jacket Material	Silicon Carbide
Aerospike Cooling Jacket	Silicon Carbide
Aerospike Tip Material	Silicon Carbide
LOX Pipe Material	INCONEL 718
LH2 Pipe Material	INCOLOY 909

Table 6.12: Materials Options for DEAN Components

Component	Materials
Chamber Structural Jacket	Copper, INCOLOY 909, INCONEL 718, INCONEL 625, Alloy 188, Aluminum 7075 T6, Aluminum 2024 T6, Oxygen-Free Copper, Titanium, Cobalt
Chamber Cooling Jacket	Copper, Silicon Carbide, INCOLOY 909, INCONEL 718, INCONEL 625, Alloy 188, Cobalt
Aerospike Structural Jacket & Tip	Copper, INCOLOY 909, Alloy 188, Oxygen-Free Copper, Cobalt
Aerospike Cooling Jacket	Copper, Silicon Carbide, INCOLOY 909, Alloy 188, Cobalt
LOX Plumbing	Copper, INCOLOY 909, INCONEL 718, INCONEL 625, Alloy 188, Oxygen-Free Copper, Cobalt
LH2 Plumbing	Copper, INCOLOY 909, Alloy 188, Oxygen-Free Copper, Cobalt

For each material selection trade study, a design of experiments was configured with a parameter scan of the available materials for the component under consideration. To ensure the results were valid for a wide range of engines, the design of experiments also included the design variables with significant influence on the weight of the component being studied as determined by the cooling channel design studies. These trade studies are technically parameter scans as the material selection is a discrete variable. However, they may be treated as full factorial designs since the trade study tests all available combinations of engine designs.

The chamber cooling jacket material was tested first using the throat area and vacuum thrust to vary engine designs (Table 6.13). Of the material options for the chamber cooling

jacket (Figure 6.7), only one, silicon carbide, consistently yielded values below the melting point, with many of designs falling below the 60% of melting point constraint, indicating silicon carbide is the only viable material option for the chamber cooling channel. This result matches the third generation DEAN results.

Table 6.13: Design Variables for Chamber Cooling Jacket Material Study

Variable	Low	High	Levels
Throat Area (in ²)	7	22	3
Vacuum Thrust (lbf)	10,000	35,000	3
Chamber Cooling Jacket Material	-	-	Parameter Scan

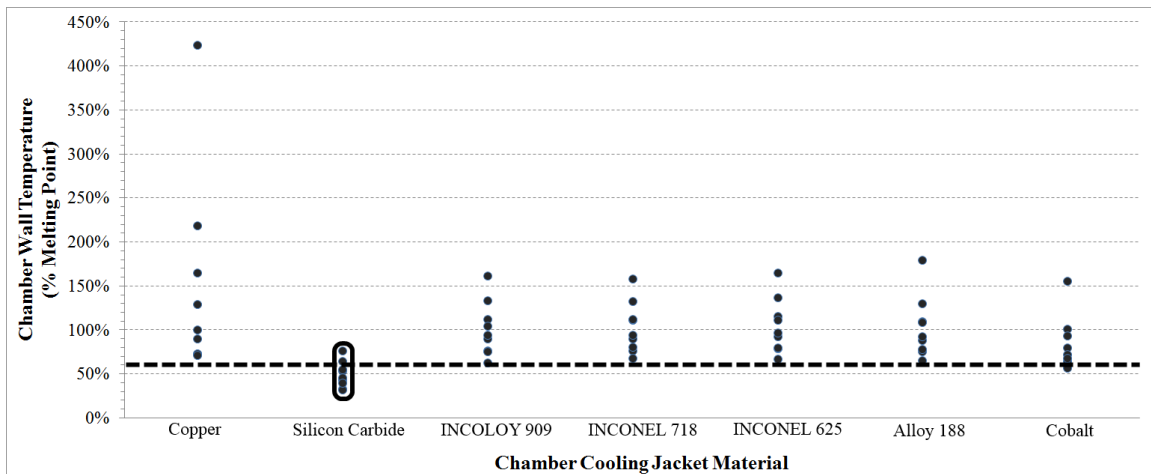


Figure 6.7: Chamber Percent Melting Point Variation with Material for Various Throat Areas and Thrust Levels

The aerospike cooling jacket material was tested next varying the engine designs using the throat area and vacuum thrust (Table 6.14). As with the chamber cooling jacket, the only

material which consistently yielded values below the melting point, with many of designs falling below the 60% of melting point constraint, was silicon carbide, Figure 6.8. This result differs from the third generation DEAN material selection of oxygen-free copper.

Table 6.14: Design Variables for Aerospike Cooling Jacket Material Study

Variable	Low	High	Levels
Throat Area (in ²)	7	22	3
Vacuum Thrust (lbf)	10,000	35,000	3
Aerospike Cooling Jacket Material	-	-	Parameter Scan

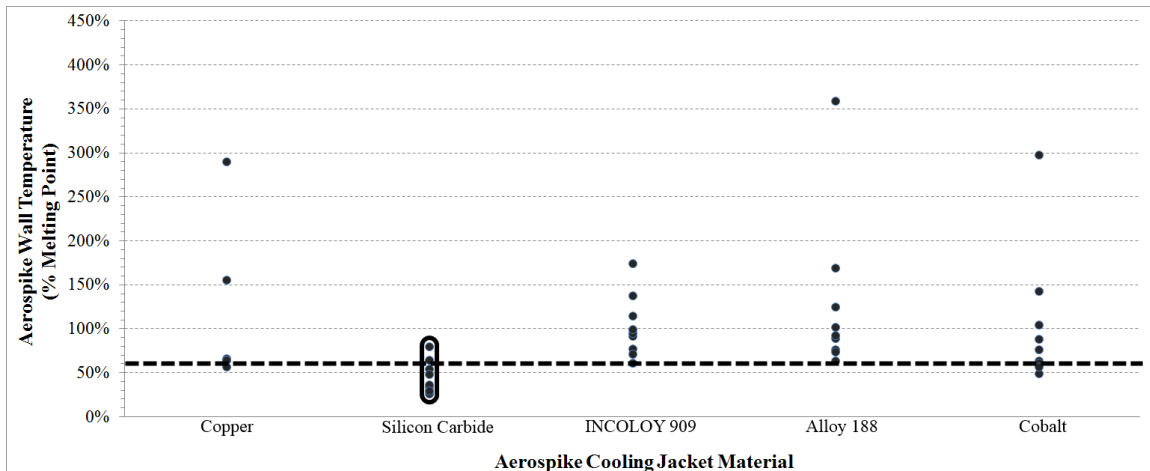


Figure 6.8: Aerospike Percent Melting Point Variation with Material for Various Throat Areas and Thrust Levels

The third material study tested the chamber structural jacket material using the expansion ratio and vacuum thrust to vary engine designs (Table 6.15). Figure 6.9 and Figure 6.10 show large ranges for the results. The structural jacket wall thickness varied

from under 1.0 in to well over the 2.5 in shown. Similarly, the structural jacket weight varied from under 9 lbf to more than the 500 lbf in the figure. For both the wall thickness and the weight, two materials stood out as candidates: INCOLOY 909 and INCONEL 718. They both produced low weight designs with little variation across engine designs. However, INCONEL 718 is also the material proposed for use in the LOX pump and the LOX plumbing [4, 26], so selecting it for the structural jacket would yield a single metal for all LOX components, eliminating the need to mitigate galvanic corrosion. Further, INCONEL 718 is compatible with LOX so the chamber cooling jacket would not require a cover. This material selection is a change from the Aluminum 7075-T6 selected in the third generation DEAN research.

Table 6.15: Design Variables for Chamber Structural Jacket Material Study

Variable	Low	High	Levels
Expansion Ratio	6.0	25.0	3
Vacuum Thrust (lbf)	10,000	35,000	3
Chamber Structural Jacket Material	-	-	Parameter Scan

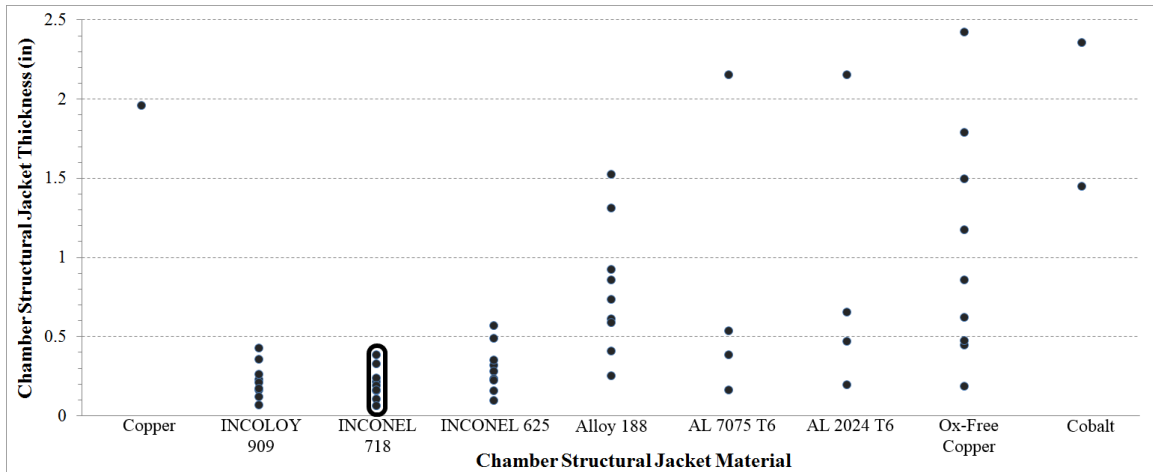


Figure 6.9: Chamber Structural Jacket Thickness Variation with Material Selection for Various Expansion Ratios and Thrust Levels

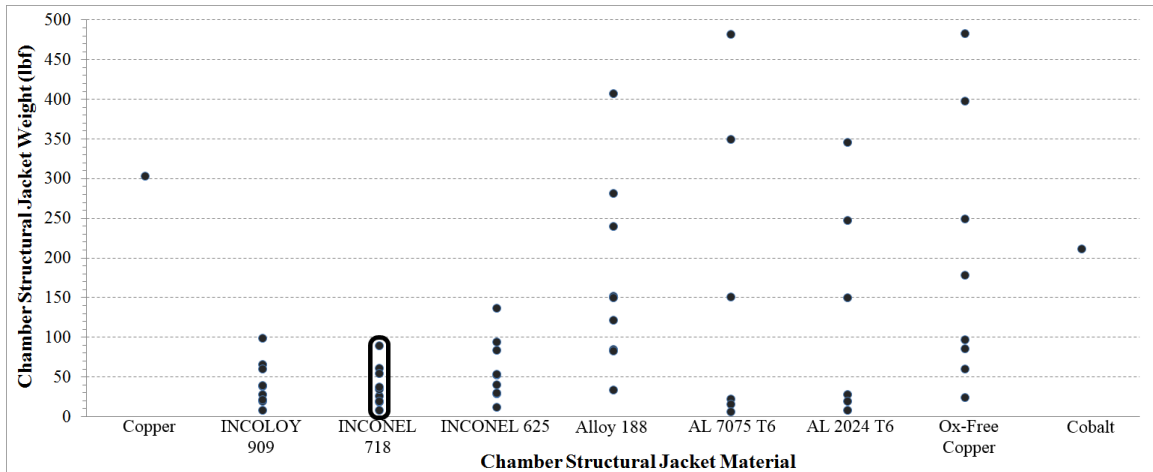


Figure 6.10: Chamber Structural Jacket Weight Variation with Material Selection for Various Expansion Ratios and Thrust Levels

The aerospike structural jacket material was tested next using the expansion ratio and vacuum thrust to vary engine designs (Table 6.16). As discussed above, the aerospike tip

was set to the same material as the aerospike structural jacket. Figure 6.11 and Figure 6.12 display the results of aerospike structural jacket material study. For both the wall thickness and the total aerospike weight one material stood out as a candidate material: INCOLOY 909. The INCOLOY 909 produced low weight aerospikes with little variation across engine designs. Further, INCOLOY 909 is compatible with LH2, so the aerospike cooling jacket would not require a cover. INCOLOY 909 is also the previously selected LH2 plumbing material, and selecting the same metal for all of the LH2 components eliminates the need to mitigate galvanic corrosion.

Table 6.16: Design Variables for Aerospike Structural Jacket Material Study

Variable	Low	High	Levels
Expansion Ratio	6.0	25.0	3
Vacuum Thrust (lbf)	10,000	35,000	3
Aerospike Structural Jacket Material	-	-	Parameter Scan

The results confirmed the third generation DEAN research indicating material selection for the aerospike tip has little influence on its weight, Figure 6.13. Across the range of material options, the aerospike tip weight stayed within the range of 5 lbf to 50 lbf, varying due more to the aerospike geometry than due to the material selection. The selection of INCOLOY 909 for the aerospike structural jacket and tip is a change from the oxygen-free copper selected in the third generation DEAN research.

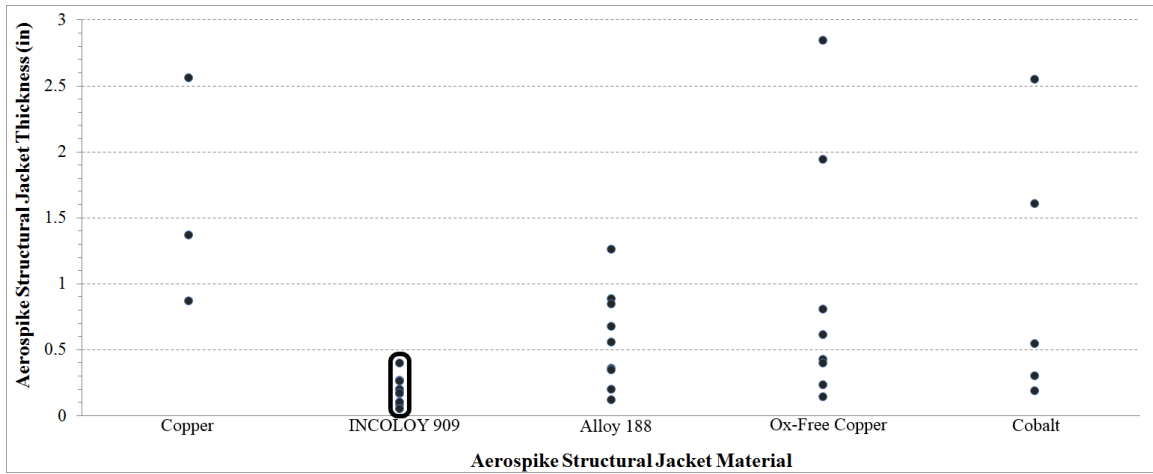


Figure 6.11: Aerospace Structural Jacket Thickness Variation with Material Selection for Various Expansion Ratios and Thrust Levels

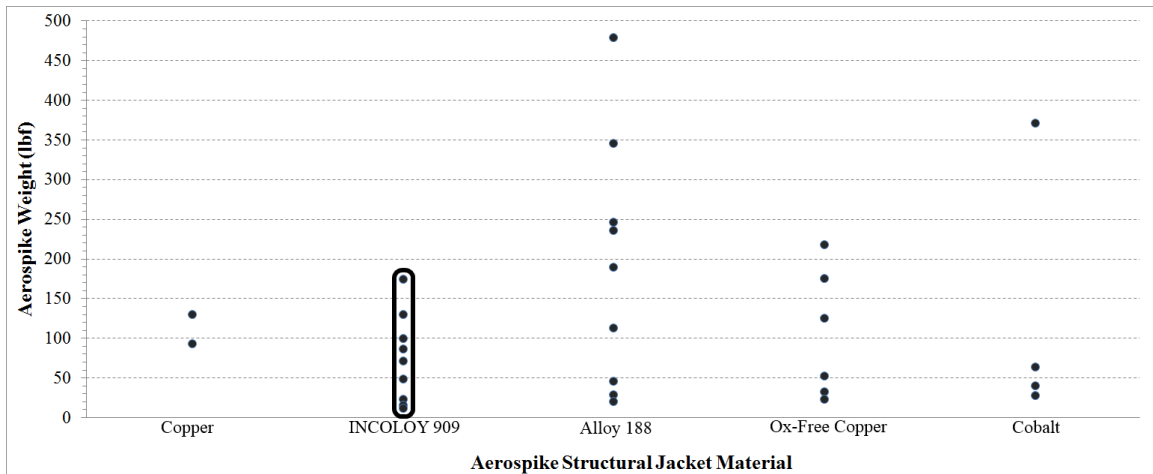


Figure 6.12: Aerospace Weight Variation with Material Selection for Various Expansion Ratios and Thrust Levels

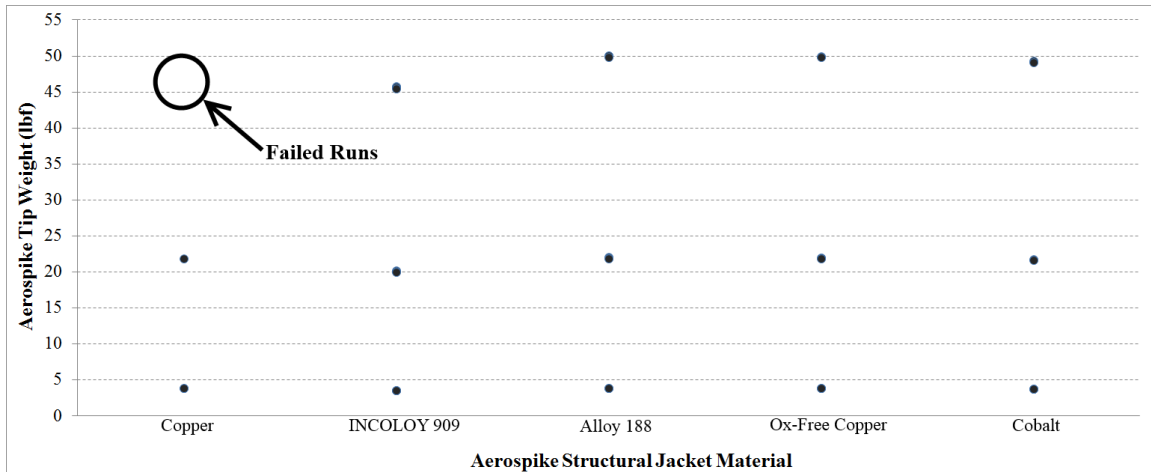


Figure 6.13: Aerospike Tip Weight Variation with Material Selection for Various Expansion Ratios and Thrust Levels

The fifth material study tested the LOX plumbing material using the expansion ratio and vacuum thrust to vary engine designs (Table 6.17). The LOX plumbing weight (Figure 6.14) accounted for between 2% and more than 30% of the engine's weight. INCONEL 718, the material selected during the third generation DEAN research, was among best performing materials over the full range of engine designs and has already shown to perform well in the other LOX components (pump and chamber structural jacket), confirming its selection as the LOX plumbing material.

Table 6.17: Design Variables for LOX Plumbing Material Study

Variable	Low	High	Levels
Expansion Ratio	6.0	25.0	3
Vacuum Thrust (lbf)	10,000	35,000	3
LOX Plumbing Material	-	-	Parameter Scan

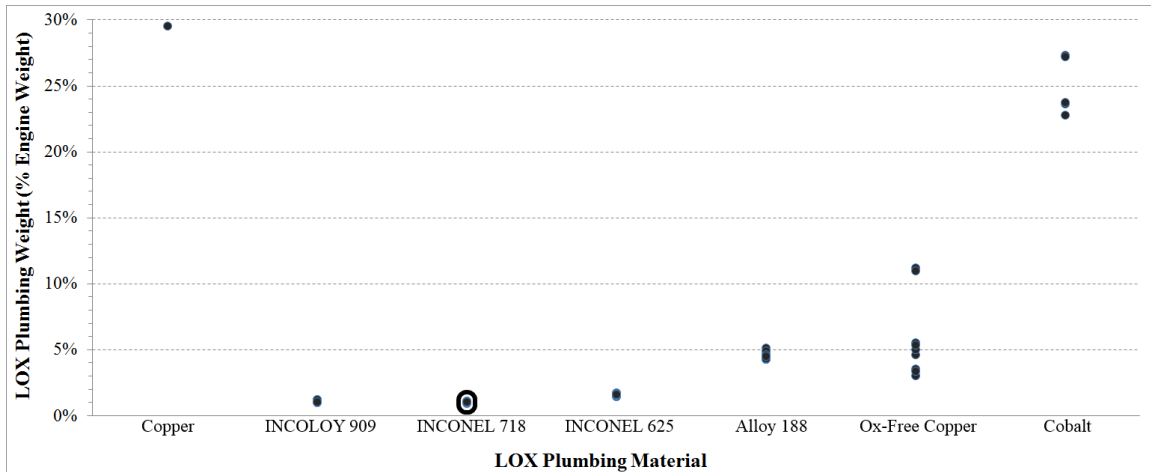


Figure 6.14: LOX Plumbing Weight Variation with Material Selection for Various Expansion Ratios and Thrust Levels

The LH2 plumbing material was tested last using the expansion ratio and vacuum thrust to vary the engine designs (Table 6.18). The LH2 plumbing weight (Figure 6.15) accounted for between 2% and more than 50% of the engine’s weight. One option stands out as a candidate material: INCOLOY 909. The data points for INCOLOY 909 are tightly clustered indicating the change in plumbing weight is very small compared to changes in engine designs. This selection matches the results in the third generation DEAN research.

Table 6.18: Design Variables for LH2 Plumbing Material Study

Variable	Low	High	Levels
Expansion Ratio	6.0	25.0	3
Vacuum Thrust (lbf)	10,000	35,000	3
LH2 Plumbing Material	-	-	Parameter Scan

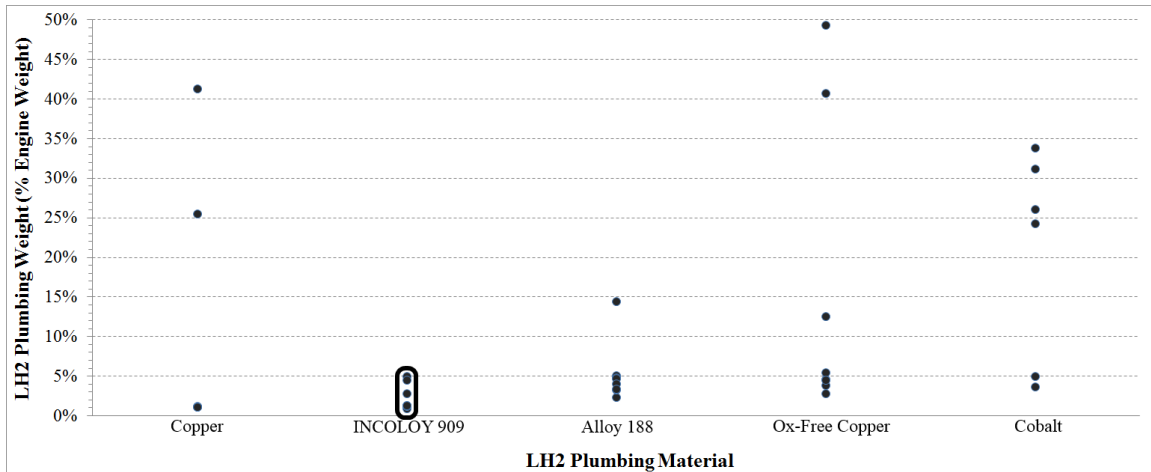


Figure 6.15: LH2 Plumbing Weight Variation with Material Selection for Various Expansion Ratios and Thrust Levels

Table 6.19 summarizes the results of the materials selection study. It includes the use of silicon carbide for both the chamber and aerospike cooling jackets, the use of INCONEL 718 for the chamber structural jacket and LOX plumbing, and the use of INCOLOY 909 for the aerospike structural jacket and tip and the LH2 plumbing. It also includes an update to the cooling channel geometry option to use the structural jacket as the cooling jacket cover as both structural jackets are now compatible with the fluids in the cooling jackets.

Table 6.19: Generation 4 DEAN Design Materials Selection

Component	Material
Chamber Structural Jacket	INCONEL 718
Chamber Cooling Jacket	Silicon Carbide
Aerospike Structural Jacket	INCOLOY 909
Aerospike Cooling Jacket	Silicon Carbide
Aerospike Tip	INCOLOY 909
LOX Plumbing	INCONEL 718
LH2 Plumbing	INCOLOY 909
Cooling Geometry Option	Structural Jacket is Cover

6.5 Conclusion

The materials study yielded an updated materials selection covering a wide range of engine designs. The materials study also confirmed the following findings from previous research: the aerospike tip material selection has little influence on the engine's thrust-to-weight ratio, the chamber cooling jacket should be manufactured from silicon carbide, the LOX plumbing should be manufactured from INCONEL 718, and the LH2 plumbing should be manufactured from INCOLOY 909. The material study also found material selections for the aerospike cooling jacket (silicon carbide), chamber structural jacket (INCONEL 718), and the aerospike structural jacket (INCOLOY 909) which produced low weight engines across a wide range of designs compared to previous material selections.

VII. Optimization Studies of Dual-Expander Aerospike Nozzle Upper Stage Rocket Engine

The text of this chapter was submitted to the AIAA Journal of Spacecraft and Rockets in July 2014. It is unaltered from the submitted version except in its formatting as required by the AFIT dissertation style guide.

7.1 Introduction

Prices for space launches are literally astronomical. The cost to deliver payload to orbit is estimated to be as much as \$10,000 per pound [15]. These costs mean placing satellites in orbit costs hundreds of millions of dollars. Savings from improved thrust-to-weight ratio and specific impulse can be significant. However, achieving these gains in performance will require more than incremental improvements in rocket engine technology. The thrust-to-weight ratio of high powered liquid rocket engines has been relatively constant with respect to propellant selection for decades, regardless of thrust levels and designs [23].

The Air Force Institute of Technology (AFIT) is researching a modification to the expander cycle as a means of breaking the performance barrier. The result of this research is the Dual-Expander Aerospike Nozzle (DEAN) rocket engine (Figure 7.1). The DEAN is a liquid oxygen (LOX)/liquid hydrogen (LH₂) reusable upper stage engine offering performance advantage over traditional upper stage engines in a compact package leading to dramatically improved thrust-to-weight ratios while maintaining a vacuum specific impulse comparable to current LOX/LH₂ upper stage engines. AFIT's goal with its research into the DEAN is to determine the viability of the DEAN architecture by finding those missions and designs for which the DEAN has a competitive advantage over traditional upper stage engines. Additionally, the DEAN architecture is a forerunner to a

similar boost stage architecture, where the aerospike nozzle's global performance could result in event greater performance gains.

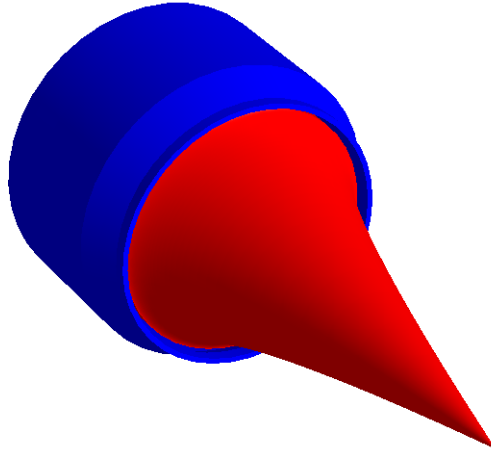


Figure 7.1: The Dual-Expander Aerospike Nozzle Upper Stage Engine

7.2 Background

7.2.1 *DEAN Architecture.*

The DEAN architecture, shown in Figure 7.2, uses two novel design choices. The first is the use of separate expander cycles for the fuel and the oxidizer. In a traditional expander cycle, the fuel is pumped through a cooling jacket for the chamber and nozzle. The energy transferred to the fuel from cooling the chamber and nozzle is then used to drive the turbine turning both the fuel and oxidizer pumps before the fuel is introduced into the chamber [5]. In the DEAN, the fuel and oxidizer each drive their own turbines and power their own pumps.

The second novel design choice of the DEAN is the use of an aerospike, or plug, nozzle. Aerospike nozzles are a center body in the combusted propellant flow often forming

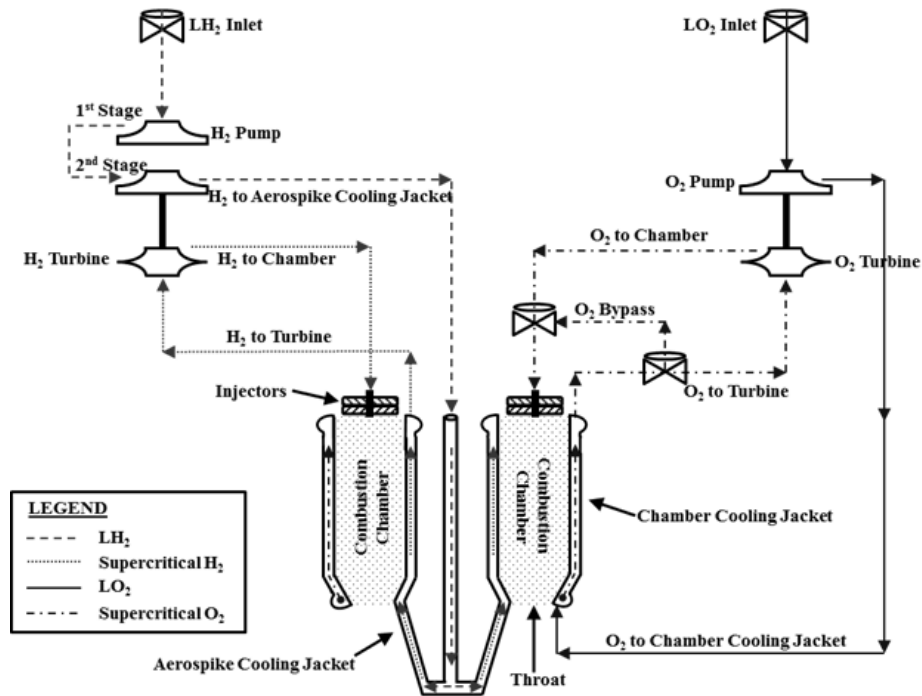


Figure 7.2: DEAN Architecture, credit J. Hall (unpublished)

the inner wall of the chamber. The ambient atmosphere forms the outer boundary for the flow for these nozzles. The combusted propellant flow expands against the aerospike nozzle and radially outward to match ambient pressure at each location in the nozzle flow field. The interaction with the ambient atmosphere gives aerospike nozzles altitude compensation ability, making them more efficient as altitude changes for the rocket. Similar bell nozzles must be designed for a single, specific altitude [24]. In the DEAN, the use of an aerospike nozzle provides a second, physically separate cooling loop from the chamber for use in the fuel expander cycle, greatly simplifying the implementation of a dual-expander cycle.

The second cooling loop increases the surface area inside the chamber, transferring greater energy to the propellants and providing more power to the turbines when compared to traditional expander cycle engines such as the RL10. This increased power is transferred to the pumps and in turn leads to increased chamber pressures. The increase in

chamber pressure yields engine performance improvements. This improved performance (thrust/weight) leads to smaller engines, in terms of both weight and physical dimensions, for similar levels of thrust and specific impulse. The separate expander cycles also ensure the fuel and oxidizer remain physically separated until entering the combustion chamber, eliminating the catastrophic failure mode in traditional expander cycles; failure of an inter-propellant seal [2, 25–27].

The DEAN architecture is not without its challenges, though. For example, the LOX cycle requires a turbine material capable of operating in an oxygen environment. Material surveys at AFIT have shown Inconel 718 provides both satisfactory oxygen resistance and suitable mechanical performance for use in both the pump and the turbine in the LOX cycle [26]. Also, the expansion ratio of aerospike nozzles is limited by the chamber geometry as shown in Equation (7.1) [4, 24]. Due to this limit, aerospike nozzles generally need larger chamber diameters to reach useful expansion ratios, potentially limiting the range of engines which offer improved thrust-to-weight while also delivering the required specific impulse.

$$\epsilon_{aerospike} = \frac{A_{c_throat}}{A_t} \quad (7.1)$$

7.2.2 Previous Research.

The current research builds on three generations of DEAN simulations. The performance goals for the DEAN have been a vacuum thrust of 50,000 lbf, a vacuum specific impulse of 464 s, and a thrust-to-weight ratio of 106.5. All three generations use NASA’s Numerical Propulsion System Simulation (NPSS) to explore cycle performance. NPSS is a computer simulation tool for modeling aircraft and rocket engines developed by the NASA Glenn Research Center with assistance from the aerospace propulsion industry. Engine simulations built in NPSS provide higher fidelity results than engine cycle studies [31]. The DEAN cycle simulation balances the fluid flows, mechanical power, and thermal

flows in the two expander cycles to converge on the engine performance parameters for a given design point.

Two of the three previous DEAN simulations extended the cycle model by embedding it into a system level engine simulation built in Phoenix Integration's ModelCenter. ModelCenter is a multidisciplinary modeling environment used to study the trade space of and optimize a design. ModelCenter can combine analyses developed in a variety of tools including MATLAB, Mathcad, Excel, and command line executables into a single system level simulation [60]. The system level DEAN simulation includes a parameterized version of the cycle model and connects it to additional analyses to estimate the DEAN's geometry and weight in order to compute the DEAN's physical dimensions and thrust-to-weight ratio.

The first generation research focused on developing the initial cycle balance of the DEAN for a single design. This design, shown in Figure 7.3(a), included an assumed expansion ratio of 125, producing a vacuum thrust of over 57,000 lbf and a vacuum specific impulse of 472 s with a thrust-to-weight ratio of 119 [2]. The second generation research implemented parametric modeling of the DEAN by refactoring the cycle model and integrating it into the first system level simulation. The new DEAN simulation retained the assumed expansion ratio. Through a series of trade studies, a new scaled DEAN was developed to more closely match the original design goals. The resulting design, shown in Figure 7.3(b), had a vacuum thrust of 50,900 lbf and a vacuum specific impulse of 489 s, while being 25% shorter in total length and reducing the size of the turbomachinery [27]. The third generation research extended the system simulation to include additional calculations including materials options, structural sizing, nozzle contour, and engine weight. The third generation DEAN research also moved from an assumed value for the expansion ratio to a calculated value based on the DEAN's geometry, resulting in lower values for the vacuum specific impulse. The final design for the third generation

research, shown in Figure 7.3(c), used silicon carbide for the chamber cooling jacket, Aluminum 7075-T6 for the chamber structural jacket, and oxygen-free copper for the complete aerospike. This design provided a vacuum thrust of just over 50,000 lbf, vacuum specific impulse of just over 430 s and a thrust-to-weight ratio of 142 in a 27 inch long engine [4].

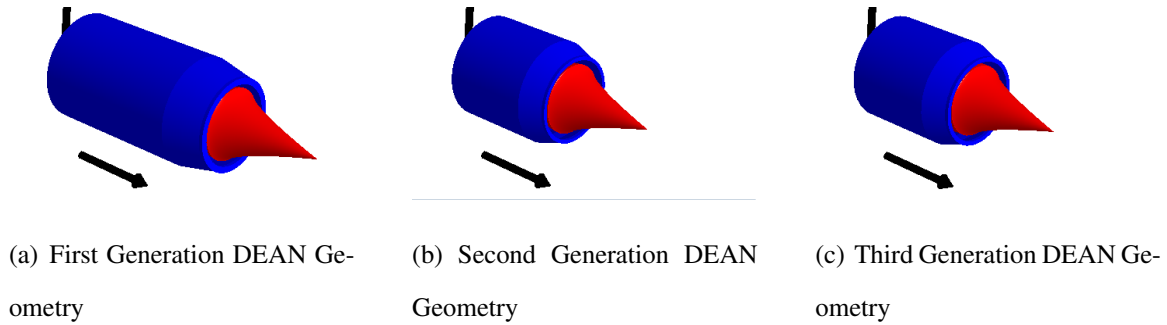


Figure 7.3: Comparison of First, Second, and Third Generation DEAN Geometry

7.2.3 Government Demand for Improved Upper Stage Rocket Engines.

Two US Air Force programs have been used as reference points when developing DEAN performance requirements. The first program, used to develop the initial DEAN requirements, is the Integrated High Payoff Rocket Propulsion Technology (IHRPT) program. One of the main goals of the IHRPT program is to double the thrust-to-weight ratio achieved by traditional LOX/LH2 engines. DEAN research quantified this thrust-to-weight ratio (T/W) requirement by specifying a minimum value of 106.5 [2]. The second reference point is the Next Generation Engine (NGE) program. The NGE mission requirements include a vacuum thrust (F_{vac}) between 25,000 lbf and 35,000 lbf with a minimum vacuum specific impulse ($I_{sp,vac}$) of 465 s. The NGE physical constraints include a maximum engine length of 90 inches and a maximum exit diameter of 73 inches [18]. As can be seen in Table 7.1, the IHRPT/NGE requirements represent a significant

improvement in weight and packaging over traditional expander cycle engines, while requiring better performance in terms of thrust and specific impulse.

Table 7.1: IHPRPT/NGE Requirements Compared to RL10 Performance

Variable	IHPRPT/NGE [2, 18]	RL10A-4-2 [24]	RL10B-2 [11, 24]
F_{vac} (lbf)	25,000-35,000	22,300	24,750
I_{sp_vac} (s)	465	450.5	465.5
T/W	106.5	60.8	37.3
Engine Length (in)	90.0	-	(stowed) 86.5 (deployed) 163.5
Outer Radius (in)	36.5	-	42.25

The DEAN will also benefit the X-37 Space Maneuvering Vehicle, shown in Figure 7.4(a); the reusable space plane designed to test various spaceflight hardware and technologies. The X-37 currently uses an AR2-3 hydrogen-peroxide/kerosene engine for on orbit maneuvers. The AR2-3, seen on the rear of the X-37 in Figure 7.4(b), has a vacuum thrust of 6600 lbf, a vacuum specific impulse of 246 s, and a thrust-to-weight ratio of 29.3. It is 32 inches long and has an outer radius of 10 inches [14, 20, 21].



(a) X-37 Space Maneuvering Vehicle [9]



(b) Rear View of X-37 Including the AR2-3 Engine [10]

Figure 7.4: X-37 Space Maneuvering Vehicle, credit US Air Force

NASA's upper stage engine requirements are centered on the Space Launch System (SLS). The SLS is a shuttle-derived super-heavy lift human-rated launch system which is still in the design phase. Four upper stage configurations are being considered for the SLS with two being relevant to DEAN research. The first of these designs, shown in Figure 7.5(a), is an upper stage powered by four RL10 engines. This design provides a vacuum thrust of 99,000 lbf and a vacuum specific impulse of 462.5 s, with a thrust-to-weight ratio of 37.3. The second design, shown in Figure 7.5(b), is an upper stage powered by a single J-2X engine providing a vacuum thrust of 294,000 lbf and a vacuum specific impulse of 448 s, with a thrust-to-weight ratio of 55 [8, 12, 22]. Table 7.2 shows the difference between these designs and the performance available from a single RL10B-2.



(a) SLS Upper Stage Design 1: Four RL10 Engines [8]



(b) SLS Upper Stage Design 2: Single J-2X Engine [8]

Figure 7.5: SLS Upper Stage Designs, credit The Boeing Corporation

Table 7.2: SLS Designs Compared to RL10 Performance

Variable	SLS-1 [8, 11, 24]	SLS-2 [12, 37]	RL10B-2 [11, 24]
Engine Cycle	Expander	Gas Generator	Expander
F_{vac} (lbf)	99,000	294,000	24,750
I_{sp_vac} (s)	462.5	448.0	465.5
T/W	37.3	55.0	37.3
Engine Length (in)	(stowed) 86.5	180.0	(stowed) 86.5
	(deployed) 163.5		(deployed) 163.5
Outer Radius (in)	108	60.0	42.25

7.3 Current Research

The fourth generation DEAN simulation builds on the lessons learned from the previous generation models. The new simulation includes an updated geometry parametrization, simplified structure, and a custom solver to compute initial estimates for the cycle balance. The improvements allowed for the exploration of a wide range of designs while improving fidelity. Figure 7.6 and Table 7.3 outline the overall structure of the fourth generation DEAN simulation.

The updated set of parametric design variables were derived from common conceptual design relationships. The top level design variables include the expansion ratio, the throat area, the chamber length, the characteristic length, the vacuum thrust, and the oxidizer-to-fuel ratio. Additional design variables include controls for the internal geometry of the cooling channels in both expander cycles and the materials used for key DEAN components. The response variables for the DEAN include the vacuum specific impulse, thrust-to-weight ratio, the maximum Mach numbers in the cooling channels, the wall temperatures of the cooling jackets, and the power required by the pumps.

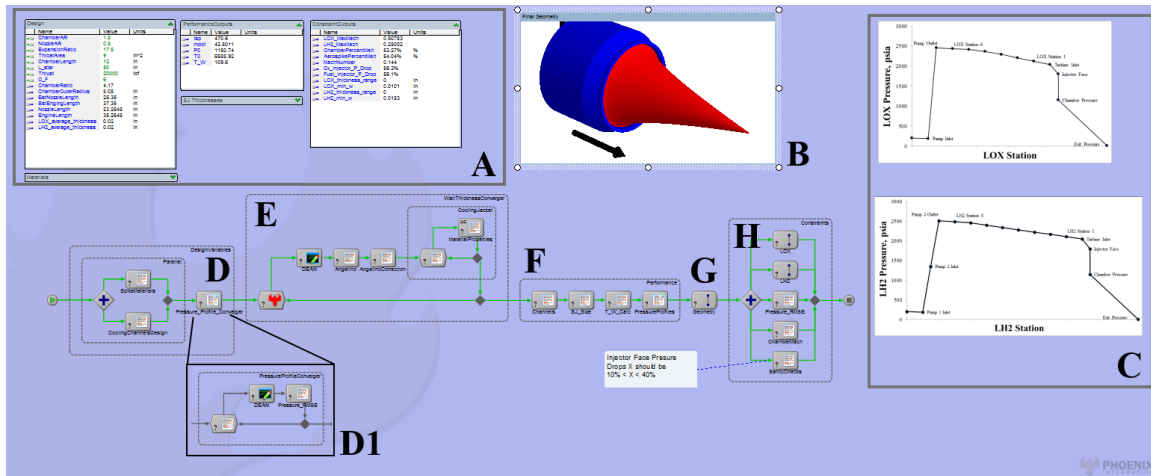


Figure 7.6: Fourth Generation DEAN Model

After completing the fourth generation DEAN simulation, the underlying models and the DEAN architecture were put through a detailed verification process. Inspection of the simulation ensured source code for each module in the simulation agreed with the underlying physics. The data flow connections between the modules were also inspected to verify the system level model passed the correct values between modules and in turn calculates the correct performance for the DEAN.

Following the simulation's inspection, the DEAN architecture was verified through a combination of inspection and testing. The inspection consisted of a detailed review of previous research, noting where previous research demonstrated the feasibility of the architecture, how the previous research designs compared to research objectives, and lessons learned regarding the DEAN simulation. The testing consisted of six trade studies comparing critical performance metrics of the DEAN to liquid rocket engine theory and the RL10 family of upper stage engines over a wide range of DEAN designs.

The results of the six trade studies show the DEAN's performance matched expectations based on liquid rocket engine theory. Further, the results confirmed the

Table 7.3: Fourth Generation DEAN Model Components

Label	Name	Description
A	Data Monitors	ModelCenter Data Monitors to provide access to key design and response variables
B	Final Geometry	DEAN geometry (chamber and aerospike) after sizing wall thicknesses
C	Pressure Profile Plots	pressure profiles for the LOX and LH2 expander cycles
D	Design Variables	system level design variables and the preprocessing analyses, including cooling channel design and initial estimates for the turbopump pressure ratios
D1	Pressure Profile Converger	a secondary module, solves for the initial estimates for the turbopump pressure ratios
E	Wall Thickness Converger	module to balance the pressure and mechanical systems and to size the cooling channel wall thicknesses
F	Performance	performance values, structural jacket wall thicknesses and T/W
G	Geometry	geometry module
H	Constraints	constraint module; maximum Mach numbers in the cooling channels and the pressure drops across the injector face

DEAN's advantages over single expander cycle engines. The DEAN achieved more than double the chamber pressure of the RL10A-4 and RL10B-2. Similarly, specific impulse results showed the DEAN can match the RL10B-2's vacuum specific impulse in an engine

producing greater thrust and 80% smaller in length and diameter. The trade studies also demonstrated the DEAN architecture is highly scalable. This scalability included designs ranging in thrust levels from 10,000 lbf to 35,000 lbf, expansion ratios from 6.0 to 25.0. Further, the fourth generation DEAN simulation has greatly improved in robustness, converging in 98.7% of the 1500 designs studied.

After completing the verification study, the materials selection study was updated to cover a wide range of engine designs. The objective of this series of trade studies was to optimize the design of the cooling channels and then the materials for each of the major DEAN components. The updated materials selection confirmed previous research: aerospoke tip material selection has little influence on the engine's thrust-to-weight ratio, chamber cooling jacket should be manufactured from silicon carbide, LOX plumbing should be manufactured from INCONEL 718, and LH2 plumbing should be manufactured from INCOLOY 909. The results of the current research found updated material selections for the aerospoke cooling jacket (silicon carbide), chamber structural jacket (INCONEL 718), and the aerospoke structural jacket (INCOLOY 909). These material selections consistently produce low weight engines across a wide range of designs.

7.4 Results and Analysis

Comparison of the DEAN to traditional upper stage engines was carried out in three studies. The first study looked at the US Air Force's need for new launch capability as expressed in the IHPRT and NGE programs. The second study looked at the propulsion needs on US Air Force space planes as embodied by the X-37. The final study looked at the upper stage requirements for NASA's SLS. All three of these studies are designed to optimize the DEAN by maximizing its specific impulse and its thrust-to-weight ratio subject to physical constraints and mission requirements.

Previous results showed most of the design variables have little influence on the responses allowing fixed values to be used and moving them to the list of preassigned

parameters. The vacuum thrust was also considered a preassigned parameter as each mission profile has a required vacuum thrust level. The selection of preassigned parameters (Table 7.4) leaves five independent design variables, Table 7.5.

Each optimization study began by finding an updated base design. These new designs were found by scaling a 20,000 lbf vacuum thrust engine. The scaling for each design started with setting the vacuum thrust to the required mission value and then adjusting each of the five design variables until a suitable base design was found. The updated base design was then used for all related trade and optimization studies.

Table 7.4: DEAN Preassigned Parameters

Variable	Value
Vacuum Thrust	Mission Specific
Chamber Throat AR	1.0
Chamber Stations Adjustment	1.2
Chamber Station 5 Adjustment	1.0
Chamber Cooling Channels Ratio	14.4
Nozzle Throat AR	0.86
Nozzle Station 1 Adjustment	1.7
Nozzle Stations Spike Adjustment	1.0
Aerospike Cooling Channels Ratio	9.4
Ambient Pressure Decision	Operational
Operational Pressure (psia)	0.001
Cooling Geometry Option	Structural Jacket is Cover
Percent Weight of Hardware	5.0
Cowl Length	0.1
Factor of Safety	1.5
Material Strength Option	Yield Strength
Chamber Structural Jacket	INCONEL 718
Chamber Cooling Jacket	Silicon Carbide
Aerospike Structural Jacket and Tip	INCOLOY 909
Aerospike Cooling Jacket	Silicon Carbide
LOX Plumbing	INCONEL 718
LH2 Plumbing	INCOLOY 909

Table 7.5: DEAN Design Variables

Variable
Expansion Ratio
Throat Area
Chamber Length
Characteristic Length
Oxidizer-to-Fuel Ratio

7.4.1 *Physical Constraints.*

From the beginning, DEAN research has targeted reusability as one of its objectives. During the first generation DEAN research, this objective was met by constraining the cooling jacket wall temperatures to 50% of the melting point for the selected material [2]. The third generation DEAN research indicated this requirement was overly conservative and so it was modified to 60% of the melting point [4].

Constraints on the maximum Mach number in the cooling channels have been consistently used to ensure shock waves do not form in the cooling channels and drag does not overcome pump capabilities. The requirements are the maximum Mach number in the LOX cooling channels must be less than or equal to 0.6 and the maximum Mach number in the LH2 cooling channels must be less than or equal to 0.9 [2]. The DEAN optimization studies included a 10% margin in the Mach number constraints to ensure the optimization algorithms yielded survivable designs.

The power required by the pumps in both expander cycles was limited to current technical capabilities. Strain's contribution to the first generation DEAN research focused on modeling the complete turbopump for the LOX cycle. His work showed the feasibility of a LOX pump powered by a LOX turbine requiring 2441 HP [26]. The current research assumed an additional 10% margin on his results to yield a maximum power required by the

LOX pump of 2685 HP. Research and development from previous US Air Force Research Lab programs show an LH2 pump producing 5900 HP is feasible [25].

To ensure the pressure balance produced by the NPSS model conformed to accepted engineering practice, the pressure drop across the injector face was constrained for both the LOX and the LH2 cycles to between 10% and 40% of chamber pressure [24].

A key manufacturing constraint for the DEAN is the difference between the outer and inner radii at the throat. The inner and outer throat radii specify the throat area, and changes to the throat area impact operation by leading to changes in the chamber pressure, thrust, and specific impulse. Assuming a manufacturing tolerance for the radii at the throat of 0.001 inch, a minimum value for the difference in throat radii of 0.1 inch limited the variation in throat area to $\pm 2.0\%$.

7.4.2 Optimizing for the IHPRT/NGE Programs.

The first optimization study looked at the US Air Force's need for new launch capability as expressed in the IHPRT and NGE programs. The objective was to maximize the vacuum specific impulse and the thrust-to-weight ratio for DEAN engines with vacuum thrust between 25,000 lbf and 35,000 lbf; minimum vacuum specific impulse of 465 s and a minimum thrust-to-weight ratio of 106.5. The NGE physical constraints and maximum exit diameter were adjusted to fit the fourth generation DEAN. The NGE requirement for the maximum engine length of 90 inches was shortened by 25% to create a conservative buffer for the engine mounting hardware and installation of the turbopumps. The NGE requirement for the maximum exit diameter is the maximum outer chamber radius. The chamber represents the largest diameter in the DEAN architecture and the model returns radial values for this output. The base design point for the IHPRT/NGE optimization study used the average value for the program's thrust range as the specified vacuum thrust (Table 7.6).

Table 7.6: Base Design for IHPRPT/NGE Optimization Study

Variable	Value
Design Variables	
Expansion Ratio	16.0
Throat Area (in ²)	10.25
Chamber Length (in)	12
Characteristic Length (in)	55
Vacuum Thrust (lbf)	30,000
Oxidizer-to-Fuel Ratio	6.0
Responses	
Vacuum Specific Impulse (s)	465.1
Thrust-to-Weight Ratio	112.7
Engine Length (in)	35.4
Outer Chamber Radius (in)	8.5

Before beginning the optimization study, a final design of experiments focused on the variable influences for the final selection of design variables. The vacuum thrust was included in this trade study to ensure the results covered a wide range of engine designs. The design of experiments used 500 data points made up of a 343 point Design Explorer Orthogonal Array with 157 additional points from a Latin-Hypercube, Table 7.7.

This design of experiments yielded three key results: identification of the design variables with significant influence on the optimization objectives and constraints, identification of the key constraints, and selection of the optimal oxidizer-to-fuel ratio. Figure 7.7 lists the influence of the design variables on the objectives and constraints in the optimization problem. The rows list the design variables; columns list the response variables. Cells with an 'X' indicate a significant variable influence which can vary with

the value of the design variable. Cells with a ‘+’ indicate a direct relationship between the design variable and the response variable. Cells with a ‘-’ indicate an inverse relationship between the design variable and the response variable.

Table 7.7: Design Variables for IHPRPT/NGE Optimization Study DOE 1 - Trade Space Exploration

Variable	Low	High	Levels
Expansion Ratio	15.0	25.0	Space Filling
Throat Area (in ²)	9.0	13.0	Space Filling
Chamber Length (in)	7.5	13.0	Space Filling
Characteristic Length (in)	40	75	Space Filling
Vacuum Thrust (lbf)	25,000	35,000	Space Filling
Oxidizer-to-Fuel Ratio	5.0	8.0	Space Filling

These relationships were determined in two phases. The first phase used ModelCenter’s Variable Influence Profiler to determine the general variable influence relationships. The Variable Influence Profiler uses Analysis of Variance methods over a Kriging model of the trade study data to compute variable importance levels. These levels are reported as percentages of relative importance [60]. The second phase used scatter plots to look for consistent trends in the data between variables with significant influence relationships. Figure 7.8 shows the inverse relationship between chamber wall temperature and the throat area. Figure 7.9 gives an example of a strong but complex relationship between the thrust-to-weight ratio and the characteristic length. This relationship was limited to structural and thermal effects as the minimum characteristic length of 40 in was assumed to be sufficient to give complete combustion yielding equilibrium products and conditions.

simultaneously. The wall temperature constraints for the DEAN represented a single failure mode where the temperatures exceed the thermal limits. Conversely, the injector face pressure drop constraints could take the form of insufficient pressure drops, representing operational safety concerns, or excessive pressure drops, representing inefficient designs. All of the infeasible designs related to injector face pressure drops are of the latter variety with the LOX pressure drops reaching as high as 60% and the LH2 pressure drops reaching as high as 70%.

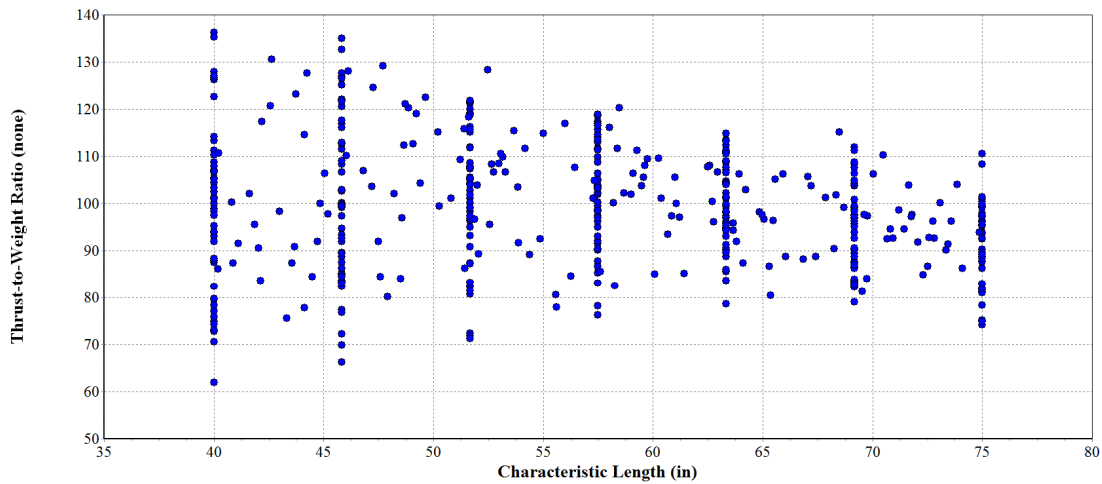


Figure 7.9: Thrust-to-Weight Ratio Variation with Characteristic Length

Table 7.8: Key Constraints for the DEAN Engine

Variable	Violation Rate
Chamber Wall Temperature	20.0%
Aeropsike Wall Temperature	27.3%
LOX Injector Face Pressure Drop > 40%	22.7%
LH2 Injector Face Pressure Drop > 40%	76.2%

Identifying the key constraints reduced the key responses from fifteen to six: the four key constraints plus the two objectives. The decrease is a significant reduction in the size of the optimization problem.

Another key result from this design of experiments was the selection of an optimal value for the oxidizer-to-fuel ratio, moving it from the list of design variables to the list of preassigned parameters. Throughout the second and third generation DEAN research, optimal designs have all come from using a value of 6.0 for the oxidizer-to-fuel ratio. The fourth generation research confirmed this result for a wide range of engine designs. The relationship between the oxidizer-to-fuel ratio and the vacuum specific impulse based on this design of experiments resulted in a maximum specific impulse at an oxidizer-to-fuel ratio of 6.0, Figure 7.10. The vertical bands at each oxidizer-to-fuel ratio represent changes in the expansion ratio.

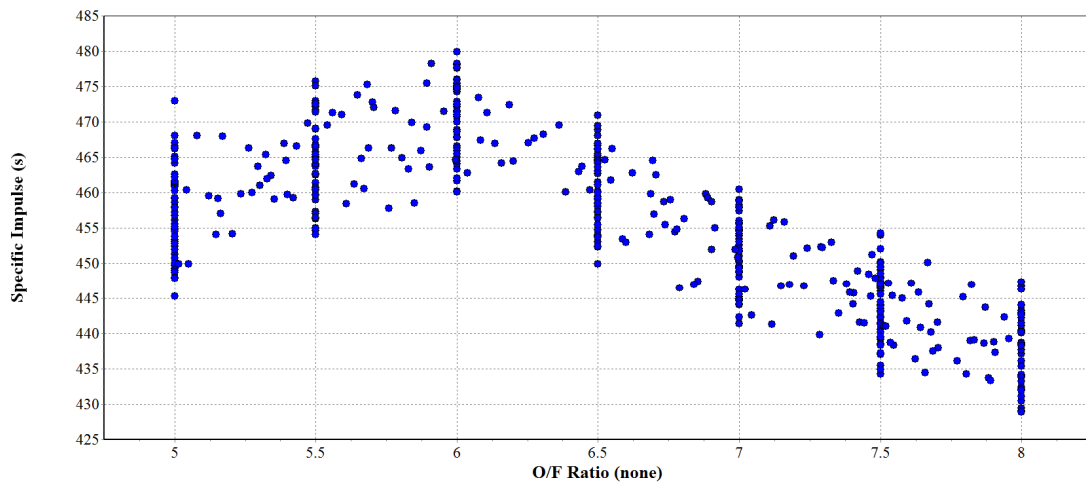


Figure 7.10: Vacuum Specific Impulse Variation with Oxidizer-to-Fuel Ratio

To confirm this conclusion, the constraints influenced by the oxidizer-to-fuel ratio were inspected to determine any adverse affects. Of the four constraints influenced by the

oxidizer-to-fuel ratio, only one, the injector face pressure drop in the LH2 expander cycle is a key constraint, Figure 7.11. The pressure drop increases approximately 5% over the range of oxidizer-to-fuel ratios, with a value of 6.0 yielding an acceptable range for the pressure drop. With this result being the most profound impact indicated, the conclusion that no adverse impacts on the constraints for an oxidizer-to-fuel ratio of 6.0 is confirmed, making it the globally optimal value for the DEAN.

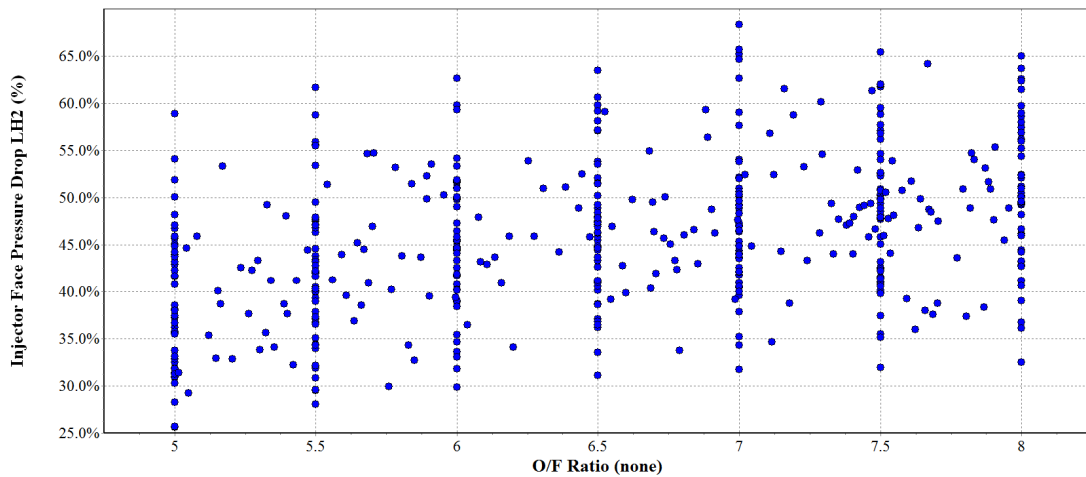


Figure 7.11: LH2 Injector Face Pressure Drop Variation with Oxidizer-to-Fuel Ratio

These results provided a framework for an efficient optimization process for the DEAN, Table 7.9. The first two steps use the variable influence and key constraints results to address the wall temperature constraints. The wall temperatures are driven directly by the vacuum thrust and inversely by the throat area (Figure 7.7). Therefore, missions with higher thrusts will need larger throat areas to keep from melting the walls. However, larger throat areas also increase the pressure drops at the injector face (Figure 7.7). Therefore, each thrust level must be limited to the smallest throat area that yields wall temperatures below 60% of their melting point. Using the smallest throat area possible is also consistent

with designing smaller engines, and in turn higher thrust-to-weight ratios [5]. The third step uses the variable influence and key constraints results to address the other key constraints, the injector face pressure drops, by finding the ranges of values for the expansion ratio and chamber length yielding acceptable designs. The remaining steps combine the results from the previous steps to define and execute the optimization problem in ModelCenter's Darwin optimizer. The Darwin optimizer is a trade study tool in ModelCenter implementing a genetic optimization algorithm. The 30,000 lbf IHPRPT/NGE case will be used to present the process.

Table 7.9: DEAN Optimization Process

Step	Description
1	Set the vacuum thrust per the mission requirements/current case
2	Find the smallest throat area with the chamber and aerospike wall temperatures below 60% of their materials' melting points
3	Run a design of experiments over the expansion ratio and chamber length to determine the bounds on these variables confining the trade space to designs satisfying the key constraints
4	Create the formal definition for the multi-objective optimization problem
5	Configure the Darwin Optimizer in ModelCenter to implement the optimization problem defined in step 4
6	Seed the Darwin Optimizer with the Pareto designs from the design of experiments study in step 3
7	Run the Darwin Optimizer to generate the Pareto front for the design problem defined in step 4

The simulation vacuum thrust was set to 30,000 lbf; the oxidizer-to-fuel ratio was set to 6.0. Then, a parametric study was used to determine the smallest acceptable throat area. This trade swept the throat area from 9.0 to 13.0 square inches in 0.1 square inch increments. The wall temperature limits for both the chamber and aerospike, Figure 7.12, resulted in a throat area of 10.7 in², circled in the figure (1% margin for both wall temperature constraints).

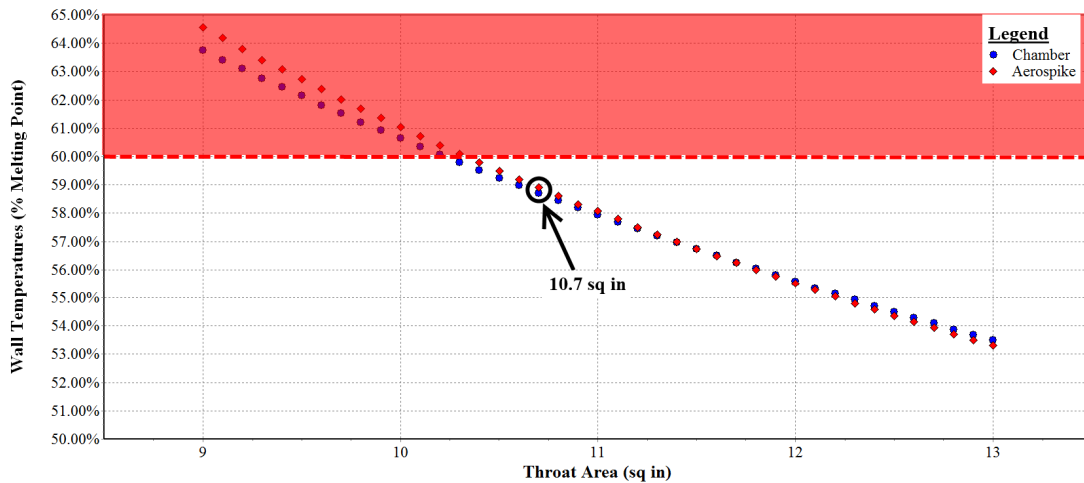


Figure 7.12: Wall Temperatures Variation with Throat Area for 30,000 lbf DEAN

The next step used a design of experiments (Table 7.10) to determine the range of values for the expansion ratio and chamber length yielding the highest percent of valid designs. The parameter scan design ensured the data was regularly spaced and was well filled for both design variables.

Table 7.10: Design Variables for IHPRPT/NGE 30,000 lbf Step 3 DOE

Variable	Low	High	Levels
Expansion Ratio	15.0	25.0	21
Chamber Length (in)	7.0	13.0	13

In Figure 7.13 the horizontal axis is the chamber length, the vertical axis is the vacuum specific impulse, and the axis running into the page is the expansion ratio. Points vary directly in size with the thrust-to-weight ratio. Light gray points represent invalid designs due to one or more constraint violations. Points highlighted with cross marks are those points which lie on the Pareto front for the trade study results. Each of these Pareto points represents a design which would have to decrease one of the two objectives in order to increase the other. These points were used in the sixth step of the optimization process to reduce the number of designs the optimization algorithm tested in order to find the global Pareto front. The black box shows the region of the trade space bounding all of the feasible designs and includes one step beyond the feasible range to capture any valid designs which may be in the gap.

The fourth step in the optimization process is to formalize the optimization problem statement. First, values which have already been determined were listed as updated preassigned parameters. The updated preassigned parameters were the throat area, determined in the second step, the vacuum thrust, determined by the mission/case, and the oxidizer-to-fuel ratio. Table 7.11 lists these parameters and their values for the 30,000 lbf IHPRPT/NGE case.

Then, the optimization problem was stated mathematically: listing the objectives, remaining design variables with their ranges, and the constraints. Equation (7.2) lists the formal problem statement for the 30,000 lbf IHPRPT/NGE case. The ranges for the design

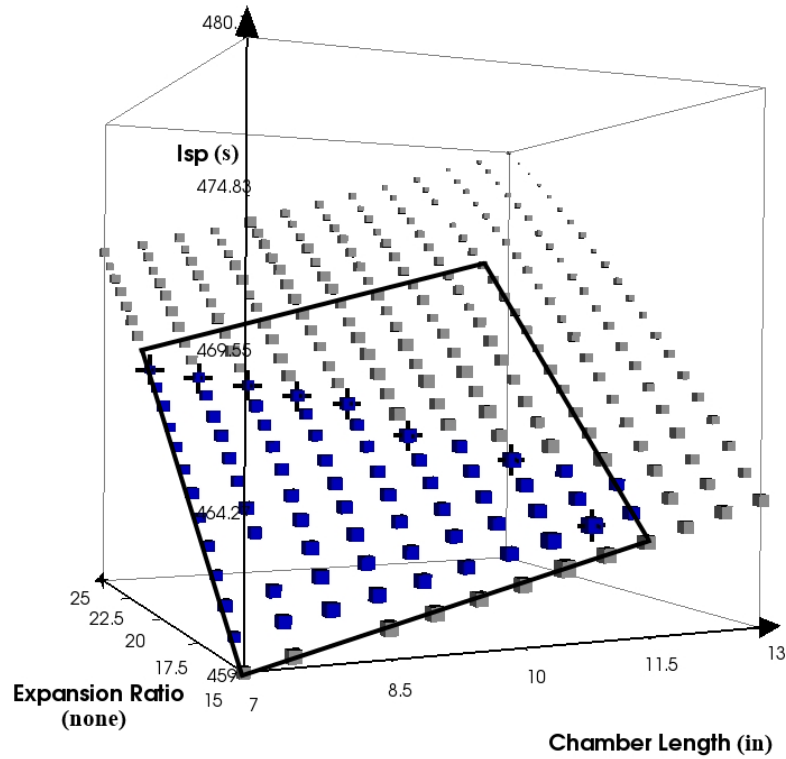


Figure 7.13: Specific Impulse Variation with Expansion Ratio and Chamber Length for 30,000 lbf DEAN

Table 7.11: Preassigned Parameters for IHPRT/NGE 30,000 lbf Optimization Study

Variable	Value
Throat Area (in ²)	10.7
Vacuum Thrust (lbf)	30,000
Oxidizer-to-Fuel Ratio	6.0

variables have been limited to discrete steps to facilitate the use of the selected genetic optimization algorithm for efficiency [60]. The throat area and chamber length varied in

increments of 0.1 (square inches and inches respectively). The characteristic length varied in steps of 1.0 inch.

$$\text{Find } \mathbf{X} = \left\{ \begin{array}{l} \text{Expansion Ratio} \\ \text{Chamber Length} \\ \text{Characteristic Length} \end{array} \right\} \text{ which maximizes}$$

Vacuum Specific Impulse(\mathbf{X})

Thrust-to-Weight Ratio(\mathbf{X})

where

$$\mathbf{X} = \left\{ \begin{array}{l} 15.0, 15.1, \dots 21.5 \\ 7.0, 7.1, \dots 11.5 \\ 45, 46, \dots 75 \end{array} \right\}$$

subject to

Max Mach Number in LOX Channels ≤ 0.54

Max Mach Number in LH2 Channels ≤ 0.81

Wall Temperatures $\leq 60\%$ Melting Point

$10\% \leq \text{Inj Face Pres Drop LOX \& LH2} \leq 40\%$

Required Power for LOX Pump ≤ 2685 HP

Required Power for LH2 Pumps ≤ 5900 HP

$\Delta r_{\text{throat}} \geq 0.1$ in

Vacuum Specific Impulse ≥ 465 s

Thrust-to-Weight Ratio ≥ 106.5

Engine Length ≤ 67.5 in

Outer Chamber Radius ≤ 36.5 in

(7.2)

The fifth and sixth steps involve configuring the genetic optimization algorithm. The preassigned parameter values were assigned to the DEAN model's input variables. The optimization problem was entered into the Darwin user interface as shown in Figure 7.14. The Pareto points from the design of experiments in the third step were then entered into the Darwin user interface using the Design Seeding option.

The default values were used for the genetic optimization algorithm options. The population size for the optimization was set to 10. The selection scheme was *multiple elitist*, with the number of preserved designs set to 3, passing on the best 3 designs from the combined population of the current generation and its parent designs. The selected convergence criteria was set to the number of generations without improvement, with a value of 15 and improvement defined as 15% or less of the Pareto optimal designs changing between generations. The genetic crossover probability was set to 1.0 and the mutation probability was 15%. The maximum constraint violation equaled 0.05 and the percent penalty for constraint violations was 50% [60].

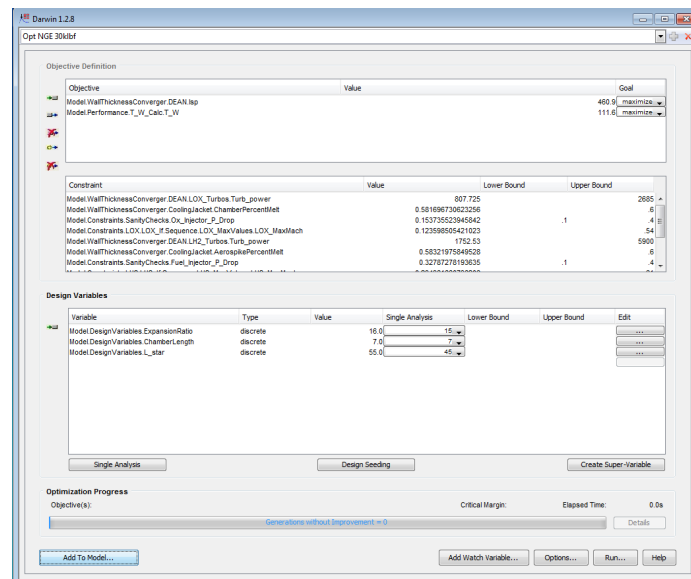


Figure 7.14: Darwin Configuration for the 30,000 lbf IHPRT/NGE Case

The genetic algorithm then generated the Pareto front, Figure 7.15. The Pareto front for the vacuum specific impulse variation with thrust-to-weight ratio falls above the dashed lines marking the mission requirements of a minimum specific impulse of 465 s and a minimum thrust-to-weight ratio of 106.5. Points with an 'X' through them are marginal designs exceeding the allowable injector face pressure drop in the LH2 expander cycle by one to two percent. While the marginal designs have desirable performance and could be separately optimized to address the injector face pressure drop, this additional optimization is outside the scope of the current study. From the remaining two candidate designs for the 30,000 lbf IHPRPT/NGE case, the one with the higher vacuum specific impulse, circled in the figure, was selected as the optimal design (see Table 7.12).

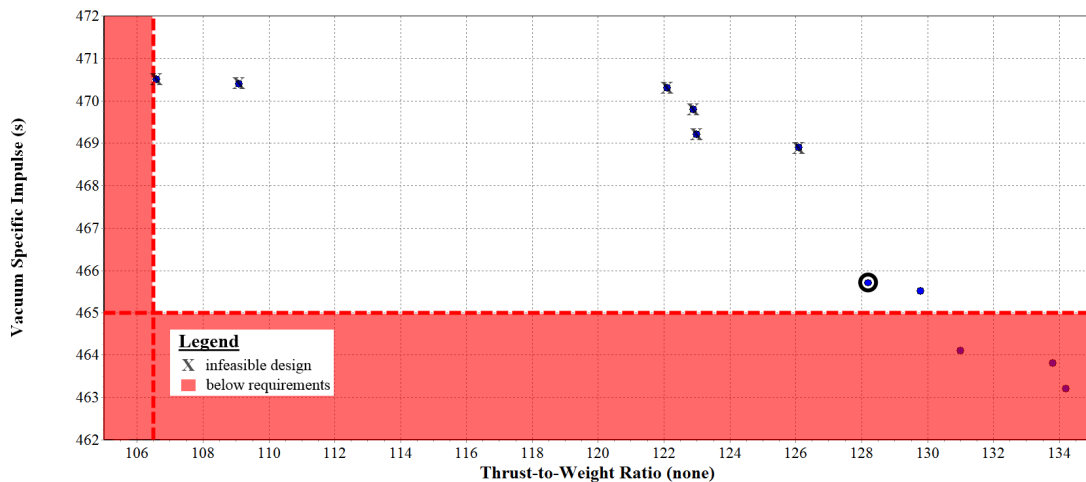


Figure 7.15: Specific Impulse Variation with Thrust-to-Weight Ratio Pareto Front for the 30,000 lbf IHPRPT/NGE Case

The geometry for the optimal design has a shorter chamber than previous DEAN designs, Figure 7.16. Comparing the optimal design to the RL10B-2 showed the DEAN offers significant improvements. Producing 30,000 lbf of thrust, this DEAN design

outperforms the RL10B-2 by 20% in thrust while matching its specific impulse in a much smaller package. The DEAN is approximately one quarter of the deployed length of the RL10B-2, or approximately one half of its stowed length, and one fifth of the RLB-2's diameter. Further, this compact size gives the DEAN a thrust-to-weight ratio which is more than three times that of the RL10B-2.

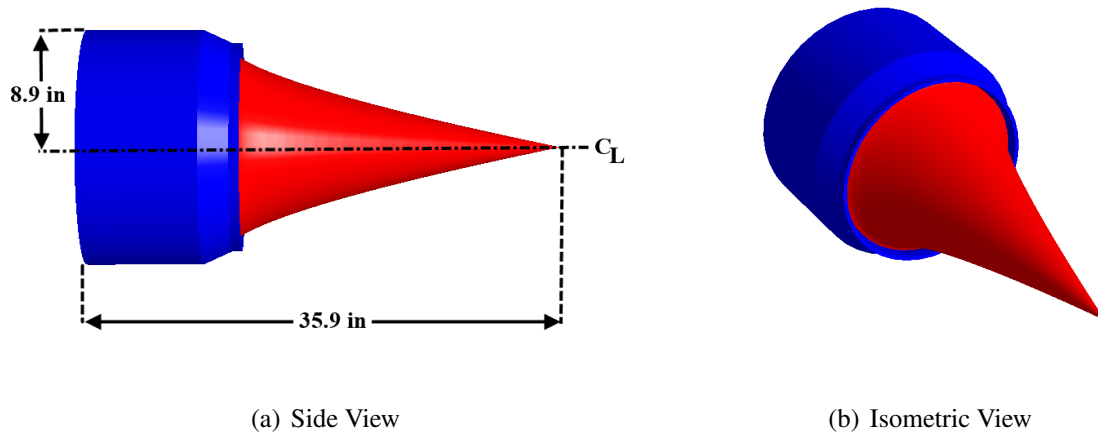


Figure 7.16: 30,000 lbf IHPRPT/NGE DEAN Optimal Design Geometry

Simulations for both a 25,000 lbf case and a 35,000 lbf case covered the full range of the NGE requirements. As with the 30,000 lbf case, a number of marginal designs exceeded the pressure drop constraint for the LH2 expander cycle, Figure 7.17. Excluding the marginal designs left one or two choices for each case, selected choices (maximum specific impulse) marked with circles in the figure.

The three optimal designs have similar thrust-to-weight ratios, over 100, Table 7.12 and Figure 7.17. Further, the first two cases, providing 25,000 lbf and 30,000 lbf thrust respectively, have nearly identical specific impulse. The third case offers 3.5 s of additional specific impulse.

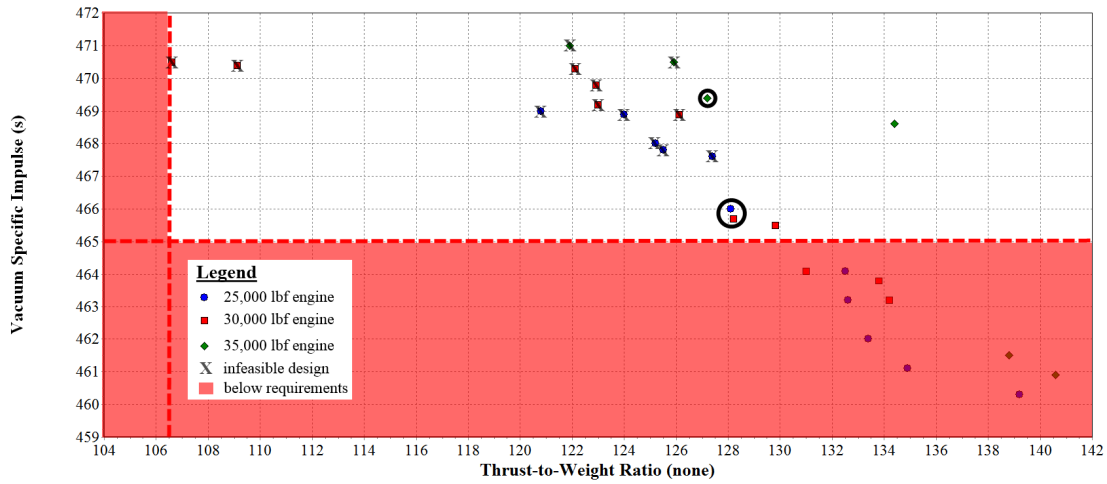


Figure 7.17: Specific Impulse Variation with Thrust-to-Weight Ratio Pareto Fronts for IHPRPT/NGE Cases

To provide a more direct comparison between the DEAN and the RL10, a simulation was applied to the RL10B-2 using Gibb's free energy to model the combustion process in REDTOP-Lite [29]. For each case, the simulation matched the design vacuum thrust. The results captured four critical response variables: vacuum specific impulse, thrust-to-weight ratio, engine length, and outer radius. As with the DEAN simulation, the engine length was calculated for the combined length of the chamber and nozzle.

Table 7.12: IHPRPT/NGE Optimal Designs

	Case 1	Case 2	Case 3
Design Variables			
Expansion Ratio	17.7	16.0	20.9
Throat Area (in ²)	9.2	10.7	12.2
Chamber Length (in)	8.6	11.0	7.6
Characteristic Length (in)	49	57	46
Vacuum Thrust (lbf)	25,000	30,000	35,000
Oxidizer-to-Fuel Ratio	6.0	6.0	6.0
Responses			
Vacuum Specific Impulse (s)	466.0	465.7	469.4
Thrust-to-Weight Ratio	128.1	128.2	127.2
Chamber Pressure (psia)	1408	1456	1475
Chamber Temperature (R)	6545	6564	6550
Total Weight Flow (lb/s)	53.7	64.4	74.6
Maximum Mach Number, LOX	0.20	0.27	0.24
Maximum Mach Number, LH2	0.21	0.24	0.24
Chamber Wall Temperature (% Melt)	58.6	58.6	58.2
Aerospoke Wall Temperature (% Melt)	58.7	58.8	59.1
Injector Face Pressure Drop, LOX (%)	28.9	33.7	22.7
Injector Face Pressure Drop, LH2 (%)	40.0	40.0	39.4
Required Power for LOX Pump (HP)	606	763	735
Required Power for LH2 Pumps (HP)	1307	1487	2075
Δr_{throat} (in)	0.21	0.23	0.22
Engine Length (in)	32.4	35.9	38.3
Outer Chamber Radius (in)	8.5	8.9	10.3

The length and outer radius are normalized to the constraint values used in the optimization study. These results are consistent with the comparison between the 30,000 lbf case to the production RL10B-2, Table 7.13. For all three cases, the DEAN meets or exceeds the RL10's specific impulse with three times the thrust-to-weight in an engine which is approximately one quarter the length and one fifth the diameter.

Table 7.13: IHPRPT/NGE Optimal Designs Compared to RL10B-2

Case	Engine	$I_{sp,vac}$ (s)	T/W	Length (L/L_{NGE})	Outer Radius (r/r_{NGE})
Case 1: 25,000 lbf					
	DEAN	466.0	128.1	0.48	0.23
	RL10	464.1	42.9	1.98	1.16
Case 2: 30,000 lbf					
	DEAN	465.7	128.2	0.53	0.24
	RL10	464.1	43.5	2.15	1.28
Case 3: 35,000 lbf					
	DEAN	469.4	127	0.58	0.28
	RL10	464.1	43.9	2.31	1.38

A basic Low Earth Orbit (LEO) launch cost analysis was run to determine the savings associated with the DEAN's performance improvements over the RL10. The 25,000 lbf thrust DEAN was compared to the R10A-4 on the Atlas V 401 and the RL10B-2 on the Delta IV Heavy. These two launch vehicles represent the lower and upper bounds of US Air Force launch capability in the Evolved Expendable Launch Vehicle program. The analysis combined data from the *Atlas V Launch Services User's Guide* [68] and the *Delta IV Launch Services User's Guide* [69] with the ideal rocket equation to compute the change

in payload weight provided by replacing the RL10 with the DEAN. The first calculation in the analysis is to compute the change in velocity provided by the upper stage using the stage's specific impulse, empty stage weight, payload weight, and propellant weight. The next calculation uses the DEAN's performance data to determine the final stage weight for a DEAN powered upper stage assuming the same initial stage weight as the RL10 powered upper stage. The analysis then calculates a new empty weight for the stage by replacing the RL10's weight with the DEAN's weight. The new empty weight is then used to compute a new payload weight by subtracting it from the updated final stage weight. The analysis concludes by calculating an updated launch cost (\$/lb) by dividing the estimated mission cost by the new payload weight.

The LEO launch cost analysis determined DEAN powered upper stages offer increased payloads and in turn reduced launch costs. For the Atlas V 401 with its RL10A-4 providing 450.5 s of specific impulse, the DEAN upper stage gave an additional 1077 lb of payload (+5.0%) over the RL10 upper stage. The increased payload came from a combination of reduced engine weight (175 lb) and reduced propellant weight (902 lb). Together, these weight savings translated into a reduction in payload launch costs of 4.75%. The Delta IV Heavy with its RL10B-2 providing 465 s of specific impulse saw a smaller improvement. The DEAN upper stage for the Delta IV Heavy increased the payload by 557 lb, the majority of which came from engine weight savings (468 lb). The cost savings for the DEAN upper stage were similarly reduced, with the DEAN only saving 1.1% on payload launch costs over the RL10B-2. It should be noted, the above results are conservative estimates, ignoring the reduced weight from using shorter interstages to account for the DEAN's more compact size.

Taken together, the results of the IHRPT/NGE optimization study clearly show the DEAN exceeds the requirements for the IHRPT and NGE programs. Further, the DEAN outperforms traditional engine choices such as the RL10 in thrust-to-weight

ratio, packaging efficiency, and launch costs while matching the highest available specific impulse for US Air Force launch vehicles.

7.4.3 Optimizing for the X-37 Mission.

The second study looked at the propulsion needs for US Air Force space planes as embodied by the X-37. The X-37's AR2-3 engine produces 6600 lbf of vacuum thrust with a thrust-to-weight ratio of 29.3. The AR2-3 is 32 in long and has an outer radius of 10 in. It uses hydrogen-peroxide/JP-4 or hydrogen-peroxide/JP-5 propellants. The physical dimensions limit its vacuum specific impulse to 246 s. The RL10A-4 makes a better comparison design than the RL10B-2 for this mission. The RL10A-4 lacks the extended nozzle of the RL10B-2, making it significantly shorter while still delivering approximately 450 s of vacuum specific impulse [14, 24].

Combining the thrust level and dimensions of the AR2-3 with the specific impulse of the RL10A-4 and past results for the DEAN architecture gave the following requirements for the X-37 DEAN design. The X-37 DEAN needed to produce 6600 lbf vacuum thrust with a minimum vacuum specific impulse of 450.5 s and a minimum thrust-to-weight ratio of 106.5. As with the IHPRPT/NGE design, the X-37 DEAN's length requirement is set 25% shorter than the physical constraint to leave room for engine mounting hardware and turbopumps; maximum length 24 inches and maximum outer radius of 10 inches. Using these requirements as a guide, the DEAN was sized to create a base design for the X-37 optimization study, Table 7.14.

Initial results using the X-37 base design indicated the chamber wall temperature and the injector face pressure drop in the fuel expander cycle exceeded constraint values across nearly all tested designs. The limitation of the simulation resulted from fixed values used for some of the independent variables. To address this problem, parametric studies over the chamber cooling channel design, the aerospike cooling channel design, and the oxidizer-to-fuel ratio were performed. The updated values for the preassigned values for the oxidizer-

to-fuel ratio and one of the chamber cooling channel design variables (chamber stations adjustment) yielded the greatest number of valid designs.

The optimization process, Table 7.9, then found optimal designs for the X-37 DEAN. Table 7.15 shows values for the vacuum thrust and the throat area along with the updated oxidizer-to-fuel ratio and chamber stations adjustment for the X-37 optimization study.

Table 7.14: Base Design for X-37 Optimization Study

Variable	Value
Design Variables	
Expansion Ratio	16.0
Throat Area (in ²)	3.0
Chamber Length (in)	5.0
Characteristic Length (in)	55
Vacuum Thrust (lbf)	6,600
Oxidizer-to-Fuel Ratio	5.5
Chamber Stations Adjustment	2.5
Responses	
Vacuum Specific Impulse (s)	454.9
Thrust-to-Weight Ratio	101.2
Engine Length (in)	17.8
Outer Chamber Radius (in)	5.1

Table 7.15: Preassigned Parameters for X-37 Optimization Study

Variable	Value
Throat Area (in ²)	3.2
Vacuum Thrust (lbf)	6,600
Oxidizer-to-Fuel Ratio	5.5
Chamber Stations Adjustment	2.5

Once the ranges for the expansion ratio and chamber length were determined the optimization problem specification could be expressed mathematically, Equation (7.3).

$$\text{Find } \mathbf{X} = \left\{ \begin{array}{l} \text{Expansion Ratio} \\ \text{Chamber Length} \\ \text{Characteristic Length} \end{array} \right\} \text{ which maximizes}$$

Vacuum Specific Impulse(\mathbf{X})

Thrust-to-Weight Ratio(\mathbf{X})

where

$$\mathbf{X} = \left\{ \begin{array}{l} 15.0, 15.1, \dots 18.0 \\ 4.5, 4.6, \dots 6.3 \\ 45, 46, \dots 75 \end{array} \right\}$$

subject to

Max Mach Number in LOX Channels ≤ 0.54

Max Mach Number in LH2 Channels ≤ 0.81

Wall Temperatures $\leq 60\%$ Melting Point

$10\% \leq \text{Inj Face Pres Drop LOX \& LH2} \leq 40\%$

Required Power for LOX Pump ≤ 2685 HP

Required Power for LH2 Pumps ≤ 5900 HP

$\Delta r_{\text{throat}} \geq 0.1$ in

Vacuum Specific Impulse ≥ 450.5 s

Thrust-to-Weight Ratio ≥ 106.5

Engine Length ≤ 24.0 in

Outer Chamber Radius ≤ 10.0 in

(7.3)

The system simulation then generated the Pareto front for the vacuum specific impulse variation with thrust-to-weight ratio as shown in Figure 7.18. As with the previous

optimization study, a number of marginal designs resulted exceeding the pressure drop constraint for the LH2 expander cycle; marked with an 'X'. Ignoring these designs left four candidate designs for the X-37 DEAN. The highest vacuum specific impulse, circled in the figure, was selected as the optimal design (summarized in Table 7.16).

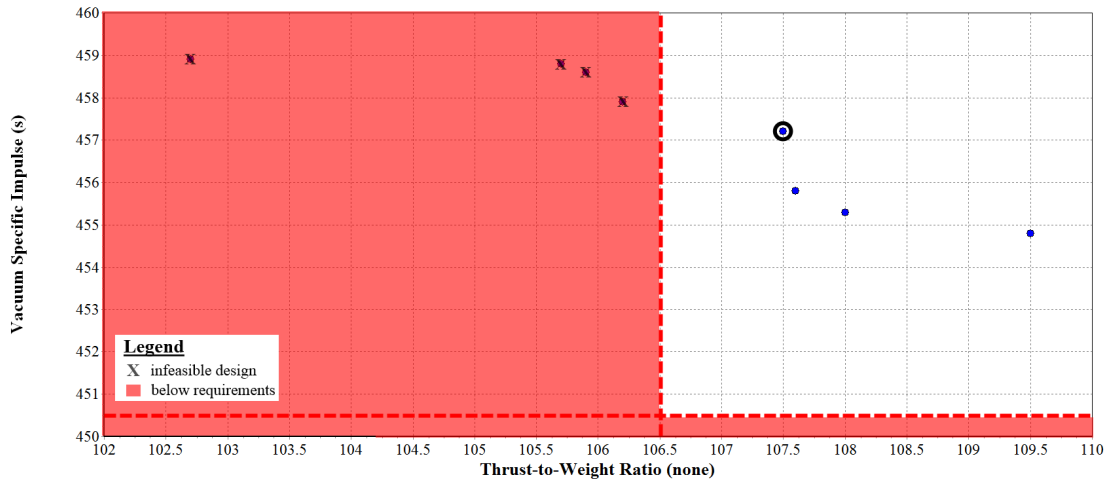


Figure 7.18: Specific Impulse Variation with Thrust-to-Weight Ratio Pareto Front for the X-37 DEAN Engine

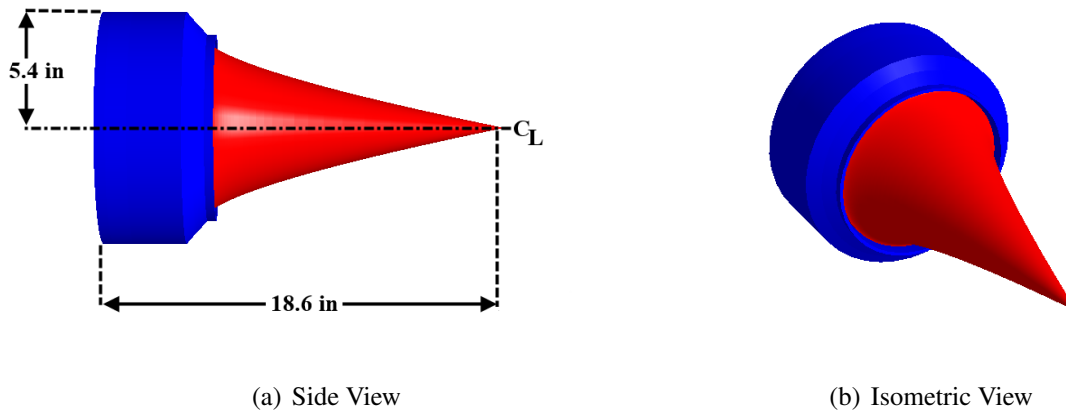


Figure 7.19: X-37 DEAN Optimal Design Geometry

Table 7.16: X-37 Optimal Design

	Value
Design Variables	
Expansion Ratio	17.0
Throat Area (in ²)	3.2
Chamber Length (in)	4.8
Characteristic Length (in)	45
Vacuum Thrust (lbf)	6,600
Oxidizer-to-Fuel Ratio	5.5
Responses	
Vacuum Specific Impulse (s)	457.2
Thrust-to-Weight Ratio	107.5
Chamber Pressure (psia)	1077
Chamber Temperature (R)	6110
Total Weight Flow (lb/s)	14.4
Maximum Mach Number, LOX	0.05
Maximum Mach Number, LH2	0.09
Chamber Wall Temperature (% Melt)	58.0
Aerospike Wall Temperature (% Melt)	59.3
Injector Face Pressure Drop, LOX (%)	21.9
Injector Face Pressure Drop, LH2 (%)	40.0
Required Power for LOX Pump (HP)	115
Required Power for LH2 Pumps (HP)	345
Δr_{throat} (in)	0.12
Engine Length (in)	18.6
Outer Chamber Radius (in)	5.4

The geometry for the optimal design is significantly smaller than the AR2-3, Figure 7.19. The optimal design is more than 20% shorter than the AR2-3 and is more than 45% smaller in diameter. The DEAN has a vacuum specific impulse which is 1.8 times the specific impulse of the AR2-3. The DEAN's thrust-to-weight ratio is 3.6 times that of the AR2-3.

To provide a more direct comparison between the DEAN and the RL10, a simulation of the RL10A-4 was performed. The RL10A-4 was modeled using the same approach as the RL10B-2 model in the IHPRPT/NGE optimization study. The results of this comparison study are shown in Table 7.17. The length and outer radius are normalized for both the DEAN and the RL10 to the constraint values used in the X-37 DEAN optimization study. Not only does the DEAN outperform the RL10 in specific impulse and thrust-to-weight ratio, it is dramatically smaller. Further, a simple scaling of the RL10 yielded a design which exceeds the size constraints for the X-37. The RL10 would have to reduce the size of its nozzle, and in turn reduce its specific impulse, to meet the size constraints.

Table 7.17: X-37 Optimal Design Compared to RL10A-4

Engine	$I_{sp,vac}$	T/W	Length	Outer Radius
	(s)		(L/L_{AR2-3})	(r/r_{AR2-3})
DEAN	457.2	107.5	0.78	0.54
RL10	449.7	48.0	1.91	1.24

Taken together, the results of the X-37 optimization study clearly show the DEAN's performance and compact size make it an excellent candidate for space planes. The DEAN's benefits make it an option when traditional engine choices such as the RL10 must sacrifice performance in order to meet the size constraints.

7.4.4 Optimizing for the Space Launch System.

Two designs were considered as part of the optimization study of NASA's SLS. The first uses four RL10 engines to achieve a vacuum thrust of 99,000 lbf with vacuum specific impulse of 462.5 s and thrust-to-weight ratio of 37.3. The second uses a single J-2X, which is powered by a gas generator cycle, to produce a vacuum thrust of 294,000 lbf and a vacuum specific impulse of 448.0 s with thrust-to-weight ratio of 55.0. Given the significant performance differences between the two designs, all comparisons were made directly between the DEAN and the selected propulsion system for each SLS design [8, 12].

Starting with the four engine SLS design, the DEAN was sized to create a base design at the lower thrust level. The cooling channel design used with the IHPRT/NGE optimization study would not work for this thrust level as constrained. As with the X-37 optimization study, various constraints, including the power required for the propellant pumps and maximum Mach numbers in the cooling channels, exceeded allowable levels across nearly all tested designs. The cooling channels were adjusted using the process developed for the IHPRT/NGE optimization study. Additionally, the fourth generation DEAN model only scaled up to approximately 100,000 lbf. Beyond 100,000 lbf, the model's trade space became constrained by several physical limitations. To address this limit, the optimization study focused on the four engine SLS design, using a cluster of three DEAN engines for J-2X SLS design. The DEAN base design for the SLS optimization study is shown in Table 7.18.

Table 7.18: Base Design for SLS Optimization Study

Variable	Value
Design Variables	
Expansion Ratio	16.0
Throat Area (in ²)	36.5
Chamber Length (in)	11.5
Characteristic Length (in)	55
Vacuum Thrust (lbf)	100,000
Oxidizer-to-Fuel Ratio	6.0
Chamber Throat AR	0.4
Chamber Stations Adjustment	3.25
Chamber Station 5 Adjustment	1.0
Chamber Cooling Channels Ratio	7.25
Nozzle Throat AR	1.90
Nozzle Station 1 Adjustment	1.7
Nozzle Station Spike Adjustment	1.0
Aerospike Cooling Channels Ratio	7.0
Responses	
Vacuum Specific Impulse (s)	460.1
Thrust-to-Weight Ratio	121.8
Engine Length (in)	55.7
Outer Chamber Radius (in)	15.2

The optimization process (Table 7.9) then provided an optimal design for the SLS DEAN. The vacuum thrust, throat area, and oxidizer-to-fuel ratio, form the list of preassigned parameters for the SLS optimization study, Table 7.19.

Table 7.19: Preassigned Parameters for SLS Optimization Study

Variable	Value
Throat Area (in ²)	37.1
Vacuum Thrust (lbf)	100,000
Oxidizer-to-Fuel Ratio	6.0

The process then provided the ranges for the expansion ratio and chamber length. Combining these values with the performance of the IHPRPT/NGE DEAN gave the optimization problem specification shown in Equation (7.4).

$$\text{Find } \mathbf{X} = \left\{ \begin{array}{l} \text{Expansion Ratio} \\ \text{Chamber Length} \\ \text{Characteristic Length} \end{array} \right\} \text{ which maximizes}$$

Vacuum Specific Impulse(\mathbf{X})

Thrust-to-Weight Ratio(\mathbf{X})

where

$$\mathbf{X} = \left\{ \begin{array}{l} 15.0, 15.1, \dots 19.5 \\ 11.0, 11.1, \dots 12.0 \\ 45, 46, \dots 75 \end{array} \right\}$$

subject to

Max Mach Number in LOX Channels ≤ 0.54

Max Mach Number in LH2 Channels ≤ 0.81

Wall Temperatures $\leq 60\%$ Melting Point

$10\% \leq \text{Inj Face Pres Drop LOX \& LH2} \leq 40\%$

Required Power for LOX Pump ≤ 2685 HP

Required Power for LH2 Pumps ≤ 5900 HP

$\Delta r_{\text{throat}} \geq 0.1$ in

Vacuum Specific Impulse ≥ 465 s

Thrust-to-Weight Ratio ≥ 106.5

(7.4)

The Pareto front for the vacuum specific impulse variation with thrust-to-weight ratio showed no marginal designs resulted, Figure 7.20. However, the required pump power for both cycles approached their constraints. Three designs met the objectives, from which

the one with the highest vacuum specific impulse, circled in the figure, was selected as the optimal design.

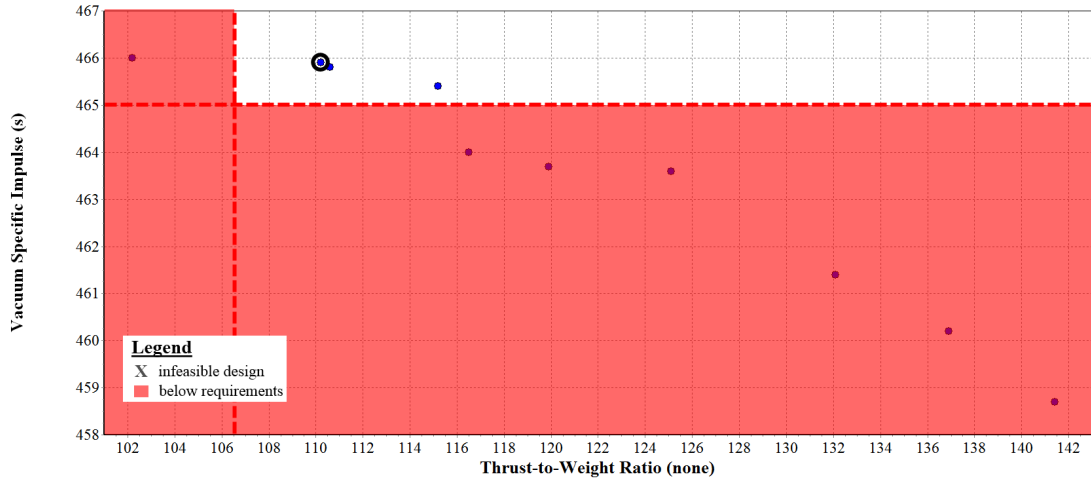


Figure 7.20: Specific Impulse Variation with Thrust-to-Weight Ratio Pareto Front for the SLS DEAN Engine

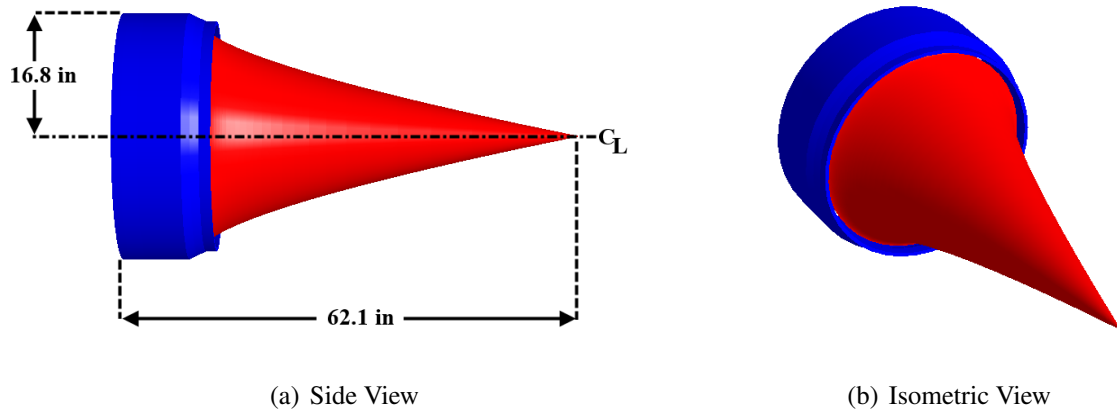


Figure 7.21: SLS DEAN Optimal Design Geometry

As can be seen in Figure 7.21, the geometry for the optimal design is significantly smaller than the cluster of RL10s from the four engine SLS design. The optimal design is approximately the same length as the stowed configuration for the four engine SLS design and is more than 84% smaller in diameter, Table 7.21. Further, the DEAN exceeds the vacuum specific impulse of the four engine SLS design while achieving a thrust-to-weight ratio nearly three times greater than the RL10 configuration. While the required pump power in both the LOX and LH2 cycles was close to constraint boundaries, margin still existed (LOX requiring 94%, LH2 88%).

The comparison of the optimal DEAN design to the two SLS baseline designs (Table 7.20) shows performance exceeding both the RL10 cluster and the J-2X in a significantly smaller package. The cluster of DEAN engines matches the J-2X in vacuum thrust while delivering 4% greater specific impulse and twice the thrust-to-weight ratio in a design which is approximately one-third the length and half the diameter.

Table 7.20: SLS Optimal Design compared to Baseline Designs

Case	Engine	F_{vac} (lbf)	I_{sp_vac} (s)	T/W	Length (in)	Outer Radius (in)
Case 1: 4 RL10s						
	DEAN	100,000	465.9	110.2	62.1 ¹	16.8
	SLS Design [8, 11]	99,000	462.5	37.3	86.5 ²	108.0
Case 2: 1 J-2X						
	3 DEANs	300,000	465.9	110.2	62.1 ³	36.2
	SLS Design [12, 37]	294,000	448.0	55.0	180.0 ⁴	60.0

Table 7.21: SLS Optimal Design

	Value
Design Variables	
Expansion Ratio	19.5
Throat Area (in ²)	37.1
Chamber Length (in)	11.2
Characteristic Length (in)	53
Vacuum Thrust (lbf)	100,000
Oxidizer-to-Fuel Ratio	6.0
Responses	
Vacuum Specific Impulse (s)	465.9
Thrust-to-Weight Ratio	110.2
Chamber Pressure (psia)	1390
Chamber Temperature (R)	6506
Total Weight Flow (lb/s)	214.7
Maximum Mach Number, LOX	0.54
Maximum Mach Number, LH2	0.65
Chamber Wall Temperature (% Melt)	51.2
Aerospike Wall Temperature (% Melt)	56.1
Injector Face Pressure Drop, LOX (%)	18.9
Injector Face Pressure Drop, LH2 (%)	35.0
Required Power for LOX Pump (HP)	2534
Required Power for LH2 Pumps (HP)	5205
Δr_{throat} (in)	0.39
Engine Length (in)	62.1
Outer Chamber Radius (in)	16.8

The LEO launch cost analysis from Section 7.4.2 was repeated for the two SLS designs, substituting SLS design and performance data for the Atlas V and Delta IV data. As with the IHPRT/NGE DEAN, the launch cost analysis showed DEAN powered upper stages offer increased payloads and in turn reduced launch costs. For the first SLS design, using 4 RL10s providing 462.5 s of specific impulse, the DEAN provided 2540 lb of additional payload (1746 lb from engine weight savings and 794 lb from propellant savings). This weight savings translated to a 1.2% reduction in launch costs. The second SLS design, powered by a single J-2X engine providing 448.0 s of specific impulse, had a more significant improvement. In this case, the DEAN upper stage increased the payload by 8580 lb, with 2622 lb coming from engine weight savings and 5957 lb from propellant savings. The related launch cost savings amount to a 3.7% reduction over the baseline SLS design. As before, the results of this analysis are conservative estimates.

The results taken together support the conclusion that the DEAN's performance, compact size, and cost savings make it an excellent candidate for super-heavy lift launch vehicles. The DEAN is not only an improvement over single expander cycle engines, it is also competitive with gas generator cycle engines like the J-2X.

7.5 Conclusion

The results of this study support conclusions in two areas: critical constraints and the viability of the DEAN architecture. The optimization studies revealed two critical constraints on the DEAN architecture; injector face pressure drop and pump horsepower requirements. For engines operating below the original design goal of 50,000 lbf thrust, the LH2 pressure drop across the injector face frequently exceeded the constraint limit of 40%. For high thrust engines the limiting factor was the required pump power for both the LOX pump (requiring 94% of the constraint value) and the LH2 pumps (requiring 88% of the constraint value).

The DEAN is a viable and compelling alternative to traditional upper stage engines across a wide range of missions. The DEAN offers significant improvements in thrust, size, thrust-to-weight ratio, and launch costs over the RL10 for the IHPRPT/NGE mission. The DEAN is also competitive for space plane missions, offering dramatic improvements in specific impulse, size, and thrust-to-weight ratio over the AR2-3 and the RL10A-4. The DEAN meets or exceeds the performance of SLS design options with more than twice the thrust-to-weight, 4% greater specific impulse, and payload launch cost savings as high as 3.7%.

VIII. Conclusions and Recommendations

8.1 Research Objectives Answered

The goal of this research was to determine the viability of the DEAN architecture by finding those missions and designs for which the DEAN's performance and physically compact packaging give it a competitive advantage over traditional upper stage engines. Addressing this goal required answering the following questions.

- What are the operational limits of the DEAN architecture in terms of thrust and specific impulse?
 - The DEAN was optimized for designs ranging from 6600 lbf vacuum thrust for the X-37 to 100,000 lbf vacuum thrust for the SLS. Trade studies conducted during the SLS optimization study indicated the current model could not reliably solve for DEAN designs above 100,000 lbf due to a number of physical constraints.
- What are the limiting constraints of the DEAN architecture?
 - The optimization studies revealed two critical constraints on the DEAN architecture; injector face pressure drop and pump horsepower requirements. For engines operating below the original design goal of 50,000 lbf thrust, the LH2 pressure drop across the injector face frequently exceeded the constraint limit of 40%. For high thrust engines the limiting factor was the required pump power for both the LOX pump (requiring 94% of the constraint value) and the LH2 pumps (requiring 88% of the constraint value).
- How does the DEAN compare to single expander cycle engines like the RL10 in terms of specific impulse, thrust-to-weight ratio, and size?

- The DEAN exceeded the performance of the RL10. The DEAN generated up to four times the thrust of the RL10 and exceeded the RL10B-2's vacuum specific impulse. The DEAN's second cooling loop gave it more than four times the pumping power of the RL10A-3 and more than twice the thrust-to-weight ratio of the RL10A-4 and RL10B-2. The increased pumping power gave the DEAN more than twice the chamber pressure of the RL10A-4 and RL10B-2 while being less than half the length.
- What missions does the DEAN offer significant advantages over traditional upper stage engines?
 - The DEAN is a viable and compelling alternative to traditional upper stage engines across a wide range of missions. The DEAN offers significant improvements in thrust, size, thrust-to-weight ratio and launch costs over the RL10 for the IHPRT/NGE mission. The DEAN is also competitive for space plane missions, offering dramatic improvements in specific impulse, size, and thrust-to-weight ratio over the AR2-3 and the RL10A-4. The DEAN met or exceeded the performance of SLS design options with more than twice the thrust-to-weight, 4% greater specific impulse, and payload launch cost savings as high as 3.7%.

8.2 Research Summary

Work at AFIT predating this research resulted in the development of an engine cycle model of the DEAN for a single design. This cycle model was built in NPSS and calculated the DEAN's thrust, specific impulse, and state values for the propellants as they flowed through the two expander cycles.

The first phase of this research built on the initial cycle model leading to the development of a proof of concept parametric system model of the DEAN. The initial

system model used a direct parametrization of the NPSS cycle model favoring model simplicity over traditional rocket engine design variables. This approach limited the range of designs the model could explore. Specifically, this model had a low reliability rating during trade studies varying radial geometry, crucial for studying the impact of the expansion ratio. In spite of these limitations, parametric studies using this model resulted in an improved design, demonstrating the utility of parametric modeling in rocket engine design. The improved design was 25% shorter than the original design and reduced the propellant weight flow by 14%.

The improved design showed the DEAN architecture offers significant performance gains over single-expander cycle-based upper stage engines such as the RL10B-2. The first phase design had a chamber pressure twice that of the RL10B-2 and twice the vacuum thrust. Finally, this improved DEAN engine was 69% shorter than the RL10B-2, despite its increased thrust.

The first phase results led to additional DEAN research efforts extending the DEAN system model to include improved engine performance and estimate the engine weight. These new analysis modules were incorporated into the second phase of this research. The second topic converted the DEAN cycle model to a LOX/Methane engine to explore the architecture's capabilities with an alternate fuel.

The second phase of this research covered the development of a new system level DEAN model integrating the lessons learned from the previous efforts to arrive at a model with the necessary fidelity, flexibility, and reliability to address the overall research questions. The development of this new model was driven by the limited trade space size and low reliability of the prototype system model and later models built from it. Improvements made in this new model included an updated parametrization, model simplification, and calculating initial estimates for the NPSS solver. The updated parametrization derived the engine geometry from traditional rocket engine parameters,

ensuring consistent designs and results. The model simplification replaced less reliable external analysis modules with a modified NPSS rocket nozzle element to compute the DEAN's thrust from values available in the DEAN cycle model. Initial estimates for the NPSS solver were calculated using a custom solver replacing previously static values with design specific values.

The improvements in the new system level model had significant impacts on the model's flexibility and reliability. The trade studies using the new model showed it supported a wide range of designs, including expansion ratios from 6.0 to 25.0. Trade studies also indicated the new model's reliability had improved significantly, with 98.7% of the 1500 runs succeeding. The new system level DEAN model was used throughout the remainder of this research.

The third phase of this research involved a detailed verification of the DEAN models and architecture. The verification process began at the individual analysis level. The source code for each engineering analysis was inspected and its methods and equations were compared to engineering principles to ensure proper implementation. Additionally, tests were run on key analysis modules to compare their calculations to expected results. Once the individual analyses were verified, the DEAN architecture and system model were tested using a series of parametric studies. These studies compared the DEAN's responses to rocket engineering theory and the RL10 family of expander cycle engines covering a wide range of engine designs.

The verification studies confirmed the DEAN architecture is feasible and delivers improved performance over single expander cycle engines in a compact package. The studies also demonstrated the DEAN model is consistent with the scientific and engineering principles of rocket propulsion. Finally the verification studies showed the DEAN exceeds the performance of the RL10 for comparable thrust levels and proved the DEAN architecture was ready for mission-specific comparisons to existing upper stage engines

The fourth phase of this research looked at the materials selection for the DEAN to find a materials selection offering consistently low-weight engines across a wide range of designs. This phase began with the development of an optimization process for the design of the cooling channels in both expander cycles. This process was applied to a base design for the materials selection study. The materials selection study then compared the performance of the material options for each DEAN component over a variety of engine designs.

The materials study yielded an updated materials selection covering a wide range of engine designs. The materials study also confirmed the following findings from previous research: the aerospike tip material selection has little influence on the engine's thrust-to-weight ratio, the chamber cooling jacket should be manufactured from silicon carbide, the LOX plumbing should be manufactured from INCONEL 718, and the LH2 plumbing should be manufactured from INCOLOY 909. The material study also found updated material selections for the aerospike cooling jacket (silicon carbide), chamber structural jacket (INCONEL 718), and the aerospike structural jacket (INCOLOY 909) which produced low weight engines across a wide range of designs compared to previous material selections.

Finally, the fifth phase of this research covered a series of optimization studies of the DEAN for the IHPRPT/NGE, X-37, and SLS missions and compared the DEAN's performance and size to traditional upper stage engines. This phase began by defining the top level design variables, preassigned parameters, and constraints for the DEAN optimization studies. A sensitivity study over the design variables identified key response variables and relationships between the design variables and key response variables. These results were used to develop an optimization process for the DEAN architecture.

The optimization process was then applied to the IHPRPT/NGE, X-37, and SLS missions. The DEAN outperformed traditional upper stage engines for all three missions.

For the NGE program, the optimized design delivers 35,000 lbf of vacuum thrust and 469.4 seconds of vacuum specific impulse with a thrust-to-weight ratio of 127.2 in an engine one quarter the size of a comparable RL10. For the X-37 mission, the optimized design operates at 6,600 lbf of vacuum thrust and has a vacuum specific impulse of 457.2 seconds with a thrust-to-weight ratio of 107.5. For the SLS, the optimized design produces a vacuum thrust of 100,000 lbf and a vacuum specific impulse of 465.9 seconds with a thrust-to-weight ratio of 110.2. When configured in a cluster of three engines, the DEAN matches the J2-X vacuum thrust with a 4% increase in specific impulse while more than doubling the J2-X's thrust-to-weight ratio. Payload launch cost savings to Low Earth Orbit for DEAN powered upper stages ranged from 1.1% to 4.75% depending on mission.

8.3 Research Contributions

1. A method for parametrically modeling rocket engines in NPSS was demonstrated including calculation of initial estimates for key parameters in the NPSS model and calculation of fluid Mach numbers in the cooling channels. The method mapped traditional rocket engine parameters to the geometry and other engine design parameters in the NPSS model. The initial estimates for the specific impulse and pump pressure ratios were calculated using a custom external solver. Mach numbers were calculated using Kriging Response Surface Models (RSMs) configured with data from National Institute of Standards and Technology. This work is covered in Chapter 3 (published in the *AIAA Journal of Spacecraft and Rockets* [27]) and Chapter 4.
2. The DEAN architecture was verified through a series of six parametric studies. These parametric studies covered relationships driven by the top level design variables: thrust, throat area, expansion ratio, oxidizer-to-fuel ratio, chamber length, and characteristic length. Responses tested with the trade studies included chamber

pressure, propellant weight flow, specific impulse, and engine weight. Each trade study varied the design variable under test plus an additional design variable to ensure the results covered a wide range of designs and not a narrow band of designs. The results from these trade studies verified the DEAN architecture conforms to rocket engine theory and exceeds the RL10's performance. This work is covered in Chapter 5 (submitted to the *AIAA Journal of Propulsion and Power*).

3. The materials selection proposed in previous research was refined to support a wide variety of missions and engine designs. Using optimized cooling channel designs for both expander cycles, a series of trade studies were run to find material selections yielding consistently low engine weight. These trade studies varied engine designs and material selections to give results spanning a wide range of engine designs. The results confirmed a number of previous findings and improved upon others. This work is covered in Chapter 6.
4. An optimization process for DEAN engines using the DEAN system level model was developed and demonstrated. The optimization problem solved by this process is a multi-objective problem seeking to maximize the DEAN's specific impulse and thrust-to-weight ratio. This process used the results of a sensitivity analysis to efficiently scope the optimization problem before solving it using a genetic algorithm to generate a Pareto front of specific impulse variation with thrust-to-weight ratio. The process was applied to the mission requirements for the IHRPT/NGE programs, the X-37 space plane, and two upper stage configurations of the SLS. This work is covered in Chapter 7 (submitted to the *AIAA Journal of Spacecraft and Rockets*).
5. Optimal DEAN engine designs were found for three IHRPT/NGE cases, the X-37 space plane, and two upper stage configurations of the SLS. The results of applying the optimization process above to these three missions show the DEAN is a viable

and compelling alternative to traditional upper stage engines across a wide range of missions. Across all three missions, the DEAN meets or exceeds traditional upper stage engines in thrust and specific impulse while offering improved size and thrust-to-weight ratios. This work is covered in Chapter 7 (submitted to the *AIAA Journal of Spacecraft and Rockets*).

8.4 Recommendations for Future Research

The recommendations in this section fall into two categories: extending current results and fifth generation DEAN research. The extending current results recommendations cover work building on results from this research without requiring additional simulation runs in the fourth generation DEAN model. The fifth generation DEAN research recommendations cover updates and additional parametric studies for the DEAN system model.

8.4.1 Extending Current Results.

8.4.1.1 Update Turbopump Design Studies.

During the first generation DEAN research Arguello and Strain designed the turbopumps for the LH2 and LOX cycles respectively. Their work verified the results from the cycle model and the first generation DEAN design [25, 26]. Repeating these design studies for the designs presented in Chapter 7 would further verify the fourth generation DEAN model and the optimized designs for the IHP RTP/NGE, X-37, and SLS DEAN engines. Given the number of designs to be considered (two turbopumps for five designs totaling ten turbopump designs), parametric modeling techniques should be explored for turbopump design software, Pumpal and RITAL, before running the individual design studies.

8.4.1.2 Update the Methane DEAN Study.

The Methane DEAN research suffered from similar challenges to those of the second and third generation DEAN research studies. The fourth generation DEAN system model's improvements successfully addressed those challenges for the LOX/LH2 DEAN

architecture. It is possible these changes could improve the Methane DEAN model's reliability and trade space size as well. A second generation Methane DEAN model should be built based on the lessons learned in the fourth generation DEAN model to determine if its improvements can yield improved results for the design of the Methane DEAN.

8.4.2 Fifth Generation DEAN Research.

8.4.2.1 Recommended Model Updates.

The fourth generation DEAN model was a major step forward in simulating the DEAN. However, it represents the limits of what can be done with the current DEAN cycle model. Future DEAN modeling should begin with a clean implementation of the DEAN cycle model in NPSS. This new implementation can address a number of outstanding concerns about the current cycle model. First and foremost, this clean implementation can be built from the ground up to support parametric design. Post research analysis indicated the current cycle model still contains a small number of fixed geometry elements that should be sized to match the current design. Additional post research analysis indicated there may be modeling elements in the cycle model needing their thermal connections verified. These thermal connections may be contributing to the high pressure drops across the injector face. Updating the cycle model implementation would also facilitate moving from NPSS v1.6.5 to the current commercial release.

To improve simulation execution time, the pre and post processing steps from the DEAN system model should be incorporated into the NPSS source code, making the NPSS model the DEAN system model, and reserving ModelCenter for integration with outside tools and automation of the DEAN model. Finally, unit tests should be developed for the individual analysis modules in the DEAN model to further verify their implementations and provide a framework for supporting future upgrades to the DEAN models.

8.4.2.2 Additional Design Studies.

The anticipated improvements in the fifth generation DEAN model make it suitable for additional DEAN design studies. Possible design studies include revisiting the third generation DEAN research into truncated nozzles, further improving the cooling channel design and optimization processes, investigating alternative materials for the cooling jackets, and investigating the marginal designs from the optimization studies in Chapter 7. While Chapter 6 confirmed the aerospike tip does not have a significant impact on the DEAN's thrust-to-weight ratio, the tip does have a significant impact on the overall engine length and in turn the length of the interstage hardware impacting stage weight. With the wall temperatures being one of the key constraints in the DEAN architecture, continuing to study and improve the cooling channel designs and material selections for the cooling jackets can only improve the results of DEAN research. Finally, the proposed improvements in the fifth generation DEAN model should address some of the causes of the high pressure drops across the injector face, possibly bringing the marginal designs from Chapter 7 back into compliance with the constraint boundaries.

8.4.2.3 Detailed Comparison of DEAN to RL10 and J-2X Using an Upper Stage Model.

The fifth generation DEAN model should be used to perform a detailed comparison between the DEAN and traditional upper stage engines using an upper stage model. The upper stage model should be parametric and include design variables to vary payload weight and orbit, propulsion system (including the DEAN, RL10, and J-2X), and controls for the sizing method (size stage for payload or size payload for stage). The upper stage model should then be used to compare the DEAN's performance to the RL10 and J-2X for a variety of missions and payloads. Potential figures of merit include total stage weight for a given payload weight, available payload weight for a given stage weight, and percent growth of stage weight per percent growth in payload weight.

Appendix A: Verification and Validation of the Fourth Generation DEAN Model

A.1 Introduction

This appendix covers the verification and validation of the individual analysis modules making up the fourth generation DEAN system model, shown in Figure A.1 and Table A.1. The organization of the appendix follows the structure of the model, beginning with the Design Variables analyses and continuing through the Constraints. Each section covers the purpose, assumptions, underlying engineering models, and implementation for the analysis modules under consideration. Verification is carried out through source code inspection and isolated analysis level testing. The source code inspection uses line by line review of the analysis source file and comparing the source code to the engineering principles used in the analysis. Validation is conducted by comparing the results of the analysis module to its purpose.

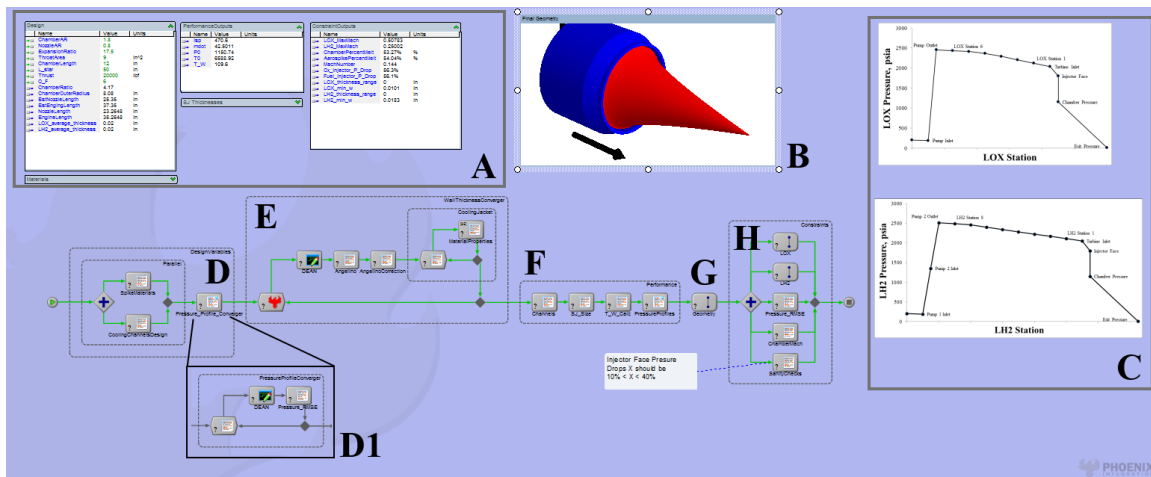


Figure A.1: Fourth Generation DEAN Model

Table A.1: Fourth Generation DEAN Model Components

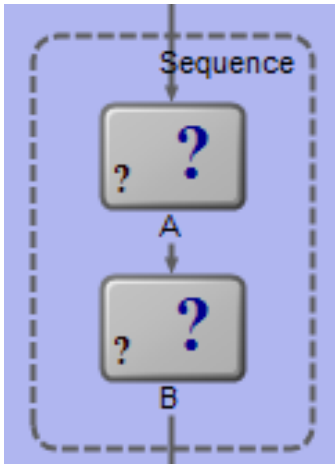
Label	Name	Description
A	Data Monitors	ModelCenter Data Monitors to provide access to key design and response variables
B	Final Geometry	DEAN geometry (chamber and aerospike) after sizing wall thicknesses
C	Pressure Profile Plots	pressure profiles for the LOX and LH2 expander cycles
D	Design Variables	system level design variables and the preprocessing analyses, including cooling channel design and initial estimates for the turbopump pressure ratios
D1	Pressure Profile Converger	a secondary module, solves for the initial estimates for the turbopump pressure ratios
E	Wall Thickness Converger	module to balance the pressure and mechanical systems and to size the cooling channel wall thicknesses
F	Performance	performance values, structural jacket wall thicknesses and T/W
G	Geometry	geometry module
H	Constraints	constraint module; maximum Mach numbers in the cooling channels and the pressure drops across the injector face

The fourth generation DEAN model is built using ModelCenter's process modeling feature. Process modeling gives model developers access to new model elements and alters how existing elements affect the execution of the model. In models built using

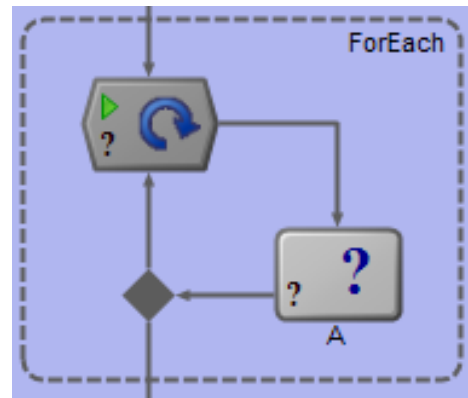
these features, often called process models, the analyses are run from left to right or top to bottom depending on the model's layout, and may include various control structures. The DEAN system level model uses several of these structures including *sequences*, *for-each loops*, *parallel branches*, and *if branches*. *Sequences*, shown in Figure A.2(a), provide a means of visually organizing analysis components in ModelCenter and for storing system level variables. Analyses in a *sequence* execute in the same order as the containing model. *For-each loops*, shown in Figure A.2(b), take scalar analyses and run them iteratively over arrays of inputs while capturing the results in output arrays turning scalar analyses into vector analyses. *Parallel branches*, shown in Figure A.2(c), organize analyses which are not interdependent in a parallel structure. Analyses which support parallel execution run simultaneously when organized under *parallel branches*. Finally, *if branches*, (Figure A.2(d)) provide a means of controlling the execution of analyses. During model execution, *if branches* select one or more paths to execute based on the specified branch condition. Using *if branches*, model developers can selectively run analyses to switch model fidelity, model required work flows, or implement model level exception handling [67].

In addition to process modeling features, the DEAN model uses a specialized looping structure and a built-in geometry component. The looping structure is the Converger, shown in Figure A.3. The Converger is a ModelCenter component which implements a fixed-point iteration solver to find designs where a calculated value matches the guessed value for one or more parameters. The Converger creates a loop when used in process models [67].

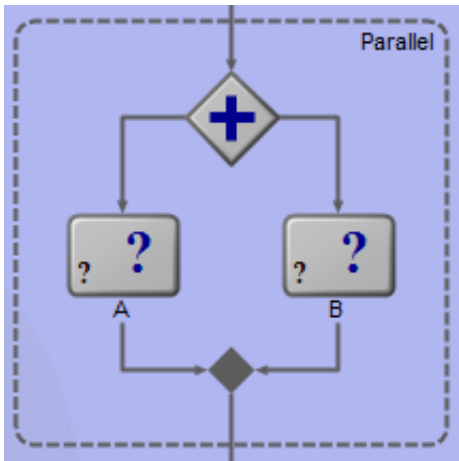
The built-in geometry component used in the DEAN system level model is the GenericSOR (Surface of Revolution) component. The GenericSOR, shown in Figure A.4, renders a surface of revolution in ModelCenter's geometry views, such as the embedded geometry of a cone shown in Figure A.4. The revolved surface is defined by a string input variable containing a list of points defining the curve to be revolved around the x-axis [67].



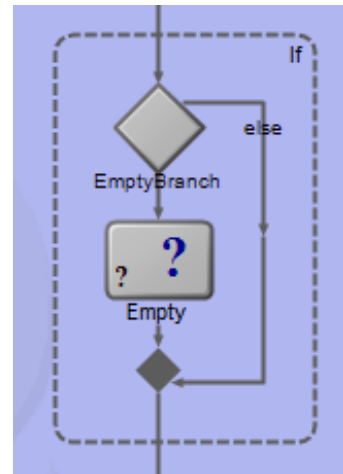
(a) Sequence Component



(b) For-Each Loop



(c) Parallel Branch



(d) If Branch

Figure A.2: ModelCenter Process Components

In the DEAN model, GenericSOR components are used to render the primary elements of the DEAN including the chamber and the aerospike.

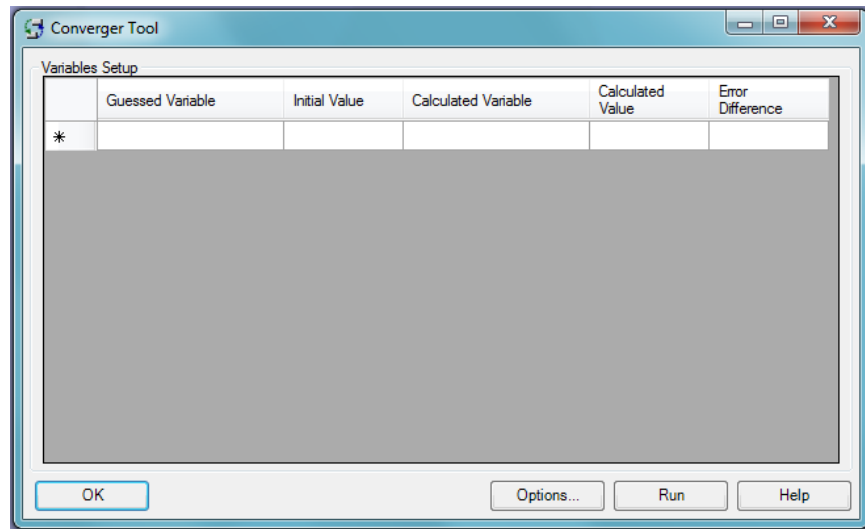


Figure A.3: ModelCenter Converger

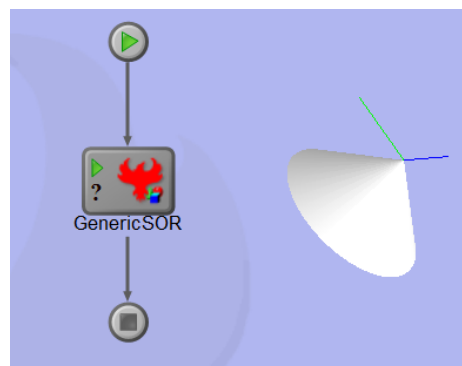


Figure A.4: ModelCenter Surface of Revolution Component

A.2 Preprocessing Step: Design Variables

The preprocessing steps in the DEAN system model are implemented by the Design Variables *sequence*, shown in Figure A.5. The first two analyses, running in a *parallel branch*, manage the material selections for the aerospike and the designs for the cooling channels. The final component is an embedded ModelCenter sub-model implementing a custom solver process to find the initial estimates for design variables relating to the pressure profiles in the two expander cycles.

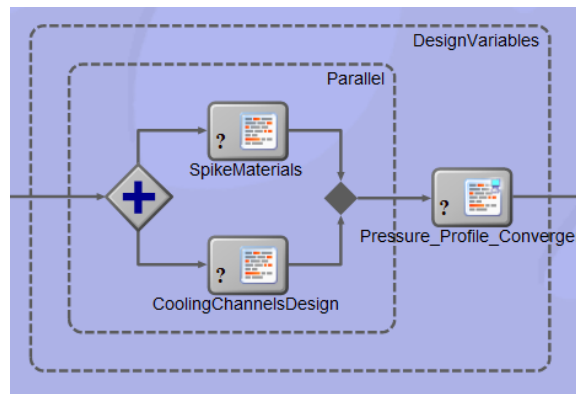


Figure A.5: DEAN Preprocessing Components

In addition to the analysis modules, the Design Variables *sequence* contains the declarations for the DEAN system level design variables. These design variables fall into three categories: engine design variables (Table A.2), modeling assumptions (Table A.3), and cooling channel design variables (Table A.4).

Table A.2: DEAN Engine Design Variables

Variable	Description
Expansion Ratio	Ratio of the exit area (A_e) to the throat area (A_t)
Throat Area (in ²)	Area of the nozzle at the throat
Chamber Length (in)	Length of the chamber, runs from the back of the engine to the throat
Characteristic Length (in)	Ratio of the chamber volume (V_c) to the throat area (A_t)
Vacuum Thrust (lbf)	Specified thrust to be produced by the engine
Oxidizer-to-Fuel Ratio	Ratio between the propellants

Table A.3: DEAN Modeling Assumption Design Variables

Variable	Description
Ambient Pressure Decision	Controls whether aerospike geometry is modeled for design or operational altitude
Operational Pressure (psia)	Ambient pressure (for vacuum, assumes 0.001 psia)
Cooling Geometry Option	Controls whether the cooling channels include a separate cover or if the structural jacket is the cover
Percent Weight of Hardware	Percent of the overall engine mass accounted for by miscellaneous hardware
Cowl Length (% Spike Radius)	Length of the engine cowl (normalized to aerospike radius at the throat)
Factor of Safety	Factor of safety for structural sizing modules
Material Strength Option	Controls whether structural sizing modules use ultimate or yield strength for stress tests
LOX Tank Pressure (psia)	Tank pressure for the LOX tank
LH2 Tank Pressure (psia)	Tank pressure for the LH2 tank

Table A.4: DEAN Cooling Channel Design Variables

Variable	Description
Chamber Throat AR	Aspect ratio of the chamber cooling channels at the throat
Chamber Stations Adjustment	Controls how the aspect ratio of chamber cooling channels vary over the length of the engine
Chamber Station 5 Adjustment	Controls the aspect ratio of the chamber cooling channels at station 5
Chamber Cooling Channels Ratio	Ratio of the number of chamber cooling channels to the chamber circumference at the throat
Nozzle Throat AR	Aspect ratio of the aerospike cooling channels at the throat
Nozzle Station 1 Adjustment	Controls the aspect ratio of the aerospike cooling channels at station 1
Nozzle Stations Spike Adjustment	Controls how the aspect ratio of aerospike cooling channels vary over the length of the engine
Aerospike Cooling Channels Ratio	Ratio of the number of aerospike cooling channels to the aerospike circumference at the throat

A.2.1 Spike Materials.

The purpose of the Spike Materials component is to manage the material selections for the aerospike components during trade studies, allowing for parametric studies over material selections for multiple engine components when they use the same material. Each material selection is coded as an integer based on the values used in the Material Properties component. The source code for the Spike Materials component is shown in Listing A.1. It is structured as a series of cases. The three cases are: the aerospike is made of a single material (lines 2-7), the structural jacket and tip are the same material (lines 8-13), and each component is controlled individually (lines 14-18).

Listing A.1: Spike Materials Source Code

```
1 function run() {
2   if (Unified_Spike.value) {
3     Spike_Cool_Mat.value = All_Spike_Mat.value;
4     // shift over 1 for SJ material
5     SJSpike_Mat.value = All_Spike_Mat.value + 1;
6     Spike_Tip_Mat.value = All_Spike_Mat.value;
7   }
8   else if (UnifiedSJandTip.value) {
9     Spike_Cool_Mat.value = Spike_Cool_Mat_In.value;
10    SJSpike_Mat.value = SJSpike_Mat_In.value;
11    // shift back by 1 for tip material
12    Spike_Tip_Mat.value = SJSpike_Mat_In.value - 1;
13  }
14  else {
15    Spike_Cool_Mat.value = Spike_Cool_Mat_In.value;
16    SJSpike_Mat.value = SJSpike_Mat_In.value;
17    Spike_Tip_Mat.value = Spike_Tip_Mat_In.value;
18  }
19 }
```

Inspection of the source code showed the component was implemented correctly. Consider the first case, where the aerospike is made of a single material. Line 2 determines if this is the currently selected case by testing the boolean variable Unified_Spike. Then, lines 3-6 assign the unified material selection (All_Spike_Mat) to each of the three aerospike components: the cooling jacket, the structural jacket, and the tip. The material coding for the structural jacket is one greater than the cooling jacket and the tip, so the structural jacket is assigned a value one greater than the unified material code. A similar process is used

for the other two cases. As is shown from this inspection, the Spike Materials component correctly manages the materials selection for the aerospike components for all three use cases, fulfilling its purpose.

A.2.2 Cooling Channels Design.

The purpose of the Cooling Channels Design component is to determine physical design parameters of the chamber and aerospike cooling channels. The physical design parameters for the cooling channels include the number of cooling channels and the scheduling of the cooling channels' aspect ratios along the length of the engine. The component was verified through inspection of its source code.

The number of cooling channels in each of the expander cycles is proportional to the circumference of the element being cooled (either the chamber or the aerospike), and is constrained by the minimum channel spacing of 0.02 inches. The Number of Channels component calculates the circumferences for both the chamber and the aerospike, then applies scaling factors to determine the number of channels in each expander cycle.

The aspect ratios for the cooling channels are based upon Martin's approach to designing the cooling channels. In the first generation DEAN research, Martin used varying aspect ratios along the length of the cooling channels to balance the cooling needs with the maximum Mach number constraints. In both cooling jackets, Martin selected low aspect ratios (shorter channels, smaller cross-sectional area) at the throat to increase the cooling rate and higher aspect ratios (taller channels, larger cross-sectional areas) at the end of the cooling jacket to maintain a velocity below the maximum allowable Mach number. The smaller cross-sectional area in the low aspect ratio regions increases the fluid velocity and in turn the power required to pump the fluid. This increase in required pump power drives the solver in the cycle model toward designs yielding more power from the turbine by increasing the amount of heat extracted from cooling the engine, effectively increasing the cooling rate in those regions. The larger cross-sectional areas in the high aspect ratio

regions reduce the velocity of the fluid and account for the decrease in density (increase in volume) caused by heating the fluid. Combined, these two effects ensure the fluid stays below its Mach number limit, preventing catastrophic failure of the engine [2]. In the Cooling Channels Design component, the throat station is used as the specified aspect ratio and scaling multipliers are used to control how the aspect ratios change along the length of the engine.

Listing A.2 contains the source code for the Cooling Channels Design component. Line 2 calculates the outer throat radius, which is also the radius of the exit area. Rearranging the definition of expansion ratio, see Equation (A.1), and combining it with the relationship between the area of a circle and its radius gives Equation (A.2), implemented in Line 2. Line 3 calculates the inner throat radius from the throat area. The DEAN throat is the annulus defined by the inner and outer throat radii which correspond to the nozzle and chamber structures at the throat. Equation (A.3) is the equation for the area of an annulus. Solving this equation for the inner radius yields Equation (A.4) and is implemented by Line 3. Lines 5 and 6 compute the number of channels by multiplying the circumference ($2r\pi$) of the chamber and aerospike by their respective scaling factors and rounding the results to yield integer values.

The remainder of Listing A.2 computes the aspect ratios. Lines 8-25 calculate the aspect ratios for the chamber cooling channels. The *for loop* defined in Line 8 iterates over the six stations in the chamber. The *if statements* within the loop select the appropriate scaling factor for each station: no scaling factor for the throat on Lines 9 and 10, the station 5 scaling factor on Lines 11-13, and the default scaling factor on Lines 14-24. In Martin's scheduling for the chamber aspect ratios, station 1 has an approximately 25% higher aspect ratio than the preceding stations. This adjustment is applied in Line 17 unless the scaling factor equals 1.0. In the case of the scaling factor equaling 1.0, the component applies

a constant aspect ratio along the entire length of the engine. Lines 18-20 implement the branch to handle this case for station 1. Finally, Lines 22-24 cover the remaining stations.

Similarly, Lines 27-47 calculate the aspect ratios for the nozzle cooling channels. The *for loop* defined in Line 27 iterates over the eight stations in the nozzle. Using Martin's scheduling approach, the throat is not scaled (Lines 28-29), the stations immediately before and after the throat are scaled up 20% unless the aspect ratios are constant (Lines 30-35), the final station is scaled by the spike scaling factor (Lines 36-38), the first two stations are scaled by the station 1 scaling factor (Lines 39-41), and the remaining stations linearly adjust their aspect ratios from station 2 to station 5 (Lines 42-46). The linear transition is implemented by computing and applying a step increment.

Listing A.2: Cooling Channels Design Source Code

```

1 function run() {
2   var r_to = Math.sqrt(ExpansionRatio.value * ThroatArea.value / Math.PI);
3   var r_ti = Math.sqrt(Math.pow(r_to,2) - (ThroatArea.value / Math.PI));
4
5   ChamberN.value = Math.round(2 * r_to * Math.PI * ChamberNRatio.value);
6   NozzleN.value = Math.round(2 * r_ti * Math.PI * NozzleNRatio.value);
7
8   for (i = 0; i < ChamberStationsAR.length; i++) {
9     if (i == 5)
10      ChamberStationsAR.value(i) = ChamberThroatAR.value;
11     else if (i == 4)
12      ChamberStationsAR.value(i) = ChamberThroatAR.value *
13      ChamberStation5Adjustment.value;
14     else if (i == 0) {
15       if (ChamberStationsAdjustment.value != 1.0) // Matching Martin
16        ChamberStationsAR.value(i) = ChamberThroatAR.value *
17        ChamberStationsAdjustment.value * 1.25;
18       else // if adjustment == 1.0, no additional scaling
19        ChamberStationsAR.value(i) = ChamberThroatAR.value *
20        ChamberStationsAdjustment.value;
21     }
22     else
23      ChamberStationsAR.value(i) = ChamberThroatAR.value *
24      ChamberStationsAdjustment.value;
25   }
26
27   for (i = 0; i < NozzleStationsAR.length; i++) {
28     if (i == 5)
29      NozzleStationsAR.value(i) = NozzleThroatAR.value;
30     else if ((i == 6) || (i == 4)) {
31       if (NozzleStationsSpikeAdjustment.value != 1.0)
32        NozzleStationsAR.value(i) = NozzleThroatAR.value * 1.2;
33       else // if spike adjustment == 1, no additional scaling
34        NozzleStationsAR.value(i) = NozzleThroatAR.value;
35     }
36   }
37 }

```

```

36  else if (i == 7)
37      NozzleStationsAR.value(i) = NozzleThroatAR.value *
38      NozzleStationsSpikeAdjustment.value;
39  else if ((i == 0) || (i == 1))
40      NozzleStationsAR.value(i) = NozzleThroatAR.value *
41      NozzleStation1Adjustment.value;
42  else {
43      var step = (NozzleStationsAR.value(0) - (NozzleThroatAR.value +
44      NozzleThroatAR.value * NozzleStationsSpikeAdjustment.value)/2)/3;
45      NozzleStationsAR.value(i) = NozzleStationsAR.value(i-1) - step;
46  }
47  }
48  }

```

$$\epsilon = A_e/A_t \quad (\text{A.1})$$

$$r_{t_o} = \sqrt{\epsilon * A_t/\pi} \quad (\text{A.2})$$

$$A = \pi(r_o^2 - r_i^2) \quad (\text{A.3})$$

$$r_i = \sqrt{r_o^2 - A/\pi} \quad (\text{A.4})$$

Calculating the required number of cooling channels based on changes to the radial size and determining the cooling channel aspect ratios for the DEAN is essential to making the DEAN model capable of operating over a wider range of design points. As the above inspection shows, the Cooling Channels Design component correctly calculates these values, validating this component.

A.2.3 Pressure Profile Converger.

The purpose of the Pressure Profile Converger, implemented as an embedded ModelCenter sub-model and shown in Figure A.6, is to determine the initial estimates for the vacuum specific impulse and the pressure ratios of the LOX and LH2 pumps. These four values drive the calculations for the estimated pressure profiles in the two expander cycles, and have a significant impact on the reliability and the results of the DEAN cycle

model. Prior to the inclusion of the Pressure Profile Converger, the DEAN system level model used a static set of estimates for these variables, despite their dependance on design variables such as thrust and expansion ratio. The Pressure Profile Converger sub-model includes a custom solver, a copy of the DEAN cycle model, and an error calculation analysis to determine the quality of the estimated pressure profiles. This component was verified through inspection and testing.

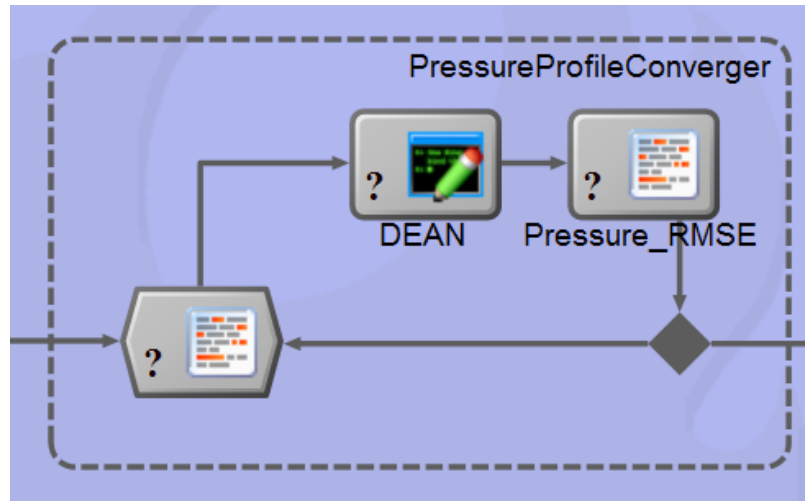


Figure A.6: Pressure Profile Converger Components

The custom solver iteratively calls the other components to determine the best values for the four required initial estimates. First, the solver calls the DEAN cycle model, stepping through values for the specific impulse and pump pressure ratios until the DEAN analysis runs to completion and returns a calculated value for the specific impulse. The DEAN cycle model is very sensitive to the pump pressure ratios and will often fail when given poor estimates. However, the specific impulse calculation is not strongly affected by these variables. Therefore, the first successful run of the DEAN cycle model is sufficient to yield a high quality estimate for the specific impulse.

The custom solver then uses the estimated specific impulse for the remaining iterations carried out in two loops. The first loop solves for the LOX pump pressure ratio by finding a series of working pressure ratios and selecting the one with the lowest root mean square error across the entire LOX cycle. The second loop uses a similar approach to solve for the pressure ratio of the first LH2 pump. Note, the solver always assumes the second LH2 pump has a pressure ratio of 2.0 based on current design assumptions for the DEAN.

Listing A.3 contains the source code for the custom solver in the Pressure Profile Converger. Lines 4-11 initialize the design variable estimates and internal arrays used to track intermediate results in the solver. Note, the estimated specific impulse (TargetIsp) is initialized to -1.0 s, making the success condition for the specific impulse loop any specific impulse greater than zero. Lines 14-18 solve for the estimated specific impulse by iteratively calling the findTargetIsp function (Listing A.4). To save iterations, the *for loop* declared in Line 14 uses a series of decreasing step sizes (the value *n*) in the findTargetIsp function. Lines 16-17 contain the success criteria, testing for positive values of specific impulse and breaking out of the *for loop* when one is found. Lines 20-23 conclude the estimation process for the specific impulse by testing for success after the specific impulse iteration, throwing an error if the *for loop* was unsuccessful and setting the specific impulse value used in later iterations to the updated estimate otherwise.

Lines 26-46 solve for the estimated value of the LOX pump pressure ratio. Line 26 calls the setGuessLowerValues function (Listing A.5) to initialize the limits of the *for loop* used to solve for the LOX pump pressure ratio (Lines 28-29). Lines 30-31 set the pressure ratios used in the cycle model for the current iteration. The *try-catch* block in Lines 32-42 stores the current estimate for the LOX pump pressure ratio (Line 33) and executes the DEAN cycle model and the root mean square error calculation component (Line 34). The DEAN cycle model generates a ModelCenter error when it fails to find a solution for the current design, using the *try-catch* block enables the custom solver to trap the ModelCenter

error and continue executing the current iteration loop (Lines 40-41). Lines 35-38 break out of the iteration loop when the current results yield an error value greater than the previous iteration. Otherwise the loop is continued. This early exit is included to save computation time by eliminating unnecessary iterations. Solving for the estimated LOX pump pressure ratio concludes with Lines 45-46 which call the findBestPR function to iterate through the results and find the pressure ratio with the lowest root mean square error and setting the DEAN cycle model and the Pressure Profile Converger results to this value.

A similar process is applied to find the LH2 pump 1 pressure ratio estimate in Lines 49-68. Finally, Line 71 executes the DEAN cycle model and the root mean square error calculation one final time to compute and record the root mean square error for the final estimates found by the Pressure Profile Converger.

Listing A.3: Pressure Profile Converger Source Code

```

1 void function run() {
2
3     // initialize key vars
4     TargetIsp.value = -1;
5     LH2Pump2PRGuess.value = LH2Pump2PRGuessDefault;
6     PRdes_Pump2F.value = LH2Pump2PRGuessDefault;
7
8     var LOXPumpPRGuessValues = new Array();
9     var LOX_RMSEValues = new Array();
10    var LH2Pump1PRGuessValues = new Array();
11    var LH2_RMSEValues = new Array();
12
13    // solve for TargetIsp
14    for (var n = 4; n >= 1; n = n/2) {
15        findTargetIsp(n);
16        if (TargetIsp.value > 0)
17            break;
18    }
19
20    if (TargetIsp.value < 0)
21        throw "Unable to find TargetIsp";
22    else
23        IspGuess.value = TargetIsp.value;
24
25    // solve for LOX Pump PR
26    setGuessLowerValues();
27    var iLOX = 0;
28    for (LOXpr = LOXPumpPRGuessLower; LOXpr <= LOXPumpPRGuessUpper;
29        LOXpr += PumpPRGuessStep) {
30        LOXPumpPRGuess.value = LOXpr;
31        LH2Pump1PRGuess.value = LH2pr;
32        try {
33            LOXPumpPRGuessValues[iLOX] = LOXpr;

```



```

34     LOX_RMSEValues[iLOX] = LOX_RMSE.value;
35     if ((iLOX > 0) && (LOX_RMSEValues[iLOX-1] < LOX_RMSEValues[iLOX]))
36         break;
37     else
38         iLOX++;
39 }
40 catch (err) {
41     // continue
42 }
43 }
44
45 PRdes_Pump0.value = findBestPR(LOXPumpPRGuessValues, LOX_RMSEValues);
46 LOXPumpPRGuess.value = PRdes_Pump0.value;
47
48 // solve for LH2 Pump 1 PR
49 setGuessLowerValues();
50 var iLH2 = 0;
51 for (LH2pr = LH2Pump1PRGuessLower; LH2pr <= LH2Pump1PRGuessUpper;
52     LH2pr += PumpPRGuessStep) {
53     LH2Pump1PRGuess.value = LH2pr;
54     try {
55         LH2Pump1PRGuessValues[iLH2] = LH2pr;
56         LH2_RMSEValues[iLH2] = LH2_RMSE.value;
57         if ((iLH2 > 0) && (LH2_RMSEValues[iLH2-1] < LH2_RMSEValues[iLH2]))
58             break;
59         else
60             iLH2++;
61     }
62     catch (err) {
63         // continue
64     }
65 }
66
67 PRdes_Pump1F.value = findBestPR(LH2Pump1PRGuessValues, LH2_RMSEValues);
68 LH2Pump1PRGuess.value = PRdes_Pump1F.value;
69
70 // run the analysis one more time with final values to get RMSEs
71 var LH2_RMSE_value = LH2_RMSE.value;
72 }

```

Listing A.4 contains the source code for the `findTargetIsp` function. This function iteratively runs the DEAN cycle model to find an estimate for the specific impulse and is driven by the *for loop* declared in Line 3. This *for loop* iterates over a series of estimates for the specific impulse until the DEAN cycle model returns a final estimate for the specific impulse. For each estimated specific impulse, the DEAN cycle model is set to use the current estimate (Line 4), initialize the limits for the pressure ratios used in the nested *for loops* below by calling the `setGuessLowerValues` function (Line 5), and then uses a pair of nested *for loops* to iteratively call the DEAN cycle model with a series of pressure ratio estimates until the cycle model returns a valid specific impulse estimate. The two *for loops*

(Lines 6-7 and Lined 9-10) use the stepN argument to modify the step size, with larger step sizes giving fewer iterations. The *try-catch* block in Lines 12-18 captures ModelCenter errors from failed runs of the cycle model and exits the function using the return statement (Line 14) when the estimated specific impulse is found.

Listing A.4: Find Taget Isp Function Source Code

```

1 function findTargetIsp(stepN) {
2     // looking for first successful run to get target isp
3     for (var isp = IspGuessLower; isp <= IspGuessUpper; isp += IspGuessStep) {
4         IspGuess.value = isp;
5         setGuessLowerValues();
6         for (LH2pr = LH2Pump1PRGuessLower; LH2pr <= LH2Pump1PRGuessUpper;
7             LH2pr += (stepN*PumpPRGuessStep)) {
8             LH2Pump1PRGuess.value = LH2pr;
9             for (LOXpr = LOXPumpPRGuessLower; LOXpr <= LOXPumpPRGuessUpper;
10                LOXpr += (stepN*PumpPRGuessStep)) {
11                 LOXPumpPRGuess.value = LOXpr;
12                 try {
13                     TargetIsp.value = IspResult.value;
14                     return;
15                 }
16                 catch(err) {
17                     // continue
18                 }
19             }
20         }
21     }
22 }

```

Listing A.5 contains the source code for the setGuessLowerValues function. Originally designed to calculate the lower limits for the pump pressure ratio estimates, this function was later modified to compute both the upper and lower limits. Lines 2-3 break up the calculation of the estimated chamber pressure into two steps. The chamber pressure can be found from the characteristic velocity, thrust, specific impulse, and throat area as shown in Equation (A.5). Line 2 calculates the weight flow, Equation (A.6), for use in the chamber pressure calculation in Line 3. Substituting the definition for the weight flow from Equation (A.6) into the chamber pressure calculation gives Equation (A.7), which is implemented in Line 3.

The remaining lines use the estimated chamber pressure to compute the upper and lower limits for the pressure ratios. The pressure ratios are computed from the ratio of the

of the chamber pressure to the pressure coming into the pump times the estimated pressure losses in the plumbing. The upper limits are set to 250% of this ratio and the lower limits are set to 175% of this ratio.

Listing A.5: Set Guess Lower Values Function Source Code

```

1 function setGuessLowerValues() {
2     var wdot = Thrust.value / IspGuess.value;
3     var P_c_guess = wdot * c_star / (ThroatArea.value * g0);
4     LH2Pump1PRGuessLower = Math.floor((1.75 * P_c_guess) /
5         (P_TankH * plumbingLosses) / LH2Pump2PRGuessDefault);
6     LH2Pump1PRGuessUpper = Math.floor((2.5 * P_c_guess) /
7         (P_TankH * plumbingLosses) / LH2Pump2PRGuessDefault);
8     LOXPumpPRGuessLower = Math.floor((1.75 * P_c_guess) / (P_Tank0 * plumbingLosses));
9     LOXPumpPRGuessUpper = Math.floor((2.5 * P_c_guess) / (P_Tank0 * plumbingLosses));
10 }

```

$$p_c = \frac{c^* F}{I_{sp} A_t g_0} \quad (\text{A.5})$$

$$\dot{w} = \frac{F}{I_{sp}} \quad (\text{A.6})$$

$$p_c = \frac{c^* \dot{w}}{A_t g_0} \quad (\text{A.7})$$

The simulation results and reliability of the DEAN system model before and after integrating the Pressure Profile Converger demonstrated it is functioning correctly. Before integrating the Pressure Profile Converger, initial surveys of the DEAN trade space indicated the pressures in the cooling channels were inversely proportional to the thrust and directly proportional to the expansion ratio. A design of experiments over the thrust, expansion ratio, and throat area was run to test these results (Table A.5).

The results of cooling channel pressure study are shown in Figure A.7. In the figure, the horizontal axis is the expansion ratio, the vertical axis is the pressure in the LOX cooling channel at the throat, and the axis running into the page is the throat area. Additionally,

Table A.5: Design Variables for Cooling Channel Pressure Study

Variable	Low	High	Levels
Vacuum Thrust (lbf)	20,000	50,000	5
Expansion Ratio	12	22	5
Throat Area (in ²)	7	12	5

the color of the data points represents the thrust level, with blue points representing thrust levels of 20,000 lbf at the low end, and red points representing thrust levels of 50,000 lbf at the high end. These results support the conclusions from the initial surveys of the DEAN trade space. For a given thrust level, indicated by points of a single color, the pressure in the LOX cooling channel increased with increasing expansion ratio. Further, the highest pressure levels were associated with the lowest thrust (blue points or 20,000 lbf) and the lowest pressures were associated with the highest thrust (red points or 50,000 lbf). These results do not agree with rocket engine theory. The expected results would be a direct relationship between the thrust and internal pressures (including pressures in the cooling channels) and no significant relationship between the pressures in the cooling channels and the expansion ratio [5].

The cooling channel pressure study was repeated after integrating the Pressure Profile Converger into the system level DEAN model. The updated results are shown in Figure A.8. The axes are the same as in Figure A.7. Several key differences are shown in the updated results, all of which counter the original conclusion. First, for a given thrust level, indicated by points of a single color, the pressure in the cooling channel was independent of the expansion ratio. Second, the highest pressures were associated with the highest thrust levels (red points or 50,000 lbf) and the lowest pressures were associated with the lowest thrust levels (blue points or 20,000 lbf). Further, the pressure levels increased with

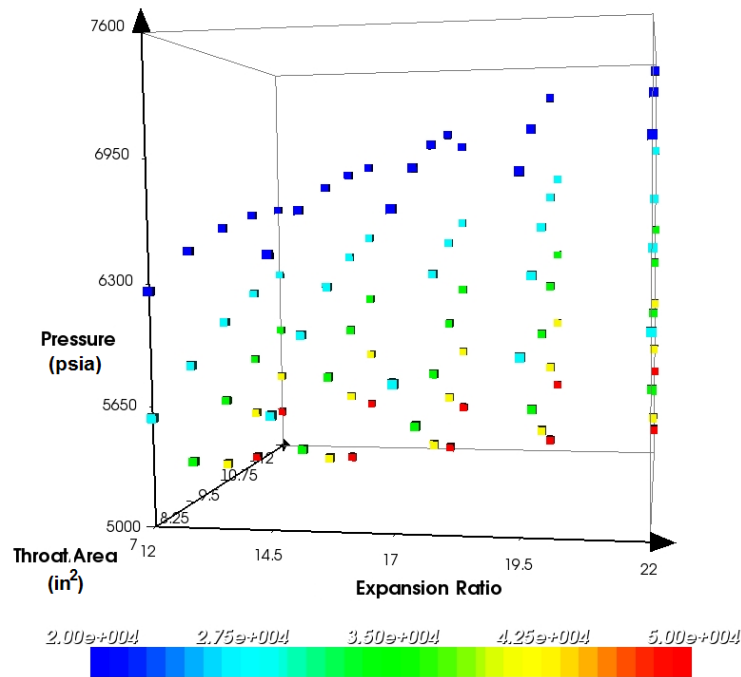


Figure A.7: Cooling Channel Pressure Study Results (without converger)

decreasing throat area. All of these results are consistent with expectations for expander cycles indicating the addition of the solver improves the model.

Finally, the reliability of the DEAN system model improved significantly with the addition of the Pressure Profile Converger. Before the inclusion of the Pressure Profile Converger, the system level verification tests had a reliability of 93.2%. After integrating the Pressure Profile Converger, the reliability of the DEAN system model during system level verification tests increased to 98.6%.

Starting with high quality estimates for the vacuum specific impulse and pump pressure ratios improves the results and reliability of the DEAN system model. The inspection and tests of the Pressure Profile Converger above demonstrate this sub-model

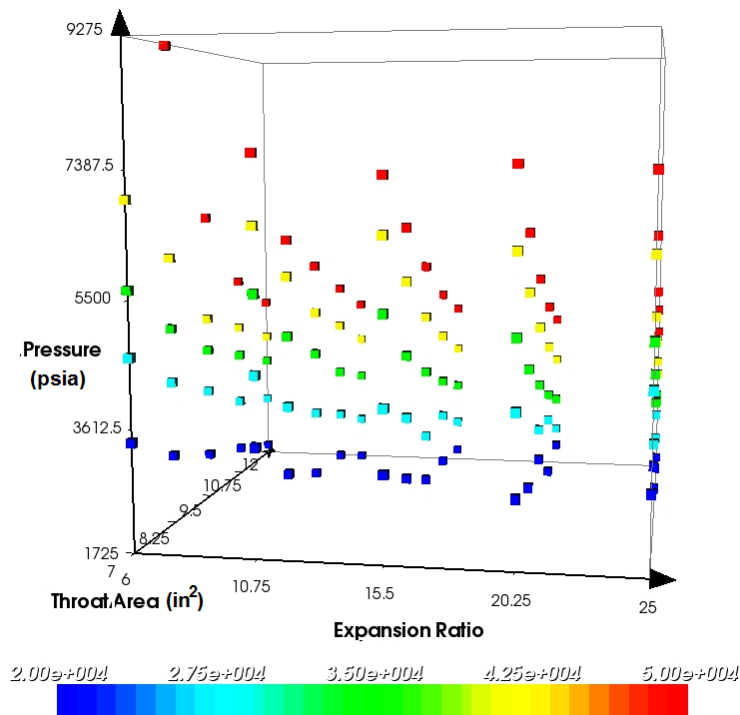


Figure A.8: Cooling Channel Pressure Study Results (with converger)

calculates significantly improved estimates for these values compared to the static estimates from earlier models, fulfilling its purpose.

A.2.3.1 DEAN.

The DEAN component in the Pressure Profile Converger sub-model is a copy of the DEAN cycle analysis (see Section A.3 for complete modeling details). The cycle model is built in NASA's Numerical Propulsion System Simulation (NPSS). This model balances the fluid flows, mechanical power, and thermal flows in the two expander cycles to converge on the engine performance parameters for a given design point. It is included in the Pressure Profile Converger loop to calculate the pressure profiles in the two expander cycles based for each set of estimated design variables under test by the solver loop. These values are

compared to the estimated pressure profiles using the root mean square error component to determine the quality of the estimated values.

A.2.3.2 Pressure RMSE.

The purpose of the Pressure RMSE component is to compute the root mean square error between the estimated pressure levels and the actual pressure levels in the two expander cycles of the DEAN engine. The root mean square error is computed by taking square root of the average of the squares of the difference between the expected and actual values. Inspection of the source code demonstrated the component functioned correctly and delivered the desired result.

Lines 2-3 compute the square root of the average value for the squares of the differences for each cycle as computed by the mse function (Lines 6-16). The mse function uses a *for loop* (Lines 10-12) to sum up the squares of the differences. Line 14 then divides the sum by the number of stations in the given cycle to compute the average before returning the average in Line 15.

Listing A.6: Pressure RMSE Source Code

```

1 function run() {
2   LOX_RMSE.value = Math.sqrt(mse(Est_LOX_PressProfile, LOX_PressProfile));
3   LH2_RMSE.value = Math.sqrt(mse(Est_LH2_PressProfile, LH2_PressProfile));
4 }
5
6 function mse(est, actual) {
7   var n = est.length;
8
9   var mse_val = 0;
10  for (i = 0; i < n; i++) {
11    mse_val = mse_val + (Math.pow(est.value(i) - actual.value(i),2));
12  }
13
14  mse_val = mse_val/n;
15  return mse_val;
16 }

```

A.3 Engine Cycle Analysis: Wall Thickness Converger

The engine cycle analysis portion of the DEAN model is defined by the Wall Thickness Converger loop, shown in Figure A.9 and the analyses contained within it.

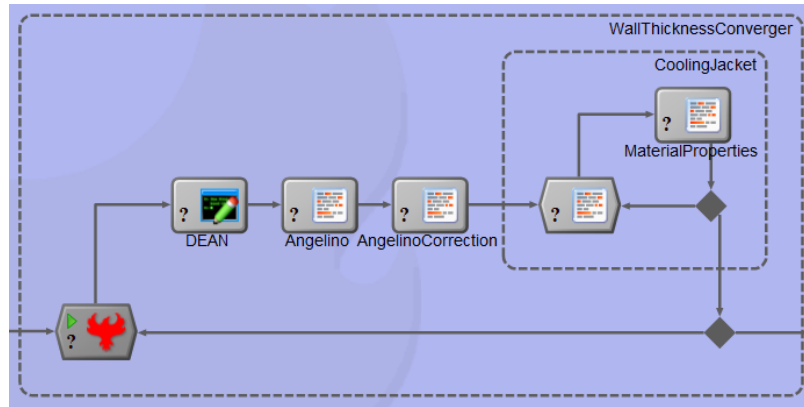


Figure A.9: Engine Cycle Analysis Components

There are five components contained in the Wall Thickness Converger loop. The first is the DEAN cycle model. This component is the core of the DEAN analysis, using NPSS to balance the two expander cycles. The second and third components are the Angelino and Angelino Correction analyses. These components work together to create an approximate geometry for the aerospike used in later sizing analyses. Finally, the fourth and fifth components, in their own internal sizing loop, are the Cooling Jacket and Material Properties components. These last two components work together to determine the wall thickness for the cooling jackets in both the combustion chamber and the aerospike. The outer converger loop iterates over these components until the guessed cooling jacket wall thicknesses match the calculated wall thicknesses in the Cooling Jacket component.

A.3.1 DEAN.

As mentioned above, the DEAN cycle model, an NPSS model of the DEAN engine, is the core of the system analysis for the DEAN engine. This component uses NPSS to balance the fluid flows, mechanical power, and thermal flows in the two expander cycles to converge on the engine performance parameters for a given design. The DEAN cycle model, originally developed by David Martin as part of his thesis, remains essentially the

same in the DEAN system model [2]. Specifically, the modeling of the two expander cycles is identical to Martin's model except for the use of parametrization as documented in Chapter 3 and an update to station numbering to make the model consistent with published documentation. The primary changes in this version of the DEAN cycle model are updated preprocessing calculations, to address the robustness of the model, the new parametrization discussed in Section 4.3.1, and updated performance calculations, to eliminate the need for TDK which greatly simplifies the system level model. The component was verified through inspection of its source code.

NPSS is a computer simulation tool for modeling aircraft and rocket engines. Engine simulations built in NPSS provide higher fidelity results than engine cycle studies. NPSS has been developed by the NASA Glenn Research Center, with assistance from the aerospace propulsion industry. Models built in NPSS consist of a series of interconnected software objects representing the components of the engine under consideration. The object connections are made using NPSS Application Programming Interfaces modeling fluid flows, mechanical power, and thermal flows called "ports". A built-in solver in NPSS is then used to drive the model design variables to converge on a design point by balancing the fluid flows, mechanical power, and thermal flows in the model [31].

The NPSS model of the DEAN engine includes elements to simulate the various components of the engine. Many of the engine components are modeled using built-in NPSS simulation elements. For example, the combustion chamber is modeled using a RocketComb1 element and the aerospike nozzle is modeled using a RocketNozzle element. The primary complexity in the NPSS DEAN model is in the elements used to model the plumbing in the engine. This complexity is required to properly capture the fluid and thermal flows which are critical to any expander cycle. These flows are the source of the power used to drive the turbomachinery. The plumbing elements are modeled using Valve04 elements to model the pressure drop in the plumbing and customized

CoolingVolume elements to model the heat loss in the lines. Wall2 elements are used to connect the plumbing to the combustion chamber and the aerospike nozzle where the plumbing functions as part of the cooling jackets. Full details of the NPSS modeling elements used in the DEAN model can be found Section 3.2.2.

While the cooling jackets in the DEAN are continuous volumes, the NPSS model represents them as a series of eight discrete stations. Figure A.10 shows the locations of these stations in the model. The chamber consists of five equally spaced sections, with stations (represented by dots) at the mid-point of each section plus a station at the engine's throat. The oxidizer loop (the outer wall of the chamber) and the fuel loop (the aerospike) are represented by separate sets of stations. The external portion of the aerospike has two additional stations in the first half of the nozzle only in the fuel loop.

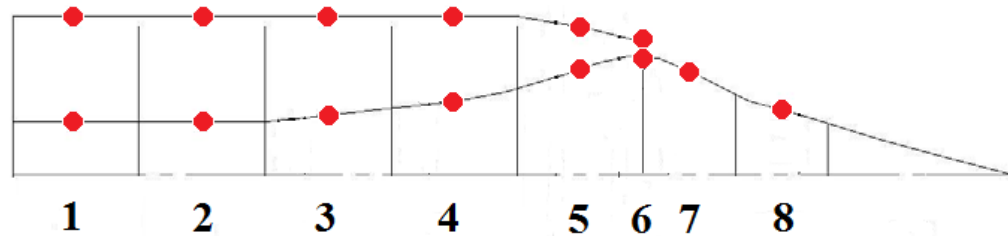


Figure A.10: DEAN Geometry

The NPSS DEAN model source file is structured into five sections both to improve readability and to simplify the process of bringing the model into the ModelCenter environment. Only the first section (design variables) is intended to be edited during design exploration, either by hand or by ModelCenter as part of automated trade studies. The design variables section is a list of declarations for the top level design variables, including the variables listed in Table A.2. Additional variables in this section include various initial

estimates required for NPSS independent variables. Table A.6 lists the critical independent variables in this section of the model.

Table A.6: DEAN Independent Variables Listing

Variable	Description
PRdes_PumpO	Initial estimate for the LOX pump pressure ratio
PRdes_Pump1F	Initial estimate for the first LH2 pump pressure ratio
PRdes_Pump2F	Initial estimate for the second LH2 pump pressure ratio
Ox_Bypass	Initial estimate for the percent of mass flow moving through the oxidizer bypass

The second section, the constants section, lists the various physical constants used in the model, including estimated values for enthalpy and density of the fluids in the expander cycles and geometric values not specified by the design variables such as the cross sectional area of the pipes. This section should only be edited as part of an update to the working fluids in the model, for example changing the propellant from liquid hydrogen to liquid methane. The third section, the derived values section, calculates the values required by the NPSS elements from the design variables and constants in the previous sections. The calculations in this section will be discussed below as part of the verification of the DEAN cycle model. The fourth section, the DEAN section, contains the declarations of the NPSS elements for the DEAN cycle model and the solver configuration and execution. This section is the portion of the model which implements and balances the two expander cycles. The fifth and final section, the output generation section, prints out a detailed report of the results of the cycle balance from the fourth section. This report includes both overall engine performance parameters such as thrust and specific impulse as well as detailed fluid state values such as temperature and pressure at each station in both expander cycles. The

remainder of this section of the text will focus on the computational parts of the NPSS DEAN model, namely the derived values and the DEAN sections.

The majority of the updates to the NPSS DEAN model occurred in the derived values section. This section includes updated engine geometry calculations and calculations to estimate the pressure levels in each expander cycle. The updated engine geometry calculations include the inner and outer radii of the chamber and the throat, the chamber's average cross-sectional area, the nozzle length, and injection ratio which is the ratio of the chamber cross-sectional area at the injector face to the throat area. Listing A.7 contains the source code which calculates the overall engine geometry from the design variables.

Listing A.7: DEAN Geometry Calculations

```

1 // calculate outer throat and chamber radii
2 real r_to = (Epsilon * A_throat / PI)**0.5; // outer throat radius
3 real r_co = r_to + 1; // per design specs
4
5 // calculate inner throat radius
6 real r_ti = (r_to**2 - (A_throat / PI))**0.5; // inner throat radius
7
8 // calculate chamber volume from L_star
9 real V_c = Lstar * A_throat;
10
11 // calculate inner chamber radius from chamber volume
12 // need some intermediate values: V2 and Z
13 real V2 = PI * 0.2 * ChamberLength *
14         (r_co**2 - (r_co**2 + r_co*r_to + r_to**2)/3);
15
16 // use quadratic formula to get r_ci
17 real A = 3;
18 real B = r_ti;
19 real C = (V_c - PI * r_co**2 * ChamberLength + V2 +
20         0.2 * PI * ChamberLength * r_ti**2) / (0.2 * PI * ChamberLength);
21 real r_ci = (-B + (B**2 - 4*A*C)**0.5) / (2*A);
22
23 // chamber average area is volume / length
24 real A_c = V_c / ChamberLength;
25
26 // Chamber ratio is the ratio of A_c to A_t
27 real chamberRatio = A_c / A_throat;
28
29 // Injection ratio is the ratio of the
30 // chamber area at the injection face to the A_t
31 real A_ci = (r_co**2 - r_ci**2) * PI;
32 real injectionRatio = A_ci / A_throat;
33
34 // Vspike_int: SOLID INTERNAL AEROSPIKE VOLUME CALCULATION
35 // 2 components: linear side and sloped side
36 // Vspike_int = Vol1 + Vol2
37 // 1st Component: Linear Side

```

```

38 // Vol1 = pi*r^2*L (Volume of Cylinder)
39 real Vol1 = 0.4 * PI * ChamberLength * r_ci**2;
40
41 // 2nd Component: Sloped side starts between stations 2 and 3
42 // and goes to station 6
43 // Vol2 = Volume of Conical Frustum - sloped portion of chamber volume (in^3)
44 // NOTE: Vol eqn is from http://mathworld.wolfram.com/ConicalFrustum.html
45 real Vol2 = PI * 0.6 * ChamberLength * (r_ti**2 + r_ti * r_ci + r_ci**2)/3;
46
47 // in^3, Solid Aerospike Volume Internal to Chamber
48 real Vspike_int = Vol1 + Vol2;
49
50 // find the nozzle length
51 real r_t = (A_throat / PI)**0.5;
52 real A_e = A_throat * Epsilon;
53 real r_e = (A_e / PI)**0.5;
54
55 // step 2: find total cone length and length of cone to throat
56 real l_total = r_e / tan(alpha);
57 real l_t = r_t / tan(alpha);
58
59 // step 3: NozzleLength is the delta of l_total and l_t
60 real nozzleLength = l_total - l_t;
61 }

```

Line 2 uses the definition of the expansion ratio to find the outer throat radius. The outer throat radius of the DEAN is the radius of the circle defining the exit area. Solving the definition of the expansion ratio shown in Equation (A.1) for the exit area and substituting the area of a circle for the exit area gives Equation (A.8). As noted above, the outer throat radius, r_{to} is the same as the exit radius, r_e . Making this substitution and solving for the outer throat radius gives Equation (A.9), which is implemented by Line 1 of Listing A.7. Based on Martin's original definition of the chamber's contour of the chamber, the chamber outer radius is one inch greater than the throat outer radius. Line 3 implements this calculation.

$$\pi r_e^2 = \epsilon A_t \quad (\text{A.8})$$

$$r_{to} = \sqrt{\epsilon A_t / \pi} \quad (\text{A.9})$$

The inner throat radius is the radius of the aerospike at the throat. This radius can be found from the throat area and the outer throat radius. The throat area is the area of a disc,

which is shown in Equation (A.3). The outer radius in Equation (A.3) is the outer throat radius, and the inner radius is the inner throat radius. Substituting these definitions, and the throat area for the area of the disc, and then solving for the inner throat radius gives Equation (A.10). Line 6 implements this calculation.

$$r_{ti} = \sqrt{r_{to}^2 - A_t/\pi} \quad (\text{A.10})$$

The chamber volume is calculated from the definition of characteristic length, shown in Equation (A.11) [5]. Solving for the chamber volume gives Equation (A.12). Line 9 implements this calculation.

$$L^* = V_c/A_t \quad (\text{A.11})$$

$$V_c = L^*A_t \quad (\text{A.12})$$

In the original parametrization of the DEAN cycle model, the chamber volume was calculated from the inner and outer chamber and throat radii. Solving the calculations from the original parametrization for the inner throat radius instead of the chamber volume yields the calculations required to calculate the final radius in the DEAN engine. The chamber volume is composed of three elements, shown in Figure A.11: a hollow cylinder running the length of the chamber representing the volume displaced by the majority of the aerospike nozzle referred to as Volume 1, the difference between a cylinder and a frustum with a shared outer radius representing the volume removed from the chamber by the reduction in chamber radius over the last 20% of the chamber (station 5 in Figure A.10) referred to as Volume 2, and a hollow conical frustum representing the volume displaced by the converging portion of the aerospike nozzle covering the last 60% of the chamber length (stations 3-5 in Figure A.10) referred to as Volume 3.

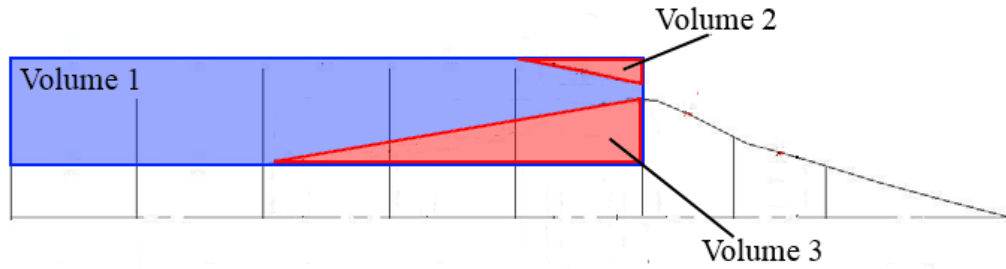


Figure A.11: DEAN Chamber Volume Elements

Equation (A.13) gives the calculation in terms of this relationship. Equation (A.14) uses the equation for the volume of a hollow cylinder to define the volume of Volume 1 in terms of the chamber radii.

$$V_c = V_1 - V_2 - V_3 \quad (\text{A.13})$$

$$V_1 = \pi L_c (r_{co}^2 - r_{ci}^2) \quad (\text{A.14})$$

Volume 2 is the volume removed by the reduction in chamber radius at the throat. This volume is the difference between a cylinder with a radius equal to the chamber's outer radius and a frustum with r_1 equal to the chamber's outer radius and r_2 equal to the chamber's inner radius. Equation (A.13) shows this relationship and Equation (A.16) shows the calculation for the volume of a frustum. Expanding Equation (A.13) with the definitions for V_c and V_f gives Equation (A.17). Dividing out the common terms, πL , gives Equation (A.18). Finally, substituting 20% of the chamber length for L , the outer chamber radius for r , and the outer chamber and throat radii for r_1 and r_2 respectively gives Equation (A.19) which calculates Volume 2.

$$V_2 = V_c - V_f \quad (\text{A.15})$$

$$V_f = \frac{1}{3}\pi L(r_1^2 + r_1 r_2 + r_2^2) \quad (\text{A.16})$$

$$V_2 = \pi L r^2 - \frac{\pi L}{3}(r_1^2 + r_1 r_2 + r_2^2) \quad (\text{A.17})$$

$$V_2 = \pi L(r^2 - (r_1^2 + r_1 r_2 + r_2^2)/3) \quad (\text{A.18})$$

$$V_2 = 0.2L_c\pi(r_{co}^2 - (r_{co}^2 + r_{co}r_{ci} + r_{ci}^2)/3) \quad (\text{A.19})$$

Finally, Volume 3, the hollow conical frustum, represents the volume displaced by the converging portion of the aerospike nozzle and can be calculated based on Equation (A.16). For Volume 3, the inner radius of the hollow portion of the frustum is the same as the second radius in the frustum volume equation. Subtracting the cylindrical volume for this radius, $\pi L r_2^2$, from Equation (A.16) gives the volume for a hollow frustum, shown in Equation (A.20). Substituting 60% of the chamber length for L , and the inner throat and chamber radii for r_1 and r_2 respectively gives Equation (A.21) which calculates Volume 3.

$$V_f h = \frac{1}{3}\pi L(r_1^2 + r_1 r_2 - 2r_2^2) \quad (\text{A.20})$$

$$V_3 = \frac{0.6L_c}{3}\pi(r_{ti}^2 + r_{ti}r_{ci} - 2r_{ci}^2) \quad (\text{A.21})$$

Taken together, Equation (A.13), Equation (A.14), Equation (A.19), and Equation (A.21) define how the chamber volume is calculated in the original parametrization of the DEAN

NPSS model. With the new parametrization, chamber volume is calculated from the characteristic length as shown in Equation (A.12) and the inner chamber radius must be calculated from the relationships above. The inner chamber radius appears in the equations for Volume 1 and Volume 3. The equation for Volume 3 is of the form of a quadratic equation which can be solved using the quadratic formula with the proper algebraic transformations. These transformations start with rearranging Equation (A.13) to solve for Volume 3 which gives Equation (A.22).

$$V_3 = -V_c + V_1 - V_2 \quad (\text{A.22})$$

Substituting the definitions of Volume 1 and Volume 3 into Equation (A.22) gives Equation (A.23). Carrying out the division of $\frac{0.6L_c}{3}$ on the left hand side and distributing the πL_c on the right hand side gives Equation (A.24). Then, dividing both sides by $0.2L_c\pi$ gives Equation (A.25).

$$\frac{0.6L_c}{3}\pi(r_{ti}^2 + r_{ti}r_{ci} - 2r_{ci}^2) = -V_c + \pi L_c(r_{co}^2 - r_{ci}^2) - V_2 \quad (\text{A.23})$$

$$0.2L_c\pi(r_{ti}^2 + r_{ti}r_{ci} - 2r_{ci}^2) = -V_c + \pi L_c r_{co}^2 - \pi L_c r_{ci}^2 - V_2 \quad (\text{A.24})$$

$$r_{ti}^2 + r_{ti}r_{ci} - 2r_{ci}^2 = \frac{-V_c + \pi L_c r_{co}^2 - \pi L_c r_{ci}^2 - V_2}{0.2L_c\pi} \quad (\text{A.25})$$

The r_{ci} term on the right hand side needs to be brought over to the left hand side to group all of the r_{ci} terms together. To do this, the r_{ci} is separated out on the right hand side which gives Equation (A.26). Canceling out terms in $\frac{\pi L_c r_{ci}^2}{0.2L_c\pi}$ gives Equation (A.27). This step gives the simplified value of $-5r_{ci}^2$ on the right hand side which can be moved to the left hand side giving Equation (A.28). Finally, moving the right hand side to the left hand side gives Equation (A.29) which is in the standard form of a quadratic equation.

$$r_{ti}^2 + r_{ti}r_{ci} - 2r_{ci}^2 = \frac{-V_c + \pi L_c r_{co}^2 - V_2}{0.2L_c\pi} - \frac{\pi L_c r_{ci}^2}{0.2L_c\pi} \quad (A.26)$$

$$r_{ti}^2 + r_{ti}r_{ci} - 2r_{ci}^2 = \frac{-V_c + \pi L_c r_{co}^2 - V_2}{0.2L_c\pi} - 5r_{ci}^2 \quad (A.27)$$

$$3r_{ci}^2 + r_{ti}r_{ci} + r_{ti}^2 = \frac{-V_c + \pi L_c r_{co}^2 - V_2}{0.2L_c\pi} \quad (A.28)$$

$$3r_{ci}^2 + r_{ti}r_{ci} + \frac{V_c - \pi L_c r_{co}^2 + V_2 + 0.2\pi L_c r_{ti}^2}{0.2L_c\pi} = 0 \quad (A.29)$$

With Equation (A.29) being a quadratic equation in standard form, the value of the inner chamber radius can be solved using the quadratic formula, Equation (A.30) by letting $a = 3$, $b = r_{ti}$, c equal the remaining terms and applying positive option for the \pm . Lines 11-21 implement these calculations.

$$\begin{aligned} &\text{For } ax^2 + bx + c = 0 \\ &x = \frac{-b \pm \sqrt{b^2 - 4ac}}{2a} \end{aligned} \quad (A.30)$$

The next three calculations, Lines 24, 27, and 32 from Listing A.7, compute various key ratios required for later calculations. The final blocks of code in Listing A.7 relate to the geometry of the aerospike nozzle. Lines 34-48 calculate the volume of the portion of the aerospike contained within the chamber using the volume of a cylinder and the volume of a conical frustum similar to previous calculations. The remaining code estimates the length of the external portion of the aerospike nozzle. According to Sutton and Biblarz, the length of an aerospike nozzle can be estimated using the length of a conical nozzle of the correct parameters. Sutton and Biblarz recommend setting the half angle equal of the conical nozzle between 10 and 12 degrees and setting its expansion ratio equal to the aerospike nozzle's expansion ratio. Computing the length of a conical nozzle involves

calculating the difference in the heights of cones with the specified half angle. The first cone has a base area equal to the throat area and the second cone has an area equal to the exit area. Figure A.12 shows how these two cones relate to calculating the nozzle length [24].

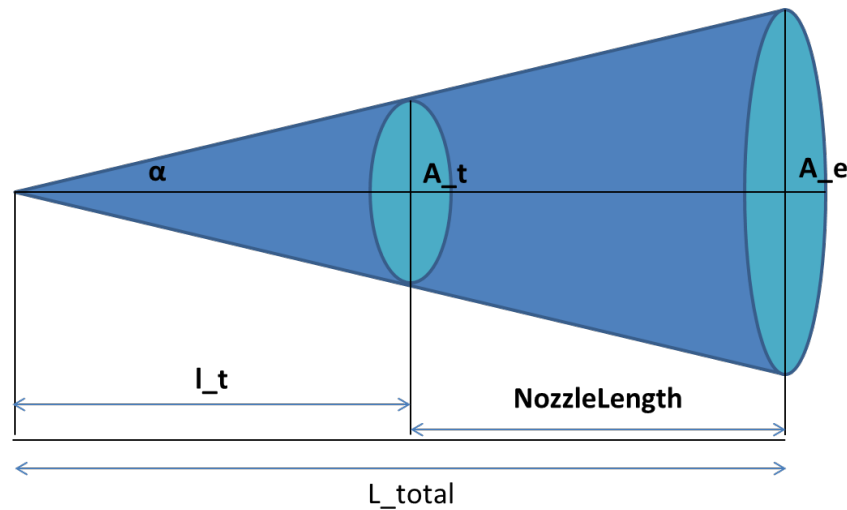


Figure A.12: Calculating Conical Nozzle Length

Lines 51-53 compute the radii for the bases of the cones with base areas of the throat and the exit area. Lines 56-57 then compute the l_{total} and l_t shown in Figure A.12 using the tangent relationship with the half angle alpha of 12 degrees, which was set in the constants section of the model. Finally, Line 60 computes the actual nozzle length from the difference of the other two lengths.

Listing A.8 shows the next block of code of the derived values section of the DEAN cycle model. This block of code estimates the pressure levels in the two expander cycles from the estimated specific impulse (TargetIsp) and notional pressure gains and losses associated with the pumps, turbines, and plumbing.

Listing A.8: DEAN Estimated Pressure Level Calculations

```

1 // Calculate the estimated pressure profile
2 real mdot = Thrust / TargetIsp;
3 real mdotO = (O_F / (O_F + 1)) * mdot; //Oxidizer mass flow rate (lbm/s)
4 real mdotH = mdot - mdotO; //fuel mass flow rate (lbm/s)
5
6 // calculate P0_guess from mdot, c and a_t
7 real P_c = mdot * c_star / (A_throat * g0);
8
9 // calculate the LOX pressure profile
10 int numLOX_stations = 11;
11 real LOX_EstPresProfile[11];
12 LOX_EstPresProfile[0] = P_TankO * .95; // start just below ox tank pressure
13 LOX_EstPresProfile[1] = LOX_EstPresProfile[0] * PRdes_PumpO;
14
15 // injector losses
16 LOX_EstPresProfile[numLOX_stations-1] = P_c * (1 + injectorPressureLoss);
17
18 // turbine losses
19 LOX_EstPresProfile[numLOX_stations-3] =
20     LOX_EstPresProfile[numLOX_stations-1] * 1.5;
21
22 // bypass pressure
23 LOX_EstPresProfile[numLOX_stations-2] =
24     (LOX_EstPresProfile[numLOX_stations-1] +
25     LOX_EstPresProfile[numLOX_stations-3])/2;
26
27 // for loop to enter values into the cooling channel stations.
28 // Assume linear pressure loss through the channels (6 stations)
29 int i;
30 for(i = 2; i < numLOX_stations - 3; i++) {
31     // From station CV01 to CV01, subtract equal pressure drops
32     // (linearly decrease) to get from exit of pump to entrance of turbine
33     LOX_EstPresProfile[i] = LOX_EstPresProfile[i-1] -
34         ((LOX_EstPresProfile[1] - LOX_EstPresProfile[numLOX_stations - 3]) / 7);
35 }
36
37 // stations (P_CV0#) are numbered forward to aft
38 real P_OCV1 = LOX_EstPresProfile[0]; // Pressure for OCV1 (psia)
39 real P_OCV2 = LOX_EstPresProfile[1]; // Pressure for OCV2 (psia)
40 real P_CV06 = LOX_EstPresProfile[2]; // Pressure for CV06 (psia)
41 real P_CV05 = LOX_EstPresProfile[3]; // Pressure for CV05 (psia)
42 real P_CV04 = LOX_EstPresProfile[4]; // Pressure for CV04 (psia)
43 real P_CV03 = LOX_EstPresProfile[5]; // Pressure for CV03 (psia)
44 real P_CV02 = LOX_EstPresProfile[6]; // Pressure for CV02 (psia)
45 real P_CV01 = LOX_EstPresProfile[7]; // Pressure for CV01 (psia)
46 real P_OCV3 = LOX_EstPresProfile[8]; // Pressure for OCV3 (psia)
47 real P_TBCV1 = LOX_EstPresProfile[9]; // Pressure for TBCV1 (psia)
48 real P_OCV4 = LOX_EstPresProfile[10]; // Pressure for OCV4 (psia)
49
50
51 // calculate the Fuel pressure profile
52 int numH2_stations = 13;
53 real LH2_EstPresProfile[13];
54 LH2_EstPresProfile[0] = P_TankH * .95; // start just below fuel tank pressure
55
56 //pump 1 pressure increase
57 LH2_EstPresProfile[1] = LH2_EstPresProfile[0] * PRdes_Pump1F;
58
59 //pump 2 pressure increase
60 LH2_EstPresProfile[2] = LH2_EstPresProfile[1] * PRdes_Pump2F;
61

```

```

62 // injector losses
63 LH2_EstPresProfile[numH2_stations - 1] = P_c * (1 + injectorPressureLoss);
64
65 // turbine losses (currently just a guess)
66 LH2_EstPresProfile[numH2_stations - 2] =
67     LH2_EstPresProfile[numH2_stations - 1] * 1.25;
68
69 // for loop to enter values into the cooling channel stations.
70 // Assume linear pressure loss through the channels (8 stations)
71 for(i = 3; i < (numH2_stations - 2); i++) {
72     //From station HCV1 to CVH1, subtract equal pressure drops (
73     // linearly decrease) to get from exit of pump to entrance of turbine
74     LH2_EstPresProfile[i] = LH2_EstPresProfile[i-1] -
75         ((LH2_EstPresProfile[2] - LH2_EstPresProfile[numH2_stations-2]) / 9);
76 }
77
78 // stations (P_CVH#) are numbered forward to aft
79 real P_HCV1 = LH2_EstPresProfile[0]; // Pressure for HCV1 (psia)
80 real P_HCV2 = LH2_EstPresProfile[1]; // Pressure for HCV2 (psia)
81 real P_HCV3 = LH2_EstPresProfile[2]; // Pressure for HCV3 (psia)
82 real P_CVH8 = LH2_EstPresProfile[3]; // Pressure for CVH8 (psia)
83 real P_CVH7 = LH2_EstPresProfile[4]; // Pressure for CVH7 (psia)
84 real P_CVH6 = LH2_EstPresProfile[5]; // Pressure for CVH6 (psia)
85 real P_CVH5 = LH2_EstPresProfile[6]; // Pressure for CVH5 (psia)
86 real P_CVH4 = LH2_EstPresProfile[7]; // Pressure for CVH4 (psia)
87 real P_CVH3 = LH2_EstPresProfile[8]; // Pressure for CVH3 (psia)
88 real P_CVH2 = LH2_EstPresProfile[9]; // Pressure for CVH2 (psia)
89 real P_CVH1 = LH2_EstPresProfile[10]; // Pressure for CVH1 (psia)
90 real P_HCV4 = LH2_EstPresProfile[11]; // Pressure for HCV4 (psia)
91 real P_HCV5 = LH2_EstPresProfile[12]; // Pressure for HCV5 (psia)

```

The pressure levels in both cycles are estimated using the same process, described in detail for the LOX expander cycle and shown in Lines 9-48. The work flow for the estimation process is to calculate the pressure gains from the pump(s) and the pressure losses from the injector and turbine and then calculate the losses in the cooling channels and other plumbing by linearly interpolating between the pressure level coming out of the pump and the pressure level going into the turbine.

Lines 12-13 estimate the pressure gain in the LOX cycle by assuming a 5% loss from the tank to the pump and a pressure gain from the pump based on the estimated pressure ratio from the Pressure Profile Converger. The initial pressure ratio, PR_{des_PumpO} , is specified in the design variables section of the DEAN cycle model. Lines 16-20 estimate the pressure loss across the injector and turbine in the LOX cycle. The assumed pressure loss across the injector is specified by multiplying the chamber pressure P_c by $1 + injectorPressureLoss$. The $injectorPressureLoss$ variable is set to a value of 0.2 in

the constants section of the DEAN cycle model, which yields an injector pressure loss of 20% of the chamber pressure, the value recommended in *Space Propulsion Analysis and Design* [5]. The pressure loss across the turbine is assumed to be 33% as specified by the 1.5 multiplier in Line 20.

This series of calculations requires an estimated chamber pressure, which is computed in Lines 2-7. The estimated chamber pressure is based on three design variables: thrust, throat area, and estimated specific impulse. The thrust and estimated specific impulse are used to compute the weight flow in Line 2 based on Equation (A.6). Then in Line 7, the computed weight flow and the throat area are combined with the characteristic exit velocity (c^*) to compute the estimated chamber pressure according to Equation (A.7) [5]. The value for the characteristic exit velocity is determined by the chemistry of the combustion reactants, and is specified in the constants section of the DEAN cycle model.

The linear interpolation between the exit pressure from the LOX pump and the inlet pressure at the LOX turbine is computed in the *for-loop* in Lines 30-35. Finally, Lines 38-48 map the estimated pressure levels to variables used in the DEAN section of the model to initialize the station pressures with the initial estimates. The same process is implemented for the LH2 cycle in Lines 52-91. An additional set of calculations in the LOX cycle on Lines 23-25 compute the pressure level in the bypass by averaging the pressure levels before the turbine and the injector face.

While the majority of the updates to the DEAN cycle model occurred in the derived values section, two key updates were made in the underlying model of the expander cycles. The first of these changes is a simple renumbering of the stations to synchronize the model with published documentation. The second change in the DEAN section of the NPSS model is to the thrust calculation. In previous versions of the DEAN cycle model, the thrust was calculated using the standard NPSS rocket nozzle element. This element calculates rocket performance assuming a bell nozzle. Hall discusses the differences between the

calculations in the rocket nozzle element and aerospike nozzle theory in his thesis. In particular, when the pressure profile across the aerospike is available, for example from an analysis in TDK, the thrust for an aerospike nozzle can be calculated with Equation (A.31) [4].

$$F = F_m + F_{cowl} + F_{pressure} + F_{nondesign} \quad (A.31)$$

Comparing Hall's results for total thrust, which include all four terms in Equation (A.31), to the results using the standard NPSS rocket nozzle element showed the majority of the difference between the two thrust values was in the $F_{nondesign}$ term. This term accounts for the thrust component from operating the engine above or below its design altitude. As can be seen in Equation (A.32), $F_{nondesign}$ is the result of the pressure difference between the exit pressure and the ambient pressure acting on the exit area.

$$F_{nondesign} = (p_e - p_{amb})A_e \quad (A.32)$$

A modified rocket nozzle element was created to account for the $F_{nondesign}$ term. This new element simply adds the $F_{nondesign}$ value to the total thrust calculated by the standard bell nozzle analysis. Since the true exit area of an aerospike nozzle depends on the ambient conditions and how those conditions affect the expansion of the exhaust flow, the updated rocket nozzle component uses the design flow exit area, which is the minimum exit area for an aerospike nozzle. Using the minimum exit area gives a conservative value for the total thrust [4].

Listing A.9 shows the single modified line of the updated rocket nozzle element. The first half of Line 1, $(Cf * Fl_l.Pt * Ath)$, is the bell nozzle thrust calculation. The second half of the Line, $((Fl_l.Pt/PRExit - Ps) * Ath * AR)$, implements Equation (A.32) using system parameters which are available in the nozzle element. The exit pressure (P_e) term is computed from the exit pressure ratio ($PRExit$) and the chamber pressure ($Fl_l.Pt$) shown

in Equation (A.33). The exit area term (A_e) is computed from the expansion ratio shown (AR) and the throat area (A_{th}) in Equation (A.1).

$$PR_e = \frac{p_0}{p_e} \quad (A.33)$$

Listing A.9: Aerospike Thrust Calculation

```
1 Fg = (Cf * FL_I.Pt * Ath) + ((FL_I.Pt/PRexit - Ps) * Ath * AR);
```

With no other changes to the cycle portions of the DEAN cycle model, the verification of the model documented in Chapter 3 is still valid. Specifically, work by Arguello and Strain demonstrated the converged pressure values calculated by the NPSS model agreed, often to within a few percent, with independently developed Pumpal® and RITAL® models of the two expander cycles. This agreement confirmed the underlying soundness of the cycle balance in the NPSS model which drives the engine performance calculations. This confirmation combined with the inspection of the geometry calculations, pressure level estimates, and improved performance calculations show the DEAN cycle model correctly predicts the DEAN's performance for a given design, which validates this model.

A.3.2 Angelino and Angelino Correction.

The Angelino and Angelino Correction components act together to perform a single analysis. The purpose of this unified analysis is to approximate the aerospike nozzle geometry using a modified Angelino approximation in place of the TDK analysis in Hall's thesis. The combined analysis was verified through testing which compared the results of the modified Angelino approximation to the results from Hall's TDK analysis. Three nozzle geometries (Martin's and Hall's similar thesis designs with similar maximum radius and expansion ratio; and Hall's design with the expansion ratio increased from 5.3 to 10) were modeled in both Hall's TDK analysis and the Angelino Approximation and Angelino

Correction components. The resulting geometry was graphically compared to verify the correct function of the Angelino and Angelino Correction components.

Figure A.13, Figure A.14, and Figure A.15 indicate the Angelino approximation alone significantly underestimates the radius of the aerospike nozzle for the majority of its length. Given the nozzle geometry is used to calculate the mass of the nozzle current design point, the linear approximation is in some ways a better fit than the Angelino approximation alone because the linear approximation's over estimate of volume will lead to conservative values for mass.

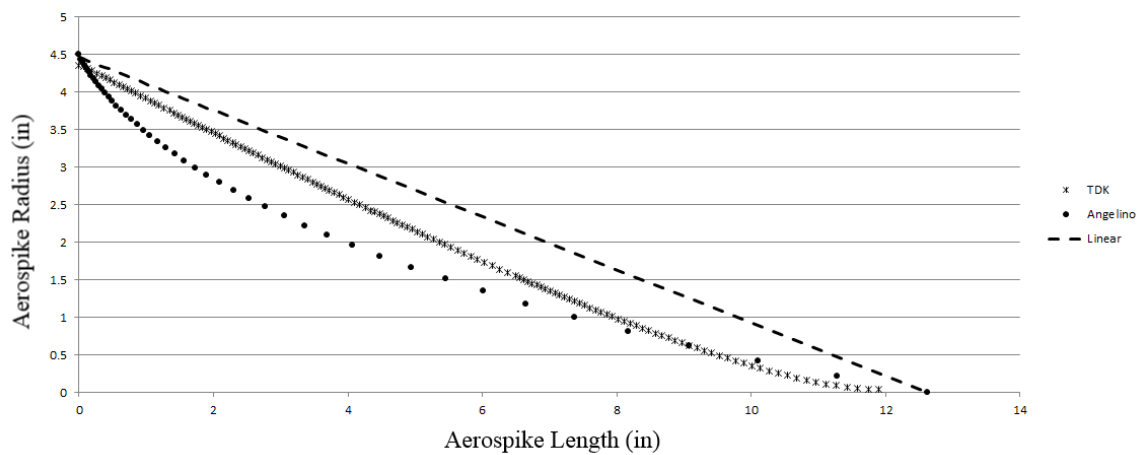


Figure A.13: Comparison of Angelino Approximation to TDK (Martin Design Point)

The error between the Angelino approximation and the TDK analysis can be quantified by calculating the volume for the surface of revolution for the two curves. The Structural Jacket Size component implements this calculation. Table A.7 summarizes the results of the error analysis. The average error in volume is nearly 34%, which supports the previous conclusion that the Angelino component is not sufficiently modeling the nozzle geometry.

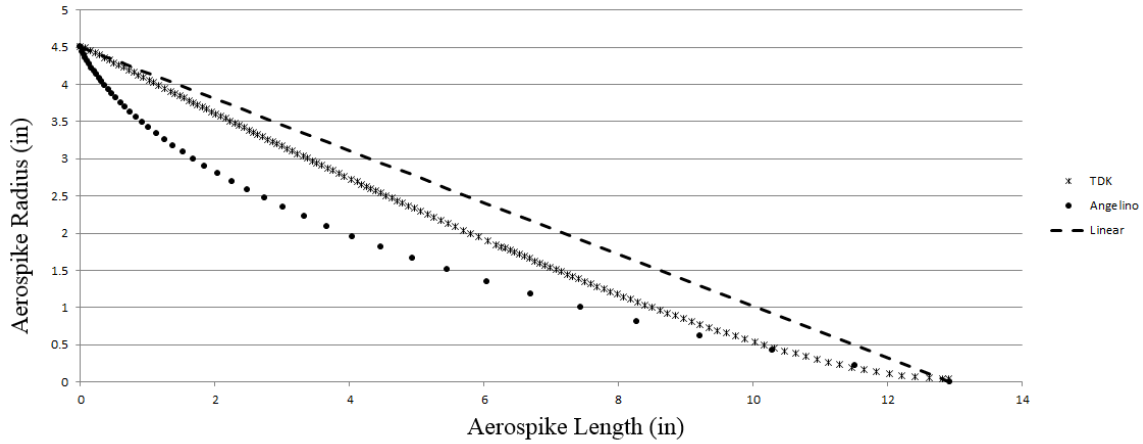


Figure A.14: Comparison of Angelino Approximation to TDK (Hall Design Point)

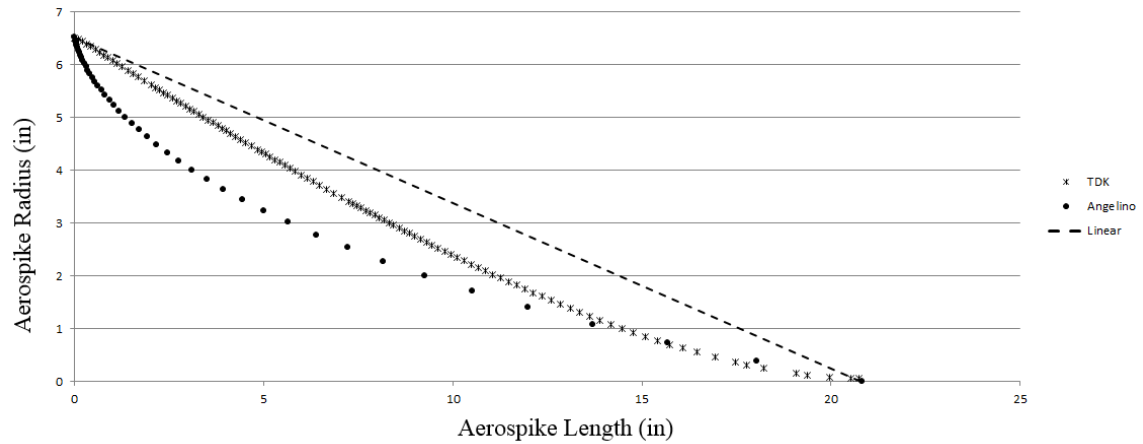


Figure A.15: Comparison of Angelino Approximation to TDK (Hall Design Point with Expansion Ratio of 10)

The discrepancy between the Angelino and TDK results indicates the TDK design is between the Angelino curve and the linear approximation. Applying a correction factor to the Hall example, shown in Figure A.16, supports this assumption. Implementing this

Table A.7: Angelino Approximation Error Analysis

Test Case	Volume, TDK (in ³)	Volume, Angelino (in ³)	Error (%)
Martin	199	138	31
Hall	223	143	36
Hall ($\epsilon = 10$)	692	455	34

correction in the Angelino Correction component leads to similar results for the Hall design with an aspect ratio of 10 as can be seen in the Figure A.17.

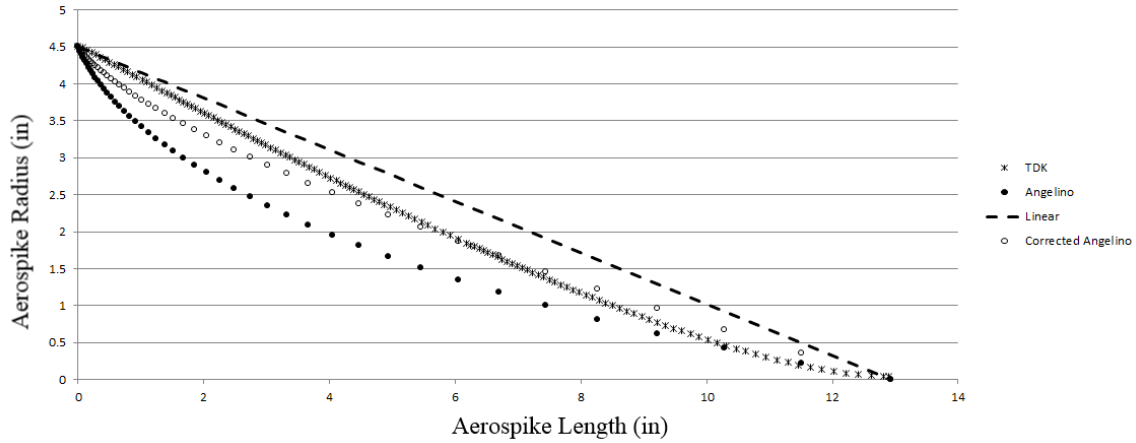


Figure A.16: Angelino Approximation Correction (Hall Design Point)

The improvements can be quantified using the same technique as above. Table A.8 summarizes the results. The improvements in the error are significant. The average is down to 5.3%, and the worst error is under 10%. Given the current architecture decision to bore out much of the aerospike's volume to save mass, an average error in the full nozzle's volume of approximately 5% should be sufficient for the level of detail in the current model.

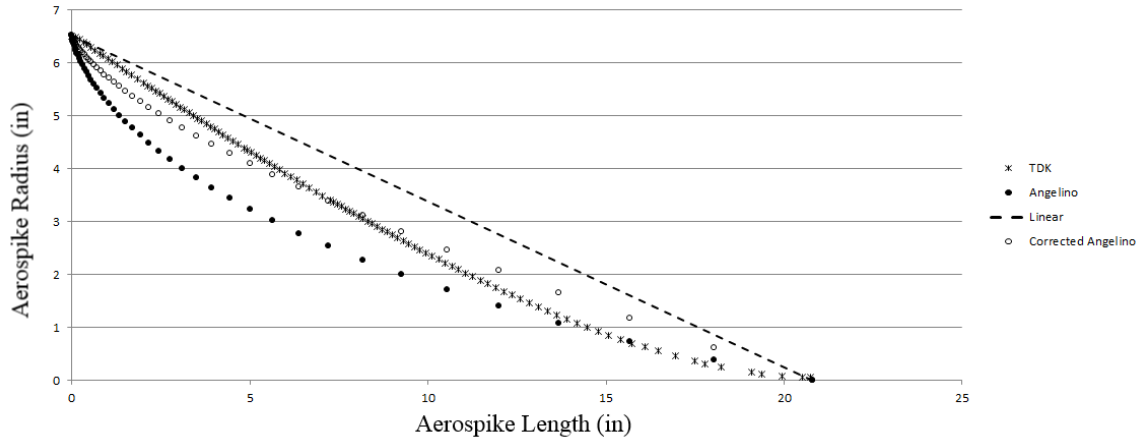


Figure A.17: Angelino Approximation Correction (Hall Design Point with expansion ratio of 10)

Table A.8: Corrected Angelino Approximation Error Analysis

Test Case	Volume, TDK (in ³)	Volume, Angelino (in ³)	Error (%)
Martin	199	194	2.5
Hall	223	202	9.4
Hall ($\epsilon = 10$)	692	665	3.9

While a linear approximation of the nozzle geometry is sufficient to calculate the heat transfer areas associated with the fuel expander cycle [4], calculations involving the volume, and ultimately the mass of the nozzle benefit from a higher fidelity approximation. As shown above, the Angelino and Angelino Correction components provide the required fidelity. The Angelino component uses Angelino’s approximation method to create an initial representation of aerospike nozzle. Note, Angelino’s approximation method assumes the ratio of specific heats and molecular weight are constant across the nozzle, the reaction

is isentropic and adiabatic, and the flow through the throat is choked (Mach number equals one) [4, 48].

As can be seen in Figure A.18, the geometry generated from the Angelino approximation (Initial Angelino) includes points to the left of the y-axis. These points represent geometry inside the chamber and need to be removed to coordinate the nozzle geometry with the internal chamber geometry of the DEAN. Removing these points is the first function of the Angelino Correction component. The second function of the Angelino Correction component is to implement the correction factor documented above. The resulting geometry from both corrections is included in Figure A.18.

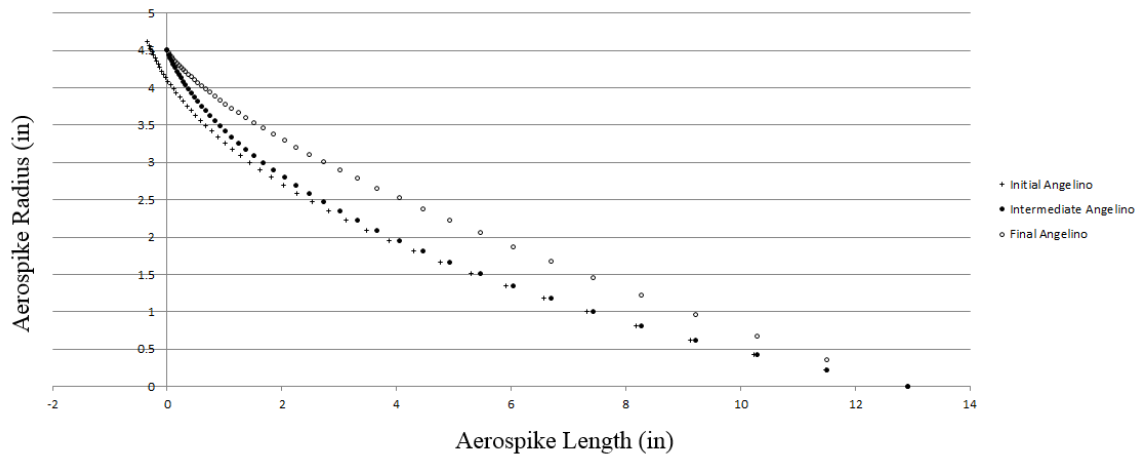


Figure A.18: Coordinating Angelino Approximation with Chamber Geometry

The generated geometry can be used in the remaining components of the DEAN model in place of the TDK generated geometry, satisfying the required output of the components. Further, these components adjust the geometry to match the current design's chamber geometry and combustion performance as was demonstrated in the verification tests involving design points of different chamber dimensions and engine performance.

Providing the required nozzle geometry over a range of designs meets the purpose of these components.

A.3.3 Cooling Jacket.

The purpose of the Cooling Jacket component is to size the cooling channel walls and to calculate the wall temperatures as a percentage of their melting points. The component was verified through inspection.

The Cooling Jacket component is a ModelCenter script component which implements a solver loop in order to iteratively run the Material Properties component. For each station in both the chamber and the aerospike, the Cooling Jacket component calculates the maximum value between the bending and shear stress at that station and the wall temperature. The component then compares the maximum stress to the limiting values from the Material Properties component for the calculated wall temperature, selected material, and the selected failure mode (ultimate or yield strength). If the stress is greater than one or more limiting values, the wall thickness is incremented and the analysis is repeated until the wall has sufficient thickness to prevent failure. It is important to note the wall temperature increases with greater wall thickness leading to lower strengths in the materials. This process can lead to designs with wall thicknesses on the order of inches instead of hundredths of an inch resulting in very low thrust-to-weight ratios.

Initial inspection of the source code for the Cooling Jacket showed it had a number of errors and repeated code blocks making inspection and error correction overly complicated. Before continuing with the verification process, the component's implementation was refactored to minimize duplicated code and improve readability. During the refactoring effort, the various errors were corrected and repeated code blocks were placed in user defined functions.

With the errors in the Cooling Jacket Analysis corrected the inspection could continue with a focus on the implementation of the governing equations. The governing equations

for the Cooling Jacket analysis code include the calculation of the bending moment, the calculation of the bending stress, the calculation of the shear stress, and the calculations of the wall temperatures on the hot and cold sides. During the inspection, the source code for each of these calculations was compared to the governing equations.

The stresses in the cooling jackets are calculated from the stresses in the individual cooling channels. A simplified view of the cooling channels' design, neglecting the curvature of the engine, is shown in Figure A.19. Along the top of the figure is the structural jacket. followed by the optional cooling jacket cover used when the structural jacket material is not compatible with the propellant. The bottom of the figure is a cross-section of half of a cooling channel. Inside the channel is the high pressure propellant and outside the channel, at the bottom of the figure, is the combustion chamber. From this view, it is clear each cooling channel can be modeled as a beam with fixed supports under a uniform load from the pressure difference between the propellant and the chamber pressures.

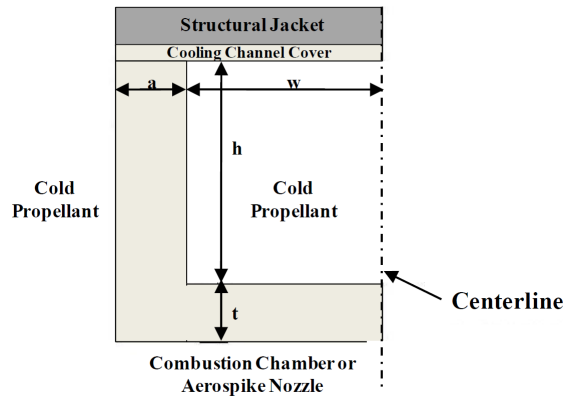


Figure A.19: Cooling Channel Design - Cross-Section View [4]

To incorporate the engine's curvature, the cooling channels are modeled as curved beams instead of simple beams under the uniform load and using the fixed supports noted above. The bending moment for such beams is shown in Equation (A.34) [70].

$$M_x = \frac{w}{12}(6lx - 6x^2 - l^2) \quad (\text{A.34})$$

Listing A.10 shows the function which calculates the bending moment. It is a direct implementation of Equation (A.34).

Listing A.10: Cooling Jacket Bending Moment Function

```

1 function Beam_Moment(load, width, position) {
2     return (load/12)*(6*width*position - 6*Math.pow(position,2) -
3         Math.pow(width,2));
4 }

```

The equations for the bending stress in a curved beam on the inner and outer surface are given by Equation (A.35) and Equation (A.36) respectively [70]. The source code in Listing A.11 implements these equations. [Note, the division by 1000 in the source code is to convert the results from psi to ksi.] A simple inspection shows the source code correctly implements the governing equations.

$$\sigma_i = \frac{Mc_i}{Aer_i} \quad (\text{A.35})$$

$$\sigma_o = \frac{Mc_o}{Aer_o} \quad (\text{A.36})$$

Listing A.11: Cooling Jacket Bending Stress Calculations

```

1 var sigma_bending_in = (M * ci) / (A * e * ri) / 1000; //ksi, Inner stress
2 var sigma_bending_out = (M * co) / (A * e * ro) / 1000; //ksi, Outer stress

```

The maximum shear stress for a rectangular cross-section is shown in Equation (A.37) where the value for S in a beam with fixed supports is given by Equation (A.38). The source code in Listing A.12 implements these equations (and incorporates the factor of safety in the final answer). Line 1 calculates the actual maximum shear stress from Equation (A.38) where load (w) equals pressure difference (*load*), the length (l) equals the channel width (*width*), the x-coordinate is set to the location of maximum shear stress, 0, and the area (A) is computed from the height (h) and length (b) of the channel. Line 2 then applies the factor of safety and converts the result from psi to ksi.

$$\tau_{max} = \frac{3}{2} \frac{S}{A} \quad (\text{A.37})$$

$$S = \frac{w}{2}(l - 2x) \quad (\text{A.38})$$

Listing A.12: Cooling Jacket Shear Stress Calculations

```

1 var tau = (3/2) * (load * width / 2) / (h * b); //psi, Shear Stress
2 tau_max = tau * fs.value / 1000; // ksi, Max shear stress w/fs

```

Calculating the wall temperatures involves solving the thermodynamic equilibrium condition shown in Equation (A.39). Using the definition for enthalpy (h) in Equation (A.40), one can get an equation for Q , Equation (A.41). Equation (A.42) and Equation (A.43) expand Equation (A.41) to define Q_{in} and Q_{out} , which when substituted into Equation (A.39) gives Equation (A.44).

$$Q_{in} = Q_{out} \quad (\text{A.39})$$

$$h = \frac{Q}{A\Delta T} \quad (\text{A.40})$$

$$Q = hA\Delta T \quad (\text{A.41})$$

$$Q_{in} = H_{T_H} A_H (T_{HW} - T_0) \quad (\text{A.42})$$

$$Q_{out} = H_{T_C} A_C (T_{cool} - T_{CW}) \quad (\text{A.43})$$

$$H_{T_H} A_H (T_{HW} - T_0) = H_{T_C} A_C (T_{cool} - T_{CW}) \quad (\text{A.44})$$

Equation (A.44) can be rearranged to form Equation (A.45). Let the value C equal the left hand side of Equation (A.45), as shown in Equation (A.46). The hot side wall temperature (T_{HW}) can be introduced by adding and subtracting it from the numerator, as shown in Equation (A.47). Recall the heat flow (Hx) is defined as the difference in temperatures between the two sides of the wall, Equation (A.48). Substituting Hx into Equation (A.47) yields Equation (A.49).

$$\frac{T_{cool} - T_{CW}}{T_{HW} - T_0} = \frac{H_{T_H} A_H}{H_{T_C} A_C} \quad (\text{A.45})$$

$$C = \frac{T_{cool} - T_{CW}}{T_{HW} - T_0} \quad (\text{A.46})$$

$$C = \frac{T_{cool} + T_{HW} - T_{CW} - T_{HW}}{T_{HW} - T_0} \quad (\text{A.47})$$

$$Hx = T_{HW} - T_{CW} \quad (\text{A.48})$$

$$C = \frac{T_{cool} + Hx - T_{HW}}{T_{HW} - T_0} \quad (\text{A.49})$$

Multiplying both sides by the $(T_{HW} - T_0)$ gives Equation (A.50). Rearranging Equation (A.50) yields Equation (A.51) which has the hot wall temperature values all on one side of the equation. Gathering the hot wall terms on the left hand side of the equation gives Equation (A.52), which can then be simplified to Equation (A.53) to give a solution for the hot side wall temperature in terms of the heat flow, the coolant fluid temperature, the chamber temperature, and the value C defined above in Equation (A.46).

$$CT_{HW} - CT_0 = T_{cool} + Hx - T_{HW} \quad (A.50)$$

$$CT_{HW} + T_{HW} = T_{cool} + Hx + CT_0 \quad (A.51)$$

$$T_{HW}(1 + C) = T_{cool} + Hx + CT_0 \quad (A.52)$$

$$T_{HW} = \frac{T_{cool} + Hx + CT_0}{(1 + C)} \quad (A.53)$$

The values necessary to calculate C are available from the DEAN cycle model, as are the coolant fluid temperature and the chamber temperature. The heat flow is then calculated in order to determine the hot side wall temperature. Begin with Equation (A.54), as defined in Hall's thesis Equation (14). Substituting the $-Hx$ for $(T_{CW} - T_{HW})$ from the definition of Hx in Equation (A.48) gives Equation (A.55). Solving for Hx gives Equation (A.56).

$$\dot{q} = \frac{-k}{\Delta l}(T_{CW} - T_{HW}) \quad (A.54)$$

$$\dot{q} = \frac{k}{\Delta l}Hx \quad (A.55)$$

$$Hx = \frac{\dot{q}\Delta l}{k} \quad (A.56)$$

The DEAN cycle model reports the total \dot{Q} , instead of the normalized \dot{q} . Equation (A.57) defines the relationship between these two terms. Using this definition to replace \dot{q} with \dot{Q} gives a form of the calculation of heat flow which can be calculated from values available from the DEAN cycle model, shown in Equation (A.58).

$$\dot{q} = \frac{\dot{Q}}{A} \quad (\text{A.57})$$

$$Hx = \frac{\dot{Q}\Delta l}{kA} \quad (\text{A.58})$$

Finally, the cold side wall temperature can be calculated simply by rearranging the definition of heat flow, Equation (A.48), to give Equation (A.59).

$$T_{CW} = T_{HW} - Hx \quad (\text{A.59})$$

Equations (A.47), (A.53), (A.58), and (A.59) form the complete set of governing equations necessary to calculate the wall temperatures. The source code in Listing A.13 implements these equations for each station in the Cooling Jacket.

Listing A.13: Cooling Jacket Wall Temperature Calculations

```

1 C = (HTCoefHot.value(i) * A_HxHot.value(i)) /
2   (HTCoefCool.value(i) * A_HxCool.value(i));
3 Hx_flow = (Qwall.value(i) * channel_thickness) / (k * A_HxHot.value(i));
4 wall_temp_hot.value(i) = (Hx_flow + fluid_temp.value(i) + C*T0.value)/(1+C);
5 wall_temp_cold.value(i) = wall_temp_hot.value(i) - Hx_flow;

```

Lines 1 and 2 implement Equation (A.47), Line 3 implements Equation (A.58), Line 4 implements Equation (A.53), and Line 5 implements Equation (A.59). A review of each of these lines shows the source code correctly implements the governing equations.

Inspection of the Cooling Jacket component shows it correctly calculates the internal stresses and temperatures of the cooling channel walls, and uses these values with the values from the Material Properties component to determine the required thickness for the

cooling channel walls. These calculations fulfill the purpose of the component which is to size the cooling channel walls and report their temperatures.

A.3.3.1 Material Properties.

The purpose of the Material Properties component is to report key material properties (density, thermal conductivity, melting point, and strengths) for the materials under consideration for the various elements in the DEAN design based on the element temperatures. The Material Properties component was verified through inspection and testing.

The Material Properties component is essentially a database of material properties by temperature with sets of variables for each of the major elements of the DEAN design (chamber cooling and structural jackets, aerospike cooling and structural jackets, aerospike tip, and the plumbing for both the LOX and the LH2). The data reported by this component (and the sources of this data) are tabulated in Hall's masters thesis in Appendix B. Tests for this component to verify its function include manual inspections of the enumerated materials for each element to ensure the component complies with material compatibility with the propellants, comparing the component's reported material properties to the tabulated data in Hall's thesis, and inspection of the material property tables to ensure each material supports a sufficient range of temperatures for thermal conductivity and strengths.

Table A.9 shows the material selections available for each element of the DEAN design. Each column lists an element of the DEAN design, and each row lists a material. An 'X' in a particular cell indicates the material is included in the component as a material option for the corresponding element. An 'x' in a particular cell indicates the material is compatible with the corresponding element of the DEAN design as documented by Hall. With this code, the component passes this manual inspection if there are only blank cells or cells which contain 'Xx'. The component does not pass if there are any cells with a

single ‘X’ or ‘x’. Two cells have single x’s in them, the cells which represent using silicon carbide for the LOX and LH2 plumbing indicating the material is compatible with the propellants, but is not an available option in the component. As noted above, this should indicate an error in the component, however, in this case, the option was left out of the component due to the difficulty in using silicon carbide to manufacture plumbing. With no other discrepancies in the table, the component passes this verification test.

Table A.9: Component Material Compatibility Analysis

Material	Chamber CJ	Chamber SJ	Spike CJ	Spike SJ	Spike Tip	LOX Plumb	LH2 Plumb
Pure Cu	Xx	Xx	Xx	Xx	Xx	Xx	Xx
Silicon Carbide	Xx	Xx	Xx	Xx	Xx	x ^a	x ^b
INCOLOY 909	Xx	Xx	Xx	Xx	Xx	Xx	Xx
Alloy 188	Xx	Xx	Xx	Xx	Xx	Xx	Xx
Beryllium Cu	Xx	Xx	Xx	Xx	Xx	Xx	Xx
Ox-Free Cu	Xx	Xx	Xx	Xx	Xx	Xx	Xx
Cobalt	Xx	Xx	Xx	Xx	Xx	Xx	Xx
INCONEL 718	Xx	Xx				Xx	
INCONEL 625	Xx	Xx				Xx	
AL 7075 T6		Xx		Xx			
AL 2024 T6		Xx		Xx			
Titanium		Xx					
Niobium					Xx		

^awhile compatible with LOX, silicon carbide is not suitable as a plumbing material

^bwhile compatible with LH2, silicon carbide is not suitable as a plumbing material

A standalone model was developed to test the material properties reported by the component. The model includes the Material Properties component and a top-level input variable to set the temperature being tested. This top-level variable is linked to all of the temperature input variables (including each element of the fluid temperature arrays) in order to drive all of the element properties to the same values. Since several of the material properties reported by the Materials Properties component are nonlinear, the component returns step functions for each property. For temperatures below the minimum tabulated value and above the maximum tabulated value, the component returns the property value corresponding to the minimum and maximum temperatures respectively. Finally, Hall reported constant density for each material as the density is only used in the mass calculation, assumed to occur when the engine is not operating and is at room temperature.

The test procedure for the component began by setting the material selections for each element to the same material (for example Beryllium Copper). A parametric study was then run over the range of temperatures included in Hall's data for the material under consideration (for example 500R to 900R in three steps for Beryllium Copper). The results of this trade study were then compared to Hall's data to ensure consistency. Table A.10 is an example results set for the component (using Beryllium Copper) and Table A.11 is the expected results from Hall's thesis. Comparing these two tables shows the Beryllium Copper results pass this verification test. Similarly, the component passes this verification tests for the entire set of included materials.

Table A.10: Parametric Study Results for Beryllium Copper

Output Variable	500 (R)	700 (R)	900 (R)
Chamber_Cool_Rho (lbm/in ³)	0.298	0.298	0.298
SJChamber_Rho (lbm/in ³)	0.298	0.298	0.298
Spike_Cool_Rho (lbm/in ³)	0.298	0.298	0.298
SJSpike_Rho (lbm/in ³)	0.298	0.298	0.298
Spike_Tip_Rho (lbm/in ³)	0.298	0.298	0.298
O2Pipe_Rho (lbm/in ³)	0.298	0.298	0.298
LH2Pipe_Rho (lbm/in ³)	0.298	0.298	0.298
Chamber_Cool_Melt (R)	2050.67	2050.67	2050.67
Spike_Cool_Melt (R)	2050.67	2050.67	2050.67
Chamber_Cool_k (BTU/in-R-s)	0.001578	0.001939	0.001939
Spike_Cool_k (BTU/in-R-s)	0.001578	0.001939	0.001939
Chamber_Cool_Ft (10 ³ psi)	180	180	180
SJChamber_Ft (10 ³ psi)	180	180	180
Spike_Cool_Ft (10 ³ psi)	180	180	180
SJSpike_Ft (10 ³ psi)	180	180	180
O2Pipe_Ft (10 ³ psi)	180	180	180
LH2Pipe_Ft (10 ³ psi)	180	180	180
Chamber_Cool_Fy (10 ³ psi)	155	155	155
SJChamber_Fy (10 ³ psi)	155	155	155
Spike_Cool_Fy (10 ³ psi)	155	155	155
SJSpike_Fy (10 ³ psi)	155	155	155
O2Pipe_Fy (10 ³ psi)	155	155	155
LH2Pipe_Fy (10 ³ psi)	155	155	155

Table A.11: Expected Results for Beryllium Copper [4]

Property	Any T	$T < 527.67 \text{ (R)}$	$527.67 \text{ (R)} \leq T$
Density (lbm/in ³)	0.298		
Melting Point (R)	2050.67		
Thermal Conductivity k (BTU/in-R-s)		0.00158	0.00194
Ultimate Tensile Strength (10 ³ psi)	180		
Yield Strength (10 ³ psi)	155		

The final verification process reviewed the material tables to ensure they provide sufficient range of values by temperature to cover range of temperatures for thermal conductivity and strengths. A limited range of temperatures for thermal conductivity disqualified the material as an option for cooling jackets as the thermal conductivity is a key factor in the performance of the cooling jacket. Similarly, a limited range of strengths disqualified the material as an option for either the cooling or structural jackets and the plumbing as the performance of these components is driven by their strengths. The property tables for each material were inspected using the number of entries and the thermal range covered by those entries used to judge the material's fitness for inclusion in the model.

Two materials were disqualified for use in cooling jackets and one material was disqualified for use in structural jackets and plumbing. Oxygen-free copper only has one value for its thermal conductivity, which is at room temperature, disqualifying it for use with cooling jackets. Beryllium copper only has one value for its strength, which is also at room temperature, disqualifying it for use with cooling jackets, structural jackets, and plumbing.

Given the high temperatures seen in liquid rocket engines and the effects of high temperatures on the material properties used in the DEAN model, these effects clearly needed to be included in the DEAN model. The verification tests demonstrated the Material Properties component, when the two disqualified materials were ignored, provides the

required temperature dependent material properties for each material option available in a DEAN design, meeting the purpose of this component.

A.4 Post Processing Step 1: Performance

The Performance *sequence*, shown in Figure A.20, contains the Thrust-to-Weight Calculation, with its supporting analyses the Channels and Structural Jacket Size analyses, and the Pressure Profiles component which renders the pressure levels for both the LOX and the LH2 expander cycles.

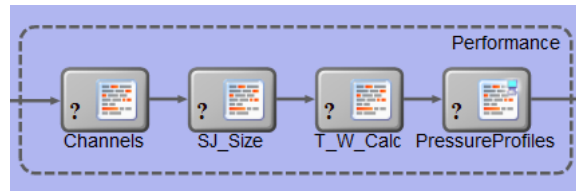


Figure A.20: Performance Sequence

A.4.1 Channels.

The purpose of the Channels component is to take the vector channel dimension data returned by the DEAN cycle model and convert this data to scalar values to be used for subsequent analyses. The component was verified by inspecting its source code.

The primary conversion used in this component is to average the channel wall thicknesses to provide the Structural Jacket Size component with an inner wall thickness for the chamber and the aerospike. To ensure the average wall thicknesses represent the actual wall thickness of the chamber and the aerospike, the component also calculates differences between the minimum and maximum wall thickness for both the chamber and the aerospike. These differences are then used as constraints to ensure the variation in the wall thicknesses is acceptable. Finally, the component also calculates the minimum channel spacing for the LOX and LH2 cooling channels for use as a design constraint.

The calculations involved in the Channels analysis are simple averaging and calculation of the minimum and maximum values in arrays. A single JavaScript function, shown in Listing A.14 iterates over input arrays and records the minimum and maximum values while calculating the average. This function is then called for the LOX and LH2 channel thickness arrays and the LOX and LH2 channel spacing arrays.

Listing A.14: Channels Component Average Function

```
1 function average(values) {
2     var avg = 0;
3     var numVals = values.length;
4     var min = values.value(0);
5     var max = values.value(0);
6
7     for (var i = 0; i < numVals; i++) {
8         avg += values.value(i);
9
10        if (values.value(i) < min)
11            min = values.value(i);
12
13        if (values.value(i) > max)
14            max = values.value(i);
15    }
16
17    avg = avg / numVals;
18
19    return [avg, min, max];
20 }
```

Inspection of the Channels component showed it properly converts the DEAN analysis' vector results to suitable scalars, with appropriate constraints, for use by the Structural Jacket sizing analysis, meeting the purpose of this component.

A.4.2 Structural Jacket Size.

The purpose of the Structural Jacket Size component is to determine the wall thicknesses for the chamber and aerospike structural jackets and the engine's plumbing. Additionally, this component calculates geometric parameters for various engine components including the plumbing cross-sectional area, the volume and weight of the structural jackets, the volume and weight of the cooling channel covers if present, and the volume and mass of the uncooled aerospike tip. The component was verified through inspection.

The DEAN engine has two structural jackets, one for the chamber and one for the aerospike. The cross-section shown in Figure A.21 shows DEAN structural jackets in relation to the cooling jackets and the ambient environment. The chamber, the black disc in the figure, is a high pressure region and the ambient environment is a low pressure region. Observe how the chamber structural jacket is containing the pressure from the chamber internally and is therefore experiencing stress in tension. Conversely, the aerospike structural jacket is containing the pressure from the chamber externally and is therefore experiencing stress in compression.

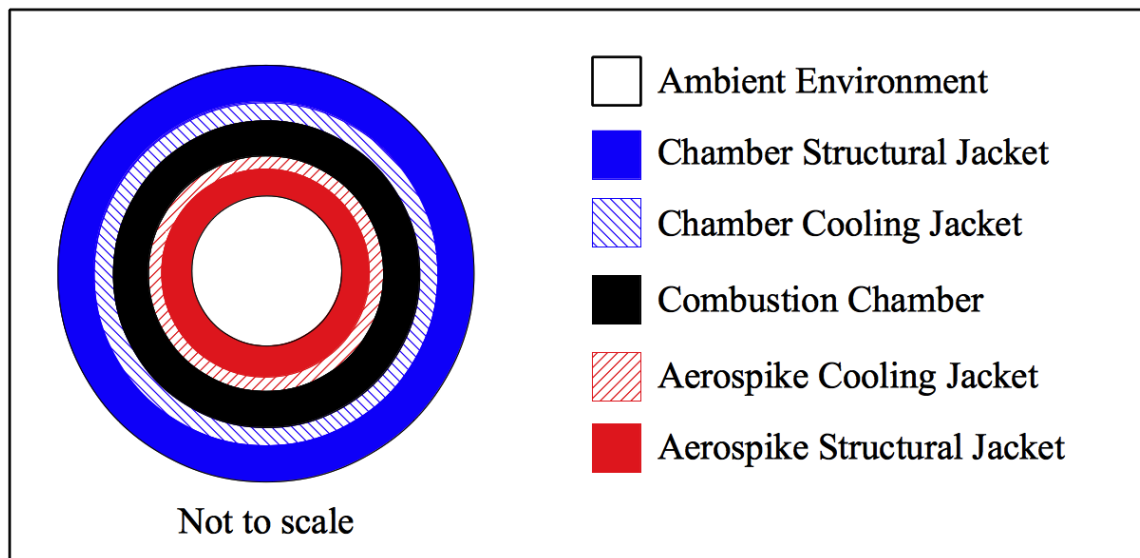


Figure A.21: Cross-Section of the DEAN Engine

The Structural Jacket Size component computes the structural jacket sizes by solving for the minimum wall thicknesses which yield a maximum stress in the structural jackets within the stress limit for the selected material, including the model's factor of safety. As part of this calculation, the wall thicknesses are increased or decreased until the stress limit is just met. The Structural Jacket Size component performs this analysis for the highest

pressure differential instead of one for each station. The system level model assumes a nearly uniform temperature in the structural jacket, and in turn constant material properties along the length of the engine. The highest pressure differential is calculated from the difference between the maximum pressure in the related cooling channel and the ambient pressure.

As with the Cooling Jacket component, initial inspection of the source code for the Structural Jacket Size component showed it had a number of errors and repeated code blocks making inspection and error correction overly complicated. Before continuing with the verification process, the component's implementation was refactored to minimize duplicated code and improve readability. During the refactoring effort, the various errors were corrected and repeated code blocks were placed in user defined functions.

With the errors in the Structural Jacket Size component corrected, the inspection could continue with a focus on the implementation of the governing equations. The governing equations for the Structural Jacket Size analysis include the radial and tangential stress in a thick walled pressure vessel and the volumes for the various components of the DEAN. During the inspection, the source code for each of these calculations was compared to its governing equation and assumptions.

Equation (A.60) shows the calculation for the tangential stress in a thick walled cylinder [70]. Listing A.15 shows the function which calculates the tangential stress. It is a direct implementation of Equation (A.60)

$$\sigma_t = \frac{p_i r_i^2 - p_o r_o^2 - r_i^2 r_o^2 (p_o - p_i) / r^2}{r_o^2 - r_i^2} \quad (\text{A.60})$$

Listing A.15: Tangential Stress in a Thick Walled Cylinder Function

```

1 function sigma_tan(ri, ro, r, Pi, Po) {
2     return (Pi*Math.pow(ri,2) - Po * Math.pow(ro,2) -
3             Math.pow(ri,2) * Math.pow(ro,2) * (Po-Pi) / Math.pow(r,2)) /
4             (Math.pow(ro,2)-Math.pow(ri,2));
5 }

```

The calculation for the radial stress in a thick walled cylinder is very similar to the calculation for the tangential stress, as can be seen in Equation (A.61). In both of these equations, positive values indicate the cylinder is in tension, as would be expected for the chamber's structural jacket, and negative values indicate the cylinder is in compression, as would be expected for the aerospike's structural jacket [70].

$$\sigma_r = \frac{p_i r_i^2 - p_o r_o^2 + r_i^2 r_o^2 (p_o - p_i) / r^2}{r_o^2 - r_i^2} \quad (\text{A.61})$$

Listing A.16 shows the function calculating the radial stress. It is a direct implementation of Equation (A.61)

Listing A.16: Radial Stress in a Thick Walled Cylinder Function

```

1 function sigma_tan(ri, ro, r, Pi, Po) {
2     return (Pi*Math.pow(ri,2) - Po * Math.pow(ro,2) +
3             Math.pow(ri,2) * Math.pow(ro,2) * (Po-Pi) / Math.pow(r,2)) /
4             (Math.pow(ro,2)-Math.pow(ri,2));
5 }

```

With these two calculations implemented, the remaining code for calculating the structural jacket thickness is a straight forward loop over increasing or decreasing thickness values until the stress limit is just satisfied. Listing A.17 shows the function which implements this sizing loop.

Listing A.17: Calculate Wall Thickness Function

```

1 // tension can take on two values: 1 == in tension, -1 == in compression
2 function calculateWallThickness(ri, ro, t, Pi, Po, stressLimit, tension) {
3     // initialize variables
4     var r = 0.0;
5     var stepSize = 0.001;
6     if (tension == 1) {
7         r = ri;
8     }
9     else {
10        r = ro;
11    }
12
13    var maxStress = 0.0;
14    if (tension == 1) {
15        maxStress = fs.value * Math.max(sigma_tan(ri, ro, r, Pi, Po),
16                                         sigma_rad(ri, ro, r, Pi, Po)) / 1000;
17    }
18    else {
19        maxStress = fs.value * Math.min(sigma_tan(ri, ro, r, Pi, Po),
20                                         sigma_rad(ri, ro, r, Pi, Po)) / 1000;
21    }
22
23    // multiply by tension to adjust for tension vs compression
24    if (maxStress < stressLimit * tension) {
25        while (maxStress < stressLimit * tension) {
26            if (tension == 1) {
27                t = t - stepSize;
28                ro = ri + t;
29                maxStress = fs.value * Math.max(sigma_tan(ri, ro, r, Pi, Po),
30                                                     sigma_rad(ri, ro, r, Pi, Po)) / 1000;
31            }
32            else {
33                t = t + stepSize;
34                ri = ro - t;
35                maxStress = fs.value * Math.min(sigma_tan(ri, ro, r, Pi, Po),
36                                                  sigma_rad(ri, ro, r, Pi, Po)) / 1000;
37            }
38        }
39    }
40    else {
41        while (maxStress > stressLimit * tension) {
42            if (tension == 1) {
43                t = t + stepSize;
44                ro = ri + t;
45                maxStress = fs.value * Math.max(sigma_tan(ri, ro, r, Pi, Po),
46                                                  sigma_rad(ri, ro, r, Pi, Po)) / 1000;
47            }
48            else {
49                t = t - stepSize;
50                ri = ro - t;
51                maxStress = fs.value * Math.min(sigma_tan(ri, ro, r, Pi, Po),
52                                                  sigma_rad(ri, ro, r, Pi, Po)) / 1000;
53            }
54        }
55    }
56

```

```
57     return t;  
58 }
```

One important detail about this function is the purpose and use of the function argument *tension*. The function argument *tension* is a flag indicating whether the sizing loop is being run for a cylinder in tension (*tension* = 1) or compression (*tension* = -1). Naturally, the function is called with a value of 1 for the chamber's structural jacket, and a value of -1 for the aerospike's structural jacket. The argument is used in one of two ways throughout the function. First, it is used as a test condition in *if statements* such as in Lines 6, 14, 26, and 42, where it controls whether the calculation should be performed for a tension or compression case. Second, it is used as a sign adjustment for the maximum stress in the cylinder such as in Lines 24 and 41. For cases where the cylinder is in tension, the stress values will be positive, as noted above, and the *tension* argument has a value of 1. When the positive stress value is multiplied by the *tension* value of 1, the stress value remains positive. For cases where the cylinder is in compression, the stress values will be negative, as noted above, and the *tension* argument has a value of -1. When the negative stress value is multiplied by the *tension* value of -1, the stress value becomes positive.

The remainder of this function performs the iterations which increase or decrease the wall thickness from the starting value provided by the function argument *t* until the stress limit is just met using a pair of *while loops*. The first *while loop*, shown in lines 25-38, implements the decreasing case for cylinders in tension, and the increasing case for cylinders in compression. This reversal of implementations is required because in compression cases, the smaller stress value is a more negative number, representing a larger magnitude of stress meaning the stress limit has been exceeded. The second *while loop*, shown in Lines 41-54, similarly implements the increasing case for cylinders in tension, and the decreasing case for cylinders in compression.

The plumbing thicknesses, one for LOX and one for LH2, are calculated by again calling the `calculateWallThickness` function, this time using the difference between the maximum fluid pressure in the cooling lines and ambient pressure for the pressure difference. The cross-sectional area for the plumbing is calculated by computing the area of an annulus, shown previously in Equation (A.3), with inner radius equal to the specified plumbing radius and the outer radius equal to the plumbing radius plus the plumbing thickness.

The remainder of the Structural Jacket Size component calculates the volumes for the structural jackets, the cooling jacket covers, and the uncooled aerospike tip. The weight of these components is calculated by simply multiplying the density of the component materials by the calculated volumes. As can be seen in Figure A.21, the DEAN engine is made up of a series of concentric elements, starting from the outside with the chamber structural jacket and working down to the aerospike's structural jacket. To calculate the volume of a particular element, the Structural Jacket Size component calculates the volume of the solids representing the outer and inner radii of the element, and then computes the difference between these two volumes. Each element is composed of one or more geometric primitives including cylinders, frustums, and surfaces of revolution. Specifically, the chamber structural jacket, and the chamber cooling jacket cover, are composed of a cylinder and a frustum. The aerospike structural jacket is composed of one or two cylinders depending on the inner most radius of the aerospike, two frustums, and a volume of revolution for a portion of the curve defined by the Corrected Angelino component. Finally, the solid aerospike tip is composed entirely of a volume of revolution for another portion of the curve defined by the Corrected Angelino component.

The code which calculates of the volume of a cylinder is straight forward, as it implements $V = \pi r^2 h$. However, the volume for a frustum and a volume of revolution are more complicated and should be handled more carefully. Recall a frustum is essentially

a cone with the point removed. Equation (A.16) shows the calculation for the volume of a frustum. Listing A.18 shows the function which computes this value. As can be seen, it is a direct implementation of Equation (A.16).

Listing A.18: Frustum Volume Function

```

1 function frustumVolume(length, r1, r2) {
2     // from http://mathworld.wolfram.com/ConicalFrustum.html
3     return 1/3 * Math.PI * length *
4         (Math.pow(r1,2) + (r1*r2) + Math.pow(r2,2));
5 }

```

Calculating a volume of revolution requires solving the integral shown in Equation (A.62). The Structural Jacket Size component uses the trapezoid method to numerically compute this integral. Equation (A.63) shows this numerical solution. To simplify the implementation, the cross-sectional area, $A(x)$ is precomputed using the definition found in Equation (A.64) [71].

$$V = \int_a^b A(x)dx \quad (\text{A.62})$$

$$\int_a^b A(x)dx = \frac{1}{2} \sum_2^N (x_i - x_{i-1}) * (A(x_{i-1}) + A(x_i)) \quad (\text{A.63})$$

$$A(x) = \pi[f(x)]^2 \quad (\text{A.64})$$

Listing A.19 shows the implementation of the volume of revolution equations for the uncooled portion of the aerospike. Similar code is used to compute the volume of revolution required for the cooled portion of the aerospike. The calculations start with the *for loop* in lines 2-8 which compute the cross-sectional areas for the values of x which will be used in the volume of revolution. This step corresponds to Equation (A.64). Lines 10 and 11 then initialize the summation value and the A_{i-1} value, represented by the variable *prevA*. The *for loop* in Lines 12-17 then implements the summation in Equation (A.63), except for the

division by two which can be factored out of the summation. Finally, Line 19 applies the factored out division by 2 to reach the final numerical solution for the volume of revolution.

Listing A.19: Volume of Revolution Volume Calculation

```

1 cross_area_nozz.length = spike_length_nozz.length;
2 for (i = 0; i < spike_radius.length; i++) {
3     if (spike_length_nozz.value(i) != 0) {
4         cross_area_nozz.value(i) = Math.PI * Math.pow(spike_radius.value(i), 2);
5     } else {
6         cross_area_nozz.value(i) = 0;
7     }
8 }
9
10 var sum = 0;
11 var prev_A = cross_area_nozz.value(i_val);
12 for (i = i_val + 1; i < cross_area_nozz.length; i++) {
13     this_A = cross_area_nozz.value(i);
14     sum += (spike_length_nozz.value(i) - spike_length_nozz.value(i-1)) *
15           (this_A + prev_A);
16     prev_A = this_A;
17 }
18
19 Vspike_tip.value = sum * 0.5;

```

Inspection of the Structural Jacket Size component shows it correctly calculates the internal stresses of the structural jacket walls and the plumbing, and uses these values to determine the required thickness for the structural jackets and plumbing. Further, inspection shows this component properly calculates the volumes for these elements. These calculations fulfill the purpose of the component: to size the structural jackets for both the chamber and the aerospike.

A.4.3 Thrust-to-Weight Calculation.

The purpose of the Thrust-to-Weight Calculation component is to calculate the total engine weight by estimating and summing up component weights, and then calculating the thrust-to-weight ratio from total engine weight and engine thrust. This analysis estimates weights for the following engine components: the chamber (made up of the chamber cooling and structural jackets), the aerospike (made up of the aerospike cooling and structural jackets and the uncooled tip), the LOX and LH2 turbopumps, the plumbing, and the miscellaneous hardware. The Thrust-to-Weight Calculation component was verified by

inspecting its source code. The purpose of the Thrust-to-Weight Calculation component is to calculate the total engine weight by estimating and summing up component masses, and then calculating the thrust-to-weight ratio (T/W) from total engine mass and engine thrust. This analysis estimates masses for the following engine components: the chamber (made up of the chamber cooling and structural jackets), the aerospike (made up of the aerospike cooling and structural jackets and the uncooled tip), the LOX and LH2 turbopumps, the plumbing mass, and the miscellaneous hardware mass. The Thrust to Weight Calculation component was verified by inspecting its source code.

To calculate the overall weight of either the chamber or the aerospike, the individual weights of the cooling and structural jackets must be calculated. The cooling jacket weights can be calculated from their volumes (calculated by the cycle model and passed in as input variables to this component) and the density of their materials. The volumes are stored in arrays by NPSS station, and must be summed to get the total volume. Note, station 6 (with an array index of 5) is a virtual station used to calculate throat conditions in the cycle model. Its volume should not be counted in the sum. Further, the cooling jackets contain the cooling channels which are fabricated by removing material from the cooling jackets, so these volumes need to be subtracted from the total volume. Finally, the cooling jackets may include a cooling jacket cover to protect the structural jacket from the fluid in the cooling channels. This weight must also be accounted for in the cooling jacket.

The source code shown in Listing A.20 calculates the total weight of the aerospike. It is identical to the code which calculates the chamber mass except for the variable names, and the inclusion of the mass of the uncooled portion of the aerospike.

Listing A.20: Aerospike Mass Calculations

```

1 Vspike_Cool = 0
2 for i = 0 to VolumeTotalFu.length - 1
3     if (i <> 5) then ' skip station 6 (index 5)
4         Vspike_Cool = Vspike_Cool + VolumeTotalFu(i)
5     end if
6 next
```

```

7
8 Vspike_Cool = Vspike_Cool - VolFluidCoolFu
9
10 MSpike_cool = Vspike_Cool * Spike_Cool_Rho 'lb, Spike Cooling Vol Weight
11 MSpike_cooltop = Vspike_cooltop * Spike_Cool_Rho 'lb, Spike Cooling Cover
12 MSpike_CJ = MSpike_cool + MSpike_cooltop
13
14 Mspike = SpikeSJ_mass + MSpike_cool + MSpike_cooltop + Mspike_tip

```

Lines 2-6 contain a *for loop* used to sum the cooling jacket volume. Note the statement “if (i <> 5)” is used to skip the volume at station 6. Following the *for loop*, the cooling channel volume is subtracted from the overall cooling jacket volume. The remainder of the source code, Lines 10-14, calculates the weights of the individual components from their volumes and densities, and then sums up the total aerospike weight as described above, demonstrating the calculations for the total chamber and aerospike masses work as required.

In *Space Propulsion Analysis and Design*, Humble defines a relationship for calculating the mass of a turbopump (combined turbine and pump system including the shaft) during the conceptual design phase of a liquid rocket engine from its performance shown in Equation (A.65) and Equation (A.66) [5].

$$M_{tp} = A\tau^\beta \quad (\text{A.65})$$

$$\tau = \frac{P_{req}}{N_r} \quad (\text{A.66})$$

These equations show the turbopump mass is proportional to the required pump power (P_{req}). Equation (A.67) shows the power required is directly related to the propellant mass flow. Therefore, the turbopump weight is proportional to the propellant mass flow.

$$P_{req} = \frac{g_0 \dot{m} H_p}{\eta_{tp}} \quad (\text{A.67})$$

The code from the component shown in Listing A.21 implements these equations to calculate the weight of the LOX and LH2 turbopumps. Note, the equations above use empirical constants which assume the values for the performance variables are in SI units.

Listing A.21: Turbopump Mass Calculations

```

1 Nr = LOX_Shaft_Speed * 2*pi * 1/60 'rad/s, using turbine power
2 tau = (LOX_Turb_pwr * 745.69987158227022) / Nr
3
4 'Pump Shaft Torque (Power in Watts, Nr in rad/s)
5 'Need metric units to utilize constants A & B
6
7 A = 1.5 'A & B recommended by Humble for conceptual design
8 B = 0.6
9
10 mass_tpm = A*tau^B '(kg) mass of turbopump (unit convert from kg to lbm)
11 Ox_TP_Mass = mass_tpm * 2.20462262 'lbm

```

Line 1 simply converts the shaft speed from RPM to rad/s for use as the value of N_r . Line 2 calculates the value for τ based on Equation (A.66), including a unit conversion for the power required from HP to Watts. Humble recommends the constants A and B use the values of 1.5 and 0.6 respectively during conceptual design. Finally, the weight is calculated from Equation (A.65) and then converted to lbm from kg. This example code clearly shows the component implements the LOX turbopump weight calculation. Similarly, the LH2 turbopump weight calculation is implemented correctly as it uses the same algorithm as the LOX turbopump.

The plumbing weight can be calculated from the estimated volume of the plumbing and the density of the material selected for the plumbing. The Structural Jacket Size component provides the cross-sectional area for both the LOX and LH2 plumbing based on strength of materials calculations discussed in Section A.4.2. Using an estimated plumbing length of twice the total engine length (conservative estimate) calculating the volume, and in turn the mass of the plumbing is a straight forward calculation shown in Listing A.22.

Listing A.22: Plumbing Mass Calculations

```

1 PipeLength = 2 * (NozzleLength + ChamberLength) 'in
2
3 'Oxidizer
4 PipeVol_Ox = PipeLength * PipeArea_Ox
5 Mpipe_Ox = PipeVol_Ox * O2Pipe_Rho

```

Line 1 calculates the estimated pipe length by doubling the total engine length (the sum of the chamber and nozzle lengths). Line 3 of the source code calculates the plumbing volume by multiplying the length by the cross-sectional area of the pipe. Finally, the last line of code calculates the weight by multiplying the volume by the material density. This sample code correctly calculates the weight for the LOX plumbing. Given the same process is used to calculate the LH2 plumbing mass, both sets of plumbing mass are calculated correctly.

The weight of the miscellaneous hardware (nuts, bolts, wiring, rivets, etc) of can be estimated as a small percentage of the overall engine weight, Equation (A.68), approximately 5% [4]. The Thrust-to-Weight Calculation component includes a design variable (*Percent_Weight_Hardware*) to control this estimate. Since the total engine weight includes the miscellaneous hardware weight, the calculation for the miscellaneous hardware weight must be related to other known values, specifically the weights of the other engine components. Equation (A.69) gives the required relationship by equating the sum of the remaining engine component weights on the right hand side to the remaining percent of the engine weight on the left hand side.

$$W_{hardware} = (Percent_Weight_Hardware/100) * W_{total} \quad (A.68)$$

$$\frac{100 - Percent_Weight_Hardware}{100} W_{total} = W_{spike} + W_{chamber} + W_{turbopumps} + W_{plumbing} \quad (A.69)$$

Dividing both sides by the percentage on the left hand side gives an equation for the total engine weight, as shown in Equation (A.70).

$$W_{total} = \frac{(W_{spike} + W_{chamber} + W_{turbopumps} + W_{plumbing})}{\frac{100 - Percent_Weight_Hardware}{100}} \quad (A.70)$$

The hardware weight can then be calculated by substituting the right hand side of the Equation (A.70) for the total engine weight in the Equation (A.68) , shown in Equation (A.71).

$$W_{hardware} = (Percent_Weight_Hardware/100) \frac{(W_{spike} + W_{chamber} + W_{turbopumps} + W_{plumbing})}{\frac{100 - Percent_Weight_Hardware}{100}} \quad (A.71)$$

Inspecting the source code related to this calculation shows there is an error. The *Percent_Weight_Hardware* is applied not to the total engine weight, but to the weight of the other components as is shown in Listing A.23. The corrected code, based on Equation (A.71), is shown in Listing A.24. As can be seen, the corrected code now properly implements the calculation for weight of the miscellaneous hardware.

Listing A.23: Incorrect Miscellaneous Hardware Weight Calculation

```

1 Mhardware = (Percent_Weight_Hardware/100)*
2             (Mspike + Mchamber + Mturbopumps + Mplumbing)

```

Listing A.24: Corrected Miscellaneous Hardware Weight Calculation

```

1 Mhardware = (Percent_Weight_Hardware/100) *
2             (Mspike + Mchamber + Mturbopumps + Mplumbing) /
3             ((100-Percent_Weight_Hardware)/100)

```

Finally, the total engine weight is simply the sum of the previously calculated component weights, and the thrust-to-weight ratio is simply the engine thrust divided by the total engine weight as is shown in Listing A.25.

Listing A.25: Final Engine Thrust-to-Weight Calculation

```

1  'TOTAL WEIGHT
2  Mtotal = Mspike + Mchamber + Mturbopumps + Mplumbing + Mhardware 'Total Mass
3
4  'THRUST-TO-WEIGHT
5  T_W = round(Thrust / Mtotal,1) 'Engine Thrust-to-Weight, round for display
6
7  Round for display
8  Mtotal = round(Mtotal,1)

```

Line 2 is the summation of the engine component weights to get the total engine weight. Note, there are sub-summation variables for the combined weight of the LOX and LH2 turbopumps and plumbing (Mturbo pumps and Mplumbing respectively). Line 5 then calculates the thrust-to-weight ratio. These are straight forward summations and multiplications and are implemented correctly.

Recall the purpose of this component is to calculate the thrust-to-weight ratio for the DEAN engine for the design under consideration. By calculating the total engine weight from the engine performance and volumes calculated in upstream components, the Thrust-to-Weight Calculation component implements the required functionality.

A.4.4 Pressure Profiles.

The purpose of the Pressure Profiles component is to produce pressure levels for the two expander cycles in the DEAN engine for the current design. The component was verified through testing.

As noted in Section 2.1.3, pressure levels can be used to visualize the results of a pressure balance analysis when designing liquid rocket engines. These visualizations can be compared with nominal results for the engine cycle being used to verify the current design. NPSS conducts a pressure balance analysis as part of its convergence process for each design, and the DEAN cycle model reports the pressures for each station in both expander cycles. An MS Excel spreadsheet, shown in Figure A.22, takes the pressure values and plots them as pressure level plots for each expander cycle.

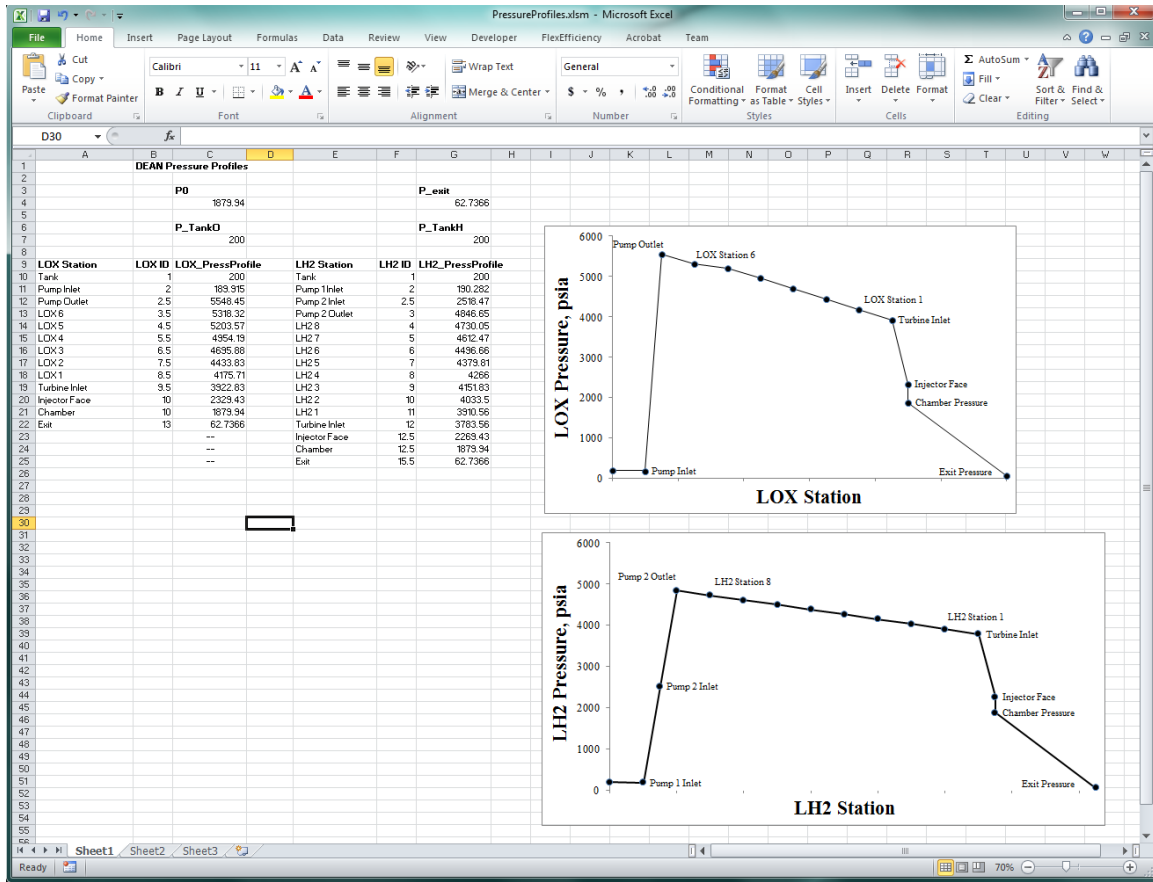


Figure A.22: Pressure Level Plots Spreadsheet

The spreadsheet is integrated into ModelCenter using an AnalysisServer scriptwrapper. Scriptwrappers are AnalysisServer command files using scripting languages such as VBScript and Python to define custom analyses or to automate external tools through vendor provides Application Programming Interfaces (APIs), such as Excel's COM API. The Pressure Profiles scriptwrapper loads the pressure levels spreadsheet, sends the pressure profile array values to Excel, and then calls a macro to save the pressure levels to disk before presenting the information in ModelCenter.

The component was tested by running parametric studies over different design variables, and ensuring the resulting pressure levels matched the pressure data calculated

by the DEAN cycle model. An example display of the pressure levels as rendered in ModelCenter is shown in Figure A.23.

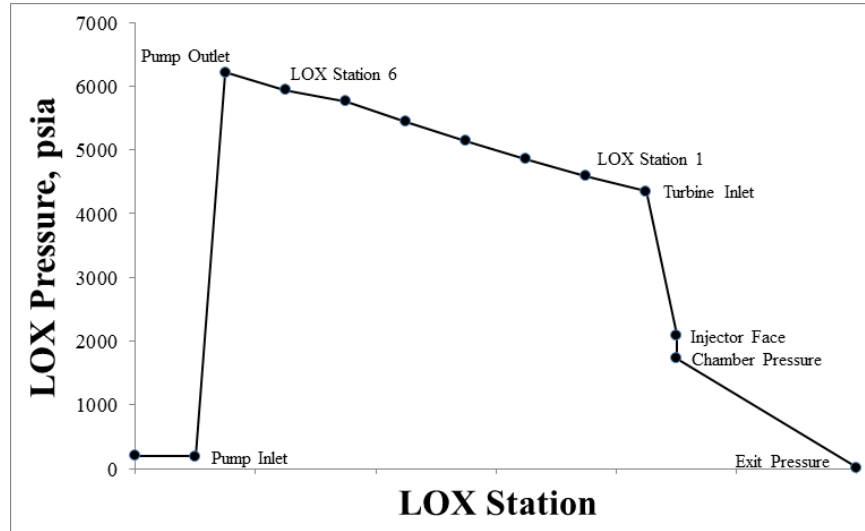


Figure A.23: Example LOX Cycle Pressure Level Plot

Automating the display of pressure levels gives users of the DEAN system level model a powerful visualization and documentation tool for use during research of the DEAN architecture. Testing of the underlying spreadsheet and its integration into ModelCenter demonstrated the component works as intended and meets its purpose.

A.5 Post Processing Step 2: Geometry

The Geometry *sequence*, shown in Figure A.24 contains two *sub-sequences*, one to render the conceptual geometry and one to render the final geometry. These renderings give the model user visual feedback about the current design. The conceptual geometry is a representation of the current design using a linear approximation for the aerospike geometry. The final geometry is a representation of the current design including all wall thicknesses, and uses the corrected Angelino approximation for the aerospike geometry.

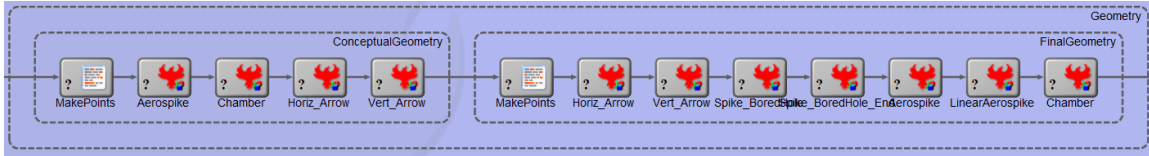


Figure A.24: Geometry Sequence

The majority of the components in both *sequences* are built-in ModelCenter geometry components, specifically GenericSOR components (discussed in Section A.1) and 12 inch long Arrow components to provide a scale reference in the geometry renderings. The remaining components are a pair of ModelCenter script components, one for the conceptual geometry and one for the final geometry, which format data about the current design for use by the GenericSOR components. These script components were verified through inspection.

The geometry string must be of the format shown in Listing A.26. Each line contains a single coordinate pair, the sequence of which defines the curve to be revolved and rendered by the GenericSOR component [64].

Listing A.26: GenericSOR Input Format

```

1  x1, y1
2  x2, y2
3  x3, y3
4  . . .

```

The geometry string is built by appending points to the end of each geometry string. The coordinates of each point are generated in previous analyses, leaving the geometry components to just build the proper format for rendering by the ModelCenter GenericSOR components. The straight forward nature of these scripts makes it easy to confirm they are creating the correct geometry strings. Further, the resulting geometry can be compared to

the current design to ensure it is rendering as expected. Figure A.25 shows the results of the Geometry *sequence*.

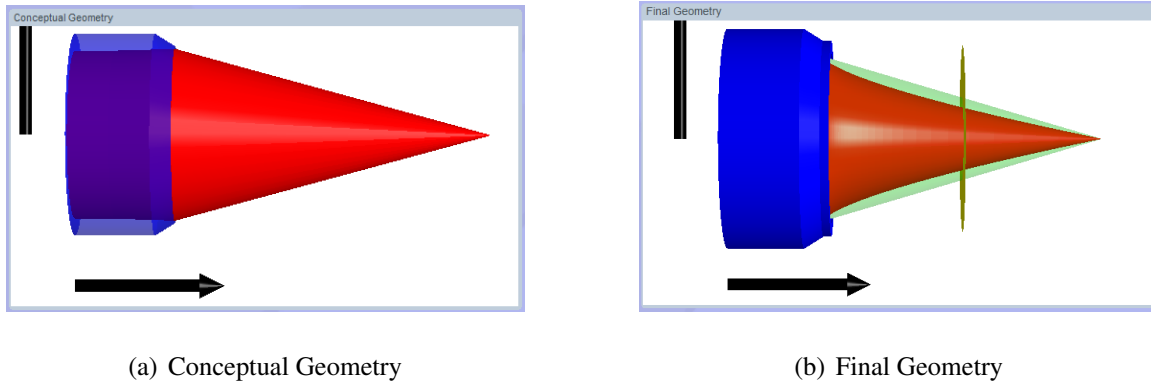


Figure A.25: Example Renderings from the Geometry Sequence

As can be seen from Figure A.25, the Geometry *sequence* provides a high level visualization of the current design point. Inspection shows the renderings accurately reflect the model's calculations, and the component meets its purpose.

A.6 Post Processing Step 3: Constraints

The Constraints *parallel branch*, shown in Figure A.26, contains analyses used to calculate the constraint values in the DEAN system level model not calculated by earlier components. These analyses include the maximum Mach number in the cooling channels for both the LOX and the LH2 expander cycles, the chamber Mach number, geometry consistency in the aerospike walls, and the expected pressure drops in the two expander cycles across the injector face.

A.6.1 LOX and LH2 Mach Numbers.

The purpose of the LOX and LH2 Mach Number *sequences* is to calculate the maximum Mach number in the LOX and LH2 cooling channels respectively. The DEAN

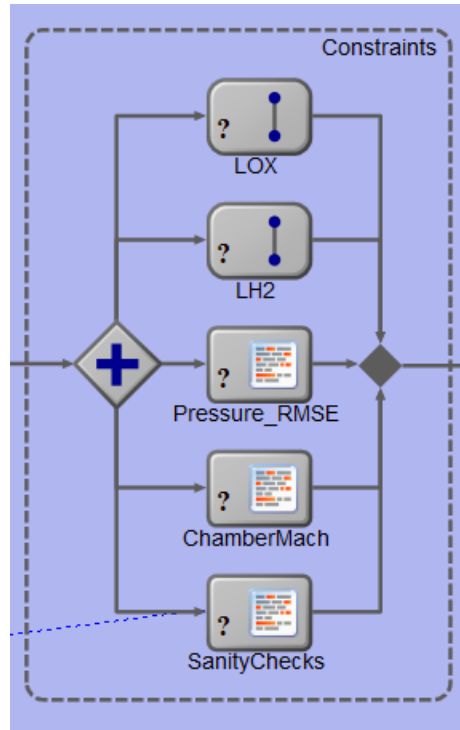
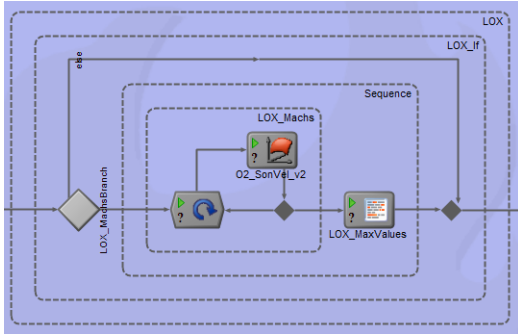


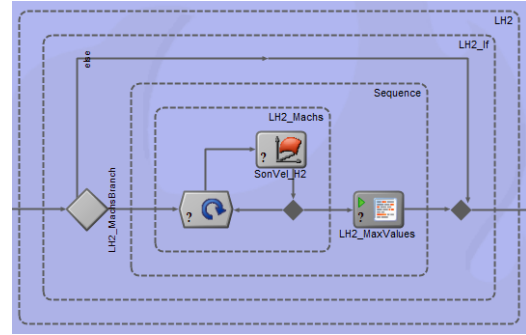
Figure A.26: Constraints Parallel Branch

system level model relies on external analyses to compute the Mach numbers because NPSS cannot calculate Mach numbers for super-critical fluids such as the LOX and LH2 in the cooling channels. Calculating the maximum Mach number in the cooling channels is critical. Exceeding the specified limits, Mach 0.6 for LOX and Mach 0.9 for LH2, would lead to a catastrophic engine failure based on previous empirical results [2].

As can be seen in Figure A.27, the same modeling structure is used to calculate the maximum Mach number in both the LOX and LH2 cooling channels. This section will focus on the LOX analysis components to discuss the methodology used in both constraint calculations, making sure to address the LH2 components when they differ significantly from the LOX components. The various components in both *sequences* were verified by inspection.



(a) LOX Mach Number Sequence



(b) LH2 Mach Number Sequence

Figure A.27: LOX and LH2 Mach Number Sequences

The LOX *sequence* contains four key analysis components. The first component is a ModelCenter *if branch*, labeled LOX_if. This branch tests the maximum pressure level seen in the cooling channel and only executes the remaining components if the maximum pressure is within the bounds of the remaining components. Without this branch, designs which violate the pressure limits of the later analyses would generate model errors instead of constraint violations preventing trade studies from collecting data for those designs. The second component, a ModelCenter *for-each loop* labeled LOX_Machs, contains the third analysis, a Response Surface Model (RSM) approximation of the speed of sound in liquid oxygen, labeled O2_SonVel_v2. The RSM analysis bounds its input variables, pressure and temperature, to prevent extrapolation of speed of sound calculations outside the range of the underlying response surface model. The final component, a ModelCenter Script Component labeled LOX_MaxValues, calculates the Mach number at each station, using the speed of sound values from the RSM component and the fluid velocity from the DEAN cycle model, and then finds the maximum Mach number.

ModelCenter *for-each loop* components are used to iteratively execute scalar analyses for a set of values from one or more input arrays. The results are then stored in one or more output arrays [67]. In the LOX_Machs loop, the input arrays are the fluid pressure and

temperature at each of the stations in the LOX expander cycle. These values are outputs of the DEAN cycle model. The output array of the LOX_Machs loop is the calculated speed of sound at each station in the LOX expander cycle. Similarly, the LH2_Machs loop iterates over speed of sound calculations for liquid hydrogen in the LH2 expander cycle. Inspection of the settings for both *for-each loops* confirms the components are properly configured. Trial runs demonstrate the loops are properly executing the RSM components for values from each station in their respective expander cycles.

The speed of sound for each LOX station is calculated by the O2_SonVel_v2 RSM component. ModelCenter RSM components are created using Phoenix Integration's RSM Toolkit. The RSM Toolkit uses trade study data to create polynomial or Kriging models from either ModelCenter analyses or external sources. Additionally, the RSM Toolkit includes a number of reports covering the quality of the generated response surface model [67]. Previous versions of the DEAN system model used the RSM Toolkit to calculate polynomial models for the speed of sound in liquid oxygen and liquid hydrogen using source data from the National Institute of Standards and Technology. The fourth generation DEAN system model replaces the polynomial speed of sound models with Kriging models to improve the quality of the fit. Further, the range of the input data from the National Institute of Standards and Technology was extended to cover a wider range of designs.

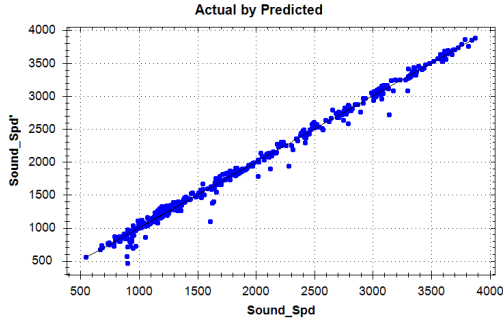
The two RSM models were verified using RSM Toolkit reports. The RSM models in the fourth generation DEAN system model need to meet two criteria to be verified. The first criteria is properly modeling the speed of sound for the working fluid being modeled. The second criteria is to improve the quality of the model over the previous polynomial models.

Three RSM Toolkit reports were used in the verification of the RSM models. The first report is the RSM rating, which is a 5 star rating summarizing a number of model statistics. Ratings of four to five stars indicate high quality models. The second report is

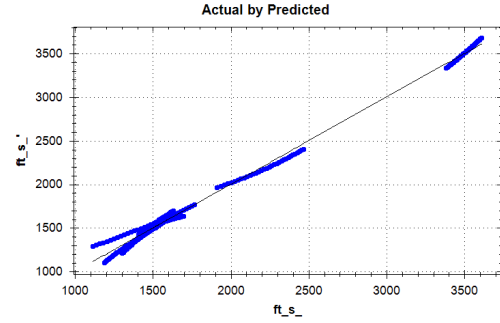
the Coefficient of Determination, or R^2 value, which represents how well the model fits the data. Values closer to 1.0 indicate models with better fits. The third report is an Actual vs Predicted plot. The Actual vs Predicted plot consists of a line representing $y = x$ for the actual data values and the values computed by the model. RSM generated points for each input condition are then plotted with the line [67].

The RSM Toolkit reports show the LOX RSM passes both verification criteria. The first criteria, properly modeling the speed of sound, can be seen from all three RSM Toolkit reports. The LOX RSM has both a high rating, five stars, and a high R^2 value, 0.994. The Actual vs Predicted plot, shown in Figure A.28(a), also indicates a good fit, showing the overwhelming majority of the predicted data points agree well with the actual values. The second criteria, improving the quality of the RSM over the previous polynomial model, is demonstrated by comparing the Actual vs Predicted plots from the new Kriging and the previous polynomial model. Figure A.28 shows both plots side by side. As described above, the Kriging model, shown on the left, shows a very good agreement with few outlying points. Compare this result to the Actual vs. Predicted data for the polynomial model, shown on the right. This data has a number of regions where points move away from the actual values and has a large gap in the middle from incomplete source data. Clearly, the LOX RSM model passes both verification criteria.

Similarly, the RSM Toolkit reports show the LH2 RSM passes both verification criteria. For the first criteria, the LH2 RSM has an RSM rating of five stars, and an R^2 value of 0.995. Both of these values indicate a good agreement of the model to the data. The Actual vs Predicted plot also indicates a good agreement, with only a few outlying data points, as is shown in Figure A.29(a). For the second criteria, the results for the LH2 RSM are very similar to the results seen with the LOX RSM. The Kriging RSM has very tight grouping of points around the diagonal line, while the polynomial RSM model has a



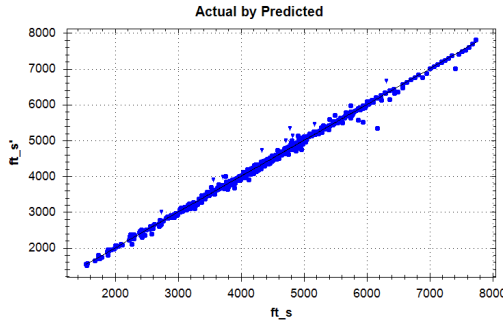
(a) Kriging LOX Actual vs Predicted



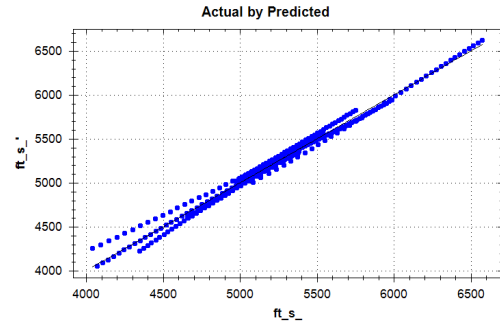
(b) Polynomial LOX Actual vs Predicted

Figure A.28: LOX RSM Actual vs Predicted Plots

section in the data moving away from the actual. As with the LOX RSM, the LH2 RSM passes both verification criteria.



(a) Kriging LH2 Actual vs Predicted



(b) Polynomial LH2 Actual vs Predicted

Figure A.29: LOX RSM Actual vs Predicted Plots

As mentioned above, the final component in both the LOX and LH2 Mach Number *sequences* combines the speed of sound data calculated during the execution of the *for-each loops* with the fluid velocities from the DEAN cycle model to compute the Mach number at each station. The component then finds the highest calculated Mach number and reports this value as the maximum Mach number in the cooling channels. Verification of

these components is done through inspection of the source code, nearly identical in both the LOX and the LH2 *sequences*. The source code for the LOX *sequence* is shown in Listing A.27.

Listing A.27: LOX Max Mach Source Code

```

1  function run() {
2      LOX_Machs.size = LOX_vel.size;
3
4      LOX_MaxMach.value = 0;
5      for (i = 0; i < LOX_vel.size; i++) {
6          LOX_Machs.value(i) = LOX_vel.value(i) / Sound_Spd.value(i);
7          if (LOX_Machs.value(i) > LOX_MaxMach.value)
8              LOX_MaxMach.value = LOX_Machs.value(i);
9      }
10 }

```

The component starts by sizing the Mach numbers output array, LOX_Machs, to match the size of the input arrays, shown in Line 2. Line 4 initializes the variable which will hold the maximum Mach number. In Line 5, the component iterates over the values in the velocity array using a *for loop*. The body of the *for loop* contains two calculations. The first, in line 6, calculates the Mach number for the i^{th} station by dividing the fluid velocity by the calculated speed of sound. The second calculation, in Lines 7-8, determines if the Mach number for the i^{th} station is greater than the previously observed maximum Mach number, and if so, stores this value as the new maximum. At the conclusion of the loop, the component has calculated the maximum Mach number for the given expander cycle, meeting its purpose.

Taken together, the four components in LOX and LH2 Mach Number *sequences* transform the fluid temperature, pressure, and velocity data from the DEAN cycle model into Mach numbers for each station in the two expander cycles, and report the maximum Mach number in the cooling channels for each expander cycle. Component level inspection shows the components correctly compute these values. Together, these components meet the required purpose of calculating the maximum Mach number seen in the cooling channels for use as constraint values.

A.6.2 Pressure RMSE.

The Pressure RMSE component is a copy of the root mean square error analysis used in the Pressure Profile Converger (see Section A.2.3.2 for complete modeling details). It is included in the Constraints block to calculate an updated evaluation of the quality of the estimated pressure profiles in the two expander cycles. These values are calculated at the end of the overall system level simulation to provide a cross check for the estimated values computed by the Pressure Profile Converger.

A.6.3 Chamber Mach Number.

The purpose of the Chamber Mach Number component is to calculate the Mach number inside the combustion chamber. Chamber Mach numbers typically range between Mach 0.1 and Mach 0.6, with values of Mach 0.1 indicating more conservative designs. Smaller engines generally have lower chamber Mach numbers [5]. The component was verified through inspection of its source code.

The Chamber Mach Number component uses a relationship between the engine's contraction ratio, the ratio of the chamber's average cross-sectional area to the throat area, and the chamber Mach number. Equation (A.72) shows this relationship.

$$\frac{A_c}{A_t} = \frac{1}{M} \left[\left(\frac{2}{\gamma + 1} \right) \left(1 + \frac{\gamma - 1}{2} M^2 \right) \right]^{\frac{\gamma + 1}{2(\gamma - 1)}} \quad (\text{A.72})$$

Note the chamber Mach number, M , appears as an inverse and a quadratic term, complicating the process of solving for the chamber Mach number symbolically. However, rearranging Equation (A.72) into a difference yields Equation (A.73). This relationship has a root greater than zero and can be solved with the secant method. The Chamber Mach Number component uses this approach to solve for the chamber Mach number as is shown in Listing A.28.

$$\frac{1}{M} \left[\left(\frac{2}{\gamma + 1} \right) \left(1 + \frac{\gamma - 1}{2} M^2 \right) \right]^{\frac{\gamma + 1}{2(\gamma - 1)}} - \frac{A_c}{A_t} = 0 \quad (\text{A.73})$$

Listing A.28: Chamber Mach Number Source Code

```

1  function run() {
2      // set up secant method
3      var x1 = 0.01;
4      var x2 = 0.02;
5      var x3 = 0.0;
6      delta.value = 1;
7
8      while (Math.abs(delta.value) > 0.01) {
9          x3 = x2 - (calculateDelta(x2)/calculateDeltaPrime(x1, x2));
10         delta.value = calculateDelta(x3);
11         x1 = x2;
12         x2 = x3;
13     }
14
15     MachNumber.value = x3;
16 }
17
18 function calculateDelta(M) {
19     var g = gamma.value;
20     var AR = ChamberRatio.value;
21
22     // break equation into parts to simplify coding
23     // this is Eqn 5.37 in SPAD
24     var a = 2 / (g + 1);
25     var b = 1 + (g - 1) * Math.pow(M,2) / 2;
26     var c = (g + 1) / (2 * (g - 1));
27
28     return Math.pow(a*b,c) / M - AR;
29 }
30
31 function calculateDeltaPrime(M1, M2) {
32     return (calculateDelta(M1) - calculateDelta(M2)) / (M1 - M2);
33 }

```

Lines 2 - 15 implement the secant root finding method. The critical block of code is the function `calculateDelta` which takes a single parameter, the guessed value for the chamber Mach number, and returns the value of the calculation corresponding to Equation (A.73). This function starts by assigning component level input variables to local variables on Lines 19 and 20. The function then breaks the calculation of the difference between the contraction ratio and the remaining terms into three small calculations on lines 24 - 26. Line 24 calculates the $\frac{2}{\gamma+1}$ term and Line 25 calculates the $1 + \frac{\gamma-1}{2}M^2$ term. Finally, Line 26 calculates the overall exponent $\frac{\gamma+1}{2(\gamma-1)}$. The difference is then easily calculated by raising the multiple of a and b to the c power, dividing by M , and subtracting the contraction ratio,

as is seen in Line 28. The remaining code uses the calculateDelta function to compute the derivative using a secant approximation.

As can be seen above, the Chamber Mach Number component correctly calculates the required value, and therefore the component meets its purpose.

A.6.4 Sanity Checks.

The purpose of the Sanity Checks component is to calculate the remaining system level constraint values. These remaining constraint values are the total thickness of the aerospike compared walls compared to the areospoke's radius at each station, the pressure drop across the injector face for the oxidizer and the fuel expander cycles, the difference between the chamber and aerospike radii at the throat, and the chamber's outer radius including wall thicknesses. The aerospike wall thickness is constrained unlike the chamber because the aerospike grows inward and physically cannot exceed the aerospike radius at any point along the nozzle. The injector face pressure drops are constrained by historical data which indicates the values should be greater than 20%. Note, some systems go as low as 5% and throttled engines generally have pressure drops of approximately 30% [5]. Given this range, the DEAN system level model uses values less than 10% and greater than 40% as constraint boundaries for the pressure drops across the injector face. The difference between the outer and inner radii at the throat must be enforced to ensure it does not impact operation of the engine. The inner and outer throat radii specify the throat area, and changes to the throat area impact operation by leading to changes in the chamber pressure, thrust, and specific impulse. Assuming a manufacturing tolerance for the radii at the throat of 0.001 in, a minimum value for the difference in throat radii of 0.1 in will limit the error in the throat area to 2.0% Finally, the outer chamber radius is computed to ensure the DEAN conforms to mission specific size constraints. The Sanity Checks component was verified by inspection.

Listing A.29: Sanity Checks Source Code

```

1  sub run
2  'The goal of this script is to check geometry for inconsistencies
3
4  fuel_length = LH2_radrii.length
5  H2_violate.length = LH2_radrii.length
6
7  'This code checks each station to verify the cooling jacket thickness plus
8  'the cooling channel height plus the structural jacket thickness
9  'is less than the aerospike radius at every station
10
11 for fuel_counter = 0 to fuel_length - 1
12     If H2_h(fuel_counter) + cooltopsike_thickness(fuel_counter)
13         + LH2_channel_thickness + SJspike_thickness
14         > LH2_radrii(fuel_counter) Then
15         H2_violate(fuel_counter) = "fail"
16     else
17         H2_violate(fuel_counter) = "pass"
18     End If
19
20     if ( H2_violate(fuel_counter) = "fail" ) then
21         location = "SanityChecks"
22         msg = "The aerospike thickness exceeds aerospike radius"
23         Err.raise vbError+1, location, msg
24     end if
25 next
26
27
28 ' This bit of code checks to make sure the injector pressure drop is between
29 ' 10 and 40% of the chamber pressure
30 Plow_check = 0.1 * P0 'Pressure drop should be more than 10% of chamber P
31 Phigh_check = 0.4 * P0 'Pressure drop should be less than 40% of chamber P
32 Ox_Injector_P_Drop_Condition = "pass"
33 Fuel_Injector_P_Drop_Condition = "pass"
34
35 if Ox_pre_Injector_pressure - P0 < Plow_check then
36     Ox_Injector_P_Drop_Condition = "fail"
37 end if
38 if Ox_pre_Injector_pressure - P0 > Phigh_check then
39     Ox_Injector_P_Drop_Condition = "fail"
40 end if
41
42 if Fuel_pre_Injector_pressure - P0 < Plow_check then
43     Fuel_Injector_P_Drop_Condition = "fail"
44 end if
45 if Fuel_pre_Injector_pressure - P0 > Phigh_check then
46     Fuel_Injector_P_Drop_Condition = "fail"
47 end if
48
49 Ox_Injector_P_Drop = (Ox_pre_Injector_pressure - P0) / P0
50 Fuel_Injector_P_Drop = (Fuel_pre_Injector_pressure - P0) / P0
51
52 ' calculate DeltaR_Throat
53 DeltaR_Throat = LOX_radrii(5) - LH2_radrii(5)
54
55 ' calculate chamber outer radius located at base of engine
56 Chamber_Outer_Radius = LOX_radrii(0) + Chamber_Thickness(0)

```

Listing A.29 above contains the source code for the Sanity Checks component. The first calculation compares the total thickness of the aerospike cooling and structural jackets to the radius of the aerospike at every station along the length of the nozzle, Lines 11 - 25. The component uses a *for-loop* to iterate over the aerospike stations and compare the total thickness (calculated by summing the cooling channel height, the cooling channel thickness, the cooling channel top thickness, and the structural jacket thickness) to the radius of the aerospike. In Lines 12 - 14, the first *if statement* implements the test for the total thickness versus the aerospike radius. If the test condition is true, the thickness exceeds the radius at the current station, and the test fails, otherwise it passes for this station, and the iteration continues. The second *if statement*, shown in Line 20, throws an exception when the test fails, causing the model execution to be halted, and the current design point to be treated as a failed run, which ModelCenter treats as an invalid design since it includes unbuildable geometry.

The second calculation compares the pressure drops at the injector faces to expected values by comparing the difference between the pre-injector pressure and the chamber pressure to the low and high pressure drop limits, 10% and 40% of chamber pressure respectively. Lines 35 - 40 implement the pressure drop calculation for the LOX expander cycle. The same process is used for the LH2 cycle in Lines 42 - 47. The last block of code in Lines 49 - 50 report the pressure drops as a percentage so they can be used by the ModelCenter Optimization Tool as constraint values to guide optimization studies toward designs which fall in the expected range of pressure drops.

The third calculation computes the difference between the outer and inner radii at the throat (*DeltaR_Throat*). Line 53 implements this calculation by taking the difference between the chamber and aerospike radii at the throat. The last calculation computes the

chamber outer radius (*Chamber_Outer_Radius*) in Line 56. This calculation is a simple summation of the radius of the chamber cooling channel at the base of the engine and the thickness of the chamber wall at the base of the engine.

The analysis above shows the component correctly detects DEAN designs with infeasible aerospike structures, correctly calculates the pressure drops across the injector face for the two expander cycles as well as the difference between the outer and inner radii at the throat and the outer chamber radius. These calculations constitute the remaining system level constraints, validating this component.

A.7 Conclusion

The results of this appendix verify and validate the individual analysis modules in the fourth generation DEAN model. The inspection of the source code for each component confirms the implementation and underlying engineering assumptions. Tests of critical analyses including the calculation of the aerospike contour and the estimation of the pump pressure ratios further demonstrate the correct function of the analysis modules. Finally, comparisons of each module's results to its purpose validate the module's inclusion in the system level DEAN model.

Appendix B: Revisiting Previous Results with the Fourth Generation DEAN Model

The three designs from previous DEAN research were reevaluated using the fourth generation DEAN model to confirm the results of earlier research. For each design, the system level design variables were entered into the updated DEAN model and then the model was run to calculate the engine performance.

Several of the system level design variables are common to all three designs. These design variables represent system level assumptions in the model and are listed in Table B.1.

Table B.1: Shared Design Variable Values for Model Comparisons

Variable	Value
Ambient Pressure Decision	Operational
Operational Pressure (psia)	0.001
Cooling Geometry Option	Channel Cover + Structural Jacket
Percent Weight of Hardware	5%
Cowl Length	0.1
Factor of Safety	1.5
Material Strength Option	Yield Strength
LOX Pipe Material	INCONEL 718
LH2 Pipe Material	INCOLOY 909

The first generation DEAN design, developed by Martin, predates any of the parameterizations of the DEAN model. It also predates the architecture update of routing all of the fuel flow through the cooling channels. In Martin's design, only half of the fuel flow was routed through the cooling channels. As such, its design variables must be

recomputed. Table B.2 lists the values for the design variables and the source for each value.

Table B.2: Design Variable Values for Generation 1 DEAN Model

Variable	Value	Source
Expansion Ratio	4.94	$\epsilon = A_e/A_t = \pi(5^2)/15.9$
Throat Area (in ²)	15.9	Gen 1 DEAN Model
Chamber Length (in)	24	Gen 1 DEAN Model
Characteristic Length (in)	126.5	Manual Testing
Vacuum Thrust (lbf)	57,231	Gen 1 DEAN Results
Oxidizer-to-Fuel Ratio	7.0	Gen 1 DEAN Model
Chamber Throat AR	3.0	Gen 1 DEAN Model
Chamber Stations Adjustment	0.95	Manual Testing
Chamber Station 5 Adjustment	1.11	Manual Testing
Chamber Cooling Channels Ratio	25.0	Manual Testing
Nozzle Throat AR	0.57	Gen 1 DEAN Model
Nozzle Station 1 Adjustment	13.0	Manual Testing
Nozzle Station Spike Adjustment	2.33	Manual Testing
Aerospike Cooling Channels Ratio	11.2	Manual Testing
Chamber Structural Jacket Material	Aluminum 7075-T6	Martin's Thesis
Chamber Cooling Jacket Material	Silicon Carbide	Martin's Thesis
Aerospike Structural Jacket Material	Silicon Carbide	Manual Testing
Aerospike Cooling Jacket Material	Aluminum 7075-T6	Manual Testing
Aerospike Tip Material	Niobium	Martin's Thesis

The first attempt to run Martin's design failed to converge on working cooling channel thicknesses in the aerospike. Martin selected copper for the aerospike material, however, the copper was being overheated (for some cases it was reaching over 500% of its melting point). The aerospike materials were updated to match the chamber materials to resolve this error. Additionally, a number of adjustments were required to Martin's design point as documented to adapt it to fit the parameterizations in the revised DEAN model. For example, the calculating the characteristic length from Martin's other design values does not yield the correct internal chamber geometry. This discrepancy is caused by the approximations used in calculating the internal geometry from the system level design variables. Similarly, the aerospike cooling channel geometry had to be corrected to account for the increased mass flow of running all of the LH2 through the cooling channels. These updated values were found using manual testing.

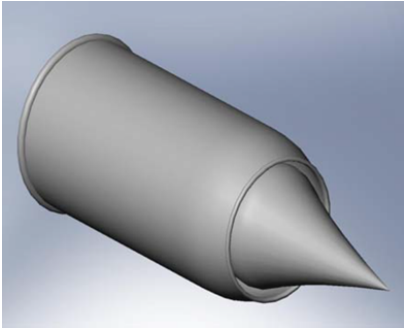
The results of the comparison for the first generation DEAN design are summarized in Table B.3. Two of the results are worth reviewing. First, many of the values are very close matches between the two models, with a few key exceptions. For example, the reported value for the specific impulse is significantly lower in the fourth generation model. This result is due to the findings from Hall's research which indicate the expansion ratio should be calculated from the aerospike geometry instead of using an assumed value such as Martin's expansion ratio of 125. Likewise, the chamber pressure, mass flow, and LH2 pump power are higher in the new model. These increased values are driven by the architecture change between Martin's model and later research which feeds all of the LH2 through the cooling channels instead of feeding half of the LH2 through a bypass around the cooling chamber and LH2 turbine. Finally, the fourth generation model gives a much lower weight, however this is to be expected with the change in materials required to get the model to run to completion.

Second, as mentioned above, Martin's material selection does not converge in the revised model. This result is driven by a difference in assumptions between Martin's research and the revised model. In Martin's research, the cooling channel wall thickness is simply assumed to be 0.02 in and does not include any structural analysis, whereas the current model sizes the cooling channel wall thickness based on the pressure in the cooling channels and the material strength for the cooling channel material at its current temperature. This additional sizing code can, under high channel pressures, experience a divergent cycle where the wall thickness grows to accommodate the channel pressure which leads to increased wall temperature, which leads to lower material strength, which in turn leads to even greater wall thickness. This cycle continues until the model times out. This behavior explains the need to change the aerospike material selection, as the copper from Martin's design was not able to withstand the pressures and temperatures in the cooling channels at only 0.02 in thick.

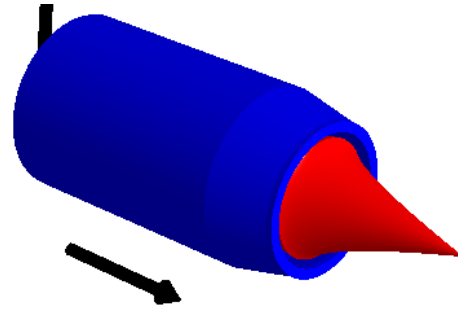
As can be seen in Figure B.1 the agreement between the two models continues with the rendered geometry. The wall thicknesses from the structural sizing codes are in proportion to the manually computed wall sizes from Martin's work. And the aerospike nozzle approximation is also a good match for the nozzle modeled by Martin.

Table B.3: Results of Generation 1 DEAN Design Comparison

Variable	Original Value[2]	Updated Value	Delta
Vacuum Specific Impulse (s)	472.7	412.9	-12.7%
Thrust-to-Weight Ratio	119.0	138.6	16.5%
Chamber Pressure (psia)	1739	1999	15.0%
Chamber Temperature (R)	6586	6630	0.7%
Total Mass Flow (lbm/s)	121.1	138.6	14.5%
Maximum Mach Number, LOX	0.57	0.48	-15.8%
Maximum Mach Number, LH2	0.67	0.74	10.4%
Chamber Wall Temp (% Melt Point)	-	65.5	-
Aerospike Wall Temp (% Melt Point)	-	69.5	-
Injector Face Pressure Drop, LOX (%)	-	23.8	-
Injector Face Pressure Drop, LH2 (%)	-	17.6	-
Required Power for LOX Pump (HP)	2587	2591	0.2%
Required Power for LH2 Pumps (HP)	3573	4562	27.7%
Δr_{throat} (in)	0.5	0.53	6.0%
Engine Length (in)	38	36.3	4.5%
Outer Chamber Radius (in)	-	6.8	-



(a) Published Geometry, credit D. Martin[2]



(b) Rendered Geometry

Figure B.1: Geometry Comparison for First Generation DEAN Design

Like the first generation DEAN design, the second generation design point predates many of the current parameterizations of the DEAN model. As such, several of its design variables also had to be recomputed. Table B.4 lists the values for the design variables and the source for each value. The materials selection followed those used in the Martin design point as the second generation model's design is a scaling of Martin's design.

The results of the comparison for the second generation DEAN design are summarized in Table B.5. Note, the second generation DEAN model did not include any structural sizing analyses, so its results do not include weight related values. There are three significant results from this comparison. First, as with the results for first generation DEAN design point, the results showed the updated model yields a much lower specific impulse than the previous models do. As before, this is due to the change in the modeling assumption for the expansion ratio first made by Hall.

Second, the maximum Mach number for the LH2 cycle was quite different between the two models. Recall, the second generation DEAN model used a static set of values for the pressure profile guesses in the two expander cycles. This decision was an artifact

Table B.4: Design Variable Values for Generation 2 DEAN Model

Variable		Value	Source
Expansion Ratio		4.16	$\epsilon = A_e/A_t = \pi(5^2)/18.9$
Throat Area (in ²)		18.9	Gen 2 DEAN Results
Chamber Length (in)		14.25	Gen 2 DEAN Model
Characteristic Length (in)		51.3	$L^* = V_c/A_t = 970.0/18.9$
Vacuum Thrust (lbf)		50,900	Gen 2 DEAN Results
Oxidizer-to-Fuel Ratio		6.0	Gen 2 DEAN Model
Chamber Throat AR		3.0	Gen 2 DEAN Model
Chamber Stations Adjustment		0.95	Manual Testing
Chamber Station 5 Adjustment		1.11	Manual Testing
Chamber Cooling Channels Ratio		25.0	Manual Testing
Nozzle Throat AR		0.57	Gen 2 DEAN Model
Nozzle Station 1 Adjustment		13.0	Manual Testing
Nozzle Station Spike Adjustment		2.33	Manual Testing
Aerospike Cooling Channels Ratio		11.2	Manual Testing
Chamber Structural Jacket Material	Aluminum 7075-T6		Martin's Thesis
Chamber Cooling Jacket Material	Silicon Carbide		Martin's Thesis
Aerospike Structural Jacket Material	Silicon Carbide		Manual Testing
Aerospike Cooling Jacket Material	Aluminum 7075-T6		Manual Testing
Aerospike Tip Material	Niobium		Martin's Thesis

from Martin's original model. The revised model calculates these guesses based on the current design point. The cooling channel pressure levels, and in turn the maximum Mach numbers, depend greatly on these guessed pressure levels. The significant difference between the dynamically generated values and Martin's static values in the LH2 cycle led

to vastly different solutions for the actual pressure profiles which yielded very different Mach numbers.

Finally, the original research in the second generation DEAN predates calculations for the thrust-to-weight ratio, and therefore had to make assumptions about the impact of its proposed design changes on the thrust-to-weight ratio. The updated DEAN model yielded a thrust-to-weight ratio 194.1 for second generation design, an improvement of 63% over the first generation DEAN results. Clearly this design achieved the desired result of further optimizing the DEAN with respect to the engine's thrust-to-weight ratio.

Figure B.2 shows the rendered geometry for the second generation DEAN design. There was no previously published geometry to compare the rendering to as there was no automated rendering available in the second generation model.

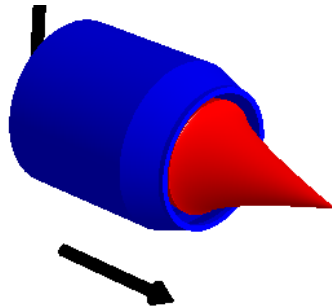


Figure B.2: Geometry for Second Generation DEAN Design

Table B.5: Results of Generation 2 DEAN Design Comparison

Variable	Original Value[27]	Updated Value	Delta
Vacuum Specific Impulse (s)	489.0	422.8	-13.5%
Thrust-to-Weight Ratio	-	194.1	-
Chamber Pressure (psia)	1310	1517	15.8%
Chamber Temperature (R)	6413	6440	0.4%
Total Mass Flow (lbm/s)	104	120.4	15.8%
Maximum Mach Number, LOX	0.37	0.46	24.3%
Maximum Mach Number, LH2	0.96	0.46	-52.1%
Chamber Wall Temp (% Melt Point)	-	57.1	-
Aerospike Wall Temp (% Melt Point)	-	35.0	-
Injector Face Pressure Drop, LOX (%)	-	19.8	-
Injector Face Pressure Drop, LH2 (%)	-	17.7	-
Required Power for LOX Pump (HP)	1053	1333	26.6%
Required Power for LH2 Pumps (HP)	3847	3688	-4.1%
Δr_{throat} (in)	0.58	0.64	10.3%
Engine Length (in)	27.9	26.0	-6.8%
Outer Chamber Radius (in)	-	6.5	-

The third generation DEAN design, developed by J. Hall, was the first to incorporate structural sizing for the cooling and structural jackets in the model's automated design loop. The initial drafts of the fourth generation DEAN model included the same sizing code as Hall's model. However, the code review conducted during the verification process revealed anomalies in Hall's structural sizing codes which led to over sized components. Addressing the anomalies led to updates to the sizing codes for both the cooling and structural jackets. These updates were expected to result in lighter weight designs. Hall's model was also the model with the closest parameterization to the current research. As such, most of the values for the design variables can be sourced directly from his model and analysis. One key set of values was missing from this documentation: the number of cooling channels in both expander cycles. Trade studies were run to find values which yielded similar maximum Mach numbers. Table B.6 lists the values for the design variables and the source for each value.

The results of the comparison for the third generation DEAN design are summarized in Table B.7. The fourth generation DEAN model was able to capture a design based on Hall's work which was quite close to his results. The key difference occurred in the values related to the thrust-to-weight ratio and the power required for the pumps. The improved thrust-to-weight ratio is driven by a weight savings of nearly 49 lbf, with a corresponding increase in the thrust-to-weight ratio. This difference in weight was driven by three factors. First, the chamber cooling channels had far lower pressures which result in a thinner wall for the chamber structural jacket. Second, the differences in the structural sizing codes between the third and fourth generation models included changes which yielded less conservative estimates for wall thicknesses, leading to thinner walls in both structural jackets. Third, the fourth generation model gave a significantly lower power required for both the LOX and LH2 pumps, which resulted in weight savings. The power savings for the pumps was

Table B.6: Design Variable Values for Generation 3 DEAN Model

Variable		Value	Source
Expansion Ratio		4.16	$\epsilon = A_e/A_t = \pi(5^2)/18.0$
Throat Area (in ²)		18.0	Gen 3 DEAN Model
Chamber Length (in)		14.5	Gen 3 DEAN Model
Characteristic Length (in)		37.8	Gen 3 DEAN Model
Vacuum Thrust (lbf)		50,161	Gen 3 DEAN Model
Oxidizer-to-Fuel Ratio		6.0	Gen 3 DEAN Model
Chamber Throat AR		1.5	Gen 3 DEAN Model
Chamber Stations Adjustment		1.0	Gen 3 DEAN Model
Chamber Station 5 Adjustment		1.0	Gen 3 DEAN Model
Chamber Cooling Channels Ratio		11.0	Manual Testing
Nozzle Throat AR		0.67	Gen 3 DEAN Model
Nozzle Station 1 Adjustment		1.0	Gen 3 DEAN Model
Nozzle Station Spike Adjustment		1.0	Gen 3 DEAN Model
Aerospike Cooling Channels Ratio		6.5	Manual Testing
Chamber Structural Jacket Material	Aluminum 7075-T6		Gen 3 DEAN Model
Chamber Cooling Jacket Material	Silicon Carbide		Gen 3 DEAN Model
Aerospike Structural Jacket Material	Oxygen-Free Copper		Gen 3 DEAN Model
Aerospike Cooling Jacket Material	Oxygen-Free Copper		Gen 3 DEAN Model
Aerospike Tip Material	Oxygen-Free Copper		Gen 3 DEAN Model

driven by lower pressure ratios which resulted from a difference between the dynamically generated values and the static values from the first generation model.

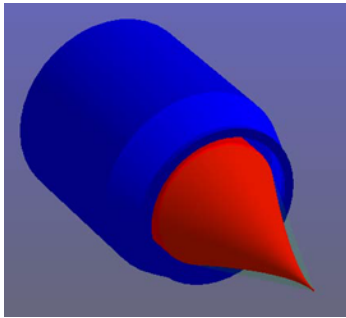
Three other results bear closer inspection. First, the values for the specific impulse and the total mass flow are very similar between the two models. Both values are within

approximately 1% between the two models. This agreement indicates the custom nozzle element used in the fourth generation DEAN model returns similar results to Hall's more complex TDK analysis. Second, Hall's values for the maximum pressures in the cooling channels are reported as approximations in the table since he reports these values in graphs and not tabular form.

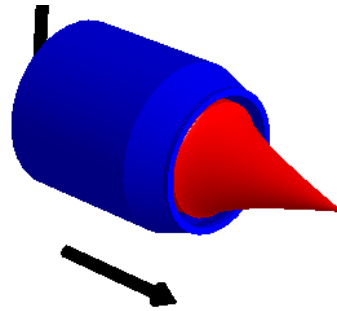
Table B.7: Results of Generation 3 DEAN Design Comparison

Variable	Original Value[4]	Updated Value	Delta
Vacuum Specific Impulse (s)	430.6	425.7	-1.1%
Thrust-to-Weight Ratio	142.2	163.9	15.3%
Chamber Pressure (psia)	1548	1565	1.1%
Chamber Temperature (R)	-	6477	-
Total Mass Flow (lbm/s)	116.5	117.9	1.2%
Maximum Mach Number, LOX	0.21	0.33	52.4%
Maximum Mach Number, LH2	0.37	0.38	-2.7%
Chamber Wall Temp (% Melt Point)	58.6	59.7	1.9%
Aerospike Wall Temp (% Melt Point)	43.0	49.1	14.2%
Injector Face Pressure Drop, LOX (%)	-	22.3	-
Injector Face Pressure Drop, LH2 (%)	-	21.2	-
Required Power for LOX Pump (HP)	1945	1442	-25.9%
Required Power for LH2 Pumps (HP)	3847	3340	-13.2%
Δr_{throat} (in)	0.61	0.61	0.0%
Engine Length (in)	26.7	26.4	-1.1%
Outer Chamber Radius (in)	-	6.5	-

As with the first generation design, Figure B.3 shows there is strong agreement between the rendered geometry for the third generation design. The simplifications made in the fourth generation model to support studying a wider trade space gave similar results for both the chamber and the aerospike nozzle in the geometry rendering.



(a) Published Geometry, credit
J. Hall[4]



(b) Rendered Geometry

Figure B.3: Geometry Comparison for Third Generation DEAN Design

Bibliography

- [1] Sloop, J., *Liquid Hydrogen as a Propulsion Fuel, 1945-1959*, National Aeronautics and Space Administration, 1978.
- [2] Martin, D. F., *Computational Design of Upperstage Chamber, Aerospike, & Cooling Jacket of Dual-Expander Rocket Engine*, (MS Thesis, Air Force Institute of Technology), 2008.
- [3] Huzel, D. and Huang, D., *Modern Engineering for Design of Liquid-Propellant Rocket Engines*, AIAA, 1992.
- [4] Hall, J., *Optimized Dual Expander Aerospike Rocket*, (MS Thesis, Air Force Institute of Technology), 2010.
- [5] Humble, R. W., *Space Propulsion Analysis and Design*, McGraw-Hill Inc, 1995.
- [6] Clark, S., "ULA's common upper stage engine to fly this year," cited June, 2014.
- [7] NASA, "Centaur upper stage being lifted.jpg (web page)," cited 06/25/2014.
- [8] Donahue, B. and Sigmon, S., "The Space Launch System Capabilities with a New Large Upper Stage," *AIAA Space 2013 Conference & Exposition*, AIAA, 2013.
- [9] USAF, "X-37 Orbital Test Vehicle (web page)," cited 04/09/2014.
- [10] Clark, S., "Inspections have begun on Air Force space plane (web page)," cited 04/09/2014.
- [11] "RL10B-2 Propulsion System," Tech. rep., Pratt & Whitney Rocketdyne, 2009.
- [12] Buzzell, J., "Testing for the J-2X Upper Stage Engine," *SpaceOps 2010 Conference*, AIAA, 2010.
- [13] NASA, "The J-2X Engine Fact Sheet," cited 04/09/2014.
- [14] Buttler, K., "AR2-3 Engine Refurbishment and Gas Generator Testing," *35th AIAA/ASME/SAE/ASEE Joint Propulsion Conference and Exhibit: 20-23 June, 1998*, AIAA, 1999.
- [15] Hammond, W., *Design Methodologies for Space Transportation Systems*, AIAA, 2001.
- [16] DoD, "Defense Budget Priorities and Choices Fiscal Year 2014," cited 06/20/2014.
- [17] Center/DD., L., "AFDD 3-14 Space Operations," cited 06/20/2014.

- [18] Command, A. F. S., "Next Generation Engine (NGE) Request for Information (web page)," cited 12/06/2011.
- [19] DeGeorge, D. and Fletcher, S., "The Integrated High Payoff Rocket Propulsion Technology Program and Tactical Missile Propulsion Status," Tech. Rep. AFRL-PR-EN-TP-2002-214, US Air Force, Air Force Research Laboratory, 2002.
- [20] Dumbacher, D., "The Development of the X-37 Re-Entry Vehicle," *55th International Astronautical Congress*, AIAA, 2004.
- [21] Pienkowski, J., Whitmore, S., and Spencer, M., "Analysis of the Aerodynamic Orbital Transfer Capabilities of the X-37 Space Maneuvering Vehicle (SMV)," *41st Aerospace Sciences Meeting and Exhibit*, AIAA, 2003.
- [22] Singer, J., Cook, J., and Singer, C., "NASA Space Launch System Operations Strategy," *SpaceOps 2012 Conference*, AIAA, 2012.
- [23] Mc Hugh, B., "Numerical Analysis of Existing Liquid Rocket Engines as a Design Process Starter," *31st AIAA/ASME/SAE/ASEE Joint Propulsion Conference and Exhibit: 10 - 12 July 1995*, AIAA, San Diego, CA, 1995.
- [24] Sutton, G. P., *Rocket Propulsion Elements, Eighth Edition*, John Wiley & Sons Inc, 2010.
- [25] Arguello, A. A., *The Concept Design of a Split Flow Liquid Hydrogen Turbopump*, (MS Thesis, Air Force Institute of Technology), 2008.
- [26] Strain, W. S., *Design of an Oxygen Turbopump for a Dual Expander Cycle Rocket Engine*, (MS Thesis, Air Force Institute of Technology), 2008.
- [27] Simmons, J. and Branam, R., "Parametric Study of Dual-Expander Aerospike Nozzle Upper Stage Rocket Engine," *AIAA Journal of Spacecraft and Rockets*, Vol. 48, No. 2, 2011, pp. 355–367.
- [28] Wiesel, W. E., *Spaceflight Dynamics, Second Edition*, McGraw-Hill, 1997.
- [29] *REDTOP-LITE version 1.85 User's Guide*, SpaceWorks Software, Atlanta, GA, 2011.
- [30] *RPA User Manual*, 2011.
- [31] *NPSS v1.6.4 User Guide*, NASA Glenn Research Center, Cleveland, OH, 2006.
- [32] *NPSS v1.6.4 Rockets Supplement*, NASA Glenn Research Center, Cleveland, OH, 2006.
- [33] Binder, M., "An RL10A-3-3A Rocket Engine Model Using the Rocket Engine Transient Simulator (ROCETS) Software," *AIAA/SAE/ASME/ASEE 29th Joint Propulsion Conference and Exhibit: June 28-30, 1993*, AIAA, Monterey, CA, 1993.

- [34] Bond, P., editor, *Jane's Space Systems and Industry 2011 - 2012*, Jane's Information Group Limited, 2011.
- [35] "RL10A-4 Propulsion System," Tech. rep., Pratt & Whitney Rocketdyne, 2009.
- [36] Baker, D., editor, *Jane's Space Directory 2006 - 2007*, Jane's Information Group Limited, 2006.
- [37] "NASA - Nano-Satellite Launch Challenge," cited January, 2011.
- [38] Corporation, T. B., "X-37B Orbital Test Vehicle (web page)," cited 04/09/2014.
- [39] Sutton, G., *History of Liquid Propellant Rocket Engines*, AIAA, 2006.
- [40] Beichel, R., O'Brien, C., and Taylor, J., "Is There a Future in Liquid Rocket Propulsion?" *AIAA/SAE/ASME 27th Joint Propulsion Conference*, AIAA, 1991.
- [41] Nguyen, T., Hyde, J., and Ostrander, M., "Aerodynamic Performance Analysis of Dual-Fuel/Dual-Expander Nozzles," *AIAA/ASME/SAE/ASEE 24th Joint Propulsion Conference*, AIAA, 1988.
- [42] Hagemann, G., Manski, D., and Kruille, G., "Dual Expander Engine Flowfield Simulations," *31st AIAA/ASME/SAE/ASEE Joint Propulsion Conference and Exhibit*, AIAA, 1995.
- [43] Froning, H. and Beichel, R., "Impact of dual fuel and dual expander rockets on RLVs," *AIAA Space Programs and Technologies Conference: 1996*, AIAA, 1996.
- [44] Buckmann, P., Shimp, N., Viteri, F., and Proctor, M., "Design and Test of an Oxygen Turbopump For a Dual Expander Cycle Rocket Engine," *AIAA/ASME/SAE/ASEE 25th Joint Propulsion Conference*, AIAA, 1989.
- [45] Besnard, E. and Garvey, J., "Development and Flight-Testing of Liquid Propellant Aerospike Engines," *40th AIAA/ASME/SAE/ASEE Joint Propulsion Conference and Exhibit*, AIAA, 2004.
- [46] Ladeinde, T. and Hsun, C., "Performance Comparison of a Full-Length and a Truncated Aerospike Nozzle," *46th AIAA/ASME/SAE/ASEE Joint Propulsion Conference & Exhibit*, AIAA, 2010.
- [47] Gross, K., "Performance Analysis of Aerospike Rocket Engines," Tech. Rep. Techdoc 19730004121, NASA, 1972.
- [48] Angelino, G., "Approximate Method for Plug Nozzle Design," *AIAA Journal*, Vol. 2, No. 10, 1964, pp. 1834–1835.
- [49] Dunn, S. and Coats, D., "Nozzle Performance Predictions Using the TDK 97 Code," *33rd AIAA/ASME/SAE/ASEE Joint Propulsion Conference and Exhibit*, AIAA, 1997.

- [50] Wuye, D., Yu, L., Xianchen, C., and Haibin, T., "Aerospike Nozzle Performance Study and its Contour Optimization," *37th AIAA/ASME/SAE/ASEE Joint Propulsion Conference and Exhibit*, AIAA, 2001.
- [51] Grieb, D. e. a., "Design and Analysis of a Reusable N₂O-Cooled Aerospike Nozzle for Labscale Hybrid Rocket Motor Testing," *47th AIAA/ASME/SAE/ASEE Joint Propulsion Conference and Exhibit*, AIAA, 2011.
- [52] O'Leary, R. and Beck, J., "Nozzle Design," *Threshold: Pratt & Whitney Rocketdyne's engineering journal of power technology*, Vol. Spring, 1992.
- [53] Sackheim, R., "Overview of United States Space Propulsion Technology and Associated Space Transportation Systems," *Journal of Propulsion and Power*, Vol. 22, No. 6, 1992, pp. 1310–1333.
- [54] Bui, T. e. a., "Flight Research of an Aerospike Nozzle Using High Power Solid Rockets," *41st AIAA/ASME/SAE/ASEE Joint Propulsion Conference and Exhibit*, AIAA, 2005.
- [55] Besnard, E. and Garvey, J., "Development and Flight-Testing of Liquid Propellant Aerospike Engines," *40th AIAA/ASME/SAE/ASEE Joint Propulsion Conference and Exhibit*, AIAA, 2004.
- [56] Besnard, E. and Garvey, J., "Aerospike Engines for Nanosat and Small Launch Vehicles (NLV/SLV)," *Space 2004 Conference and Exhibit*, AIAA, 2004.
- [57] Corporation, T. B., "Annular-Aerospike.jpg (web page)," cited 06/25/2014.
- [58] NASA, "Twin Linear Aerospike XRS-2200 Engine PLW edit.jpg (web page)," cited 06/25/2014.
- [59] Garvey, K., "Aerospike close-up.jpg (web page)," cited 06/25/2014.
- [60] *ModelCenter 10.2 User Manual*, Phoenix Integration, Blacksburg, VA, 2013.
- [61] Moen, M., *Methane Dual Expander Aerospike Nozzle Rocket Engine*, (MS Thesis, Air Force Institute of Technology), 2012.
- [62] Rao, S., *Engineering Optimization: Theory and Practice*, John Wiley & Sons, fourth edition ed., 2009.
- [63] Minick, A. and Peery, S., "Design and Development of an Advanced Liquid Hydrogen Turbopump," *34th AIAA/ASME/SAE/ASEE Joint Propulsion Conference and Exhibit: 13-15 July, 1998*, AIAA, 1998.
- [64] *ModelCenter 9.0 User Manual*, Phoenix Integration, Blacksburg, VA, 2010.
- [65] "Thermophysical Properties of Fluid Systems," cited May 27, 2010.

- [66] Krach, A. E. and Sutton, A. M., "Another Look at the Practical and Theoretical Limits of an Expander Cycle, LOX/H₂ Engine," *35th AIAA/ASME/SAE/ASEE Joint Propulsion Conference and Exhibit: 20-24 June, 1999*, AIAA, 1998.
- [67] *ModelCenter 10.1 User Manual*, Phoenix Integration, Blacksburg, VA, 2012.
- [68] *Atlas V Launch Services User's Guide, March 2010*, United Launch Alliance, 2010.
- [69] *Delta IV Launch Services User's Guide, June 2013*, United Launch Alliance, 2013.
- [70] Shigley, J. and Mischke, C., *Mechanical Engineering Design*, McGraw-Hill, fifth edition ed., 1989.
- [71] Stewart, J., *Calculus: Concepts and Contexts, Second Edition*, Wadsworth Group, Brooks/Cole, Thomson Learning, 2001.

REPORT DOCUMENTATION PAGE					Form Approved OMB No. 0704-0188	
<p>The public reporting burden for this collection of information is estimated to average 1 hour per response, including the time for reviewing instructions, searching existing data sources, gathering and maintaining the data needed, and completing and reviewing the collection of information. Send comments regarding this burden estimate or any other aspect of this collection of information, including suggestions for reducing this burden to Department of Defense, Washington Headquarters Services, Directorate for Information Operations and Reports (0704-0188), 1215 Jefferson Davis Highway, Suite 1204, Arlington, VA 22202-4302. Respondents should be aware that notwithstanding any other provision of law, no person shall be subject to any penalty for failing to comply with a collection of information if it does not display a currently valid OMB control number. PLEASE DO NOT RETURN YOUR FORM TO THE ABOVE ADDRESS.</p>						
1. REPORT DATE (DD-MM-YYYY)		2. REPORT TYPE		3. DATES COVERED (From — To)		
18-09-2014		Doctoral Dissertation		Jun 2009-Sep 2014		
4. TITLE AND SUBTITLE Design and Evaluation of Dual-Expander Aerospike Nozzle Upper Stage Engine				5a. CONTRACT NUMBER		
				5b. GRANT NUMBER		
				5c. PROGRAM ELEMENT NUMBER		
6. AUTHOR(S) Simmons, III, Joseph R.,				5d. PROJECT NUMBER		
				5e. TASK NUMBER		
				5f. WORK UNIT NUMBER		
7. PERFORMING ORGANIZATION NAME(S) AND ADDRESS(ES) Air Force Institute of Technology Graduate School of Engineering and Management (AFIT/EN) 2950 Hobson Way WPAFB, OH 45433-7765				8. PERFORMING ORGANIZATION REPORT NUMBER AFIT-ENY-DS-14-S-06		
9. SPONSORING / MONITORING AGENCY NAME(S) AND ADDRESS(ES) Intentionally Left Blank				10. SPONSOR/MONITOR'S ACRONYM(S) N/A		
				11. SPONSOR/MONITOR'S REPORT NUMBER(S) N/A		
12. DISTRIBUTION / AVAILABILITY STATEMENT APPROVED FOR PUBLIC RELEASE; DISTRIBUTION UNLIMITED						
13. SUPPLEMENTARY NOTES This work is declared a work of the U.S. Government and is not subject to copyright protection in the United States.						
14. ABSTRACT The goal of the Dual-Expander Aerospike Nozzle, a modification to traditional engine architectures, is to find those missions and designs for which it has a competitive advantage over traditional upper stage engines such as the RL10. Previous work focused on developing an initial design to demonstrate the feasibility of the Dual-Expander Aerospike Nozzle. This research expanded the original cycle model in preparation for optimizing the engine's specific impulse and thrust-to-weight ratio. The changes to the model allowed automated parametric and optimization studies. Preliminary parametric studies varying oxidizer-to-fuel ratio, total mass flow, and chamber length showed significant improvements. Drawing on modeling lessons from previous research, this research developed a new engine simulation capable of achieving a specific impulse comparable to the RL10. Parametric studies using the new model verified the Dual-Expander Aerospike Nozzle architecture conforms to rocket engine theory while exceeding the RL10's performance. Finally, this research concluded by optimizing the Dual-Expander Aerospike Nozzle engine for three US government missions: the Next Generation Engine program, the X-37 mission, and the Space Launch System. The optimized Next Generation Engine design delivers 35,000 lbf of vacuum thrust at 469.4 seconds of vacuum specific impulse with a thrust-to-weight ratio of 127.2 in an engine that is one quarter the size of a comparable RL10. For the X-37 mission, the optimized design operates at 6,600 lbf of vacuum thrust and has a vacuum specific impulse of 457.2 seconds with a thrust-to-weight ratio of 107.5. The Space Launch System design produces a vacuum thrust of 100,000 lbf with a vacuum specific impulse of 465.9 seconds and a thrust-to-weight ratio of 110.2. When configured in a cluster of three engines, the Dual-Expander Aerospike Nozzle matches the J2-X vacuum thrust with a 4% increase in specific impulse while more than doubling the J2-X's thrust-to-weight ratio.						
15. SUBJECT TERMS dual-expander, upper stage, NGE, aerospike, optimization, rocket propulsion						
16. SECURITY CLASSIFICATION OF:			17. LIMITATION OF ABSTRACT	18. NUMBER OF PAGES	19a. NAME OF RESPONSIBLE PERSON	
a. REPORT	b. ABSTRACT	c. THIS PAGE			Dr. Jonathan Black (ENY)	
U	U	U	UU	376	19b. TELEPHONE NUMBER (include area code) (937) 255-3636 x0000 jonathan.black@afit.edu	